EXPLORING RELATIONSHIPS BETWEEN GEOLOGICAL STRUCTURES DELINEATED FROM HIGH RESOLUTION GEOPHYSICAL DATA COLLECTED OVER 1:50,000 MAPSHEETS 2229AB MAPUNGUBWE AND 2229AD COILA, BEIT BRIDGE TERRANE, CENTRAL ZONE, LIMPOPO BELT, SOUTH AFRICA.

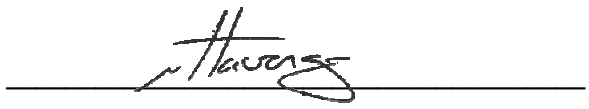
Marinda Havenga

A Dissertation submitted to the Faculty of Science, University of the Witwatersrand, Johannesburg, in fulfilment of the requirements for the degree of Master of Science.

Johannesburg, 2013

DECLARATION

I declare that this Dissertation is my own, unaided work. It is being submitted for the Degree of Master of Science at the University of the Witwatersrand, Johannesburg. It has not been submitted before for any degree or examination at any other University.



(Signature of candidate)

22nd day of February 20 13 in Johannesburg

ABSTRACT

High resolution aeromagnetic and radiometric data covering the 1:50,000 mapsheets 2229AB Mapungubwe and 2229AD Coila were collected by the Council for Geoscience and interpreted in this study. Several generations of magnetised lineaments were identified and modelled as mafic dykes. North-northwest, east-northeast and east-west trending lineaments occur in the pre-Karoo basement (~2.04 Ga to Dwyka) and east-west trending lineaments predominate in Karoo sediments (<183 Ma).

A number of circular magnetic anomalies occur in north-northwest and east-northeast trending clusters in the southwest of the study area. These were interpreted to be intrusive plugs – possibly feeders for the dolerite sills and dykes that occur in the area.

Radiometric data delineate geological units within the pre-Karoo basement. Granitic to granodioritic rocks (2.6 Ga) are enriched in uranium and thorium while tonalitic rocks are not.

Geological cross-sections, constructed along flight lines and tie-lines, suggest that there are two or more sills at depth under the southwestern portion of the study area intruded by the Venetia kimberlite pipes. In addition a large strongly magnetic anomaly with no surface expression was identified in the northeastern area and modelled to be at about 1200 m depth.

ACKNOWLEDGEMENTS

Dissertation supervision was provided by Dr. Susan Webb and Prof. Jay Barton.

Special thanks to:

- the Council for Geoscience (CGS) for financial assistance and the collection of the airborne data.
- Dr. David Mabunda (CEO SANParks) for granting permission to fly over a section of the Mapungubwe reserve.
- Mrs. Debbie Killian (CGS) for assisting in the creation of 3D images.
- My colleagues, Erna Hattingh, Annabel Graham, Janine Cole and Patrick Cole at the Council for Geoscience for their support and understanding during crunch-time.
- My family for their support and understanding when I had to work instead of spending time with them.

TABLE OF CONTENT

CHAPTER 1. Introduction **1**

CHAPTER 2. Geological Setting of the Study Area **4**

CHAPTER 3. Previous Geophysical Studies **11**

3.1. Regional Airborne Studies 11

3.2. Other Studies 17

3.3. Summary of previous geophysical studies 24

CHAPTER 4. Data Collection and Results **25**

4.1. Acquisition 25

4.1.1. Equipment specifications 26

4.1.2. Data acquisition and in-field verification 28

4.2. Data Processing 29

4.2.1. Magnetic Processing 29

4.2.2. Digital Terrain Model (DTM) Creation 32

4.2.3. Spectrometer Processing 32

4.3. Summary of data collection 39

CHAPTER 5. Geophysical Data Sets **40**

5.1. Magnetic data 40

5.1.1. International Geomagnetic Reference Field (IGRF) 43

5.1.2. Qualitative Observations 45

5.1.3. Filters 48

5.2. Digital Terrain Model Data 60

5.3. Radiometric data 62

5.3.1. Total Count 65

5.3.2. Potassium channel 67

5.3.3. Thorium channel 69

5.3.4. Uranium channel 72

5.4. Summary of datasets 74

CHAPTER 6. Qualitative Interpretation **75**

6.1. Radiometric data 75
6.1.1. Interpretation of the ternary image of the radiometric data 77
6.1.2. Interpretation of the potassium channel radiometric data 79
6.1.3. Interpretation of the uranium channel data 81
6.1.4. Interpretation of the thorium channel radiometric data 83
6.1.5. Interpretation of the total count radiometric data. 85
6.1.6. Combining the radiometric interpretations 87
6.2. Magnetic data 91
6.2.1. Lineaments 91
6.2.2. Sills 109
6.2.3. Circular and round magnetic anomalies 111
6.2.4. Summary of magnetic interpretation 116
CHAPTER 7. Quantitative Interpretation 119
7.1. Preparing to model the magnetic anomalies 119
7.1.1. Modelling software 119
7.1.3. Source body type and depth determination 120
7.1.4. Physical Properties 122
7.2. Modelling of the linear magnetic anomalies 129
7.2.1. Profile 1 131
7.2.2. Profile 2 132
7.2.3. Profile 3 133
7.2.4. Profile 4 136
7.2.5. Profile 5 138
7.2.6. Profile 6 140
7.2.7. Profile 7 142
7.2.8. Profile 8 144
7.2.9. Profile 9 146
7.2.10. Profile 10 149
7.2.11. Profile 11 150

7.2.12. Profile 12 152
7.2.13. Profile 13 154
7.2.14. Profile 14 157
7.2.15. Profile 15 158
7.2.16. Profile 16 161
7.2.17. Profile 17 163
7.2.18. Profile 18 166
7.2.19. Profile 19 167
7.2.20. Profile 20 169
7.2.21. Profile 21 170
7.2.22. Profile 22 172
7.3. Euler Deconvolution 175
7.3.1. Profile 1 177
7.3.2. Profile 2 178
7.3.3. Profile 3 179
7.3.4. Profile 4 180
7.3.5. Profile 5 181
7.3.6. Profile 6 182
7.3.7. Profile 7 183
7.3.8. Profile 8 184
7.3.9. Profile 9 185
7.3.10. Profile 10 186
7.3.11. Profile 11 187
7.3.12. Profile 12 188
7.3.13. Profile 13 189
7.3.14. Profile 14 190
7.3.15. Profile 15 191
7.3.16. Profile 16 192
7.3.17. Profile 17 193

7.3.18. Profile 18 194
7.3.19. Profile 19 195
7.3.20. Profile 20 196
7.3.21. Profile 21 197
7.3.22. Profile 22 198
7.5. Conclusion of quantitative interpretation 199
CHAPTER 8. Modelling of cross sections through the study area 202
8.1. North-south cross sections 207
8.1.1. Flight line L155 207
8.1.2. Flight line L330 210
8.1.3. Flight line L535 213
8.2. East-west cross sections 216
8.2.1. Tie-line T9020 216
8.2.2. Tie-line T9040 218
8.2.3. Tie-line T9055 221
8.2.4. Tie-line T9070 224
8.3. Comparing the geophysical interpretation with mapped geology 226
8.4. Combining the profiles to generate a three dimensional picture 229
CHAPTER 9. Conclusions 236
9.1. Magnetic Lineaments 236
9.2. Circular anomalies 236
9.3. Radiometric data as a mapping aid 237
9.4. Cross sections and 3-dimensional modelling 238
References 239

LIST OF FIGURES

Figure 1.1. Locality of the 2229AB Mapungubwe and 2229AD Coila 1:50,000 map sheets, shown in red on a plot of the 1:250,000 map sheet layout. 3

Figure 2.1 The simplified geology and structure of the Limpopo Belt (after Barton et al., 2006). The study area is indicated in red. 5

Figure 2.2. Geology of the study area (2229AB & 2229AD) taken from the 2228 Alldays 1:250,000 map (Council for Geoscience, 2000). 6

Figure 2.3. Legend description of the geology map of 2229AB and 2229AD..... 7

Figure 2.4. Locations of sample sites with relation to study area. Modified from Hanson et al (2004). 9

Figure 2.5. Distribution of dolerite sills cropping out around the Venetia Kimberlite pipes, northeast of Alldays. (Modified from Brandl, 2002). These sills are saucer-shaped in profile (Brandl, 2002)..... 10

Figure 3.1. Map showing the regional airborne data survey blocks and the corresponding companies that undertook the surveys. 12

Figure 3.2. Regional aeromagnetic data for Limpopo Belt. Data were collected at 1000 m line spacing and 200 m flight height. (SADC dataset). 1:250,000 mapsheets are indicated in black and the study area in yellow. 13

Figure 3.3. Comparison of Barton et al. (2006) simplified geology (in black) and structures inferred as part of this study (in red) from the regional magnetic data. 15

Figure 3.4. Regional total count radiometric data (1000m line spacing) over the study area with mapped quartzfeldspathic rocks indicated as hatched areas on it. 16

Figure 3.5. . Map showing orientation of shear wave splitting fast polarization directions from the Kaapvaal Seismic Array (black bars) and from the high-resolution Kimberley Seismic Array (yellow bar, array average). Purple dots represent measurements with zero anisotropy (Silver et al., 2004). 17

Figure 3.6. A scenario that could cause the anisotropic structure of the mantle and its relation to the surface geology of cratonic South Africa. From Silver et al. (2004)..... 19

Figure 3.7. Simplified geological map of the Limpopo Belt, Zimbabwe and Kaapvaal Cratons depicting the locations of the geophysical data that were reviewed by De Beer and Stettler (1992). The gravity section of Coward and Fairhead (1980) is indicated with VW, the seismic refraction line of Suart and Zengeni (1987) is indicated with XY, the gravity profiles of De Beer et al. (1984) are indicated with AA' and BB'. The position of the deep seismic reflection line from Pont Drift (Durrheim et al. 1992) is also indicated on the map. The study area is indicated in red. The numbered square dots are ultra-deep geoelectrical sounding locations. 20

Figure 3.8. Line drawing of the migrated Limpopo seismic reflection profile showing the prominent reflections. PD = Pont Drift, A = Alldays, V = Vivo, D = Dendron, K = Kalkbank and Pb = Pietersburg. (Durrheim et al., 1992) 21

Figure 3.9. Seismic velocity models, ray-trace diagrams and synthetic record sections taken from Durheim et al. (1992). The reduction velocity is 8 km/s. The seismic velocity within each polygon is given in km/s. The only difference between model A and model B is the Moho topography. Observed traveltimes are indicated with geometric symbols. P = Pietersburg, M = Messina, H = Harare. 22

Figure 3.10. Lithological section beneath the ~530 Ma Venetia kimberlite pipes in the Beit Bridge Terrane constructed from pressure and P-wave velocity data and compositions of xenoliths from Venetia kimberlite (Modified from Pretorius, 1996; Pretorius and Barton, 2003a; b) 23

Figure 4.1. Non-calibrated radiometric spectrum shape. The locations of the K, U and Th peaks are displaced relative to their energy window. 27

Figure 4.2. Spectrum shape after energy calibration. Radioelement peaks are located in the correct positions. 27

Figure 4.3. Typical airborne gamma ray spectrum showing the positions of the conventional energy windows (IAEA, 2003). 34

Figure 4.4. Example of aircraft background spectrum (IAEA, 2003) 36

Figure 4.5. Example of cosmic background spectrum (IAEA, 2003) 37

Figure 4.6. Example of a height attenuation curve from IAEA (2003) 39

Figure 5.1. Total magnetic field data, sunshaded with azimuth 45° and elevation 45°. This positions the sun at 45° clockwise from due north and 45° up from the horizon. 41
Figure 5.2. Survey lines and tie lines over an image of the magnetic data. 42
Figure 5.3. The IGRF for the study area shows an increase in total intensity towards the northeast. 45
Figure 5.4. Microlevelled magnetic field intensity data, sunshaded (azimuth 45° & elevation 45°) to emphasize features not striking 45°. Here features striking 135° are the most prominent (Cooper, 2003). The regions labelled A and A' host a number of small, round anomalies, the region labelled B outlines a prominent anomaly of 300 nT in the region mapped as Karoo and (C) is a highly magnetic region (~600 nT) in the northeast. 47
Figure 5.5. The magnetic data upward continued to 500 m. Positive amplitude (A) and negative amplitude (B) east-west trending linear anomalies, positive amplitude east-northeast trending linear anomalies (C), a large amplitude broad magnetic anomaly (D) and high amplitide broad magnetic anomaly (E) are indicated. 49
Figure 5.6. First vertical derivative of the magnetic data. Some of the linear anomalies that are not clear on the total magnetic field data are indicated in region A. 51
Figure 5.7. Second vertical derivative of the magnetic data. Features and textures not visible in the magnetic data become very clear in this data set. A, B, C and D shows examples of areas that are very quiet on the magnetic data, but have a definite texture in the second vertical derivative data. 52
Figure 5.8. Analytical Signal calculated for the magnetic data. (A) shows an example of a linear feature that is not clear on the total magnetic field data. 54
Figure 5.9. Magnetic data reduced to the pole. 56
Figure 5.10. Comparison between the results for different window sizes when applying the AGC filter to magnetic data. The 3x3, 5x5, 7x7 and 9x9 windows are shown in (a), (b), (c) and (d) respectively. The 3x3 window seems to give the sharpest and clearest results, with the results becoming noisier as with increasing window size. 58

Figure 5.11. Automatic Gain Control filter applied to the magnetic data using a 3x3 window. Features that are not clear on the total magnetic field data, but clear on the AGC map are indicated with (A) and (B). 59
Figure 5.12. Sunshaded digital terrain model data with an azimuth of 45° and sun elevation of 45°. 61
Figure 5.13. Geographic map showing roads, rivers, man-made structures and mine workings. 64
Figure 5.14. Total count radiometric data (50 m grid cell size). (A) - Very high total count values (>1400 counts). (B) - Areas of medium values (~800 to 900 counts). (C) - Venetia slimes dam. (D) - Area with values of 320 counts and less. (E) - North trending area with values between 500 and 650 counts. (F) - Higher relief area with values below 500 counts. 66
Figure 5.15. Potassium Channel Radiometric data, 50 m grid cell size. Marked differences between Total count data and K are: (A) - Low K values versus high total count, (B) - high values are more prominent on K than total count and (C) - high total count values not reflected in K. 68
Figure 5.16. Thorium Channel Radiometric data (50 m grid cell size). Main differences between Th data and the other radiometric data are: (A) - a positive Th anomaly that is negative in both K and total count data, (B) – high Th concentration versus low K concentration and (C) – a north to south trending Th low that connects the lows in the north and south. 70
Figure 5.17. Uranium Channel Radiometric data (50 m grid cell size). The data shows an area with high U concentration (A), areas with slightly elevated values (B) adjacent to topographic ridge and a north-south tending area with low U values (C). 73
Figure 6.1. Geological map of the area around the Venetia kimberlite pipes. (Barton et al., 2003). Note that the present study area extends beyond limits of this map. 76
Figure 6.2. The interpretation of the ternary image. The interpreted geology is outlined in yellow. The Venetia kimberlites are shown as purple blobs in the western part of the area inferred to be the Venetia klippe. 78

Figure 6.3. Interpretation of K channel radiometric data with the mapped geological units as thick black outlines. The rivers are indicated as navy blue lines and the interpreted geology as hatched areas. 80
Figure 6.4. Interpretation of the U channel radiometric data. Some of the anomalies in the south correlate with known geology outcrops. Low values correlate to topographic highs and medium values could be caused by deposition in the valleys. Mapped geological units are shown in thick black outline. 82
Figure 6.5. Interpretation of the Th channel radiometric data. Some of the anomalies in the south correlate with known geology outcrops. Low values correlate to topographic highs and medium to high values could be caused by transportation and deposition in the valleys. The mapped geological units are shown as thick black outline. 84
Figure 6.6. Interpretation of the total count radiometric data with the mapped geological units outlined in solid black. 86
Figure 6.7. Final radiometric interpretational map. Interpreted boundaries for the geological units are shown in black outline. 89
Figure 6.8. The geological units derived from radiometric data overlain in red on the high resolution mapped geology. 90
Figure 6.9. Qualitative interpretation of the total magnetic intensity data with IGRF removed, overlain on a faded image of the total field magnetic data. Features to note: E-W trending lineaments (A), ENE to NE trending lineaments (B), slightly ESE trending lineaments (C), negative lineaments (D), same lineament both positive and negative (E), NNW lineaments (F), horizontal displacements (a), abrupt linear edge to anomaly (b) and swarm of NNW trending disruptions (c). 93
Figure 6.10. Interpretation of magnetic data upwards continued by 500 m overlain on a faded image of the upward continued data indicating deeper bodies. An east-west linear trend (A) in the north, east-west trend in the south (B), east-northeast trend through centre (C), north-northwest trending features (D) and north-northwest disruptions (E). .. 95
Figure 6.11. Lineaments inferred from both total field magnetic data and the first vertical derivative of the data overlain on (a) a faded image of the first vertical derivative of the

data and (b) a faded image of the total field data. The thick black lines indicate the lineaments that were added from the interpretation of the first vertical derivative..... 97
Figure 6.12. Formlines from second vertical derivative data over a faded image of the second vertical derivative data (a) and over a faded image of the magnetic data (b) for reference. 98
Figure 6.13. Lineaments inferred from both total field magnetic data and Analytical signal data. The thick black lines indicate the lineaments that are more obvious in the analytical signal data. (a) Shows the lineaments overlain on a faded image of the analytical signal data, while (b) shows them overlain on a faded image of the total magnetic field data. Features that are clearer on the analytical signal data than the total magnetic field data are: lineaments in southeast (A), northeast trending lineament (B), possible faults (C) and features that seem to be part of the north-northwest trending shear zone (D)..... 99
Figure 6.14 a and b. Lineaments inferred from both total field magnetic data and automatic gain control data. The thick black lines indicate the lineaments that are more obvious in the automatic gain control data. (a) Shows the lineaments overlain on a faded image of the analytical, while (b) shows the lineaments overlain on a faded image of the TMI data. 100
Figure 6.15. Principal strike directions of faults and lineaments and dykes as determined from geological maps and aerial photographs (Chernicoff, 1984). These domains were determined from geology type, rather than lineament direction..... 102
Figure 6.16. The aeromagnetic lineament map for the northern and northeastern Transvaal subdivided into six aeromagnetic lineament pattern domains based on lineament direction inferred from the regional magnetic data (Stettler et. al. 1989). The present study area is shown in red. 103
Figure 6.17. Rose diagrams depicting principal strike directions of magnetic lineaments in the individual pattern domains (Stettler et. al., 1989). Current study area shown in red. 104

Figure 6.18. Rose diagrams of all the lineaments (dykes and faults) depicting the strike directions of lineaments in Karoo rocks (a) and basement rocks (b). In (b) the northwest trending lineaments are mostly faults. 105
Figure 6.19. Structures interpreted to be early Proterozoic (2.5 Ga to 1.6 Ga) by Barnettt (2006). The current study area is shown in red and the insert shows an inflated image of the study area. F2 represent the oldest dykes and S1 the youngest. 106
Figure 6.20. Structures interpreted to be (Paleozoic 542 Ma to 251 Ma) by Barnettt (2006). The current study area is shown in red and the insert shows an inflated image of the study area. 107
Figure 6.21. Lineaments inferred from regional magnetic data (black) and high resolution data (red) to compare with Barnettt (2006) lineaments. A, B and C indicate the lineaments inferred from regional data (black lines) correspond to lineaments in Figure 6.20..... 108
Figure 6.22. Dolerite sills inferred from the total field magnetic data in the southern portion of the magnetic data. The outline of the interpreted sill anomalies are based on spatial correspondence with outcrop and continuation of the magnetic anomaly from both the TMI image and enhanced filtered images and the mapped dolerite outcrops. 110
Figure 6.23. Plug shaped bodies inferred from total field magnetic data overlain on a faded image of the data. The extent of (a) is shown as a red rectangle on the study area (b). 112
Figure 6.24. Plug shaped bodies inferred from the first vertical derivative data overlain on a faded image of the data. The extent of the zoomed in map on the left is shown as a red rectangle on the map of the study area (right). 113
Figure 6.25. The Venetia kimberlite intrusions as well as structural features inferred from magnetic data overlain on a faded image of the analytical signal data. 114
Figure 6.26. Translation diagram for all interpreted plugs and rose diagram with 15° radial sector angles showing preferred linear directions. 115
Figure 6.27. Distribution of plug-like bodies in relation to interpreted lineaments from both regional and high resolution data 117

Figure 6.28. Compilation of the interpreted magnetic units and inferred dykes and faults from magnetic data and filtered magnetic data. S1a, S1b, S3a and S3b are inferred sills. 118

Figure 7.1. Borehole locations overlain on TMI image sunshaded from the north east at 45°. Triangles indicate boreholes that don't reach dolerite and circles indicate boreholes that intersect dolerite. Warm colours indicate shallow depth and cool colours deep depth. 121

Figure 7.2. Total magnetic intensity data with the borehole locations and flight lines indicated (a): Triangles indicate boreholes that encounter dolerite. On the right (b) is a blow-up of the area around the boreholes (shown as red rectangle in map on left.). Portion of flight lines L565 (left) and L570 (right) that will be modelled are indicated in red and are either side of the row of boreholes that intersect dolerite. 123

Figure 7.3. The logs for the 6 boreholes located on a north-south trending line of which 3 encounters dolerite (shown in green) at shallow depth. The thickness of the dolerite is unclear as drilling was stopped as soon as dolerite was encountered. (North is left and south is right). The location of tie line T9050 is indicated. 124

Figure 7.4. Flight line L565: A dolerite body modelled with a susceptibility of 0.5 SI, depth between 18 m and 5 m and thickness between a couple of cm and 15 m. 125

Figure 7.5. Flight line L565: A dolerite body modelled with a susceptibility of 0.1 SI, depth between 120 m and 5 m and thickness between a couple of cm and 35 m. 126

Figure 7.6. Flight line L565: A dolerite body modelled with a susceptibility of 0.06 SI, depth between 120 m and 0 m and thickness between a couple of cm and 70 m. 126

Figure 7.7. Flight line L570: A dolerite body modelled with a susceptibility of 0.5 SI, depth between 5 m and 3 m and thickness between 5 m and 16 m. The grid dots are spaced 10 m apart in depth. 127

Figure 7.8. Flight line L570: A dolerite body modelled with a susceptibility of 0.1 SI, depth between 55 m and 3 m and thickness between 25 m and 60 m. The grid dots are spaced 10 m apart in depth. 128

Figure 7.9. Flight line L570: A dolerite body modelled with a susceptibility of 0.06 SI, depth between 55 m and 3 m and thickness between 30 m and 150 m. The grid dots are spaced 10 m apart in depth..... 128
Figure 7.10. Locality map showing the locations of profiles 1 to 22, the locations of flight lines that will be modelled in chapter 8 and the inferred dykes, plugs and sills that are intersected by these profiles and flight lines. 130
Figure 7.11. Profile 1 displayed over the magnetic TMI data (left) and the first vertical derivative data (right). 131
Figure 7.12. Profile 1: Model displaying dykes D9 and D5 as well as sill S1. 132
Figure 7.13. Profile 2 displayed over the magnetic TMI data (left) and the first vertical derivative data (right). 133
Figure 7.14. Profile 2: Model displaying remanent dykes D10 and D20 as well as two unnamed dykes, a positive dyke between D10 and D20 and a remanent dyke similar to D20 just north of D20. 133
Figure 7.15. Profile 3, zoomed out to illustrate the proximity to dykes in north and the south..... 134
Figure 7.16. Profile 3 displayed over the magnetic TMI data (left) and the first vertical derivative data (right). 135
Figure 7.17. Profile 3: Model displaying inferred dyke D8. In the south a slight positive anomaly is visible on the first vertical derivative. This is probably the reason for the calculated and measured fields not matching in the south. 136
Figure 7.18. Profile 4 displayed over the magnetic TMI data (left) and the first vertical derivative data (right). 137
Figure 7.19. Profile 4: Model depicting P1 dipping to the west and S1 over the eastern portion of the profile. The offset between calculated and measured fields in the east is due to the sill extending beyond the profile and the model not..... 137
Figure 7.20. Locality map of profile 5 showing the proximity of a remanently magnetized dyke to the south east of the profile, indicated on the first vertical derivative data (b). .. 138

Figure 7.21. Profile 5 displayed over the magnetic TMI data (left) and the first vertical derivative data (right). 139
Figure 7.22. Profile 5: Model depicting inferred dyke D33 and an unknown dyke just north of it. 140
Figure 7.23. Location map of profile 6 showing the proximity of D4 to the northern end of the profile. 141
Figure 7.24. Profile 6 displayed over the magnetic TMI data (a) and the first vertical derivative data (b). 141
Figure 7.25. Profile 6: Model depicting dyke D23 and two dykes, one south and a remanent one north of it. 142
Figure 7.26. Profile 7 displayed over the magnetic TMI data (a) and the first vertical derivative data (b). 143
Figure 7.27. The model of profile 7 showing D4 and a second dyke north of D4. 144
Figure 7.28. Profile 8 displayed over the magnetic TMI data (a) and the first vertical derivative data (b). 145
Figure 7.29. The model of profile 8 showing dyke D16, a remanent plug and another dyke north of it. 146
Figure 7.30. Locality of profile 9 showing the proximity of the edge of a sill and a northeast trending dyke in the north as well as the effect of the plug P4 in the south. .. 147
Figure 7.31. Profile 9 displayed over the magnetic TMI data (a) and the first vertical derivative data (b). 148
Figure 7.32. The model of profile 9 showing the remanent D11, D12 and a third dyke south of D11. 148
Figure 7.33. Profile 10 displayed over the magnetic TMI data (a) and the first vertical derivative data (b). 149
Figure 7.34. Profile 10 modelled with D13 in the centre, a magnetic body to the southeast and a dyke northwest of it. 150
Figure 7.35. Profile 11 displayed over the magnetic TMI data (a) and the first vertical derivative data (b). 151

Figure 7.36. Model of profile 11 showing D14 with a dyke on either side of D14..... 151
Figure 7.37. Locality map of profile 12 showing the proximity of D25 in the north and what appears to be a remanent dyke on the first vertical derivative data (b)..... 152
Figure 7.38. Profile 12 displayed over the magnetic TMI data (a) and the first vertical derivative data (b). 153
Figure 7.39. The model for profile 12 showing D24 with a dyke on either side of D24. . 154
Figure 7.40. Locality map of Profile 13 showing the proximity to D29 in the north and D27 in the south..... 155
Figure 7.41. Close-up of Profile 13 displayed over the magnetic TMI data (a) and the first vertical derivative data (b)..... 156
Figure 7.42. Model of profile 13 showing dyke D28..... 156
Figure 7.43. Profile 14 displayed over the magnetic TMI data (a) and the first vertical derivative data (b). 157
Figure 7.44. The model of profile 14 showing a body in the south and the dyke D29.... 158
Figure 7.45. Locality map of Profile 15 showing the proximity of D1 in the northwest and D29 in the southeast. 159
Figure 7.46. Profile 15 displayed over the magnetic TMI data (a) and the first vertical derivative data (b). 160
Figure 7.47. Model of profile 15 showing a magnetic body is the southest, D7 and another dyke in the northwest. 161
Figure 7.48. Profile 16 displayed over the magnetic TMI data (a) and the first vertical derivative data (b). 162
Figure 7.49. The model for profile 16 showing D1..... 163
Figure 7.50. Locality map of profile 17 showing the proximity to dykes in the north and south..... 164
Figure 7.51. Profile 17 displayed over the magnetic TMI data (a) and the first vertical derivative data (b). 165
Figure 7.52. The model of D3 on profile 17. 165

Figure 7.53. Profile 18 displayed over the magnetic TMI data (a) and the first vertical derivative data (b). 166
Figure 7.54. The model of the data showing dyke D30 to the south and a remanent dyke to the north and a third dyke in between them. 167
Figure 7.55. Profile 19 displayed over the magnetic TMI data (a) and the first vertical derivative data (b). 168
Figure 7.56. The model of profile 19 showing D31 and D32 just north of D31. 168
Figure 7.57. Profile 20 displayed over the magnetic TMI data (a) and the first vertical derivative data (b). 169
Figure 7.58. The model of profile 20 with D25 to the south and a remanent body to the north. 170
Figure 7.59. Profile 21 displayed over the magnetic TMI data (a) and the first vertical derivative data (b). 171
Figure 7.60. The model of the data showing P3 and P4. 171
Figure 7.61. Locality map showing profile 22 and the proximity to D9 in the north and D1 in the south. 172
Figure 7.62. Profile 22 displayed over the magnetic TMI data (a) and the first vertical derivative data (b). 173
Figure 7.63. Model of the data showing the plug P2. 174
Figure 7.64. Euler results for profile 1 with the inferred bodies shown in green. 177
Figure 7.65. Euler results with inferred bodies in green. 178
Figure 7.66. Euler deconvolution results for profile 3 with the inferred body shown in green. 179
Figure 7.67. Euler deconvolution results for profile 4 with the inferred body shown in green. 180
Figure 7.68. Euler deconvolution results for profile 5 with the inferred locations of the dykes shown in green. 181
Figure 7.69. Results from Euler deconvolution over profile 6 with the possible 3 bodies shown in green. 182

Figure 7.70. Euler deconvolution results for profile 7 with the inferred bodies shown in green. 183
Figure 7.71. Euler deconvolution results for profile 8 showing three inferred bodies shown in green. The black clusters are for SI = 1 and the red cluster for SI = 2. 184
Figure 7.72. Euler deconvolution results for profile 9 with the inferred bodies shown in green. 185
Figure 7.73. Euler deconvolution results for profile 10 with the three bodies shown in green. 186
Figure 7.74. Euler deconvolution results for profile 11 with clusters of results indicating three bodies shown in green. 187
Figure 7.75. Euler deconvolution results for profile 12 with SI of 1 and window size 9. The inferred bodies are shown in green 188
Figure 7.76. Euler deconvolution results for profile 13 with SI = 1 and window size 11. The dyke is shown in green. 189
Figure 7.77. Results of Euler deconvolution for profile 14, using SI of 1 and a window size of 7. The dyke D29 is shown in green. 190
Figure 7.78. Euler deconvolution results using an SI value of 1 and a window size of 7. The positions of the bodies are shown in green. 191
Figure 7.79. Euler deconvolution results for profile 16 using SI 1 and a window size of 7. The position of the dyke is shown in green. 192
Figure 7.80. Results of Euler deconvolution for profile 17 using SI 1 and a window size of 11. The position of dyke D3 is shown in green. 193
Figure 7.81. Euler deconvolution results of profile 18 with SI 1 and window size 9. Dykes are shown in green. 194
Figure 7.82. Euler deconvolution results for profile 19 using SI 1 and window size 11. The two dykes are shown in green. 195
Figure 7.83. Euler deconvolution results for profile 20 using SI 1 and window size 9. D25 is shown in solid green outline and the possible edges of two other bodies are shown is green dashes. 196

Figure 7.84. Euler deconvolution results for profile 21 using window size 9 and SI 2. The two plugs are shown in green. 197
Figure 7.85. Euler deconvolution for profile 22 with SI 2 and window size 7. Plug position is shown in green. 198
Figure 8.1. Location of flight lines and tie-lines used in modelling, as well as the boreholes used in the modelling. 203
Figure 8.2. Borehole logs of the boreholes adjacent to L155. 208
Figure 8.3. L155 modelled in 2.5D using Mag2DC. Depth of profile is 4 km. Not all the geological units in the legend appear in the profile as it is a common key for all models. The mismatch between measured and calculated fields at the ends of the profile is simply due to edge effects of the modelling program..... 209
Figure 8.4. Simplified logs of boreholes adjacent to L330. Coal seams are indicated in solid black..... 211
Figure 8.5. Model of L330. South is to the left and north to the right. Depth of profile is 4 km. The mismatch between measured and calculated fields at the ends of the profile is simply due to edge effects of the modelling program. 212
Figure 8.6. Borehole logs of boreholes adjacent to L535. Coal package is indicated in solid black..... 214
Figure 8.7. Model of flight line L535. Depth of profile is 4 km. The mismatch between measured and calculated fields at the ends of the profile is simply due to effects of the modelling program. 215
Figure 8.8. Model of Tie-line T9020. West is left and east is right. Depth of profile is 4 km. The mismatch between measured and calculated fields at the ends of the profile is simply due to effects of the modelling program..... 217
Figure 8.9. Simplified logs of boreholes along T9040. Coal package is indicated in solid black. 219
Figure 8.10. Model of tie-line T9040. Depth of profile is 4 km. 220
Figure 8.11. Simplified logs of boreholes along T9055. Coal package is indicated in solid black. 222

Figure 8.12. Model of tie-line T9055. Depth of profile is 4 km. 223
Figure 8.13. Image from google earth showing the outline of B1 in white. 224
Figure 8.14. Model of tie-line T9070. Depth of profile is 4 km. 225
Figure 8.15. The geophysical interpretation map showing the bodies delineated from the magnetic data as hatched areas and the surface interpretation form radiometric data as solid areas. 227
Figure 8.16. Legend of geophysical interpretation and mapped geology maps. 228
Figure 8.17. The magnetic interpretation map showing the bodies delineated from the magnetic data. The location of the profiles are shown in maroon and the dykes and magnetic bodies are labelled as they are in the profiles. 231
Figure 8.18. Profiles displayed in three dimensions facing due north in Google Earth. . 232
Figure 8.19. Profiles displayed in Google Earth facing northwest overlain on the magnetic data. 233
Figure 8.20. Profiles displayed in Google Earth facing northeast overlain on the magnetic data. 234
Figure 8.21. Profiles displayed in Google Earth facing west overlain on the magnetic data. 235
Figure 9.1. Google Earth image with the round anomalies inferred from magnetic data shown as black outlines. Venetia is clearly visible on the crossing of the two clusters and none of the anomalies have surface expression. 237

LIST OF TABLES

Table 4.1. Geophysical survey specifications 25

Table 4.2. Standard gamma ray energy windows recommended for natural radioelement mapping (IAEA, 1991). The energy of the photo peak being monitored is shown in brackets after each nuclide 35

Table 7.1. Modelled remanence values. 175

Table 7.2. Structural index values based on the shape of the causative body. (Cooper, 2004i) 176

Table 7.3. Comparison between modelled body depth and width and values inferred from Euler deconvolution results. 199

Table 8.1. Physical properties for Beit Bridge gneisses (Maré and Tabane, 2004). 204

Table 8.2. Boreholes used in the modelling. 205

Table 8.3. Table of physical properties values used in the modelling of the flight lines and tie-lines. 206

LIST OF SYMBOLS

Symbol	Description
F.o.M.	Figure of merit
RMS	Root measure square
nT	Nano Tesla
GPS	Global Positioning System
DTM	Digital Terrain Model
SI	An abbreviation for 'Le Systéme International d'Unités', an international system of units adopted by many national and international authorities, associations, professional societies and agencies.
m	Meters
STP Height	Surface Texture Parameter Height
LIL	Large ion lithophile
MeV	Mega electron volt
1-s	First s atomic orbital
keV	Kilo electron volt

CHAPTER 1. Introduction

An aeromagnetic survey measures the magnetic field produced by magnetic minerals in different lithologies combined with the Earth's field and the external field. The goal of interpretation is to extract geological information from the magnetic data after careful removal of the external and main field effects. Variations in the proportions of magnetic minerals, mostly magnetite, pyrrhotite and titanohematite, produce patterns in the magnetic field data (e.g. Hunt et al., 1995; Parsons et al., 2006) that reflect the geometries of more magnetic and less magnetic lithologies. Highly magnetic lithologies such as banded iron formation (BIF), dolerite and some kimberlite may produce strong anomalies compared to the surrounding lithologies. The distribution of magnetic anomalies may provide evidence for tectonic features. For example, the displacement of linear features such as dolerite dykes and layers of BIF may reflect faults and dykes themselves. These linear features are often intruded into faults and shear zones. Circular and near-circular magnetic patterns, be they positive or negative, may reflect igneous bodies such as kimberlitic, alkaline and other volcanic intrusions. The relationship between highly magnetic and lesser magnetic rocks may provide clues to mineralization. The oxidation of magnetite to hematite, a non-magnetic mineral, may produce magnetic lows in layers of positively magnetic BIF. These lows may indicate hematite ore bodies. Olivine when it is altered to serpentine produces magnetite and as a result positive magnetic anomalies in ultramafic rocks (e.g. kimberlite intrusions). Magnetic data also may be modelled to indicate the shape of lithological features in three-dimensions.

The amount of information that may be derived from airborne magnetic data is related to the line spacing and altitude of the measurements and the depth to source. Regional surveys flown with wide line spacing (e.g. 1 km or 200 m) and at relatively high altitude (e.g. 100 m) will only provide information about large geological features. The closer the line spacing (e.g. 100 m or 40 m) and lower the altitude of the flight lines (e.g. 80 m or 40 m) will provide greater detail and information about smaller geological features.

Radiometric surveys measure the gamma ray emissions from naturally occurring radioactive isotopes of U, Th and K in minerals at or near the earth's surface. Since gamma rays only penetrate rocks and soils to about 50 cm, this type of survey only gives information about the very shallow geology, lithologies and soils. Concentrations of radioactive minerals may be identified and the distribution of lithologies with different concentrations of U, Th, and K (and U/Th ratios) may delineate different intrusions within similar lithologies.

In this dissertation, aeromagnetic and airborne gamma ray data are used to investigate the geology covered by the 1:50,000 scale topographic maps 2229AB Mapungubwe and 2229AD Coila (Figure 1.1). This area was chosen because it consists of contrasting lithologies, a basement complex of Archaean to Proterozoic age comprising predominantly quartzofeldspathic gneisses and intrusive rocks (the Beit Bridge Complex, Central Zone, Limpopo Belt, e.g. Barton et al., 2003) overlain in the north by Permian to Triassic sediments and intrusive rocks belonging to the Karoo Supergroup. The area also includes the well-studied ~520 Ma Venetia kimberlite intrusions that intrude dolerite sills of poorly constrained age. This age is estimated as younger than the last high grade metamorphic event (<2.0 Ga), since the sills show no tectonic fabric or metamorphic overprint (Brandl, 2002), and older than Venetia (>520 Ma). The geology of the basement complex where exposed has been mapped at a scale of 1:10 000 (Martin, 2002; Barton et al., 2003; Millonig, 2004; Twiggs, 2004; Zenglein, 2004; Barnettt, 2005; Chudy, 2007; Kirchenbaur, 2007) and the rock types, consisting mostly of gneisses, gabbros, pyroxenite, granulite and amphibolite, have been studied in detail. Two sets of aeromagnetic and gamma ray data cover this area, a regional data set of 1000 m line spacing and mean altitude of 150 m, flown between 1976 and 1982 by the Geological Survey of South Africa (Council for Geoscience, 1997; De Beer and Stettler, 1992) and a more detailed set flown in 2006 at a line spacing of 200 m at an altitude of 80 m flown by the Council For Geoscience for this study. Additional information about the deep geology

in this area is provided by: 1) a north to south vibroseis survey (10 second two way travel time) undertaken just outside of the study area to the west (Durrheim et al., 1992); 2) a resistivity survey along the same route (De Beer and Stettler, 1992) and 3) a vertical lithologic column, constructed by Pretorius and Barton (2003a; b) from upper lithospheric and crustal xenoliths collected from the Venetia kimberlite pipes. Finally the area has been covered by thermal imaging (Venetia Mine Geology Department, personal communication J.M. Barton Jr., 2008).

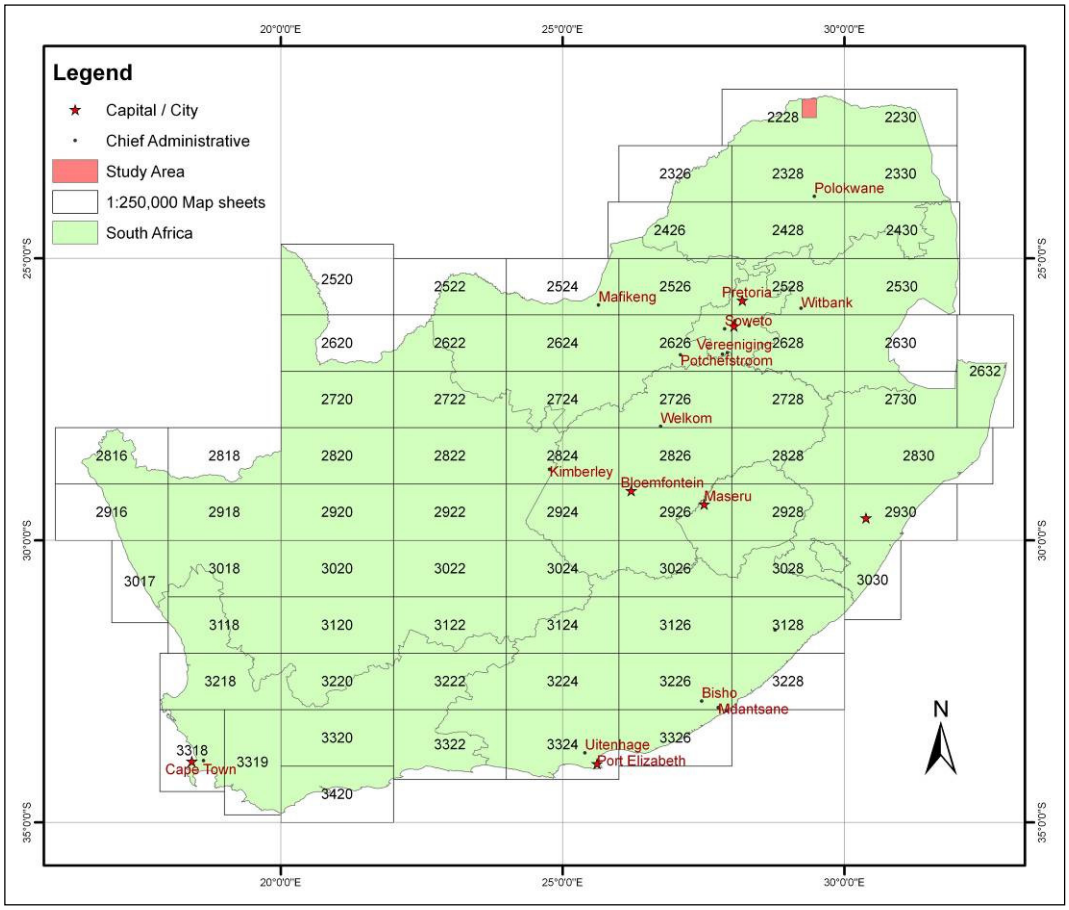


Figure 1.1. Locality of the 2229AB Mapungubwe and 2229AD Coila 1:50,000 map sheets, shown in red on a plot of the 1:250,000 map sheet layout.

The purpose of this dissertation is to develop a geological model of the study area by interpreting the magnetic fabric variations and investigate how well the gamma ray data reflect the mapped geology of the area.

CHAPTER 2. Geological Setting of the Study Area

The study area (shown in red in Figure 1.1 and Figure 2.1) is situated in the Beit Bridge Terrane, one of the terranes within the Central Zone of the Limpopo Belt between the Kaapvaal and Zimbabwe Cratons (Barton et al., 2006). It comprises a basement complex of ~2.6 and minor ~3.2 Ga granitoid igneous and metamorphic rocks (Beit Bridge Complex in Figure 2.2 and Figure 2.3) and two nappes containing Archaean and Proterozoic metasedimentary and minor granitoid rocks (e.g. Barton et al., 2003). The Beit Bridge Terrane has undergone three periods of deformation and amphibolite facies metamorphism at ~3.2 Ga, ~2.6 Ga and ~2.0 Ga (Barton et. al., 1994, Kamber et. al., 1995, Jaeckel et. al., 1997 and Kroner et. al., 1999). The basement complex is overlain in the north by clastic rocks of the Permian to Triassic Karoo Supergroup forming the southern margin of the remnant Tuli Basin (e.g. Brandl, 2002). The sediments dip to the north and the local equivalents of the Ecca and Beaufort Groups and Clarens Formation are progressively exposed going northward. Dolerite dykes and sills intrude the Karoo sediments and are believed to be feeders to local equivalents of the ~183 Ma Stormberg lavas. The ~520 Ma Venetia (Figure 2.5) (Modified Figure 1 of Brandl (2002)) kimberlite pipes intrude the basement complex in the southwestern portion of the study area as well as a dolerite sill at surface and another one at depth, determined from exposure in the mine (Brandl, 2002; Barton et al., 2003). The age of these sills are poorly constrained between the last metamorphism of the basement complex at <~2.0 Ga and intrusion of the Venetia kimberlite pipes at >520 Ma. They may be related to the ~1.9 Ga Sibasa lavas of the Soutpansberg Group that covered the area at the time of kimberlite intrusion as shown by xenoliths but were eroded away by the onset of Karoo sedimentation (e.g. Pretorius and Barton, 2003).

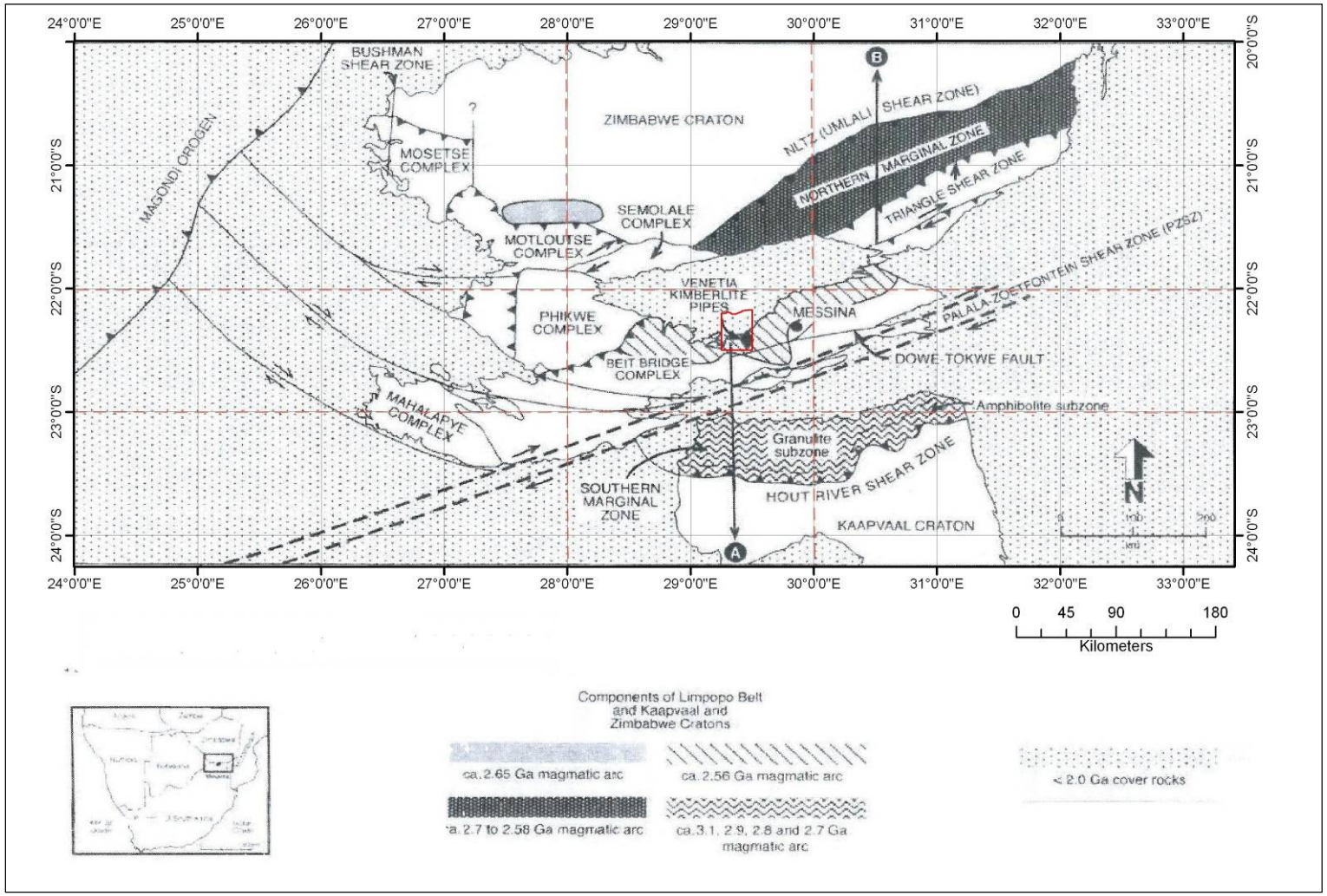


Figure 2.1 The simplified geology and structure of the Limpopo Belt (after Barton et al., 2006). The study area is indicated in red.

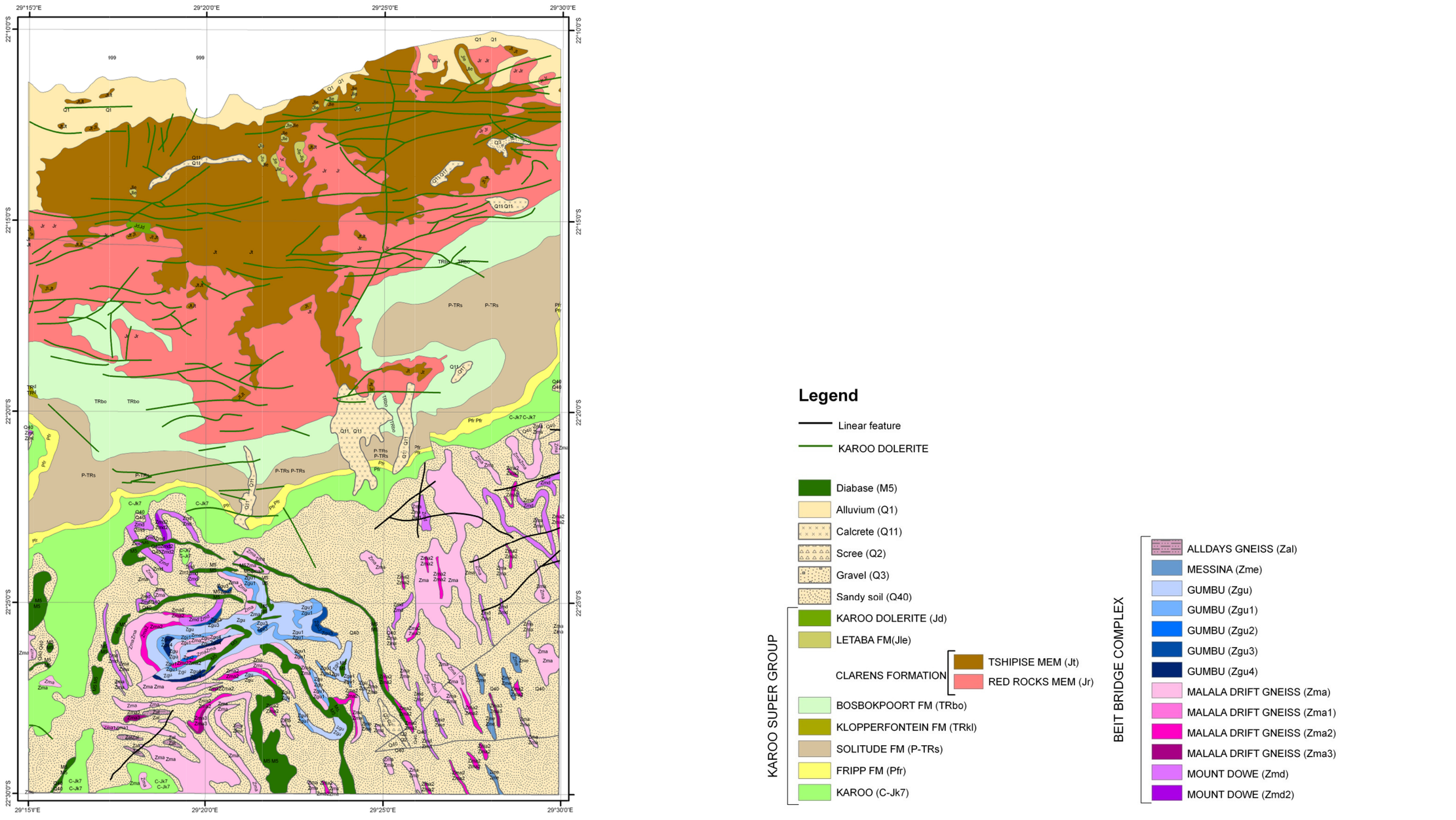


Figure 2.2. Geology of the study area (2229AB & 2229AD) taken from the 2228 Alldays 1:250,000 map (Council for Geoscience, 2000).

C-Jk7, Undifferentiated Mikambeni and Madzaringwe

Jd, Network of dolerite sills, sheets and dykes, mainly intrusive into the Karoo Supergroup

Jle, Basic volcanic rocks (tholeiites, picrite basalts and nephelinites)

Jr, Light red, fine-grained, argillaceous sandstone

Jt, Relatively hard, fine-grained, white to cream sandstone

M5, Diabase

P-TRs, Grey, purple (in upper part) and green mudrock, subordinate siltstone and sandstone

Pfr, Coarse-grained felspathic sandstone, thin conglomerate layers

Q1, Alluvium

Q11, Calcrete

Q2, Scree

Q3, Gravel

Q40, Sandy soil

TRbo, Dominantly red mudstone (plus calcareous concretions), siltstone, minor sandstone

TRkl, Fine- to coarse-grained feldspathic sandstone

Zal, Grey, medium-grained, migmatitic, tonalitic-trondhjemitic gneiss

Zgu, Calc-silicate rocks and marble, together with leucogneisses and subordinate pink hornblende granitoid gneiss, metaquartzite and amphibolite

Zgu1, Metaquartzite

Zgu2, Leucocratic quartzo-feldspathic gneiss

Zgu3, Metapelite

Zgu4, Amphibolite, mafic granulite

Zma, Leucogneiss with metaquartzite, hornblende granitoid gneiss, amphibolite, metapelite and calc-silicate rocks

Zma1, Metapelite

Zma2, Amphibolite, mafic granulite

Zma3, Metaquartzite

Zmd, Metaquartzite, leucogneiss, pink biotite-hornblende granitoid gneiss

Zmd2, Metapelite

Zme, Meta-anorthosite, metaleucogabbro, metagrabbo, metapyroxenite

Figure 2.3. Legend description of the geology map of 2229AB and 2229AD.

The dolerite intrusions in the pre-Karoo rocks display no tectonic fabric or metamorphic overprint, and can therefore be seen as postdating the Limpopo event at ca. 2.7 (Brandl, 2002). No radiometric ages are available for the dolerite intrusions in the study area (Brandl, 2007). Isotopic analyses performed by the Isotopic Geochemistry Laboratory at MIT on baddeleyite extracted from bulk rock dolerite samples from sites located between 100 km to 300 km to the southwest of the study area (Figure 2.4). This study

was commissioned by Hanson et al. (2004) and established U-Pb baddeleyite ages of 1.88 Ga and 1.1 Ga.

The dolerite intrusions (both sills and dykes) exhibit a dominant east-northeast trend in the Beit Bridge gneisses. The sills seem to be concentrated around a point south of the Venetia kimberlites (Figure 2.5) (Brandl, 2002). The outcrops form almost continuous, semicircular morphological structures, consisting of at least two concentric inward-dipping rings**.** These saucer-shaped sills are locally up to several hundred meters thick. Rb-Sr whole-rock data from areas adjacent to the map area suggest several periods of dyke activity between 2.2 Ga and 1.7 Ga (Barton, 1979).

The stress field in the area has been in extension since after the Limpopo Orogeny around 2.0 Ga (G. Brandl, personal communication, 2012). Around 130 Ma, east-southeast trending dykes ("Louisiana dykes") that form part of the Okavango dyke swarm intruded south of Alldays, indicating extension in a ~northeast–southwest direction (Brandl, 2007). According to Brandl (personal communication, 2012), the present day stress field is extension in a north-northwest –south-southeast direction.

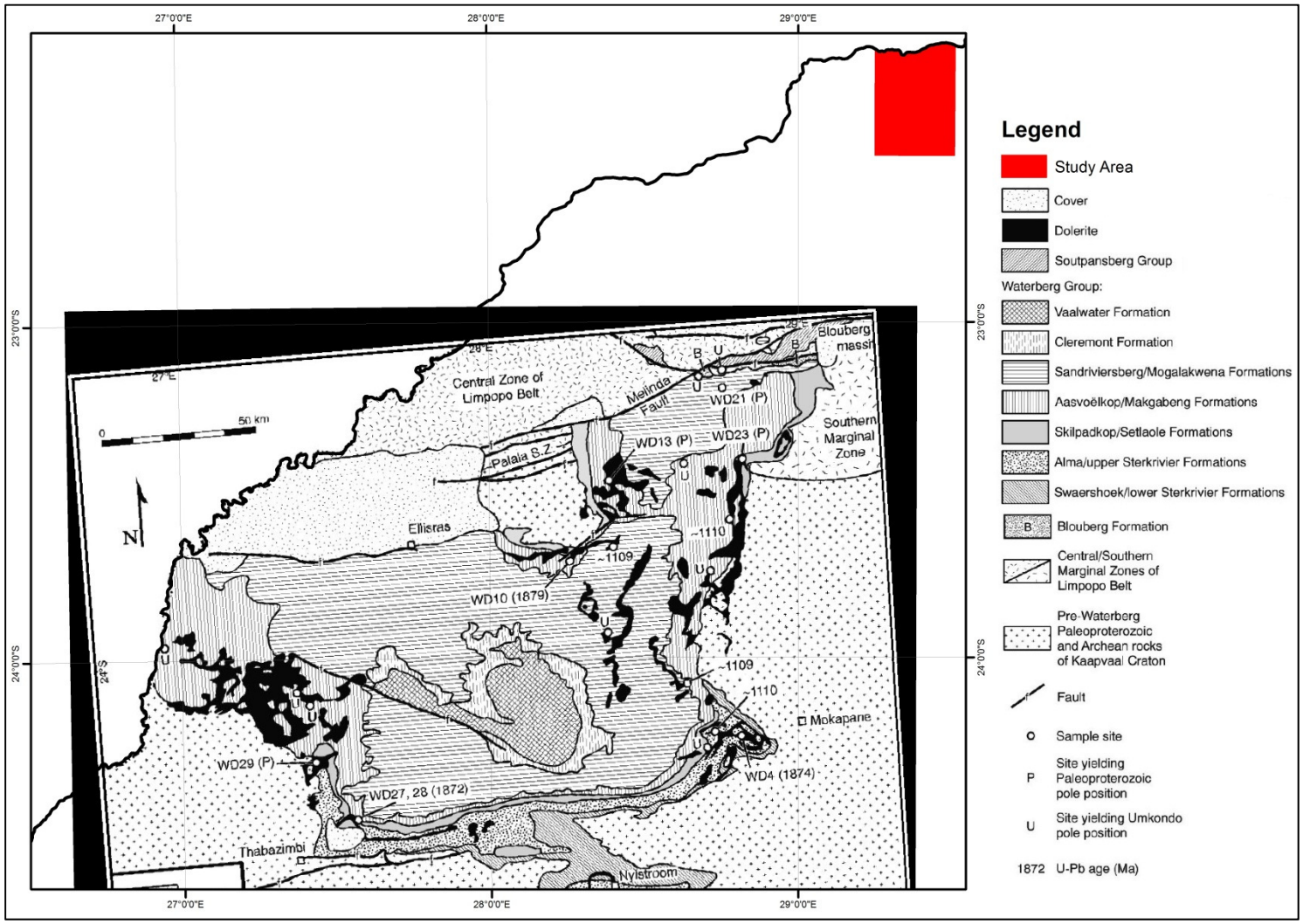


Figure 2.4. Locations of sample sites with relation to study area. Modified from Hanson et al (2004).

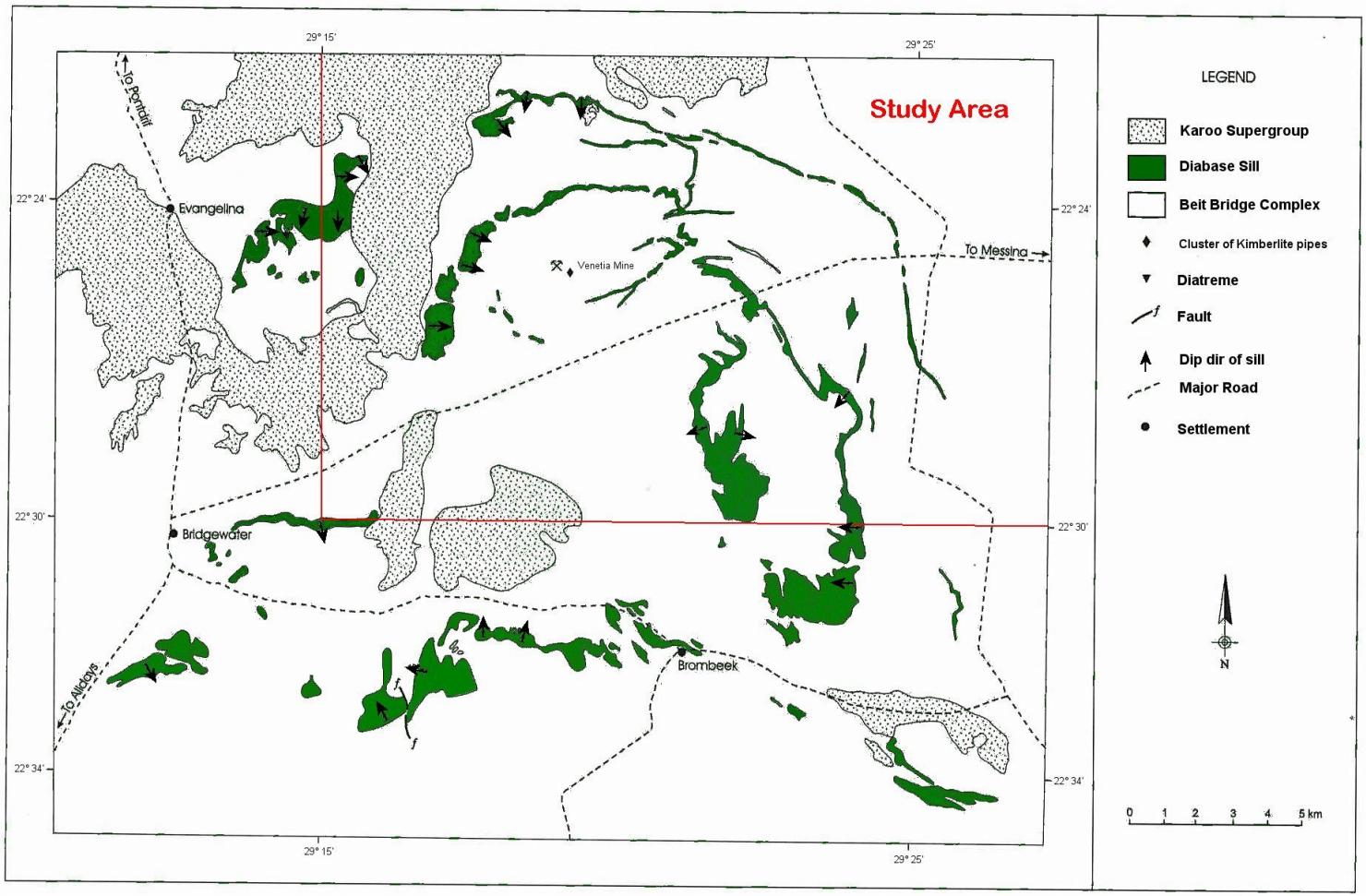


Figure 2.5. Distribution of dolerite sills cropping out around the Venetia Kimberlite pipes, northeast of Alldays. (Modified from Brandl, 2002). These sills are saucer-shaped in profile (Brandl, 2002).

CHAPTER 3. Previous Geophysical Studies

3.1. Regional Airborne Studies

In the second half of the 1900s, a national airborne survey was undertaken by the then Geological Survey of South Africa (e.g. Ledwaba et al., 2009). The survey specifications were 1000 m line spacing and average 200 m flying height. It was flown in two main sections, each section comprising various surveys performed by various companies with various specifications (see Ledwaba et al., 2009 for more information). The Karoo survey covered almost half of the country and was conducted between 1976 and 1982. The contractor performing the survey was a company called Geosearch (Pty) Ltd. (Ledwaba et al., 2009). The remaining parts of the country were surveyed by various contractors over a period of more than 30 years, starting in 1957 and ending in 1997. The map showing the various survey blocks and the contractors responsible for them is shown in Figure 3.1. For a complete list of specifications, see Ledwaba et al. (2009).

The survey consisted of both magnetic and radiometric data collection. A final total field magnetic map of the entire country was compiled in 1997 (Council for Geoscience, 1997). Unfortunately the crystals were not properly calibrated at the time of the survey and this resulted in no clear definition of the individual channels. As a consequence only total count radiometric data is available for the entire country.

The regional magnetic data for the Limpopo area, compiled from data from both the South African, Botswana and Zimbabwean national surveys, is presented in Figure 3.2. These data were merged by Dr Edgar Stettler. These surveys were all collected between 1965 and 1985 (Dr Edgar Stettler, personal communication, 2011). The data were corrected by Dr Edgar Stettler for the 1975 IGRF.

The geological interpretation of Barton et al. (2006) is overlain on the magnetic data and compared to an interpretation of this regional data by the author. The differences are

shown in Figure 3.3 with the Barton et al. (2006) in black and the current interpretation in red.

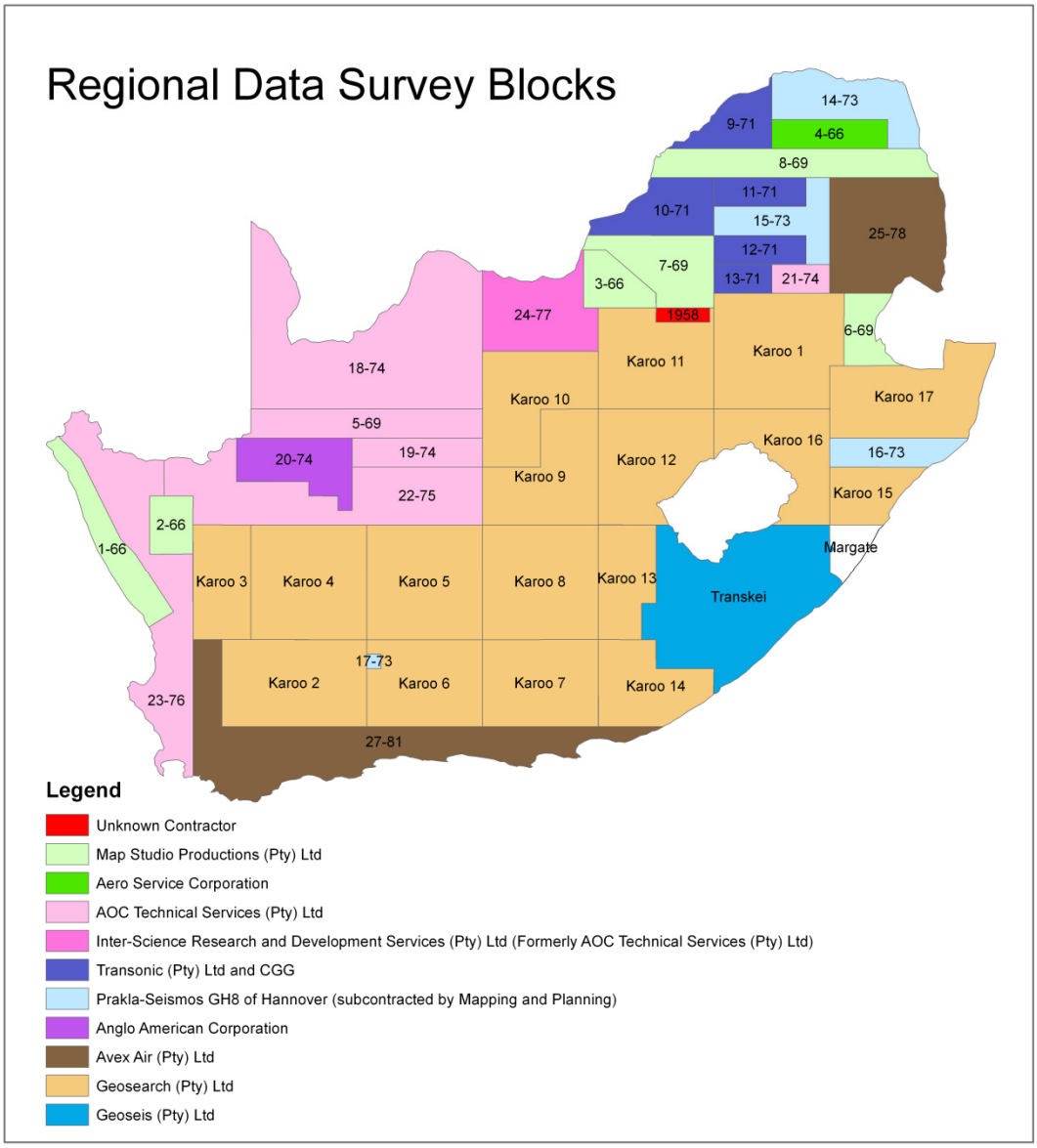


Figure 3.1. Map showing the regional airborne data survey blocks and the corresponding companies that undertook the surveys.

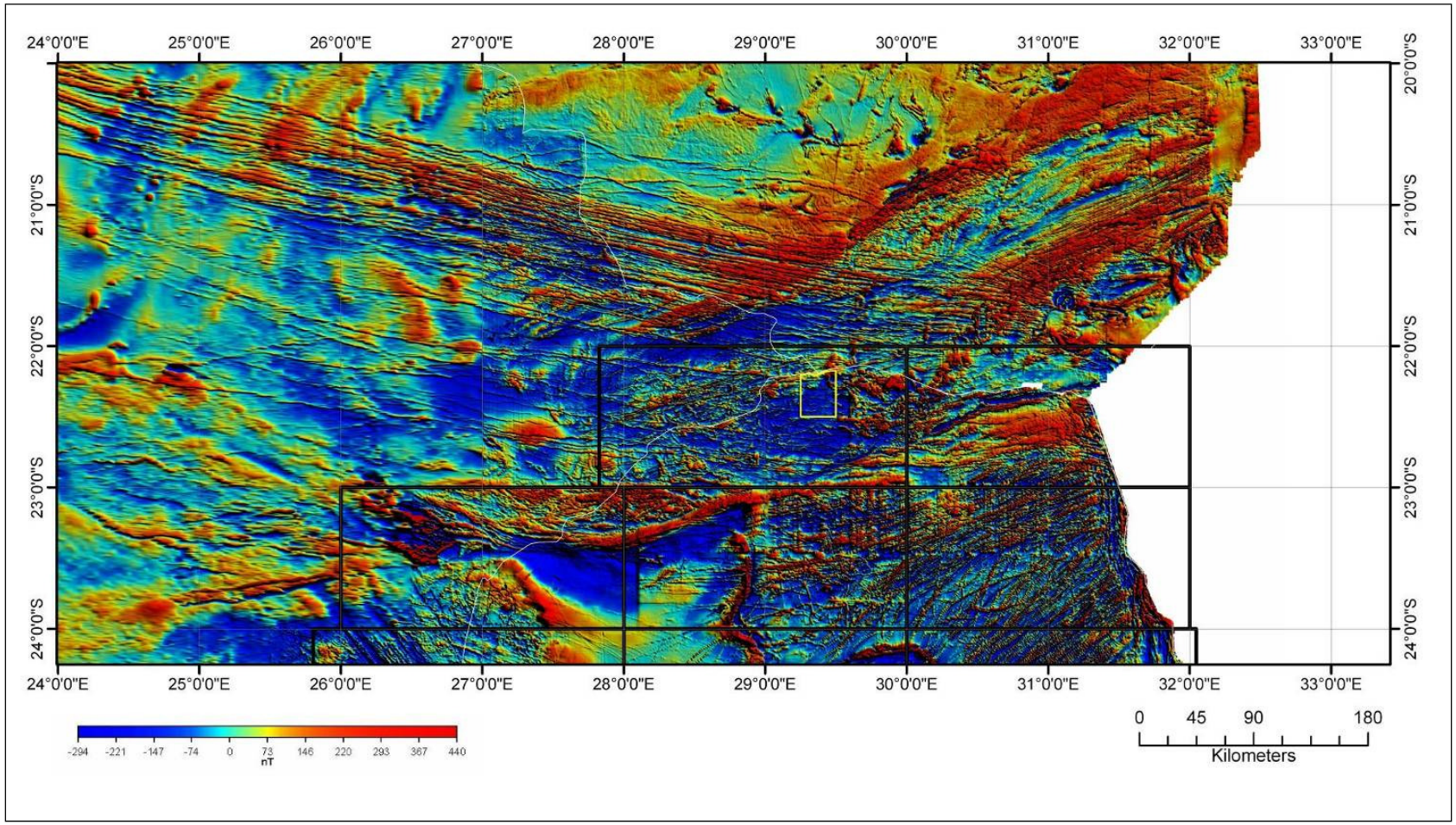


Figure 3.2. Regional aeromagnetic data for Limpopo Belt. Data were collected at 1000 m line spacing and 200 m flight height. (SADC dataset). 1:250,000 mapsheets are indicated in black and the study area in yellow.

The Palala - Zoetfontein shear zone can be seen in Figure 3.3. It was active during the Limpopo Orogeny and separates the Southern Marginal Zone of the Limpopo Belt from the Beit Bridge Complex of the Central Zone (e.g. Barton et al., 2006). It is visible on the magnetic data as a large east-northeast to west-southwest trending negative linear magnetic anomaly. At the western edge of the Southern Marginal Zone, the magnetic anomaly bends to the southwest and becomes a more prominent positive magnetic anomaly. Further west as it wraps around the Mahalapye Complex, the magnetic high becomes more east-west trending than the Palala-Zoetfontein shear zone interpreted by Barton et al. (2006).

The Dowe-Tokwe fault is also correlated with a negative magnetic lineament trending about 85°E. It extends from east of Musina westward to beyond the study area of this dissertation.

The Houtrivier shear zone is also correlated with a negative magnetic lineament. In the west, the magnetic lineament is interpreted as continuing along an east-west trend towards the Bushveld Complex rather than bending to the northwest as interpreted by Barton et al. (2006).

The national airborne geophysical survey mentioned earlier included a radiometric airborne survey of the entire country (Ledwaba et al., 2009). Unfortunately due to contractor error and faulty equipment the only reliable dataset from that survey is the total count radiometric data (Council for Geoscience, 1997). This dataset does not cover the entire country and has gaps in it, but it does cover the 2229AB and AD 1:50,000 map sheets (Figure 3.4). The high radiometric values in the south west and south east of the study area are clearly visible. When comparing these high values to the geology of the area it seems that these high values could be attributed to outcrops of certain quartzfeldspathic rocks (indicated in black hatched areas in Figure 3.4) and their weathering, transport and deposition by wind and water.

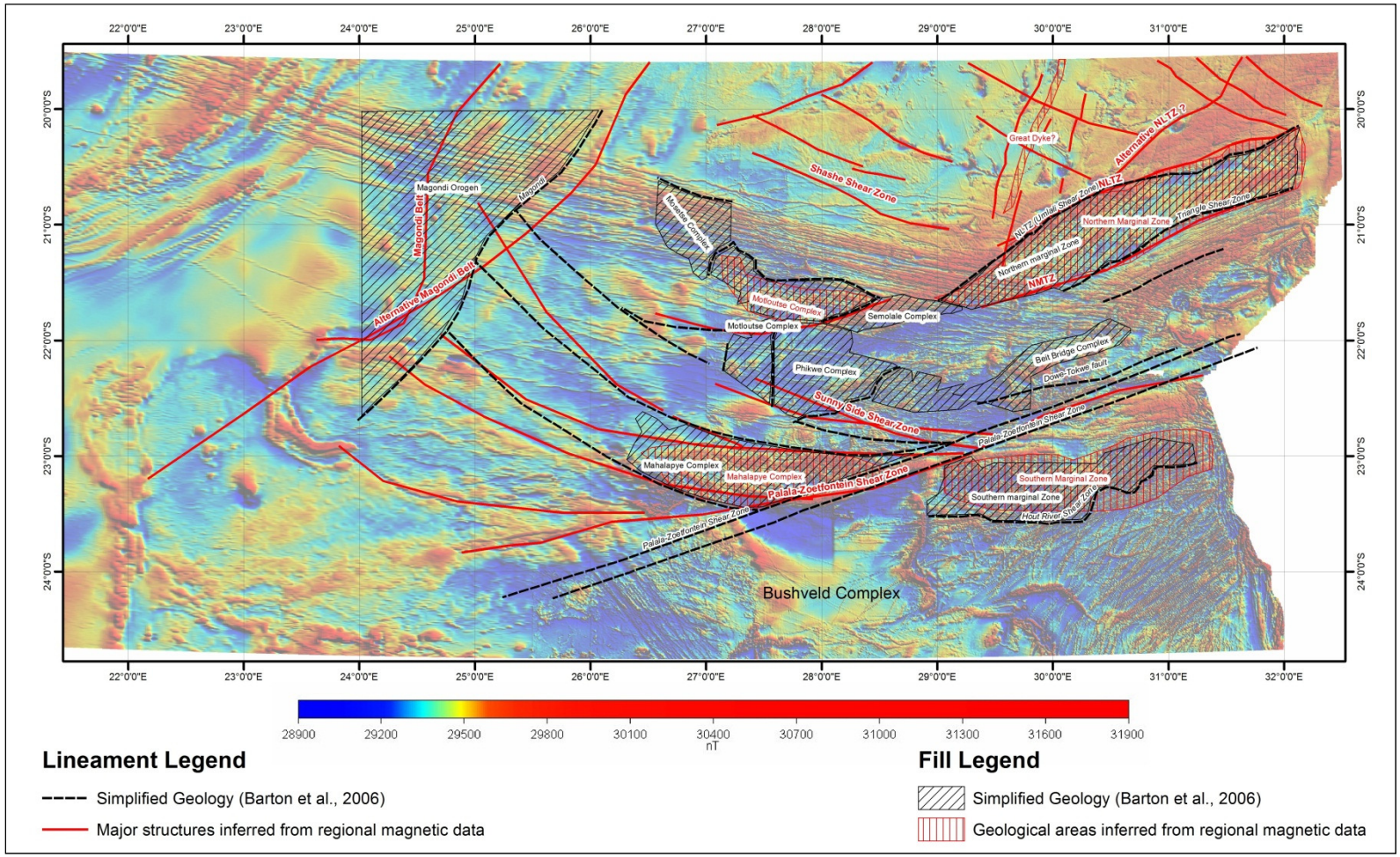


Figure 3.3. Comparison of Barton et al. (2006) simplified geology (in black) and structures inferred as part of this study (in red) from the regional magnetic data.

Shown in hatched areas on Figure 3.4 are the leucogneisses of the Malaladrift gneiss. Areas of low value include the Karoo sandstones in the north and the carbonate rocks of the Venetia klippe in the south.

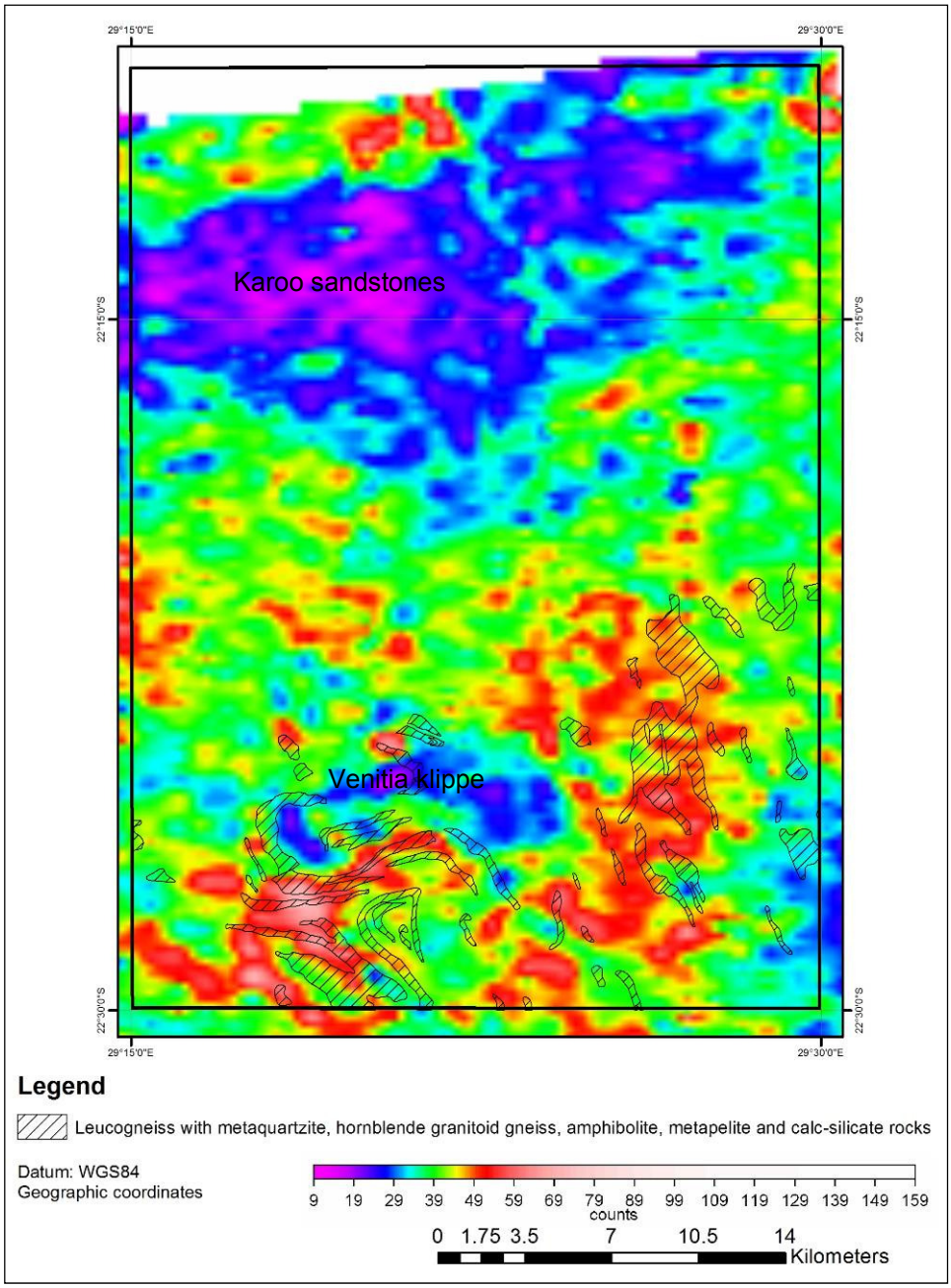


Figure 3.4. Regional total count radiometric data (1000m line spacing) over the study area with mapped quartzfeldspathic rocks indicated as hatched areas on it.

3.2. Other Studies

Seismic anisotropy studies of Silver et al. (2004) suggest that the mantle preserves a fossil anisotropy that correlates with some surface lineaments, as shown in Figure 3.5. Note that the present study area is in the terrane indicated as Limpopo Belt in Figure 3.5 and Limpopo Central Zone in Figure 3.6. The mantle fabric describes a continuous arc that extents from the southwestern to the northeastern Kaapvaal Craton, the Limpopo Belt and the southwestern Zimbabwe Craton.

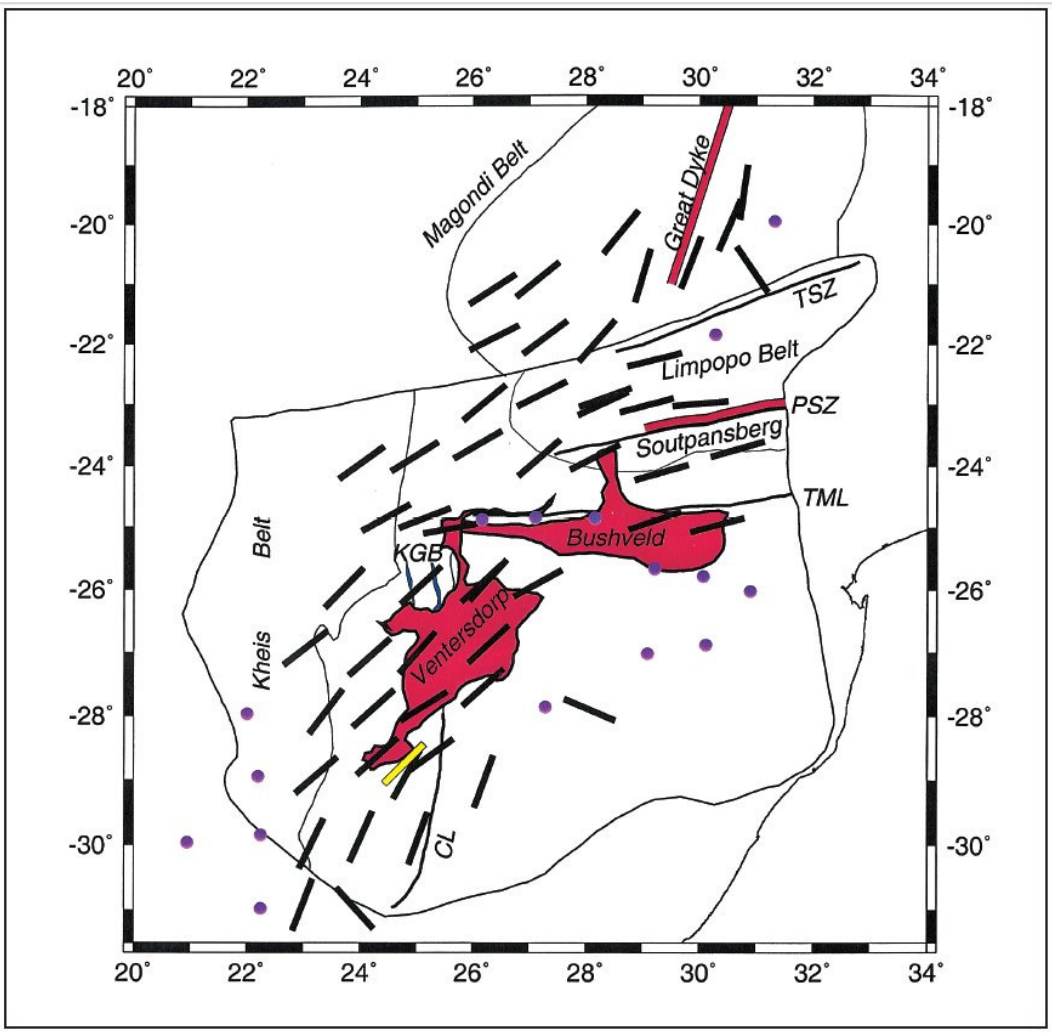


Figure 3.5. . Map showing orientation of shear wave splitting fast polarization directions from the Kaapvaal Seismic Array (black bars) and from the high-resolution Kimberley Seismic Array (yellow bar, array average). Purple dots represent measurements with zero anisotropy (Silver et al., 2004).

The mantle fabric may be explained by superimposing 5 major deformation phases, each tied to major orogenic events (Figure 3.6) (Silver et al., 2004). The first orogen is an unknown pre 3.0 Ga orogen that caused mantle fabric (shown in yellow in Figure 3.6a) in the Zimbabwe craton. The next event is a collision at ~2.9 Ga along the north and west of the Kaapvaal shield. This caused mantle fabric (shown in yellow on Figure 3.6b) in the Kimberley and Pietersburg blocks. The Colesberg Lineament (CL) and Thabazimbi Murchison Lineament (TML) form part of this fabric (Figure 3.6b). The third event is the Limpopo Orogen at ~2.6 to ~2.7 Ga that caused mantle fabric to the 3 zones of the Limpopo Belt (yellow on Figure 3.6c). It also caused two collisional rifts along pre-existing mantle fabric directions, namely the Great Dyke (2.72 – 2.57 Ga) in Zimbabwe and the Ventersdorp on the edge of the Kimberley block (shown in red on Figure 3.6c). The Magondi Orogen at ~2.0 Ga reactivated the shear zones in the Limpopo Belt (yellow on Figure 3.6d) and is interpreted to have produced a collisional rift (red in Figure 3.6d) causing the Bushveld magmatism. The final event is the ~1.8 to 1.9 Ga Kheis Orogen that again reactivated the Limpopo Belt shear zones (yellow in Figure 3.6e) and produced the Soutpansberg trough as a collisional rift (red in Figure 3.6e). These rifts all formed in directions parallel to preexisting mantle fabric. It follows that these orogens have a dual role (Silver et al., 2004) - they create the mantle fabric and they generate extentional stresses that reactivate the mantle fabric in the form of collisional rifting.

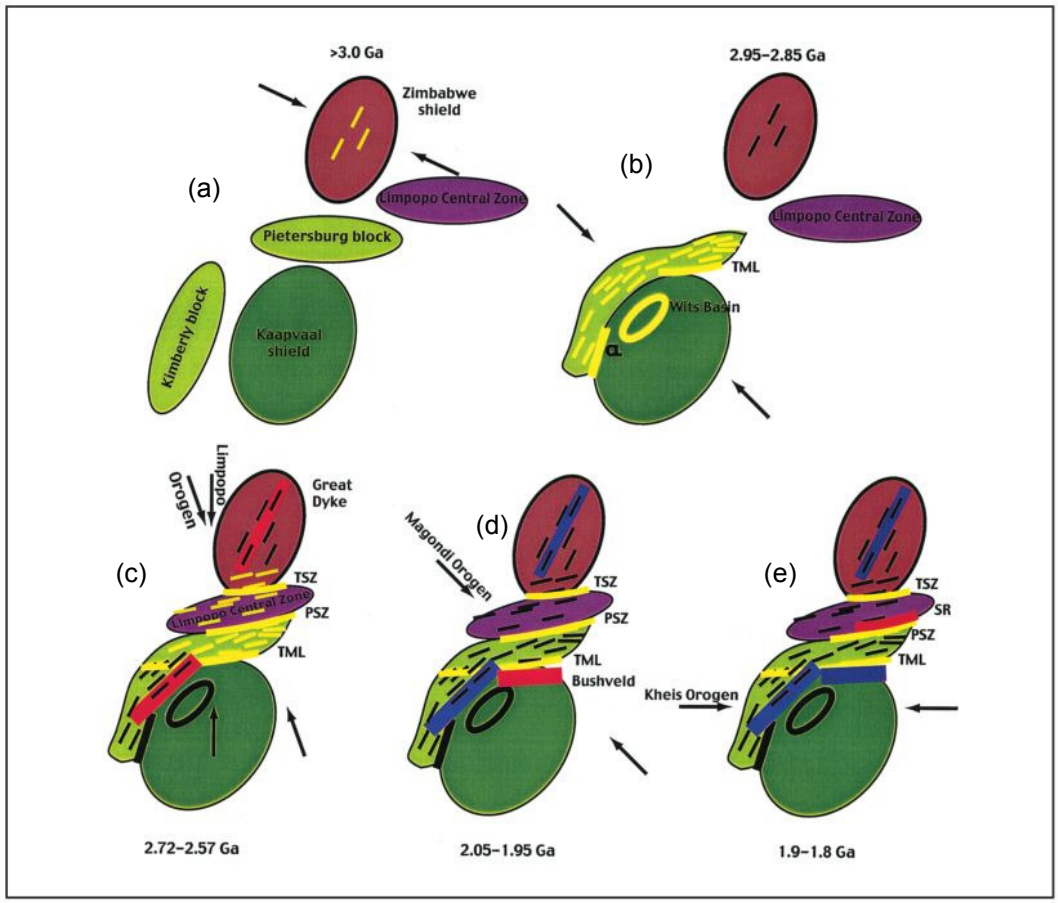


Figure 3.6. A scenario that could cause the anisotropic structure of the mantle and its relation to the surface geology of cratonic South Africa. From Silver et al. (2004).

De Beer and Stettler (1992) reviewed the results of previous geophysical studies (Figure 3.7) in the Limpopo Belt and found that the seismic and geoelectrical data sets indicate that the terrane boundaries between zones within the Limpopo Belt dip in towards the belt to give it the appearance of a pop-up structure. These studies include the gravity section of Coward and Fairhead (1980) (VW on Figure 3.7), the seismic refraction line of Stuart and Zengeni (1987) (XY on Figure 3.7), the gravity profiles of both de Beer et al. (1984) and Kleywegt et al. (1987) (AA', BB' and DD' on Figure 3.7) as well as a deep seismic reflection line from Pont Drift running south towards Pietersburg (Durrheim et al., 1992).

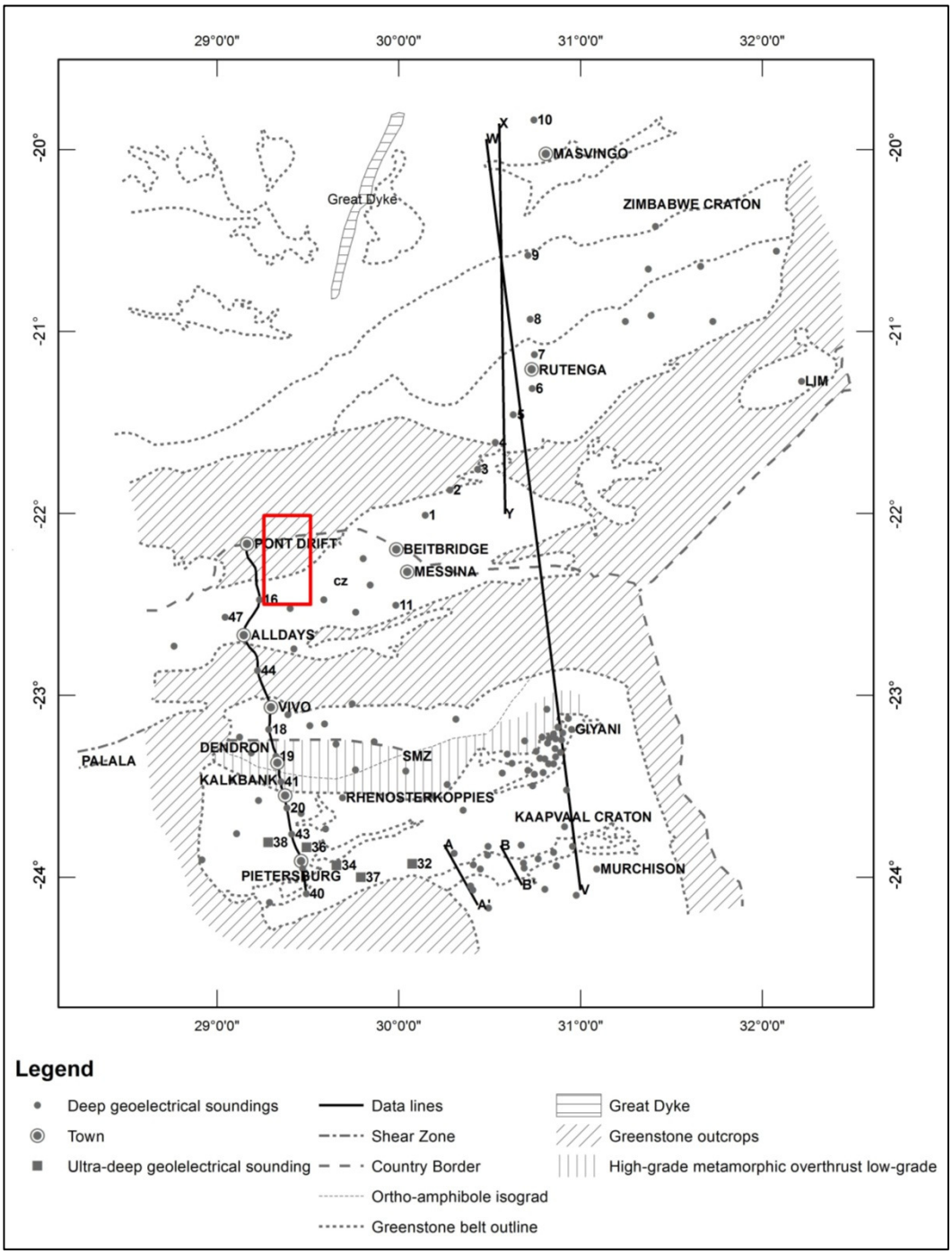


Figure 3.7. Simplified geological map of the Limpopo Belt, Zimbabwe and Kaapvaal Cratons depicting the locations of the geophysical data that were reviewed by De Beer and Stettler (1992). The gravity section of Coward and Fairhead (1980) is indicated with VW, the seismic refraction line of Suart and Zengeni (1987) is indicated with XY, the gravity profiles of De Beer et al. (1984) are indicated with AA' and BB'. The position of the deep seismic reflection line from Pont Drift (Durrheim et al. 1992) is also indicated on the map. The study area is indicated in red. The numbered square dots are ultra-deep geoelectrical sounding locations.

The results of two seismic investigations were interpreted by Durrheim et al. (1992) and will be discussed below. The first survey is a 218 km, 13 second two-way-time seismic reflection profile from Pont Drift in the Beit Bridge Terrane of the Central Zone across the Southern Marginal Zone of the Limpopo Belt to the Kaapvaal Craton ending just south of Pietersburg (Figure 3.7). Interpretation of this dataset showed sets of short, variably dipping reflections in the upper crust and a seismically transparent lower crust. (Figure 3.8). No evidence for a reflection Moho was found. This survey ran along the western edge of the study area (shown in red on Figure 3.7) which begins ~20 km north of Alldays. In this locality, seismic reflectors terminate at a depth of about 10 km.

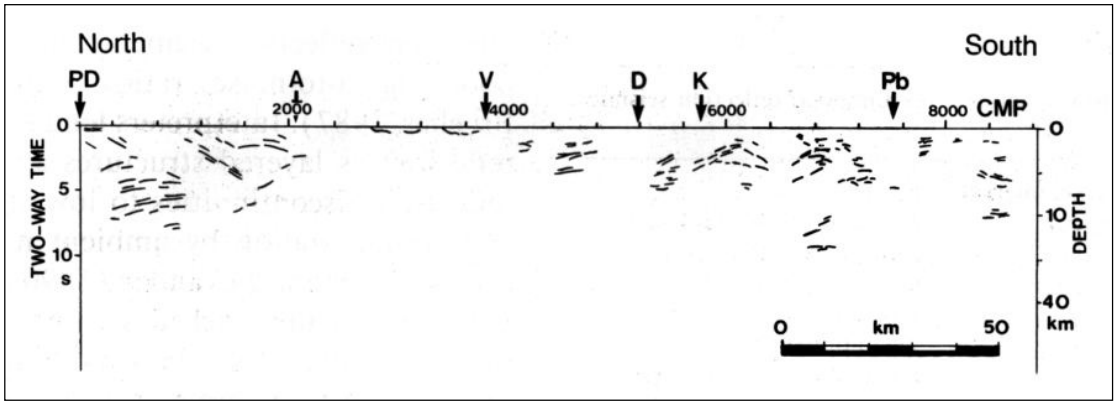


Figure 3.8. Line drawing of the migrated Limpopo seismic reflection profile showing the prominent reflections. PD = Pont Drift, A = Alldays, V = Vivo, D = Dendron, K = Kalkbank and Pb = Pietersburg. (Durrheim et al., 1992)

The second seismic investigation was the interpretation of the seismic travel times of Witwatersrand mine tremors along a profile from Pietersburg on the Kaapvaal Craton to Harare on the Zimbabwe Craton (XY on Figure 3.7.) The interpretation is shown in Figure 3.9. Durrheim et al. (1992) interpreted the Moho to be between 35 and 40 km depth under the study area although another discontinuity at about 57 km was also prominent.

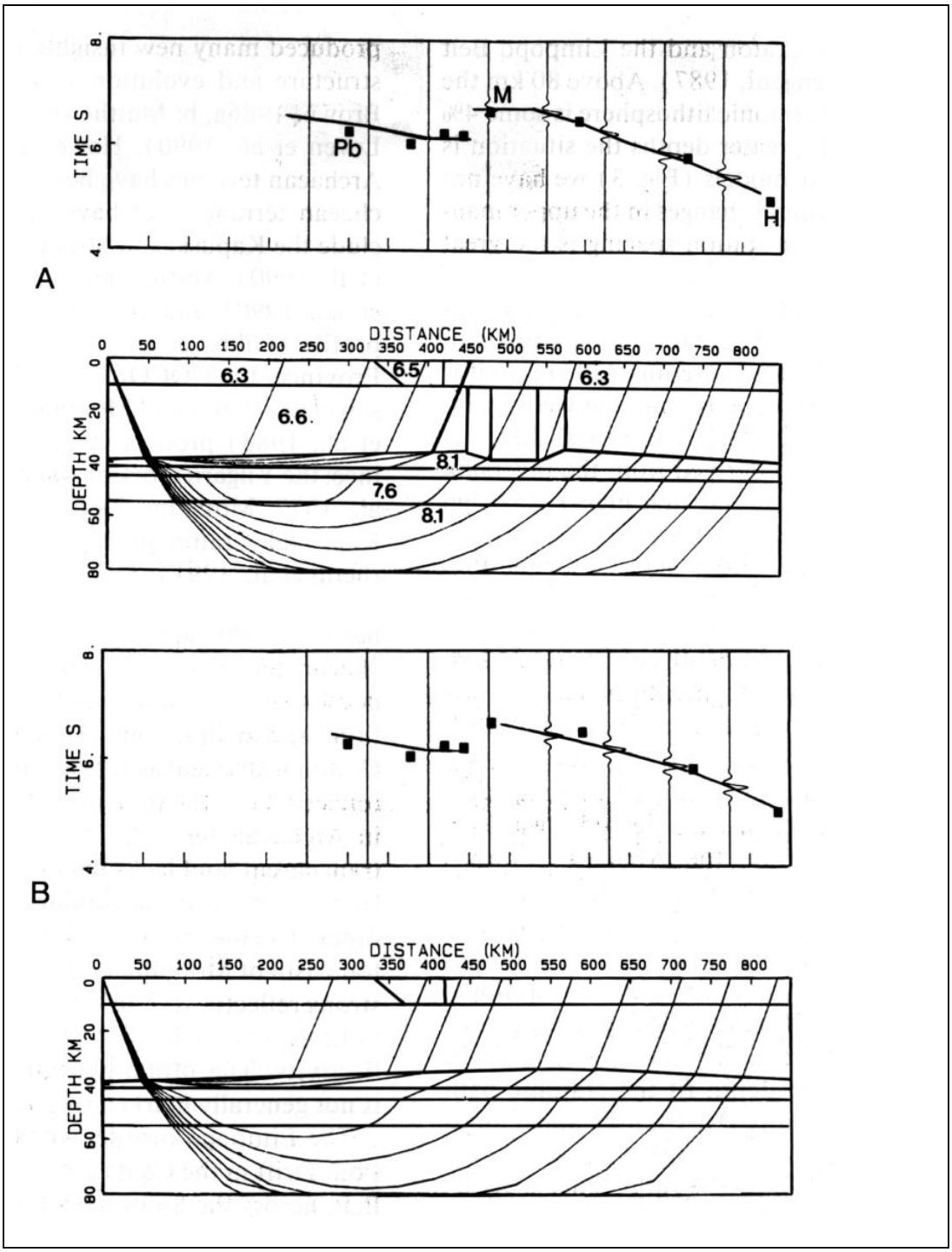


Figure 3.9. Seismic velocity models, ray-trace diagrams and synthetic record sections taken from Durheim et al. (1992). The reduction velocity is 8 km/s. The seismic velocity within each polygon is given in km/s. The only difference between model A and model B is the Moho topography. Observed traveltimes are indicated with geometric symbols. P = Pietersburg, M = Messina, H = Harare.

Pretorius and Barton (2003a; b) modelled the upper lithosphere under the Venetia kimberlite pipes by comparing P-wave velocities of xenoliths to the seismic velocities

determined under this region from Durrheim et al. (1992), (Figure 3.10). The p-wave velocities were obtained from the travel times of elastic waves through samples of known length using the pulse transmission technique of Birch (1960).

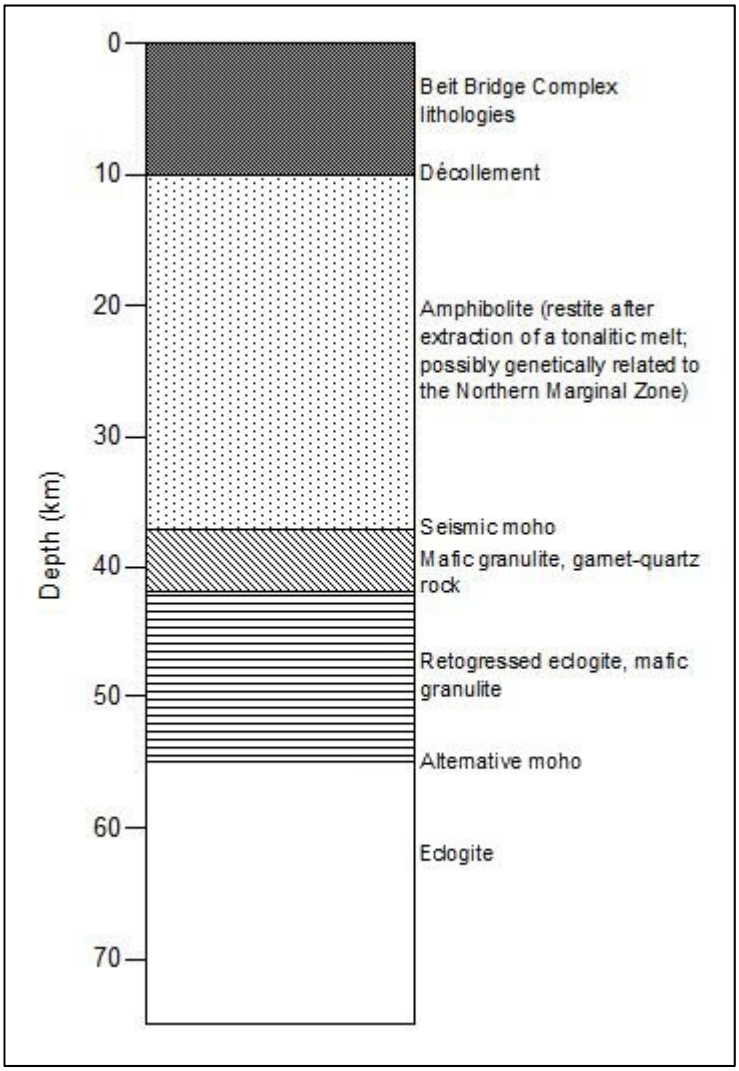


Figure 3.10. Lithological section beneath the ~530 Ma Venetia kimberlite pipes in the Beit Bridge Terrane constructed from pressure and P-wave velocity data and compositions of xenoliths from Venetia kimberlite (Modified from Pretorius, 1996; Pretorius and Barton, 2003a; b)

Amongst the conclusions of this study is that the high grade metamorphic rocks of the Limpopo Belt in this area only extend to a depth of about 10 km where they are underlain by amphibolite. At the Moho (between 35 km and 40 km) as interpreted by Durrheim et al. (1992), the amphibolites changes to mafic granulite. At about 42 km, the mafic granulite turns to regressed eclogite. At 57 km, the retrogressed eclogite changes to eclogite, forming an alternative Moho.

3.3. Summary of previous geophysical studies

Regional magnetic data collected during the 1900's show large anomalies that correspond to northwest, east-west and east-northeast trending structures in the Limpopo Belt area. Seismic anisotropy studies done by Silver et al. (2004) showed that the mantle fabric in the Limpopo Belt has a northeast, east-northeast and almost east-west trend. Interpretation of seismic and geo-electrical data by De Beer and Stettler (1992) indicate that the terrain boundaries between zones in the Limpopo Belt dip in towards the belt, thus giving the appearance of a pop-up structure. Two possible Moho depths of 35-40 km and 57 km were derived from seismic investigations by Durrheim et al. (1992) as well as P-wave velocities calculated for the high grade metamorphic rocks of the Limpopo Belt by Pretorius and Barton (2003a; b).

CHAPTER 4. Data Collection and Results

4.1. Acquisition

A new, higher resolution airborne geophysical survey collecting magnetic and radiometric data over the study area (Figure 1.1) was undertaken by the Council for Geoscience and Southern Exploration Services (SES) during April 2006 using the specifications listed in Table 4.1. The data were processed by SES. The magnetic method measures the total magnetic field intensity, which includes contributions from the Earth's main field in the core, the external field which interacts with the solar wind, and variations in magnetisation in the earth's crust. Magnetite, titanohematite, ilmenite and phyrrotite are the major magnetic minerals responsible for lithospheric magnetic anomalies.

The radiometric technique measures the natural radioactivity of the surface. Only three naturally occurring radioactive elements are of importance in exploration, potassium (K), uranium (U) and thorium (Th). Gamma-ray and photons have discrete energies that are characteristic of the source isotopes (Minty, 1997). Gamma-rays are attenuated over a short distance and therefore the method only provides information about the first half meter below the surface. The implication of this is that manmade sources that contain any of the three relevant elements (i.e. fertilisers) may severely influence the data collected over an area.

Table 4.1. Geophysical survey specifications

Item	Value
Survey flying height	± 80 m nominal
Line spacing	200 m
Tie- Line spacing	2000 m
In line sample spacing magnetics	5 m
In line sample spacing radiometrics	50 m
Flying speed	200 km/h
Flight line direction	North / South
Tie - line direction	East - West

Item	Value
Data recorded	Total field magnetics, radiometrics
Datum	WGS84
Projection	Transverse Mercator
Central meridian	29° East

4.1.1. Equipment specifications

The aircraft used was a Cessna 210. Wingtip pods for the magnetic data acquisition were installed to remove them as far as possible from the main aircraft. This is to reduce interference from the aircraft that will result in noise in the data. The ground speed during survey flying is approximately 200 km/h. It is accepted that the flying height should be as low as possible. In this case data were collected between 80 m and 100 m flying height. The pilot made the final decisions based on safety considerations.

The magnetometer used for the survey was a Geometrics G822A caesium vapour magnetometer with an instrument resolution of 0.01 nT and a total noise envelope on collected airborne data not exceeding 0.1 nT sampling at ten times a second. With the aircraft flying at 200 km/h (50 m/sec) and taking 10 readings each second, it means the footprint is one reading every ~5 m on the ground. One Exploranium GR820 spectrometer was used a 16 litre crystal looking downward and 4 litre upward. The upward crystal is used in the radon corrections. The upward looking crystal is configured by placing 4 litres of crystal on top of the 16 litre crystal, this result in all radiation from below being blocked by the 16 litre crystal and the four litre crystal measuring radiation coming mostly from above. The system records 256 channels of data between 0 and 6.0 MeV, allowing the resolution of all natural gamma energies and cosmic windows. The ^{40}K, ^{214}Bi (^{238}U-^{226}Ra series), ^{208}Tl (^{232}Th series) and total count (0.4 to 2.8 MeV) channels measured in counts per second that are dependent on equipment, the height of the survey, crystal volume, detector efficiency and window width. To make the values geologically significant they are converted to percentage K_2O, parts per million (ppm) U_3O_8 and ppm ThO_2 (mean ground-level abundances). The conversion is performed by dividing each of the corrected three channel count rates by a sensitivity coefficient,

calculated for that survey and equipment set, that takes all the above mentioned influences into account (Minty et al., 1997).

The pre-calibration spectrum is shown in Figure 4.1 and the spectrum after calibration is shown in Figure 4.2. the calibration procedure is discussed in detail in section 4.2.3 on page 32.



Figure 4.1. Non-calibrated radiometric spectrum shape. The locations of the K, U and Th peaks are displaced relative to their energy window.

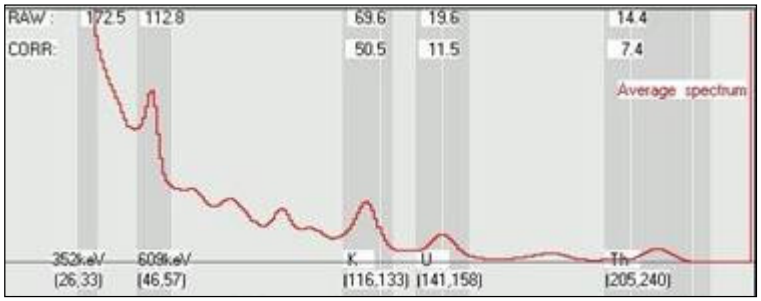


Figure 4.2. Spectrum shape after energy calibration. Radioelement peaks are located in the correct positions.

Positioning of the aircraft was achieved by using a SATLOC M3 real-time differential GPS specified to record a digital reading once a second to an accuracy of better than 2 m in x and y and 3 m in z. This system does not require a base station for differential correction as it uses Satloc's patented e-Dif technology. This technology generates internal differential corrections based on the starting location. The differential corrections are modelled over time and applied to the GPS data in order to maintain a very consistent relative position. The operator can use e-Dif over long time periods with a minimal drift in accuracy or return to the starting location at any time to update the differential corrections.

It records its position relative to WGS84 spheroid. The SATLOC GPS also controlled the navigation. A navigation light bar guided the pilot throughout the survey and was pre-programmed via the mission control software. Altitude was controlled by a highly focused Riegl laser altimeter.

A Geometrics G856AG ground station magnetometer was utilised for diurnal variation corrections. These data are logged in this ground station magnetometer every 5 seconds and since it does not move, any changes it measures are due to the changes in the magnetic field (diurnal effect). Only the low frequency component (readings taken once a second) from the ground station data is used for diurnal removal by subtracting it from the data collected during the survey, and final levelling is done utilising the tie line information.

Data acquisition was accomplished by saving all the collected data (magnetic, radiometric and GPS) directly onto an on-board PC 104 with solid state memory. All data are merged using GPS time as the constant, which is common to all collected data. This is controlled on the PC by a stand-alone Garmin GPS linked directly to the PC.

4.1.2. Data acquisition and in-field verification

Pre-flight preparations are routinely done in the field before a survey. Firstly all the equipment on board the aircraft is powered up to ensure that everything is in working order. The base station for the recording of diurnal variations is set up and checked to ensure that it is running properly. The equipment is stabilised during a period of warming up that lasts between 3 to 4 minutes. Once this is done, the all data streams have their timing set by synchronising them with a Garmin GPS. A visualisation program called CM201 supplied by Geometrics, is run to ascertain visually that the magnetometer is running smoothly and producing no spikes or spurious readings while not in motion. Once all the systems have been checked and are working without any problems, the data acquisition program is initiated. The technician conducting the survey can verify real-time on a screen that all the data channels are recording correctly. The pilot then activates the navigation on the Satloc and begins the survey. On return the technician confirms that the system functioned without problems and terminates the acquisition program.

4.2. Data Processing

The data from the airborne survey were prepared for easy importation into the processing software by pre-formatting the columns to be compatible with Intrepid, the processing software. This includes merging appropriate columns to represent the input columns expected by Intrepid. The processing software used for this project was Intrepid, an airborne processing package developed by Des Fitzgerald and Associates Pty Ltd.

4.2.1. Magnetic Processing

Altitude will cause variations in amplitude of the local magnetic anomalies due to variations in the distance between the source of the anomaly and the recording instrument (Luyendyk, 1997). This effect is especially noticeable when the survey is flown over an escarpment and the aircraft has to climb gradually in one direction while descending rapidly in the other. The shape of the flight path in the upward direction is generally significantly different than the shape of the flight path in the downward direction. This can lead to a “corrugated iron roof” effect coincident with rapid variations in topography.

The distance between the navigation reference point along the axis of the aircraft and the magnetometer recording instrument is referred to as the cable length (Luyedyk, 1997). If the cable length is not zero, then a parallax correction must be applied to synchronise the magnetic and navigational data (Luyendyk, 1997). The navigation data are interpolated to coincide with the location of the recording instrument. The parallax correction is then determined by calculating the velocity of the aircraft at each x-y point from the navigational data and then using this velocity to adjust the navigation data, allowing for the cable length (Luyendyk, 1997).

The magnetic signature of the aircraft consists of three components; the permanent magnetisation, magnetisation induced by the motion of the aircraft and a component due to flow of electrical current within the aircraft (Luyendyk, 1997). The permanent

magnetisation of the aircraft causes what is known as the heading error. This error is caused by the vector addition of the earth's field to that of the aircraft (Luyendyk, 1997). This causes a base-level shift between lines flown in opposite directions (Luyendyk, 1997).

Due to the fact that a metal object (in this case the aircraft) moving through the earth's magnetic field will produce a magnetic field of its own, magnetic compensation for the aircraft is needed. This is the second component of the magnetic signature of the aircraft mentioned earlier. Data inconsistencies between adjacent flight lines (corrugation) (Mauring and Kihle, 2006) can be caused due to this created magnetic field changing each time the aircraft turns to fly the next line in the opposite direction as well as differences caused by little swerves and dips has to be addressed as well. The process of compensation is achieved by calibrating the system and then using these values to correct the data. This calibration is done by first taking the aircraft very high in the air while readings are taken with both the Cs vapour magnetometer and a fluxgate magnetometer. It is assumed that these reading are only influenced by the aircraft. Then the aircraft is taken through a set series of manoeuvres in four different directions, while taking readings on both magnetometers. The plane undergoes a total of three pitches ($\pm 5°$), roll angles ($\pm 10°$) and yaw ($\pm 5°$) manoeuvres during the calibration flight in each of the directions of the flights lines at an altitude of approximately 3000 m above a zone ideally with no magnetic anomalies. The data generated by these flights are used by the compensation software to provide a solution for the effect of aircraft motions. The fluxgate magnetometer measures an individual component of the field. Thus, three fluxgates can measure all three components of the vector. The Cs vapour can only measure the size of the vector, not its direction. The compensation algorithm takes these fluxgate readings that are associated with the movements of the aircraft and associates them with the effect the movements had on the Cs vapour magnetometer readings. These effects will then be corrected for during the actual survey (Cole et. al., 2009). The figure of merit (FoM) is calculated during the calibration process. It is the sum of the 12 magnetic declinations caused by the rotations around the three axes of the airplane flying in the four main directions of the flight lines. The FoM varies according to the intensity of

the magnetic field, which accounts for the necessity to carry out the test close to the survey zone.

The magnetic compensation was done post process. This is purely because this is the system in use by the CGS. There are advantages to post processing compensation as opposed to real time compensation, in that one can return to the data and tweak it until one is entirely satisfied with the results. This is not the case with real-time compensation. The Geometrics MAGCOMP magnetic compensation software is state of the art and allows compensation of up to 5 magnetic sensors simultaneously. It is possible to obtain a Figure of Merit (F.O.M.) of less than 0.3 RMS (Root Mean Square) consistently with this method. Residual heading error of less than 0.2 nT is also achieved.

The airborne magnetic data are pre-levelled by subtraction of the base station magnetometer data from the airborne data to produce a new channel called *basecor*. A constant value is added to the output to eliminate negative numbers. This value is the first collected base station value. The magnetic data are then levelled via the Intrepid levelling tools. The normal method of levelling magnetic data is polynomial levelling. This involves fitting a polynomial to the intersection errors along a flight line and tie line as a function of elapsed time, by the method of least squares (Luyendyk, 1997). Intersection errors occur when the data at the point where a flight line and a tie-line cross differ from each other. These polynomials are then subtracted from the original data, reducing the intersection errors. The output is a levelled magnetic channel which is then imaged. Micro-levelling was applied to the final grid. Micro-levelling removes the remaining residual errors at the cross over intersections after standard processing and tie line levelling is applied. The INTREPID implementation of micro-levelling is a two stage operation, beginning with a grid created from the tie-line levelled data. Corrections are applied to a line dataset based upon the values in the levelled grid. Each data point is adjusted according to the value of the nearest levelled grid cell value. The processing of the data was performed by the consultant that performed the survey.

4.2.2. Digital Terrain Model (DTM) Creation

Subtracting the laser altimeter channel from the GPS altimeter channel determines the DTM. Due to the narrow beam of the laser altimeter, if the aircraft is in a steep climb or descent, some deflection on the sides of large sharp features, (e.g. cliff edges) might be apparent. Micro-levelling (see 4.2.1) was then applied and the data gridded using a grid cell size of 50 m. Elevations are located in x and y to ± 2 cm and determined at each point in z to ± 2 cm.

4.2.3. Spectrometer Processing

Scintillation detectors are used to detect the light photons which are emitted when electrons in a crystal relax after being excited by gamma rays entering the crystal. These photons have characteristic energies, with the number of photons emitted per event being determined by the energy of the incoming gamma ray. The determination of the energy of the gamma ray requires that the number of photons produced be counted. Gamma-ray spectrometers analyse the incoming pulses from a scintillation detector and use the pulse height to determine the energy of the incoming gamma-ray. These are then assigned to channels and a count rate in a number of energy channels is determined.

The role of data processing is to correct the observed data for those influences that are not related to the geology, and then reduce the airborne count rates to estimates of the ground concentrations of the radioactive elements (IAEA, 2003). Spectrometer processing consists of:

Livetime / deadtime normalisation

The spectrometer has a two-stage measuring technique whereby it will detect an incoming photon and then start to measure it. While measuring the photon all detection is suspended. Thus dead time refers to the time required for the spectrometer to process individual photons (Minty, 1997). The time during which the spectrometer is receptive to incoming pulses is the “live time” (IAEA, 2003). Most modern spectrometers automatically record the system dead time (or live time), which is output with the data stream for later processing (IAEA, 2003). There are two methods of correcting for dead

time, depending on the spectrometer used. Some spectrometers can measure the *live time*, that is the time spent on detecting the incoming photons (not measuring their energy), and this is done in milliseconds.

A typical dead time would be of the order of 5-15 μs/pulse, and can be corrected for as follows (IAEA, 2003):

$$N = \frac{n}{1 - Ct} \qquad \text{equation (4.1)}$$

where N = corrected count rate (counts/sec);

n = observed count rate (counts/sec);

C = total count rate over all channels (counts/sec);

t = the equipment dead time per pulse.

Dead time can be measured experimentally (IAEA, 1991) by connecting the spectrometer to two identical detector packages. The total-count count rates are measured with each of the detector packages connected to the spectrometer separately, and then with both packages connected to the spectrometer simultaneously. Usually the individual detector packages will yield approximately the same count rates, in which case the dead time is given by (IAEA, 1991):

$$t = \frac{2N - N_T}{NN_T} \qquad \text{equation (4.2)}$$

where N = average total count rate from the individual detector packages;

N_T = total count rate measured with both detector packages connected;

t = dead time per pulse (seconds).

Energy Calibration

Spectrometers are affected by energy drift in the measured spectra. This drift is caused by changes in the gains of the photomultiplier tubes as a result of drift in the high-voltage supply and changes in temperature (IAEA, 2003). The measured spectra need to be corrected for this instrument drift. Modern spectrometers have in-built self-stabilising features and the total drift with these instruments is less than one channel (IAEA, 2003).

The energy calibration procedure described by The International Atomic Energy Agency (IAEA) (2003) is based on the estimation of the positions of prominent photopeaks in the observed spectra (IAEA, 2003). This requires well-defined spectra. The usual approach is to sum spectra along each line over at least 600 s, and determine the peak positions from this sum spectrum. The peak positions are then used to energy calibrate each of the individual 1^{-s} spectra used in the summation. The energies of at least two prominent photopeaks are determined as the maximum value of a quadratic fitted in the vicinity of each photopeak. A linear function is then fitted to the photopeak positions (channel numbers versus energy) to estimate the energy at channel 1 and the gain (keV per channel). These parameters are then used to correct each 1^{-s} spectrum within the sample accumulation period by re-sampling each channel to its correct energy range using linear interpolation.

Figure 4.3 shows the IAEA standard energy windows. The standard spectrum ranges from 0.0 to 3.0 MeV with 256 channels (0 to 255). Each channel has a range of 11.71873 keV. The IAEA standard windows are displayed in Table 4.2.

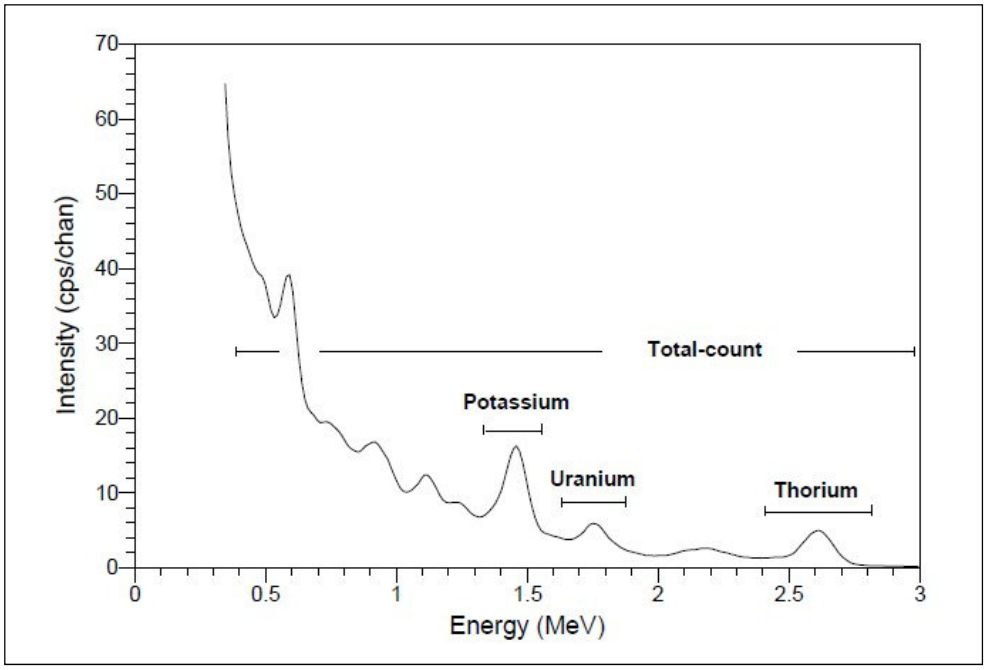


Figure 4.3. Typical airborne gamma ray spectrum showing the positions of the conventional energy windows (IAEA, 2003).

Table 4.2. Standard gamma ray energy windows recommended for natural radioelement mapping (IAEA, 1991). The energy of the photo peak being monitored is shown in brackets after each nuclide

Window	Nuclide	Energy Range (MeV)
Total Count	-	0.400 to 2.810
Potassium	^{40}K (1.460 MeV)	1.370 to 1.570
Uranium	^{214}Bi (1.765 MeV)	1.660 to 1.860
Thorium	^{208}Tl (2.614 MeV)	2.410 to 2.810

Aircraft and cosmic correction

Measured radiometric data contain data originating from the ground surface, the aircraft and outer space (cosmic) radiation. Primary cosmic radiation from outside our solar system and from our sun reacts with atoms and molecules in the upper atmosphere and generates a complex secondary cosmic radiation. This radiation reacts with the air, aircraft and detector to produce the measured cosmic gamma-ray background (Minty, 1997). Only the ground data are of interest to the survey, so the data have to be corrected for the aircraft background and the cosmic background. Aircraft background is removed by subtracting a 256 channel aircraft background spectrum directly from the measured spectrum for each data point. Figure 4.4 shows an example of such a 256 channel aircraft background spectrum.

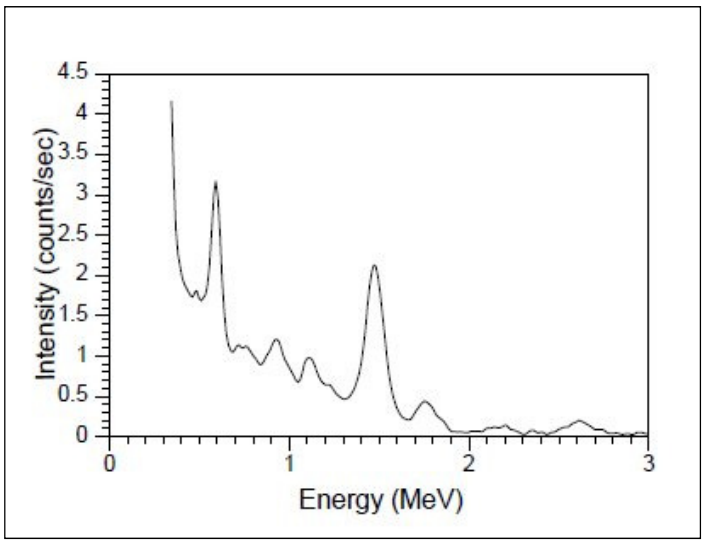


Figure 4.4. Example of aircraft background spectrum (IAEA, 2003)

To remove cosmic background, a 256 channel spectrum is used as a unit vector of coefficients. This is achieved by the acquisition of spectra over water at a number of different heights (say 1.0, 1.5, 2.0, ... 3.5 km above sea level) in an area where atmospheric radon is at a minimum (IAEA, 2003). The measured spectra are each the sum of the aircraft component (constant) and the cosmic component. Because the aircraft background remains constant, the count rate in the 3 to 6 MeV cosmic window is linearly related to the count rate in the i'th energy channel. Thus, a linear regression of the cosmic window count rate on any other particular channel yields the cosmic sensitivity (slope of regression line) and aircraft background (zero intercept) for that channel as shown in equation 4.3.

$$n_i = a_i + b_i n_{\cos} \qquad \text{equation (4.3)}$$

where n_i = aircraft + cosmic background count rate in the *i*'th channel;

n_{cos} = cosmic window count rate;

a_i = aircraft background in the i'th channel;

b_i = cosmic background in the i'th channel normalized to unit counts in the cosmic window.

An example of a cosmic background spectrum is shown in Figure 4.5.

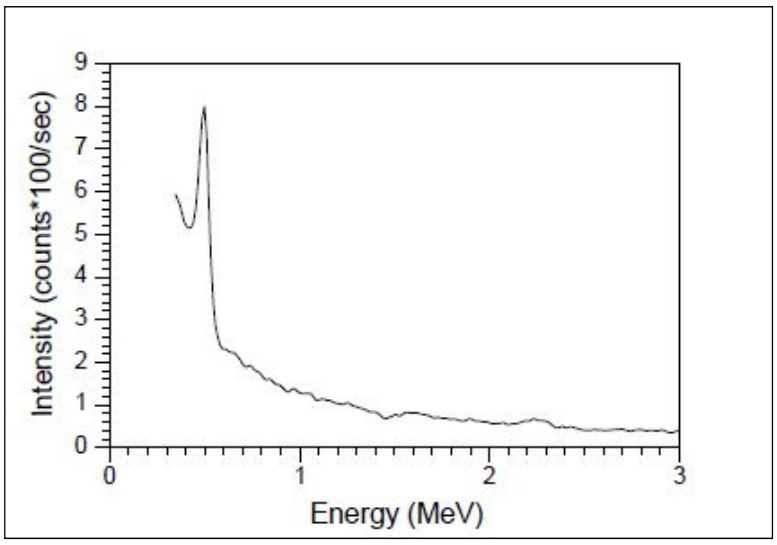


Figure 4.5. Example of cosmic background spectrum (IAEA, 2003)

Radon (Rn) correction

Rn is a radioactive gas with a response similar to that of terrestrial U. When present it will have the effect of giving the U and Total Count windows abnormally high background counts along entire flight lines or groups of lines (usually lines flown the same day). It can be removed by either using the 'Spectral Ratio Method' described by Minty (1997) which uses the shape of the gamma ray spectrum to estimate the atmospheric radon concentration or by measuring the Rn in the atmosphere with an upward-looking detector, the idea being that since Rn is a inert gas it will be in the air if present. The upward looking detector measures everything except radiation coming from below, thus it would measure Rn if it were present and not responses from the ground. The upward looking detector method was used for the processing of the current survey data.

The upward-looking detector method uses an additional crystal pack that is partially shielded from radiation from below to give the system a directional sensitivity and the ability to discriminate between radiation from the atmosphere and from the ground. The radon contribution to the uranium window of the main detector package (i.e. the "downward" U window) is given by equation 4.4 (IAEA, 1991).

$$U = \frac{u - a_1 U - a_2 T + a_2 b_t - b_u}{a_u - a_1 - a_2 a_t} \qquad \text{equation (4.4)}$$

Where

U_r = radon background in the "downward" U window;

u = count rate in the "upward" U window;

U = count rate in the "downward" U window;

T = count rate in the "downward" Th window;

and a_1, a_2, a_u, a_t, b_u and b_t are constants derived by suitable calibration.

Height attenuation correction

In airborne surveying the height of the detector changes continuously as the aircraft proceeds along a flight line, and the window data must be corrected to a nominal survey height. Window count rates vary approximately exponentially with height for the range of heights normally encountered in airborne surveying (IAEA, 2003). According to Schwarz et al. (1992) the true fall-off of radiation with height for infinite sources more closely resembles that of an exponential integral than a simple exponential. Height must be corrected for the ambient temperature and pressure since both affect the density and thus the attenuating properties of the air (IAEA, 2003). To correct for this an attenuation coefficient has to be applied to the data. This coefficient is determined by flying over a calibration range at various heights and attenuation coefficients are derived from exponential regression of each background corrected and stripped channel count rate against detector height (IAEA, 2003). An example of such an attenuation curve is given in Figure 4.6.

The calibration range should be relatively flat, have uniform K, Th and U concentrations, be over a large body of water (background measurements), have no flight restrictions, be accessible for surface measurements, easy to navigate, about 8 km long and have no hills within about 1 km of the flight path (Coetzee, 2001). Such a range has been identified at Hentiesbaai in Namibia and was used for the survey. The CGS has tried to identify a calibration site within South Africa, but none could be found. The Hentiesbaai site is internationally accepted as a calibration site.

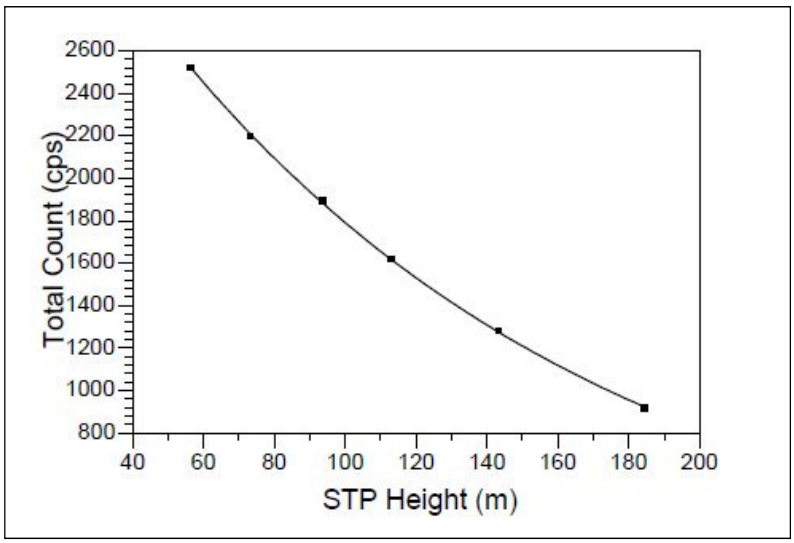


Figure 4.6. Example of a height attenuation curve from IAEA (2003)

4.3. Summary of data collection

A survey to collect higher resolution magnetic and radiometric data was performed in 2006 by the CGS and SES. The survey was performed at 80 m nominal height and 200 m line spacing. The magnetic data collected were corrected for altitude to remove errors caused by adjacent flight lines not being at the same height and levelled to remove errors caused by differences between flight line and tie-line values at their points of intersection.

A digital terrain model was created and microlevelled as by-product of the survey. Live time/dead time normalisation, energy calibration to compensate for the effect of energy drift in the measured spectra caused by changes in temperature and energy gain in the equipment, aircraft and cosmic correction to remove the effect from radiation caused by elements other than those on the surface of the earth, radon correction to remove the effect of radon gas on the data and height attenuation correction to produce a nominal window height, were performed on the spectrometer data.

These corrections and processing was performed to produce a quality dataset acceptable for interpreting.

CHAPTER 5. Geophysical Data Sets

5.1. Magnetic data

The total magnetic field intensity data collected during the survey and used in this project are shown in Figure 5.1. These data were microlevelled and gridded at 50 m cell size. The projection is Transverse Mercator, datum WGS 84 and the central meridian used is 29° east. The data were collected at 200 m flight line spacing with the flight lines running north-south (Figure 5.2) and flight height of 80 m. Tie-lines strike east-west at 2000 m intervals. These parameters were used because they are the standard for statutory high resolution surveys conducted by the CGS for government. The data are sun shaded using an azimuth of 45° and elevation of 45°. Since the most prominent features in the data strike between 45° and 60° and are visible without the aid of sun shading, the less prominent features striking between 60° and 180° are enhanced by the chosen direction for sun shading.

According to Reid (1980), if any interpretation is to be performed on a data set then the aliased power (given by equation 5.1) should not exceed 5% given a minimum value of 0.5 for $\bar{h}/\Delta x$. This means that the line spacing or sample spacing (whichever is larger) should not exceed double the distance between the sensor and the magnetic source.

$$F_T = \exp\left(-2\pi\bar{h}/\Delta x\right) \qquad \text{equation 5.1}$$

Where F_T is the fraction of the power aliased,

$\bar{h}$ is the mean height of the sensor above magnetic source

and

Δx is the line spacing

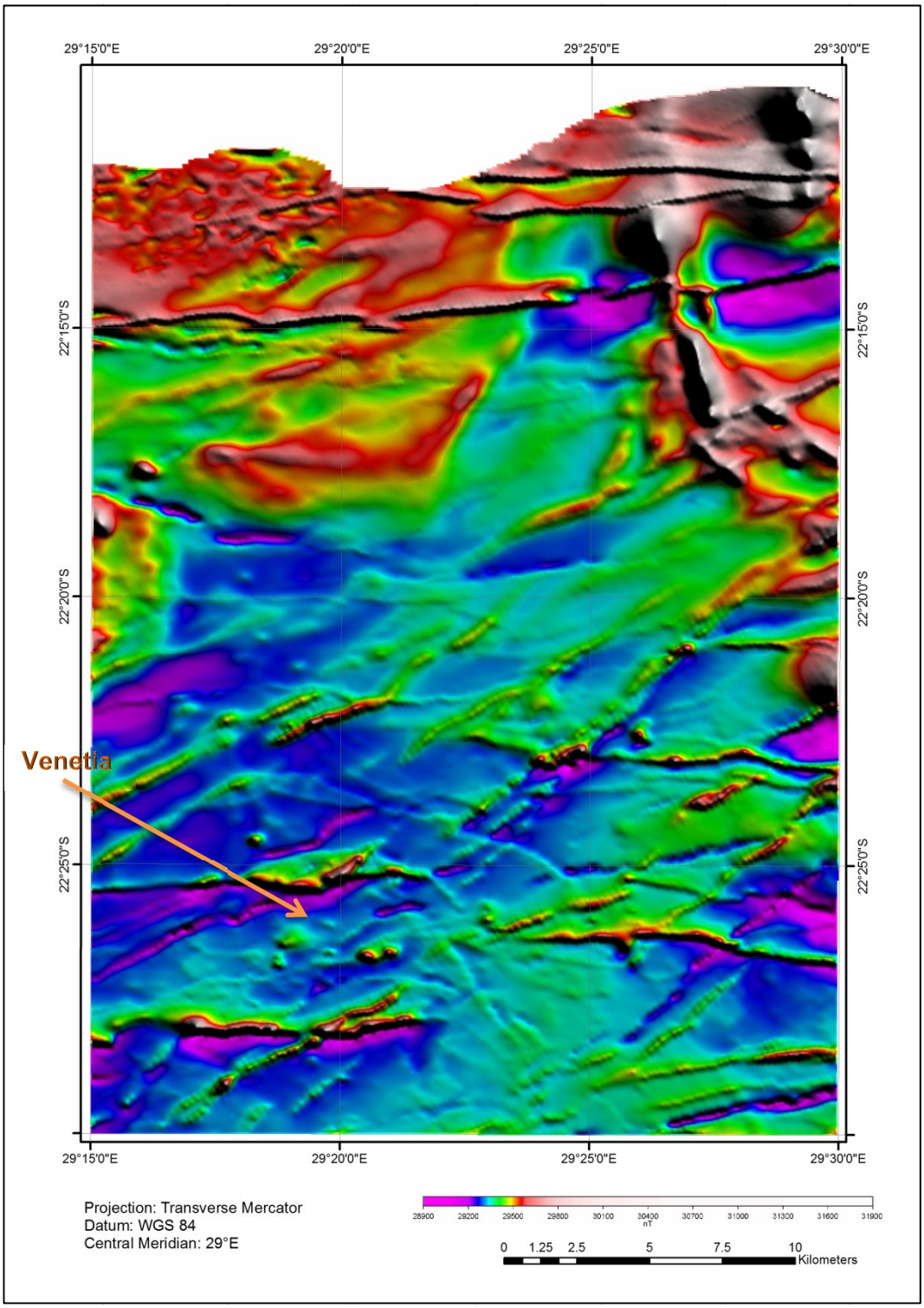


Figure 5.1. Total magnetic field data, sunshaded with azimuth 45° and elevation 45°. This positions the sun at 45° clockwise from due north and 45° up from the horizon.

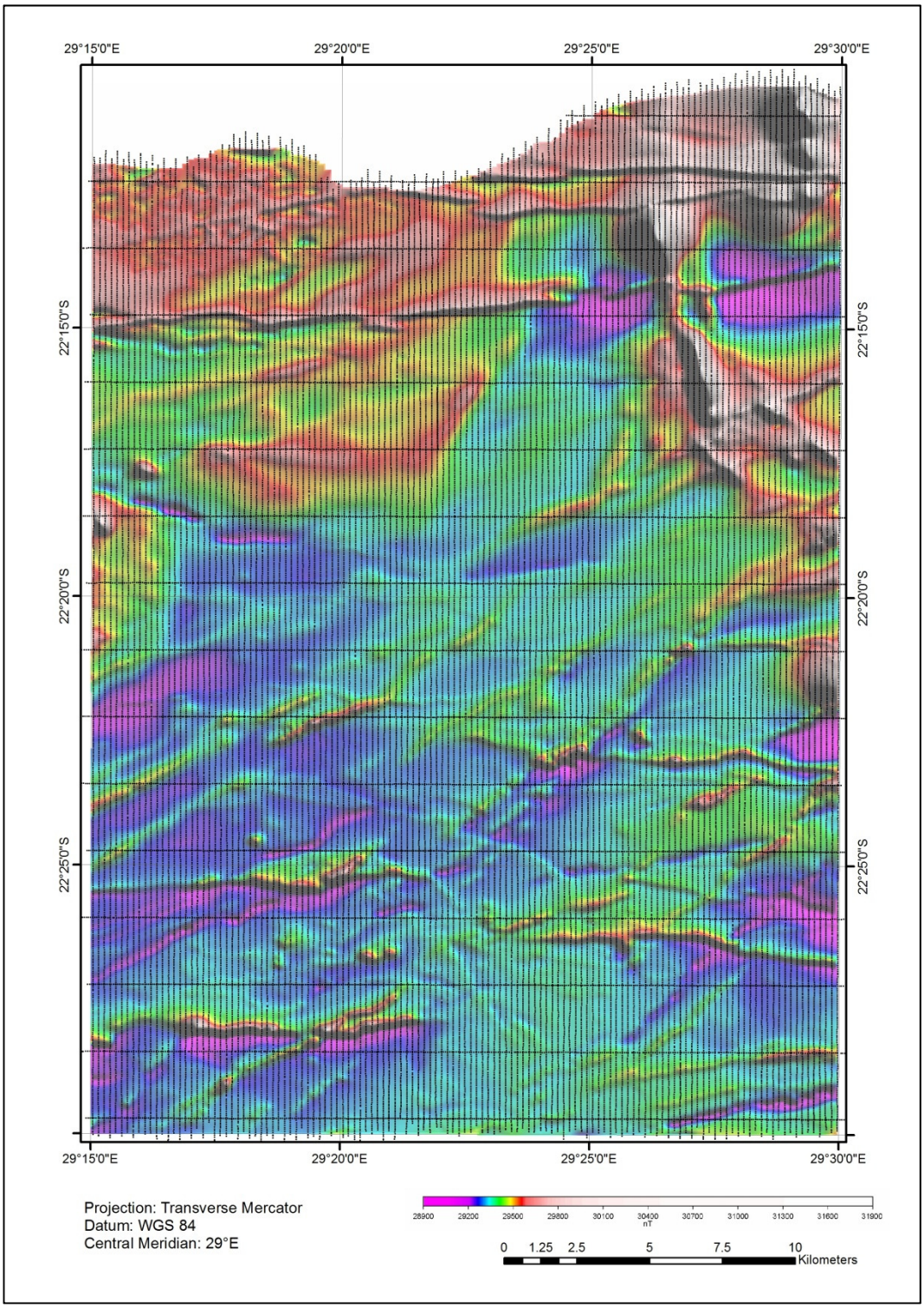


Figure 5.2. Survey lines and tie lines over an image of the magnetic data.

If a mean height of 100 m above source (80 m flight height and 20 m surficial cover and weathering zone) is assumed for this survey, then the fraction of the power aliased is 0.043 and the percentage aliased is 4.3% since the magnetic source such as dykes does not crop out but their anomalies are sharp and presumed to be near surface. Thus the

data collected satisfies Reid's criteria and single anomalies can be modelled from gridded data.

These aeromagnetic data were collected because a large part of the area is covered in sand and many of the structural features suggested on the old regional magnetic data cannot be verified in the field due to cover and severe aliasing present in the older data. Magnetic data are used to delineate structural features such as dykes and faults as well as geological lithologies and contacts at surface and at depth. Higher resolution data are necessary to get a clearer understanding of the structural and spatial relationships in the area. The older regional surveys were flown at a height of between 100 m and 150 m. According to Reid (1980) the line spacing should then not be more than between 200 m and 300 m. These old surveys were flown with a line spacing of 1000 m and therefore do not satisfy Reid's criteria. Features at 350 m depth will be 500 m from the sensor and won't be aliased for 1000 m line spacing. But those less than 350 m deep are seriously aliased. When applying equation 5.1, a feature at surface will have an aliased power of between 53% and 39% for distance between sensor and source between 100 m and 150 m.

Very high resolution (1:10,000 scale) geological mapping was done in the areas directly surrounding the Venetia diamond mine (Barton et al., 2003). These geological data are too local to aid in the investigation of the larger structures in the study area. The gap between these data sets is bridged by this higher resolution (200 m line spacing) aeromagnetic survey. Linear features, the relationships between linear features, lithologies and contacts can be mapped in greater detail and with more accuracy than was possible with the regional 1 km line spacing data. Circular bodies with diameters up to 50 m have been identified.

5.1.1. International Geomagnetic Reference Field (IGRF)

The IGRF is produced and maintained by the International Association of Geomagnetism and Aeronomy (IAGA), Working Group V-MOD. It is an established numerical model used to calculate the large scale internal part of the Earth's magnetic field at locations on

or above the surface, at times between 1900 A.D. and present (IAGA, Working Group V-MOD, 2010). This part of the geomagnetic field is almost entirely core-generated. It is the liquid outer core, an electrically conducting fluid heated by the solid inner core, that is mostly responsible for the geomagnetic field. This 'boiling' iron fluid causes a geomagnetic field that is as ever-changing as the currents in the core that cause them. These changes are measured on timescales of years to decades (IAGA, Working Group V-MOD, 2010). It is revised every five years to remain up to date.

The IGRF represents the geomagnetic field, $\mathcal{B}(r, \theta, \phi, t)$, on or above the Earth's surface (IAGA, Working Group V-MOD, 2010). This field is produced by internal sources in terms of a scalar potential $V(r, \theta, \phi, t)$. This gives us $\mathcal{B} = -\nabla V$ where V is a finite series having the numerical Gauss coefficientsg_n^m, h_n^m:

$$V(r, \theta, \phi, t) = a \sum_{n=1}^{N} \sum_{m=0}^{n} \left(\frac{a}{r}\right)^{n+1} [g_n^m(t) \cos m\phi + h_n^m(t) \sin m\phi] \times P_n^m(\cos \theta) \quad \text{equation 5.2}$$

Where r denotes radial distance from the centre of the Earth in units of km

a = 6371.2 km is the magnetic reference spherical radius

θ denotes geoscentric co-latitude

and

ϕ denotes east longitude

The IGRF was calculated for the study area and is shown in Figure 5.3. The IGRF was then removed from the data to show the magnetic field variations due to the geology in the area.

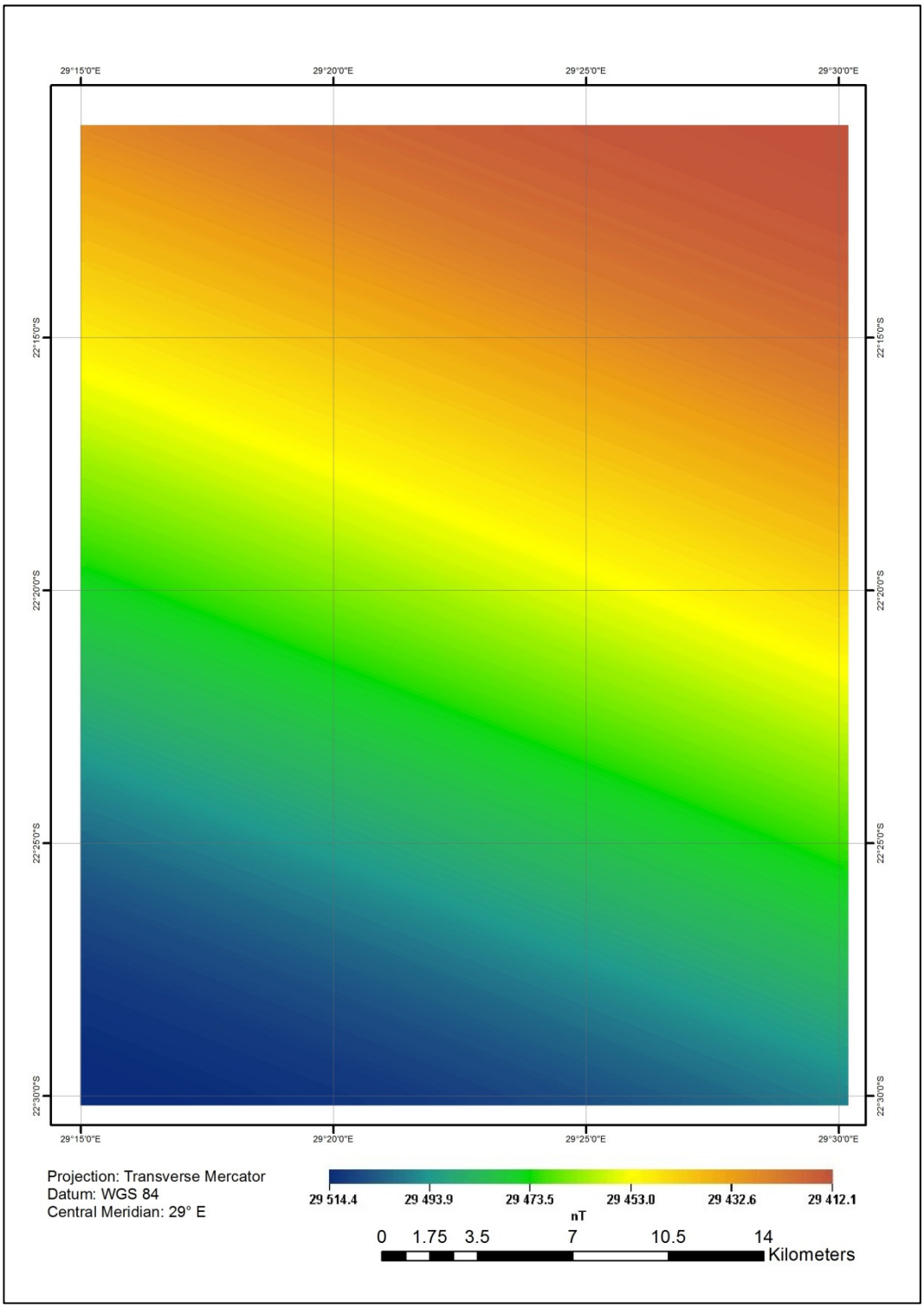


Figure 5.3. The IGRF for the study area shows an increase in total intensity towards the northeast.

5.1.2. Qualitative Observations

The magnetic data (Figure 5.1) display higher frequency signatures in the form of short wavelength linear anomalies (± 200 m width) and small round anomalies (200 m - 500 m diameter) in the south. The lineaments have two main strike directions, east to west and

northeast to southwest. There also are some northwest to southeast trending lineaments. These lineaments have prominent amplitude of up to 300 nT and are fairly narrow (about 200 m to 400 m wide). Geological ground mapping in the area (Barton et. al. 2003) show that most of these lineaments do not outcrop as dykes in the field; it is possible that they could be caused by magnetized faults or dykes buried at depth.

The abundance of the lineaments becomes less toward the north of the area with only three or four prominent east to west trending lineaments found there. Broad anomalies in the north tend to be of longer wavelength (about 500 m to 600 m) than those in the south, suggesting that the source of the anomalies is deeper. This is consistent with most of the lineaments being in the basement and progressively more deeply buried under Karoo strata going northward.

A number of small, round anomalies are visible in the southwestern portion of the survey (Figure 5.4). They are clustered in two groups, a north-northwesterly trending group and an east-northeasterly trending group, indicated by the ovals marked A and A' respectively on Figure 5.4. A prominent magnetic source of 500 nT in the north of the study area (B on Figure 5.4) has a long wavelength and is probably buried at depth. A high amplitude (600 nT) source with wavelengths between 1000 m and 2000m in the northeast of the study area is also visible on the data (C on Figure 5.4) and is probably closer to the surface than B.

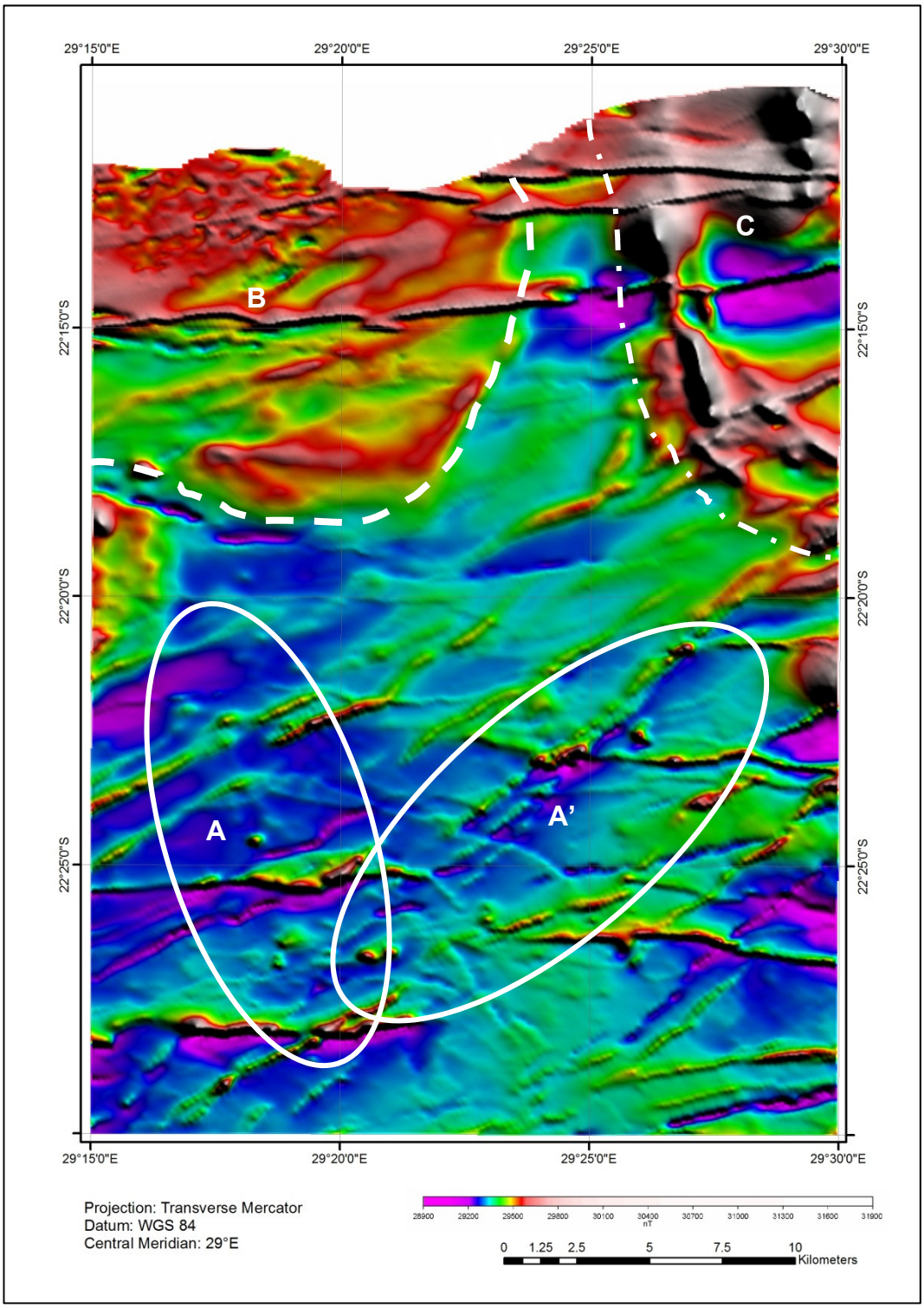


Figure 5.4. Microlevelled magnetic field intensity data, sunshaded (azimuth 45° & elevation 45°) to emphasize features not striking 45°. Here features striking 135° are the most prominent (Cooper, 2003). The regions labelled A and A' host a number of small, round anomalies, the region labelled B outlines a prominent anomaly of 300 nT in the region mapped as Karoo and (C) is a highly magnetic region (~600 nT) in the northeast.

5.1.3. Filters

The first step in developing a qualitative interpretation of aeromagnetic data is to enhance subtle features that may not be readily apparent in the total magnetic intensity map. A variety of filters can be used to enhance and highlight subtle features of the data.

Vertical Continuation

The magnetic field intensity can be determined at elevations above or below the elevation of measurement (Gunn, 1975). Upward continuation smoothes the data and downward continuation enhances detail and also noise (Cooper, 2004). The vertical continuation algorithm is applied by multiplying the Fourier transform of the field by a factor.

$$H = e^{-h\left(u^2+v^2\right)^{1/2}} \qquad \text{equation (5.3)}$$

where h is the distance above original plane of observation,

u and v are orthogonal wavelengths present in the data

which will convert the spectrum of the field measured at survey height into the spectrum of the field measured at a distance h above the original plane of observation. An example of the data upwards continued to 500 m is shown in Figure 5.5. The high frequency (mostly shallow) features are filtered out and only anomalies caused by deeper bodies are visible. Some positive (A on Figure 5.5) and negative (B on Figure 5.5) east to west trending lineaments in the north and south as well as a couple of northeasterly trending lineaments across the centre of the data set (C on Figure 5.5) are visible. A large positive anomaly (350 nT) in the northwestern portion of the area is visible (D on Figure 5.5) as well as a high positive anomaly (550 nT) in the northeastern portion (E on Figure 5.5).

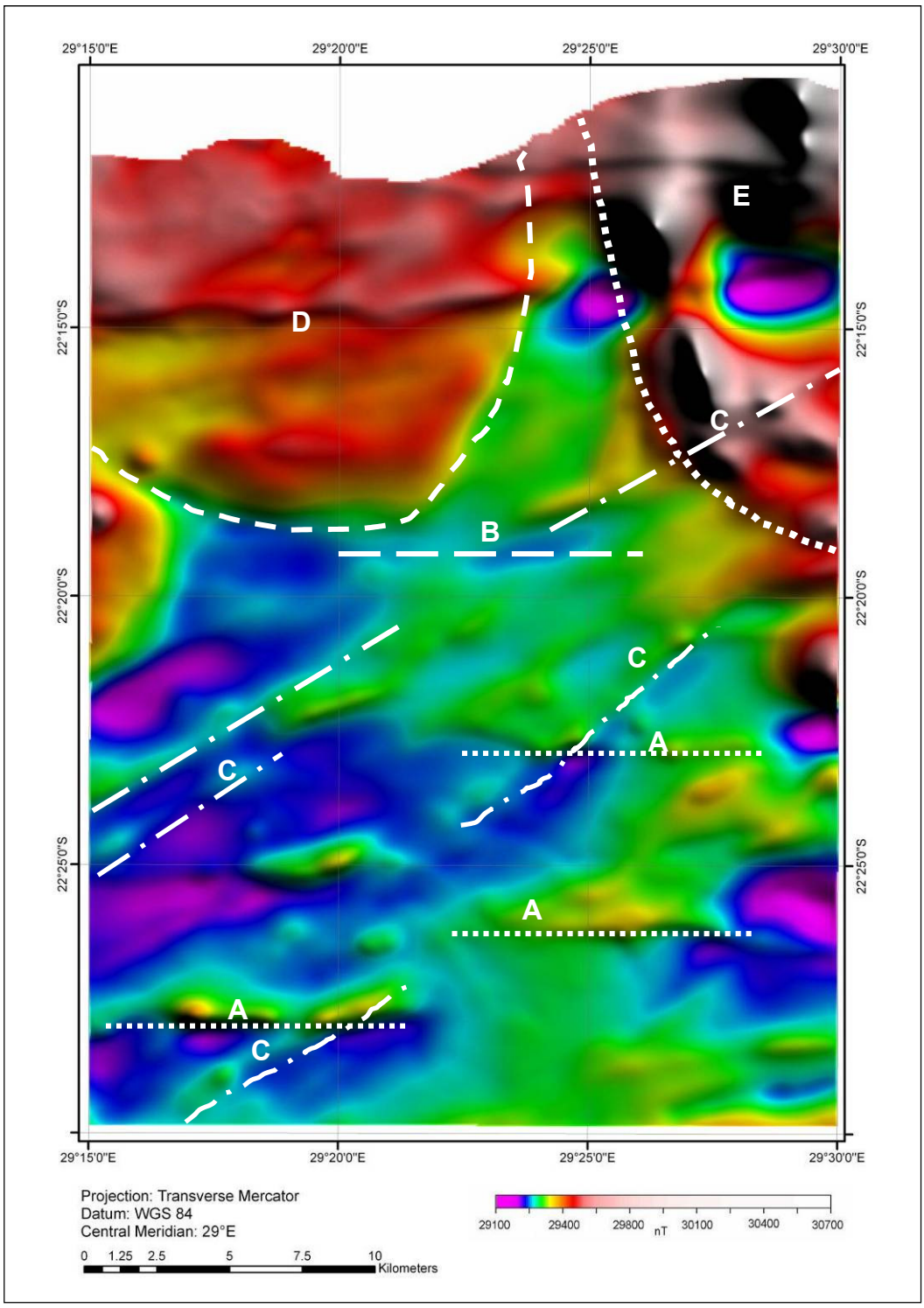


Figure 5.5. The magnetic data upward continued to 500 m. Positive amplitude (A) and negative amplitude (B) east-west trending linear anomalies, positive amplitude east-northeast trending linear anomalies (C), a large amplitude broad magnetic anomaly (D) and high amplitide broad magnetic anomaly (E) are indicated.

Vertical Derivatives

First and second vertical derivatives greatly enhances edges and subtle features in the data. They also enhance noise. In this study the first vertical derivative was calculated to enhance certain linear features that are not clear on the unfiltered total field magnetic data. In wavenumber domain, the n^{th} order vertical derivative is given by Blakely (1995) as:

$$A'(k) = A(k)|k|^n \qquad \text{equation (5.4)}$$

where $A(k)$ is amplitude at a wavenumber k ,

$k = \frac{2\pi}{\lambda}$ and

λ is wavelength

The first vertical derivative is approximately the difference between two simultaneous magnetic field measurements at two points vertically above each other divided by the spatial separation between them.

The process of creating vertical derivatives enhances high frequency data relative to low frequency data. It thus eliminates the regional effects and also resolves the effects of adjacent anomalies (Milligan and Gunn, 1997).

The first vertical derivative was calculated using the software package ER Mapper, for the magnetic data and is shown in Figure 5.6. The data were upward continued by 25 m (half of the gridding interval) during the calculation. Lineaments that are unclear on the total field magnetic data (Figure 5.4) become visible. This is especially true in the south, where lineaments on the total field data are obscured by broad magnetic highs (A on Figure 5.6).

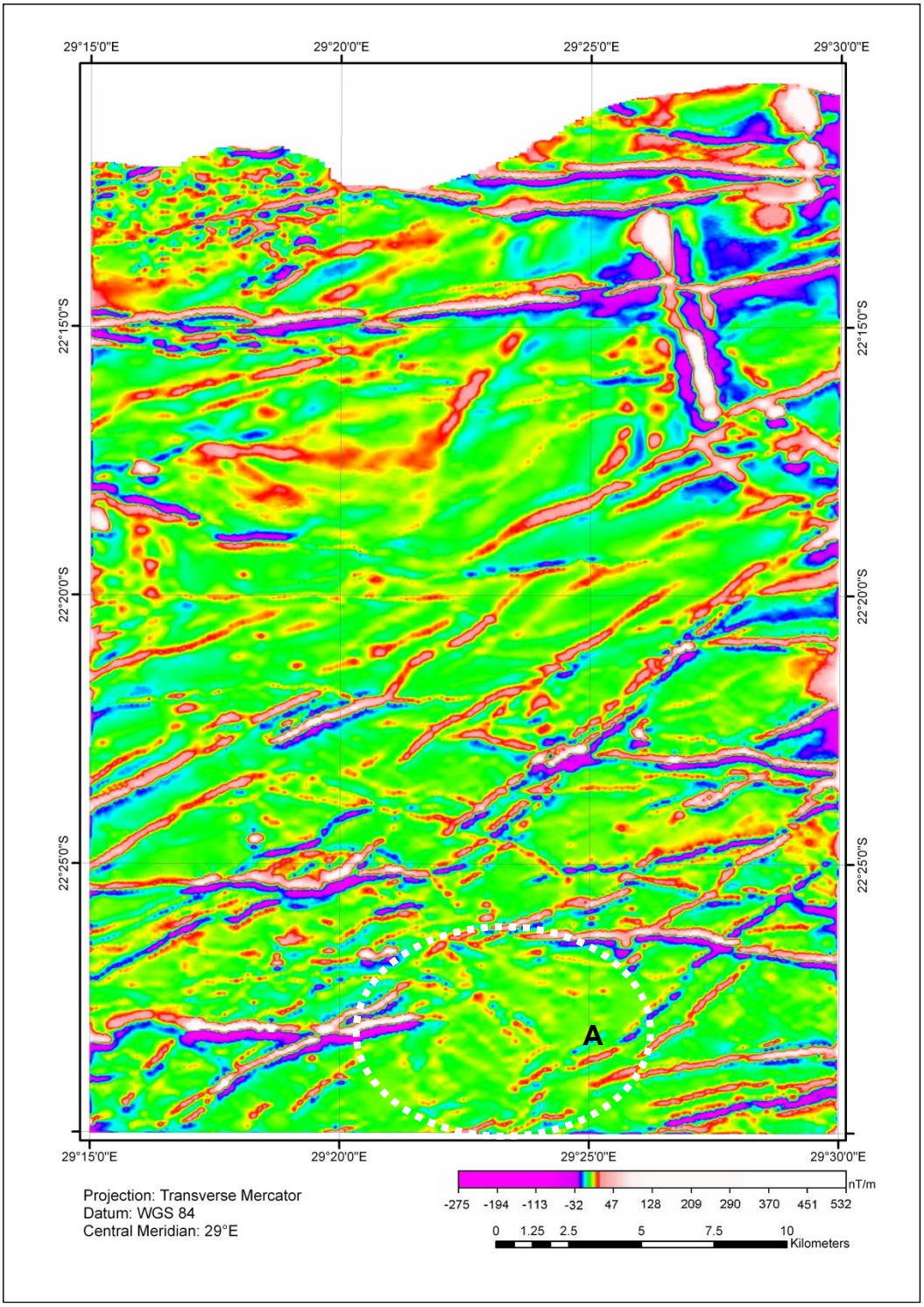


Figure 5.6. First vertical derivative of the magnetic data. Some of the linear anomalies that are not clear on the total magnetic field data are indicated in region A.

The second vertical derivative was calculated and is shown in Figure 5.7. Areas that are very quiet on the magnetic data show more detail in this dataset. Examples of such areas are marked with A, B, C and D (Figure 5.7).

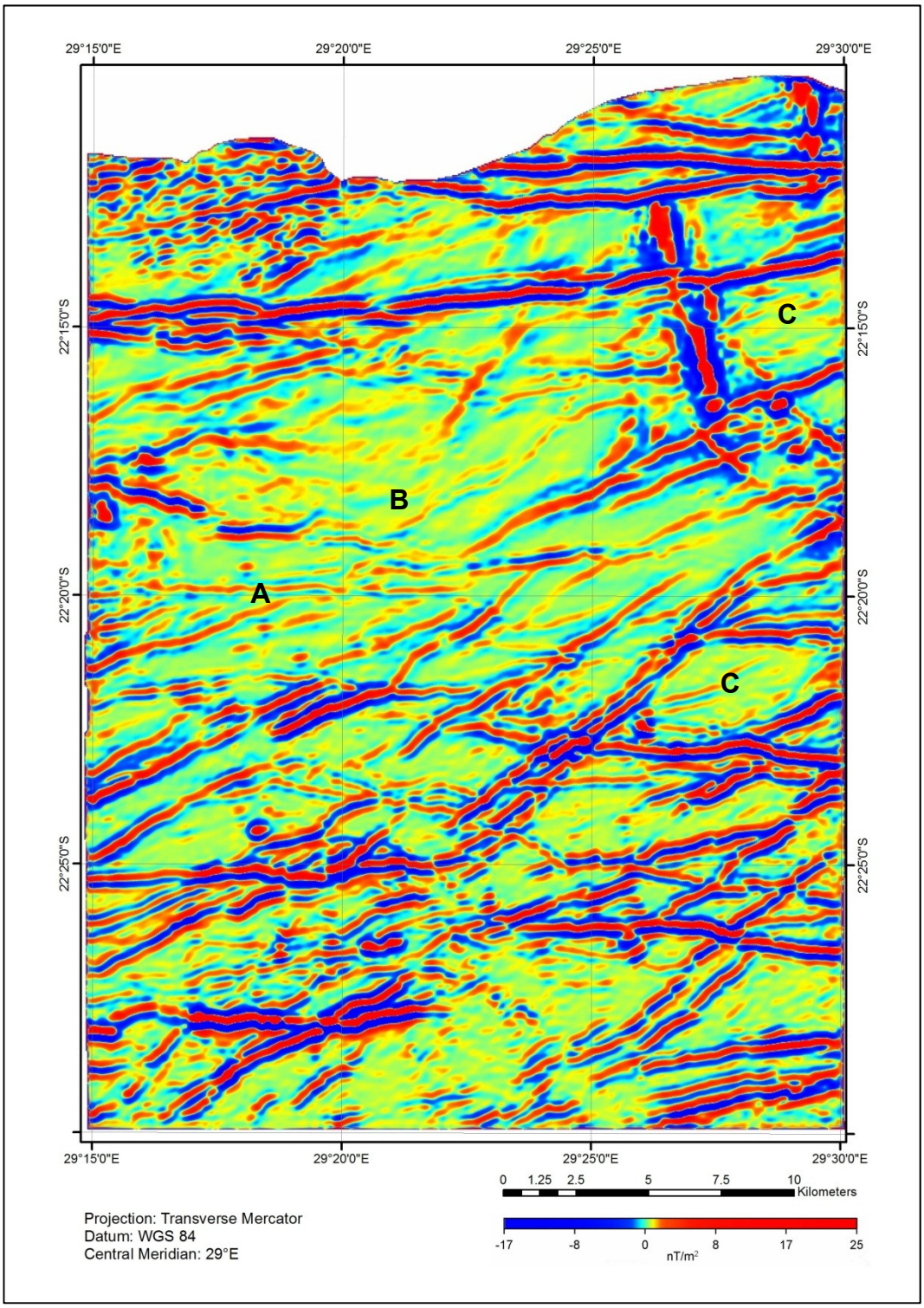


Figure 5.7. Second vertical derivative of the magnetic data. Features and textures not visible in the magnetic data become very clear in this data set. A, B, C and D shows examples of areas that are very quiet on the magnetic data, but have a definite texture in the second vertical derivative data.

Analytical Signal

According to Roest et al. (1992), the analytical signal is related to magnetic fields by the derivatives.

$$|A(x,y)| = \left(\left(\frac{\partial m}{\partial x} \right)^2 + \left(\frac{\partial m}{\partial y} \right)^2 + \left(\frac{\partial m}{\partial z} \right)^2 \right)^{1/2} \qquad \text{equation (5.5)}$$

Where *m* is the magnetic anomaly and

x, y and z are the 3 directional axes of the field.

In two dimensions this function is completely independent of the direction of magnetisation of the source and of the direction of the Earth's field (Roest et al., 1992).

The peaks of the anomalies in the analytical signal data are symmetrical and occur directly over the edges of wide bodies and the centre of narrow bodies (Milligan and Gunn, 1997). If, however, the contacts are not vertical, the three dimensional analytic signal amplitude (ASA) is not independent of the inclination and declination of the body's magnetisation and the earth's magnetic field (Li, 2006). Figure 5.8 shows the analytical signal calculated for the magnetic data in the study area. Several lineaments that are not visible or difficult to distinguish on the total field data are very clear on this dataset. This is especially true where a positive and negative anomaly are close to each other and it is not clear whether it is two lineaments or the negative of the anomaly. An example of this can be seen in the west, just south of 22°20'0"S (A on Figure **5.8**) where two thin parallel linear anomalies are visible, but on the total field data (compare with Figure 5.4) it is not clearly defined as two anomalies.

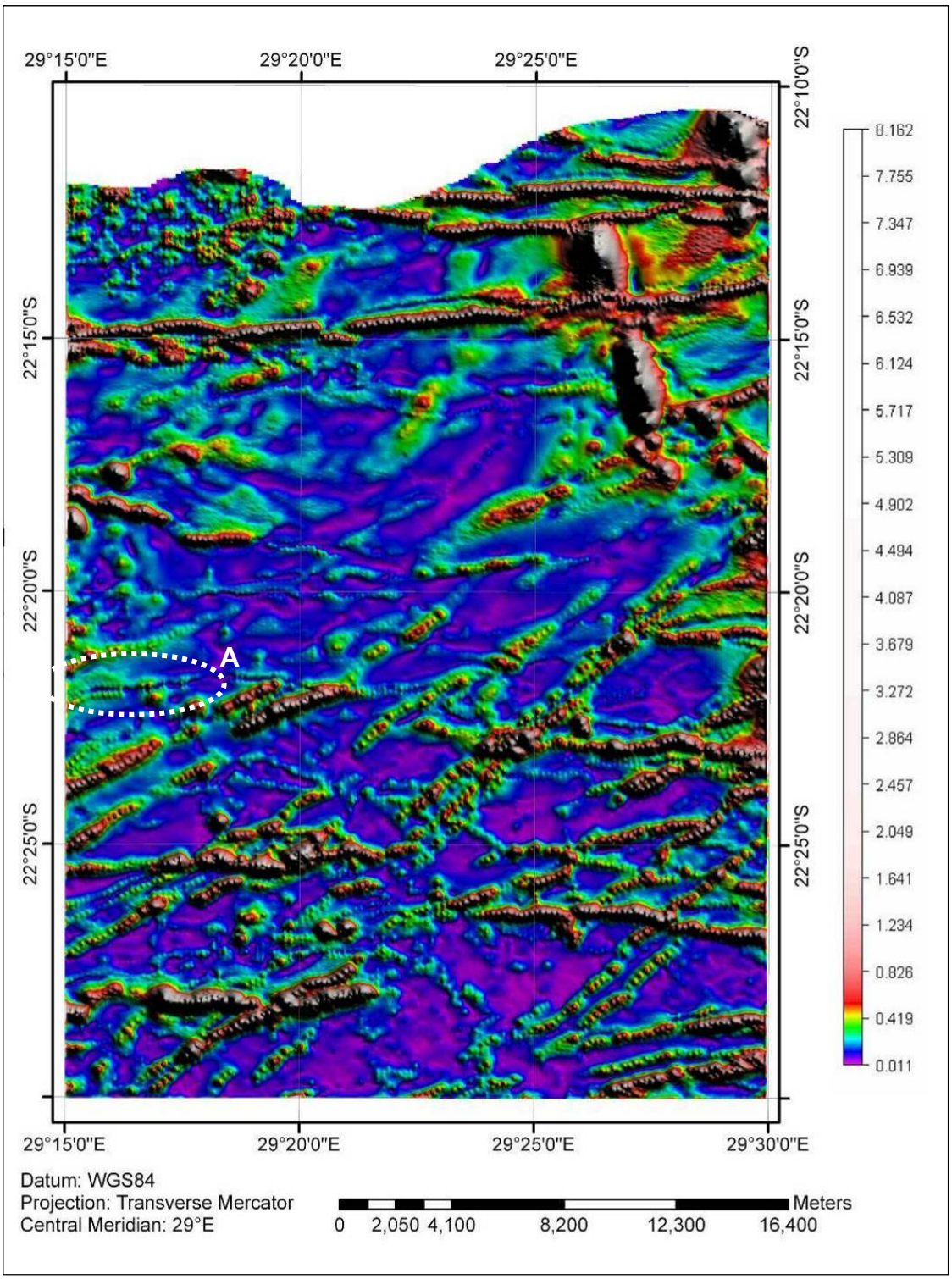


Figure 5.8. Analytical Signal calculated for the magnetic data. (A) shows an example of a linear feature that is not clear on the total magnetic field data.

Reduction to the pole

Magnetic anomalies in areas anywhere other than at the magnetic poles have an asymmetrical shape, even when the magnetic source distribution is symmetrical (Cooper and Cowan, 2005). This is due to the dipolar nature of geomagnetic data. Pole reduction is an operator that changes the asymmetric form of magnetic anomalies to the symmetrical form it would have if it were situated at a magnetic pole (Cooper and Cowan, 2005).

The frequency domain operator given by Baranov (1975) is:

$$A'(u,v) = \frac{A(u,v)}{(\sin\theta + i\cos\theta\sin(\phi+\alpha))^2} \qquad \text{equation (5.6)}$$

Where $A(u,v)$ is the amplitude at frequencies (u,v),

θ is the geomagnetic inclination,

ϕ is the geomagnetic declination and

α is $\tan^{-1}(v/u)$

Reduction to the pole has various known problems. It is unstable at low magnetic latitudes and gives incorrect values when the causative magnetic bodies possess unknown remanent magnetisation.

The magnetic data reduced to the pole is shown in Figure 5.9.

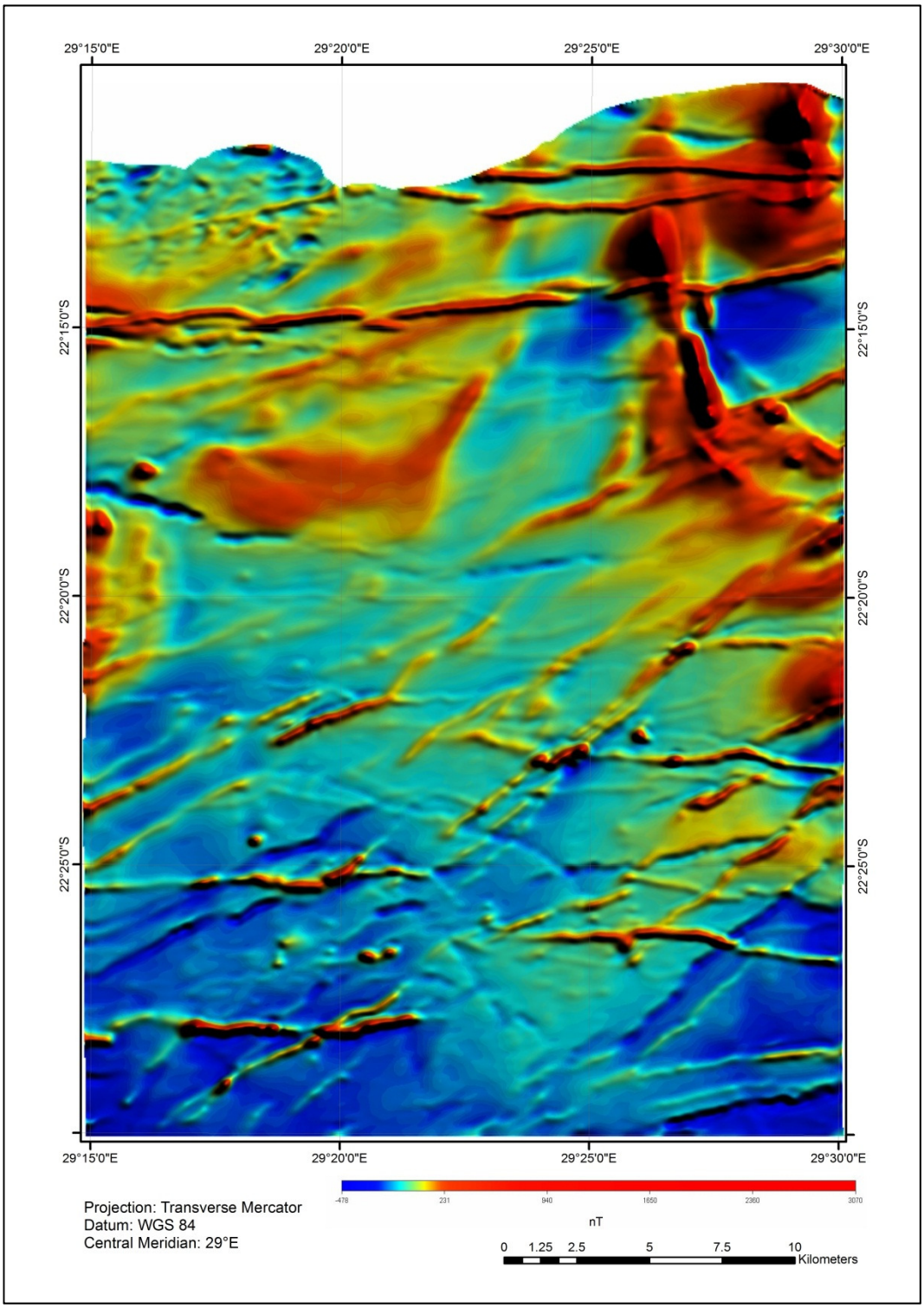


Figure 5.9. Magnetic data reduced to the pole.

Automatic Gain Control

Automatic gain control (AGC) is an example of a non-linear filter. This filter gives an equal representation of anomalies with both low and high amplitude. It does this by converting waveforms of variable amplitude into waveforms with semi-constant amplitude (Milligan and Gunn, 1997). AGC filters divide the data at each point by an average value computed in a window centered on that point (Cooper, 2009). The output depends strongly on the window size used. ACG filters are unsuitable for use with aeromagnetic data sets that contain anomalies of different amplitudes.

Within a window moving along a profile, the input signal amplitude is estimated by using the root mean square function. If the gain function of the amplifier is then taken to be inversely proportional to this amplitude value, then weak anomalies would have a large gain and strong anomalies a weaker gain. The AGC algorithm for profile data is given by:

$$A_x = Gain_x XF_x$$

$$Gain_x = \frac{1}{2w+1}\left[\sum_{i=x-w}^{x=w} F_i^p\right]^r \qquad \text{equation (5.7)}$$

Where $A_x = output$,

$2w + 1 = window\ length$,

$p = power$ and

$r = root$

The software program, Erdas ER Mapper, that was used to generate the filtered grids, has an option of four window sizes. These sizes are 3 x 3, 5 x 5, 7 x 7 and 9 x 9, where the number indicates the number of grid cell blocks the window is across. Figure 5.10 shows the results of the four window size options for comparison. The 3 x 3 window (Figure 5.10a) results are the clearest, while the features in the 9 x 9 window (Figure 5.10d) result are not clearly distinguishable and the results from window sizes in between degrading as the window size increases.

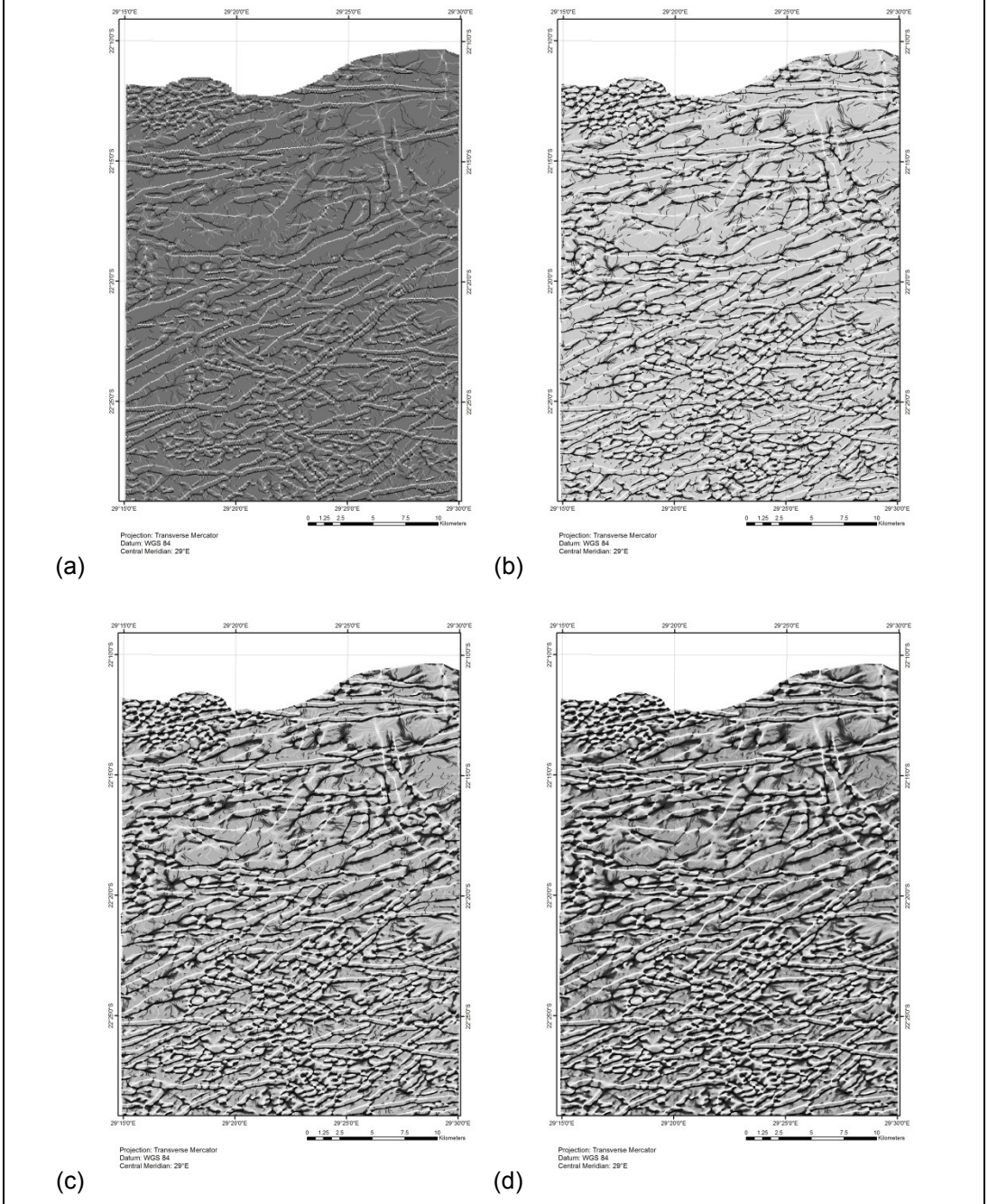


Figure 5.10. Comparison between the results for different window sizes when applying the AGC filter to magnetic data. The 3x3, 5x5, 7x7 and 9x9 windows are shown in (a), (b), (c) and (d) respectively. The 3x3 window seems to give the sharpest and clearest results, with the results becoming noisier as with increasing window size.

An example of this filter with window size 3 x 3 applied to the magnetic data can be seen in Figure 5.11. Many features that are not visible in the areas where the total field data (compare with Figure 5.4) have very low values in between linear features become clear on the AGC map (Figure 5.11). This is especially true in the area south of 22°20' S and west of 29°25' E (A on Figure 5.11),as well as in the northwest corner of the data (B on Figure 5.11).

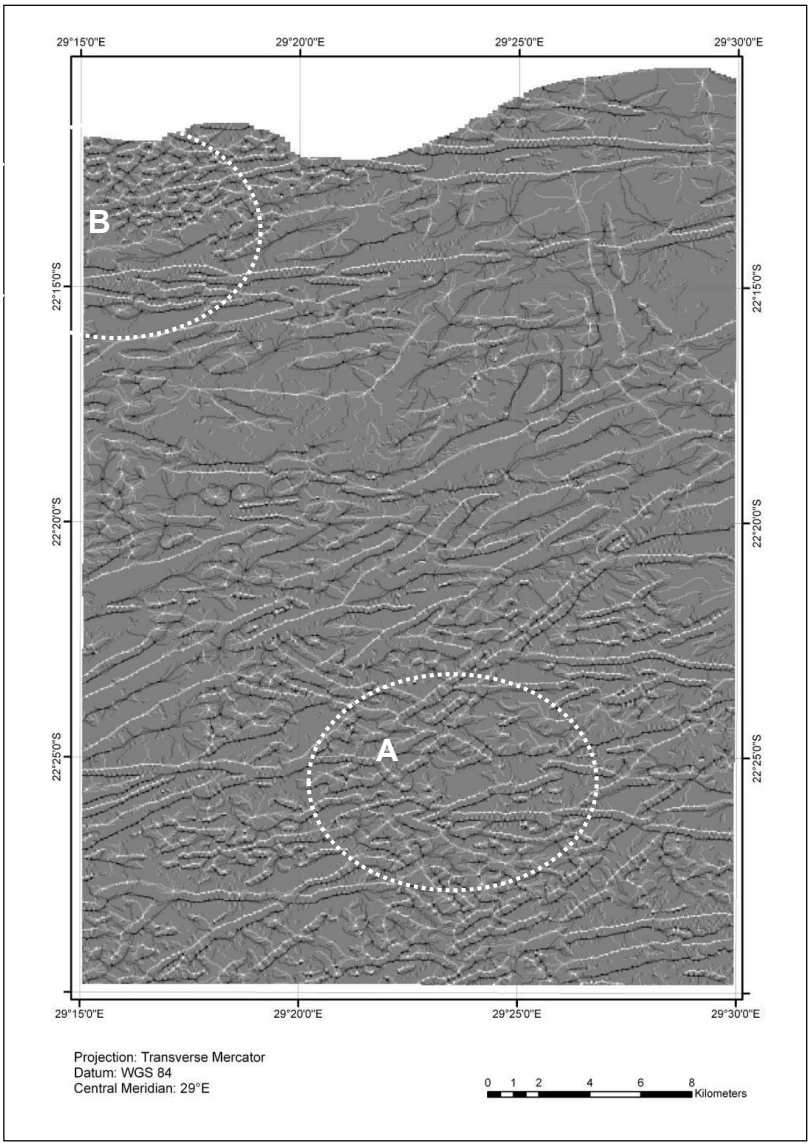


Figure 5.11. Automatic Gain Control filter applied to the magnetic data using a 3x3 window. Features that are not clear on the total magnetic field data, but clear on the AGC map are indicated with (A) and (B).

5.2. Digital Terrain Model Data

The digital terrain model data are shown in Figure 5.12. The DTM has been sun shaded with azimuth 45° and elevation 45° as this enhances relief differences of features not striking 45°, with features striking 135° the most prominent (Cooper, 2003). The reason for this choice of sun shading is that the only features on the relief data are the north-south striking ridge in the middle of the area and the east-southeast striking ridges in the north western part of the area. The digital terrain model data are used with the magnetic data to determine whether certain magnetic anomalies are associated with ridges or hills. It is also very helpful in determining whether radiometric anomalies are related to sedimentation close to rivers and streams, or low lying areas where pollution may accumulate over time.

The southern part of the area is about 250 m higher than the northern part. There is also a broad topographic high between 29° 20'E and 29° 25'E trending roughly north to south through the centre of the area. This feature is not correlated with anything on the magnetic data. The Venetia open cast pit (indicated on Figure 5.12) is a very prominent semi-circular topographic low feature in the southwest, just south of 22° 25'S and west of 29° 20'E. The slimes dam is visible directly west of the pit. The highest part of the study area, topographically, is in the southeast. A couple of ridges in the north appear to be spatially associated with negative magnetic lineaments. The western edge of the topographic high which trends north to south in the middle of the area may be following a fault (Barton, 2011; personal communication).

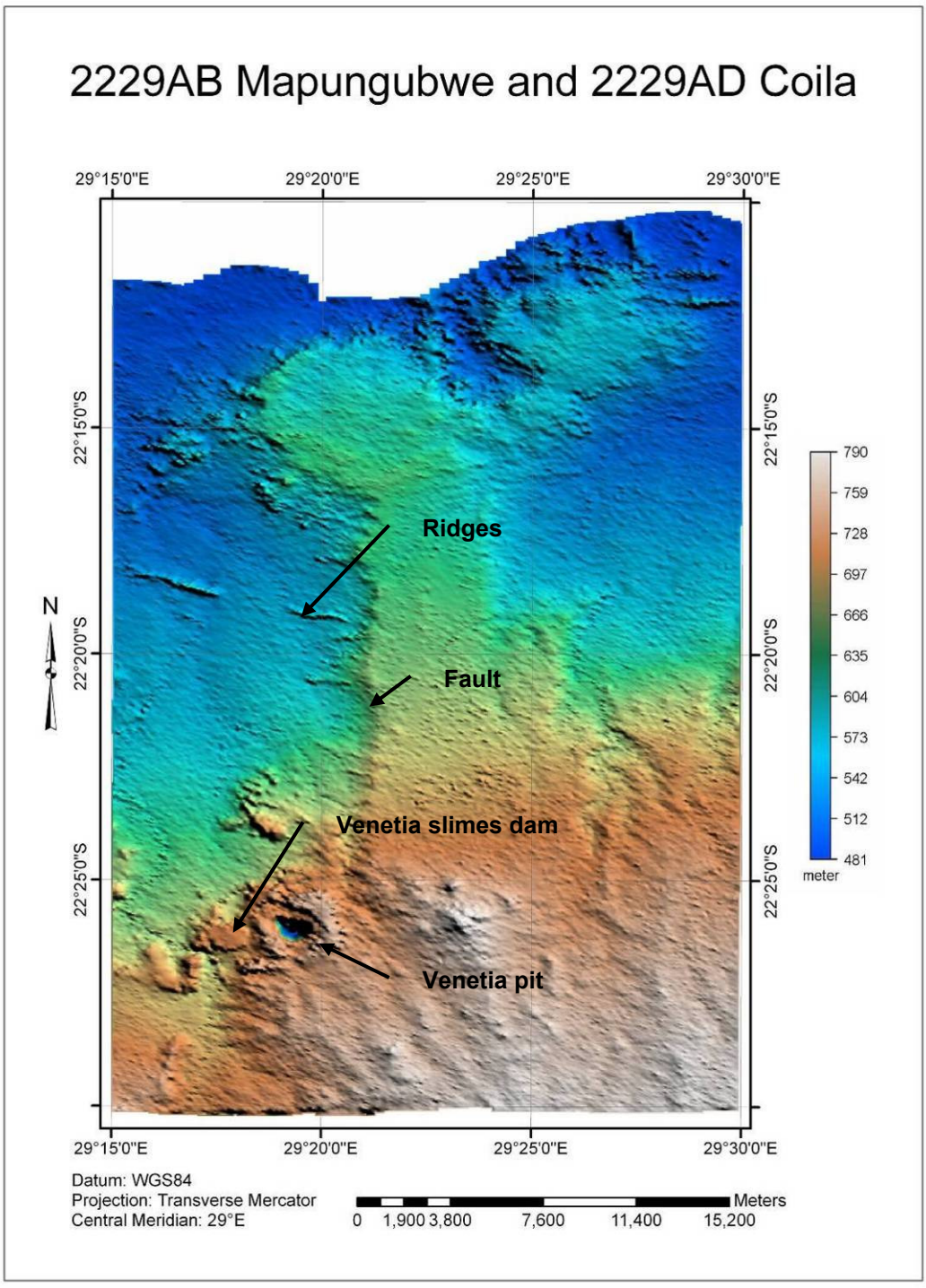


Figure 5.12. Sunshaded digital terrain model data with an azimuth of 45° and sun elevation of 45°.

5.3. Radiometric data

Radiometric data are included in the current study as they are useful for lithological mapping (Gunn et. al., 1997). This method measures the abundance of naturally occurring K, Th and U. The response measured is dominated by radiation from the top 35 cm of earth material (Gunn et. al., 1997); gamma-rays emitted from material deeper than this are absorbed by the earth.

The radiation from lithologies is affected by climate, as weathered material differs in radioelement abundance from fresh, un-weathered rocks. This is because it is the geochemical properties, such as solubility, stability during transportation, etc. of radioactive elements that govern the gamma-ray signatures in different environments (Gunn et al., 1997). Radioactive elements are released from bedrock lithological units during both chemical and physical weathering processes (Gunn et al., 1997). Groundwater characteristics such as acidity and salinity play a big part in the way that radioactive elements are removed and precipitated by chemical weathering (Gunn et al., 1997).

Two types of weathering products can be found; in situ and transported, and they differ from each other. During in situ weathering K is depleted from the host rock but forms part of K-rich clays above the bedrock. U will be soluble and enrich the clay in U. It will also precipitate in iron oxides and carbonates (Gunn et al, 1997). Th is not soluble unless the solution is acidic. Any Th released by weathering will accumulate in clays, or be associated with iron or titanium. During transportation both chemical changes and mechanical sorting will take place. Radioelements can be concentrated or diluted by transportation, depending on the source. The radiometric response will also reflect the sorting (Gunn et al., 1997). Fine grained products will be high in K, Th and U as these would have been leached from the host, and precipitated in clays and silts. Coarser products such as lithic fragments would have a greater concentration of K. Th and U can be concentrated in heavy mineral deposits (zircon and monazite) (Gunn et al., 1997). The digital terrain model data plays a big role in determining whether the anomalies observed

are located along river beds and active depositional basins which could indicate transported material.

Since radiometric data are heavily influenced by topography, water and man-made structures, a topographic map showing the rivers, roads, dams, mine workings and other structures is shown in Figure 5.13 for reference. What should be noted is the network of rivers that could influence the radiometric data by indicating deposition of radiometric material away from the source. Another thing to note is the location of various mine dumps and diggings. These could also explain certain radiometric anomalies that do not correlate with mapped geological outcrops. The radiometric data are presented in four data sets; Total Count, Potassium, Thorium and Uranium channels (Figure 5.14 to Figure 5.17).

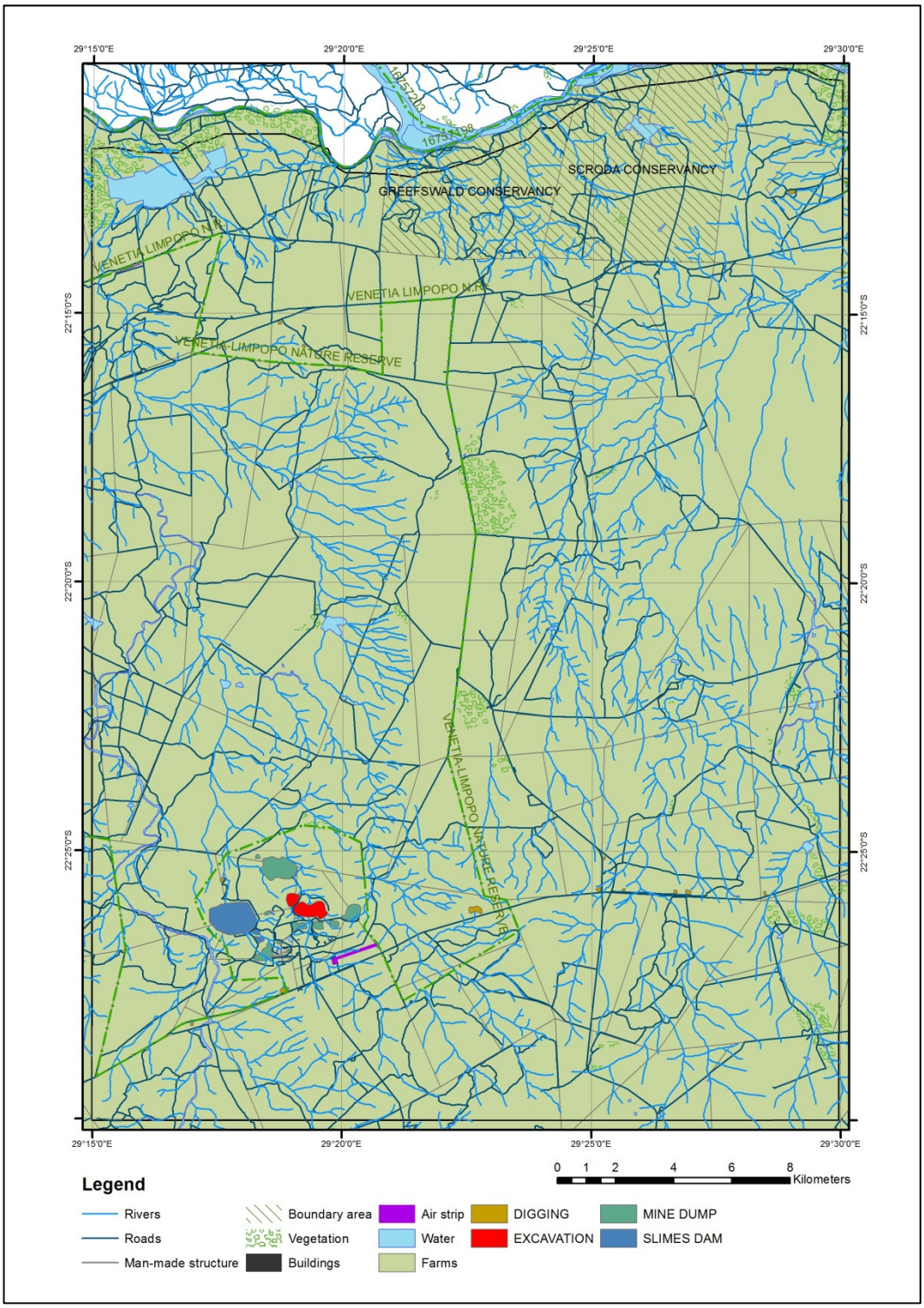


Figure 5.13. Geographic map showing roads, rivers, man-made structures and mine workings.

5.3.1. Total Count

The total count radiometric data for the study area are shown in Figure 5.14. This represents the entire spectrum ranging from 0.0 to 3.0 MeV with 256 channels (0 to 255) that is measured during the airborne survey (Figure 4.3), not only K, Th and U.

In the south, some very high total count values (>1400 counts) can be seen (A on Figure 5.14). Medium values of about 800 to 900 counts occur in two north-south trending areas on either side of the topographic high running through the centre of the area (B on Figure 5.14). This could be due to deposition of weathered basement material from the higher elevations in the south. Very low values (<330 counts) occur over the Venetia slimes dam in the southwest (C on Figure 5.14) and values of 320 counts and less are found in the middle of the southern portion of the map area (D on Figure 5.14). A north trending area on the eastern edge of the map has values of between 500 and 650 counts (E on Figure 5.14). The northern part of the study area has total count values below 500 counts (F on Figure 5.14) that seem to be related to the higher relief area on the digital terrain model. The regional total count data set was used to aid in geological mapping to delineate the contacts between geological units (Barton, personal communication, 2007). The mapping results are shown in Chapter 6.

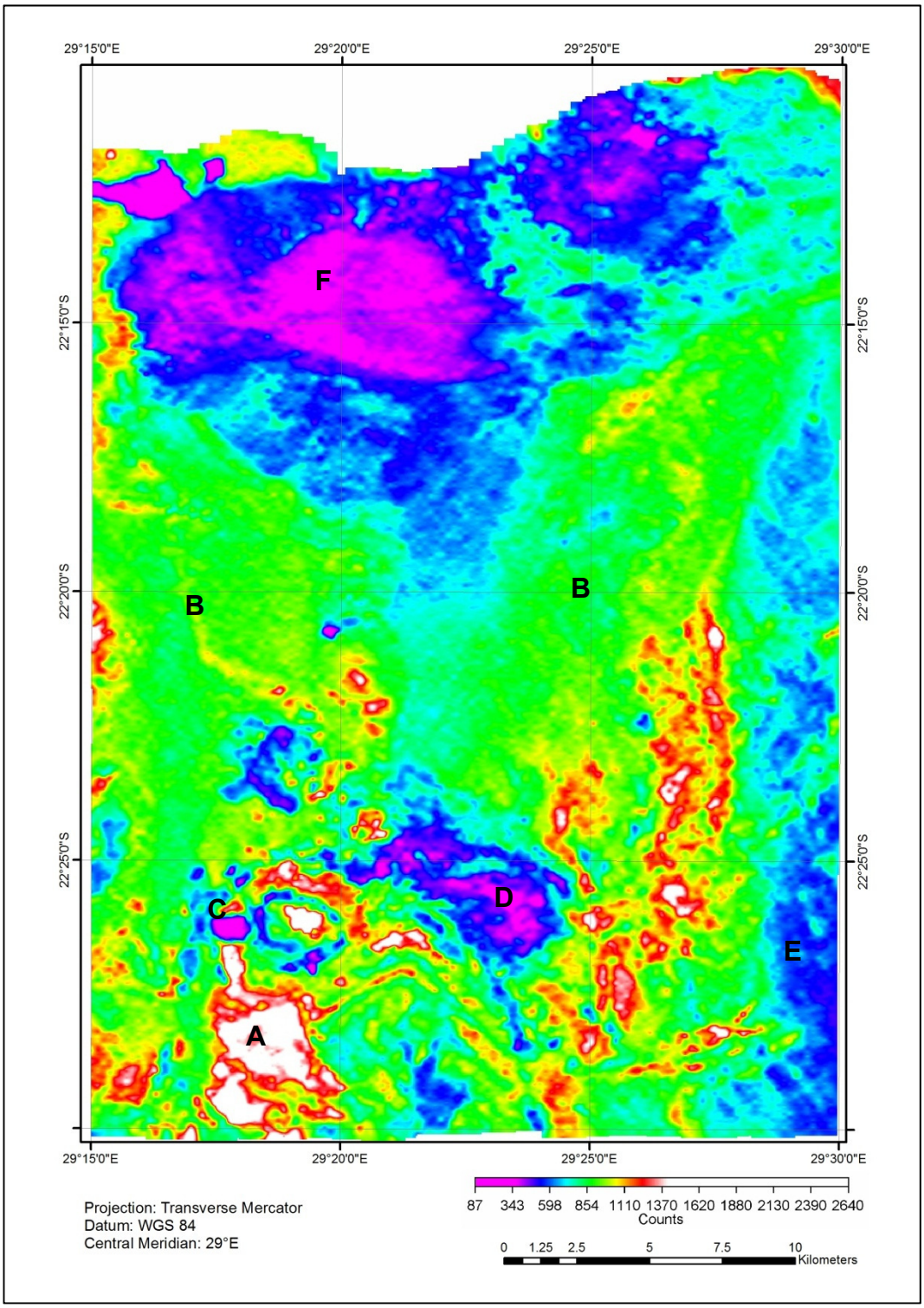


Figure 5.14. Total count radiometric data (50 m grid cell size). (A) - Very high total count values (>1400 counts). (B) - Areas of medium values (~800 to 900 counts). (C) - Venetia slimes dam. (D) - Area with values of 320 counts and less. (E) - North trending area with values between 500 and 650 counts. (F) - Higher relief area with values below 500 counts.

5.3.2. Potassium channel

^{40}K is the radioactive isotope of potassium, and occurs as 0.012 percent of natural potassium. This isotope decays to ^{40}Ar (10.7% of the time) (Emiliani, 1992) with the emission of gamma rays with energy 1.46 MeV or to ^{40}Ca (89.3% of the time) (Emiliani, 1992). Since ^{40}K occurs as a fixed proportion of K in the natural environment, these gamma rays can be used to estimate the total amount of K present (IAEA, 2003). The potassium window monitors 1.46 MeV gamma-rays emitted by ^{40}K (Gunn et. al., 1997).

Potassium is quite common in granites and shales (e.g. van Schmus, 1995). Since potassium is a common element comprising about 2% of the earth's crust (van Schmus, 1995; Gunn et al., 1997; IAEA, 2003), it is to be expected that the K channel data should be very similar to the total count data, as most of the counts come from K. This is true for most of the data collected over this study area. Marked differences are two areas right on the western boundary of the map just south of 22°20' S, showing very low K values and very high Total Count values (A on Figure 5.15). A north to south trending K high on 25°25' is more prominent and extends further north on the K data than on the total count data (B on Figure 5.15). The K values do not show the high at about 22°20' S, 29°20' E that is visible on the total count data (C on Figure 5.15).

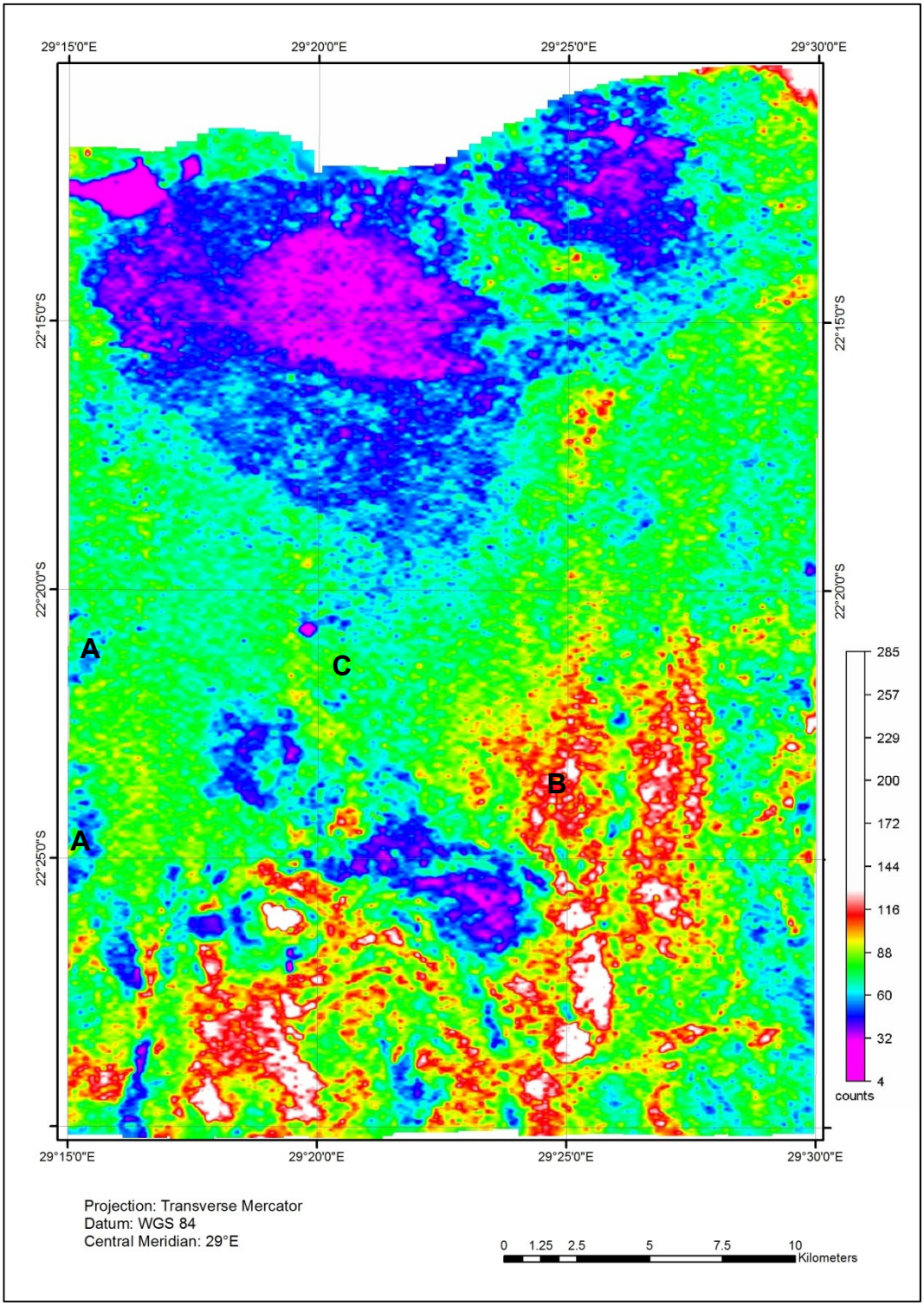


Figure 5.15. Potassium Channel Radiometric data, 50 m grid cell size. Marked differences between Total count data and K are: (A) - Low K values versus high total count, (B) - high values are more prominent on K than total count and (C) - high total count values not reflected in K.

5.3.3. Thorium channel

Thorium occurs naturally as the radio isotope ^{232}Th which decays to the stable isotope ^{208}Pb through the following series (Minty, 1997):

^{232}Th – ^{228}Ra – ^{228}Ac – ^{228}Th – ^{224}Ra – ^{220}Rn – ^{216}Po – ^{212}Pb – ^{212}Bi – (^{212}Po and ^{208}Tl) – ^{208}Pb (Minty, 1997)

Thorium does not emit gamma-rays. Instead the emissions from its daughter element, ^{208}Tl are used to establish concentration estimates (Gunn et al., 1997). Since the estimates are based on the assumption of equilibrium conditions in the source, they are usually reported as 'equivalent Th' (Gunn et al., 1997). Secular equilibrium is met when all the daughter isotopes in a decay series decay at the same rate as what they are being formed at due to the fact that the daughters' half lives are shorter than that of the parent (Minty, 1997). The Th series is usually in equilibrium (Minty, 1997).

Since Th has a lower overall abundance (along with U) than that of K (van Schmus, 1995), the data are not as smooth as the K channel, and appears 'spotty/speckled' (Figure 5.16). Minerals such as allanite, monzanite, xenotime and zircon that contain Th (or U) as essential constituents are found only as trace minerals in common rocks or as minerals in primary or secondary mineral deposits (van Schmus, 1995).

The large ion lithophile (LIL) character of Th (and U) is very similar to that of K, and as such these three elements tend to follow each other on average when bulk components of the earth are considered (van Schmus, 1995). This explains why the three datasets on average are very similar.

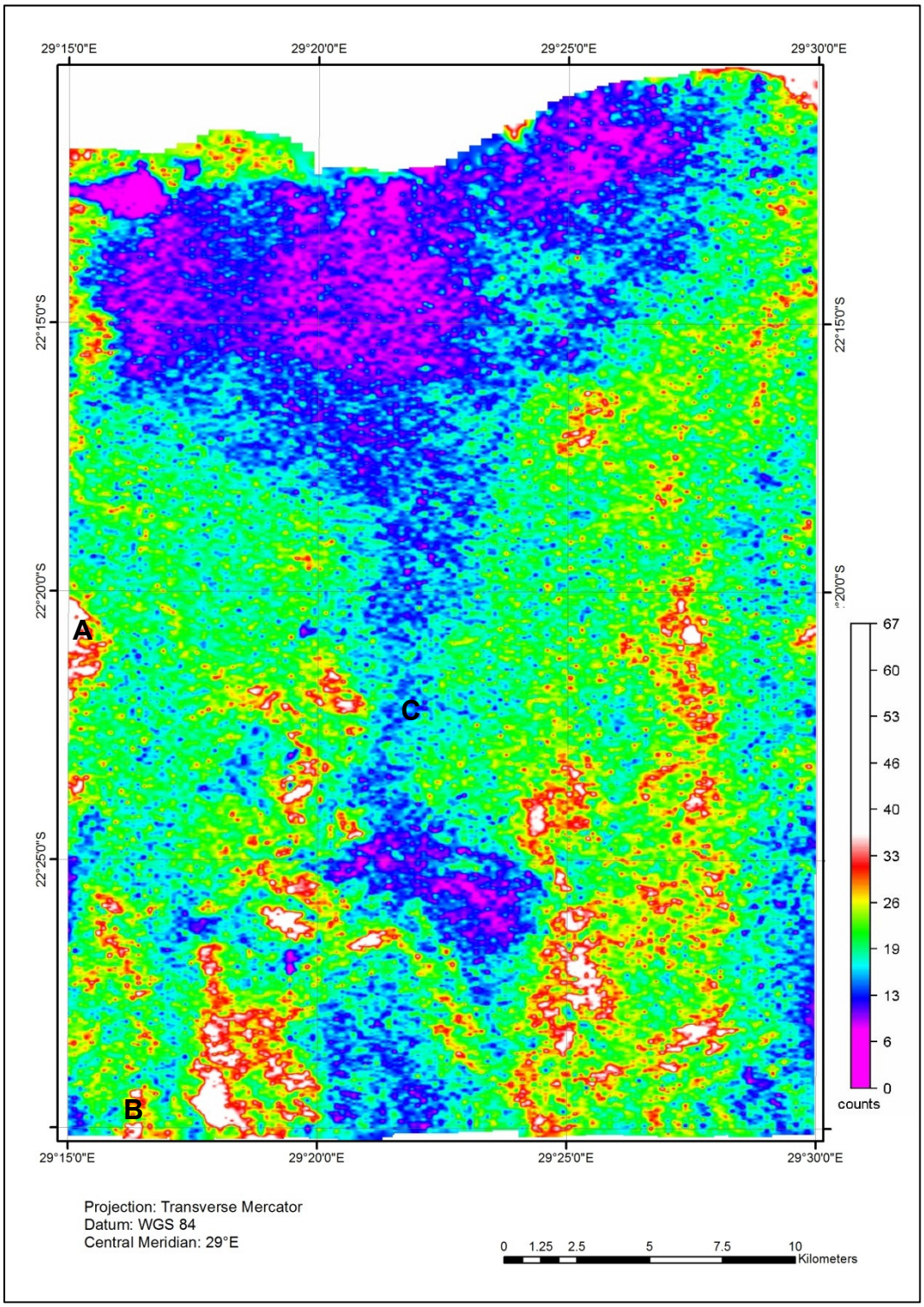


Figure 5.16. Thorium Channel Radiometric data (50 m grid cell size). Main differences between Th data and the other radiometric data are: (A) - a positive Th anomaly that is negative in both K and total count data, (B) – high Th concentration versus low K concentration and (C) – a north to south trending Th low that connects the lows in the north and south.

The high Th anomaly on the western edge of the data (A on
Figure 5.16) is one of the main differences between the Th data and both the total count (Figure 5.14) and K data (Figure 5.15). Otherwise the same areas tend to have low and high values as in the previous two data sets. The areas with high Th seem to be a bit more restricted than those in the K data, especially in the southeast. In the southwestern most corner of the data, a Th high exists where the K data shows a low concentration (B on
Figure 5.16). Another big difference is the north to south trending Th low that connects the low in the south and the low in the north in the centre of the data (C on
Figure 5.16). These two lows are not connected on the total count or K data.

5.3.4. Uranium channel

Uranium occurs as radio isotopes ^{238}U and ^{235}U which give rise to the radioactive decay series of U where ^{238}U decays to the stable isotope ^{206}Pb and ^{235}U decays to stable ^{207}Pb isotope (Gunn et. al., 1997).

The ^{238}U decay series is as follows:

^{238}U – ^{234}Th – ^{234}Pa – ^{234}U – ^{230}Th – ^{226}Ra – ^{222}Rn – ^{218}Po – (^{214}Pb and/or ^{218}At) – ^{214}Bi – (^{214}Po and/or ^{210}Tl) – ^{210}Pb – ^{210}Bi – (^{210}Po and/or ^{206}Tl) – ^{206}Pb (Minty, 1997)

The ^{235}U decay series is given as:

^{235}U – ^{231}Th – ^{231}Pa – ^{227}Ac – (^{227}Th and ^{223}Fr) – ^{223}Ra – ^{219}Rn – ^{215}Po – ^{211}Pb – ^{211}Bi – (^{211}Po and ^{207}Tl) – ^{207}Pb (Minty, 1997)

Because U doesn't emit gamma-rays, it is the emissions of its daughter product ^{214}Bi, that is used to establish concentrations (Gunn et. al., 1997). Just as with Th, the U concentration is given as 'equivalent U'; since it is based upon the assumption that the U decay series is in equilibrium (Gunn et. al., 1997). However, unlike the Th decay series which is almost always in equilibrium (Minty, 1997), the U decay series is very often not in equilibrium. Causes of disequilibrium in U are numerous; for example it can result in at least five positions in the decay series according to Minty (1997); ^{234}U can be selectively leached relative to ^{238}U in a clay matrix, or ^{238}U can be selectively leached relative to ^{234}U, ^{230}Th can be selectively leached relative to other isotopes in the chain, ^{226}Ra fractionation can occur or ^{222}Rn, a gas, which is very mobile, can escape from soil and rock fissures into the atmosphere.

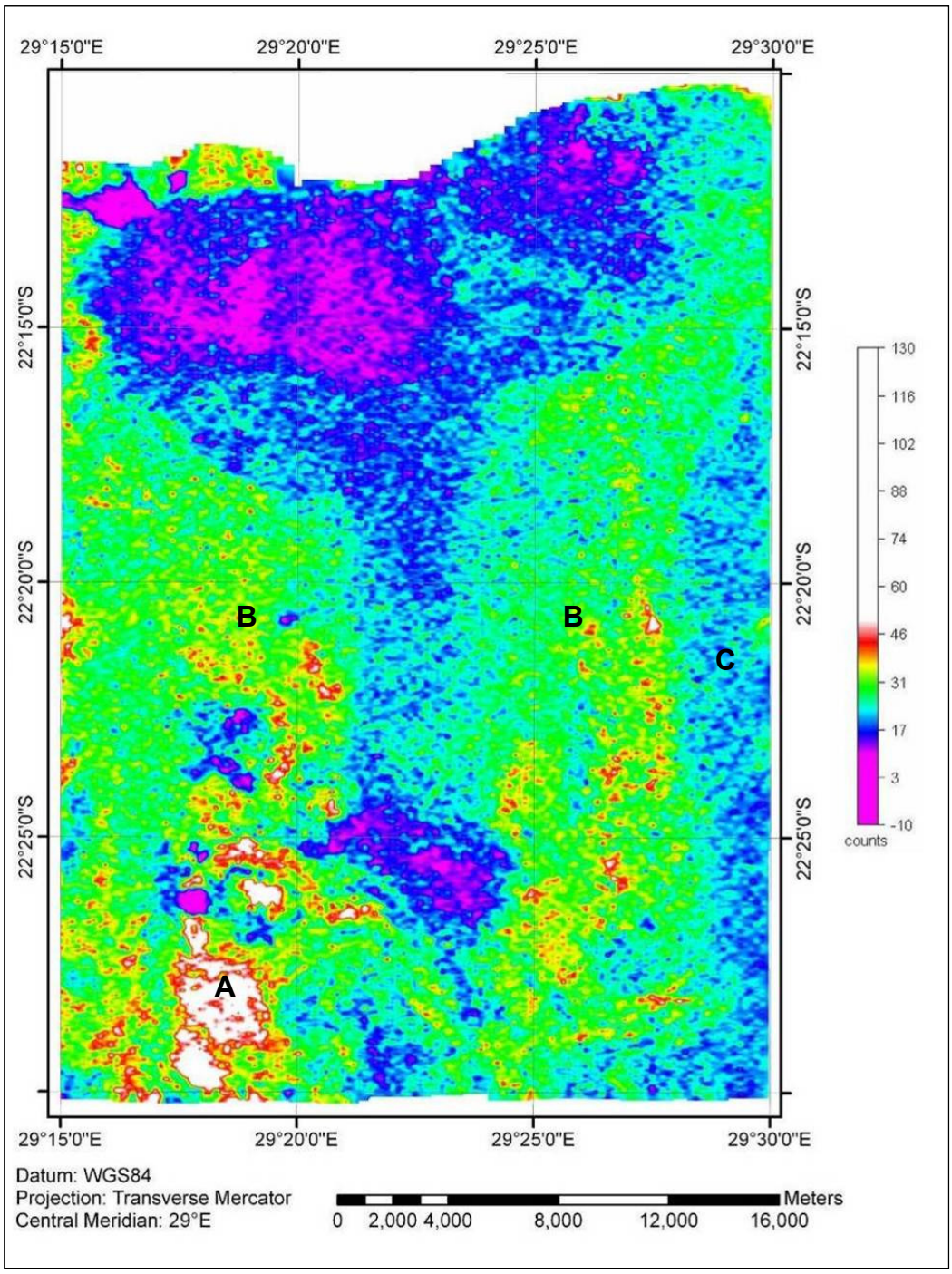


Figure 5.17. Uranium Channel Radiometric data (50 m grid cell size). The data shows an area with high U concentration (A), areas with slightly elevated values (B) adjacent to topographic ridge and a north-south tending area with low U values (C).

In the Venetia area, it was found that the concentration of U in the basement rocks are high (Barton, 2007, personal communication). The uranium data (Figure 5.17) for the study area shows a very high concentration in the southwest (A on Figure 5.17), south of

Venetia. It shows slightly elevated values to the east and west of the topographic ridge that runs from south to north through the centre of the area (B on Figure 5.17), much like the total count, K and Th data. A north to south trending area with low U values exist on the eastern edge of the map (C on Figure 5.17). This differs from the K data, but correlates with the total count data.

5.4. Summary of datasets

Some features on the available high resolution data sets for the study area seem to correlate well with some of the mapped geological features, known infrastructure and topographic features. Other features on the magnetic data do not correlate at first glance to any mapped geological lithologies.

CHAPTER 6. Qualitative Interpretation

6.1. Radiometric data

The total count, K, U and Th radiometric data are displayed in Figure 5.14 through Figure 5.17. The geology in the Venetia area was mapped (Barton et al., 2003) at high resolution and much of the mapping was done with the aid of regional total count radiometric data (discussed in 3.1). They found that the regional total count data correlated extremely well with the geology in the Venetia area. The aim of this radiometric interpretation is to determine how well the complete set of high resolution radiometric data reflects the geology in this area. The geological map generated from the mapping exercise by Barton et al. (2003) is shown in Figure 6.1.

In the interpretations that will follow, the rough outline of the geological units mapped by Barton et al. (2003) is overlain in black on the data and the interpretations, purely to aid author in pointing to areas of discussion. A final interpretation of the radiometric data and interpreted locations of these geological units will follow at the end of the chapter.

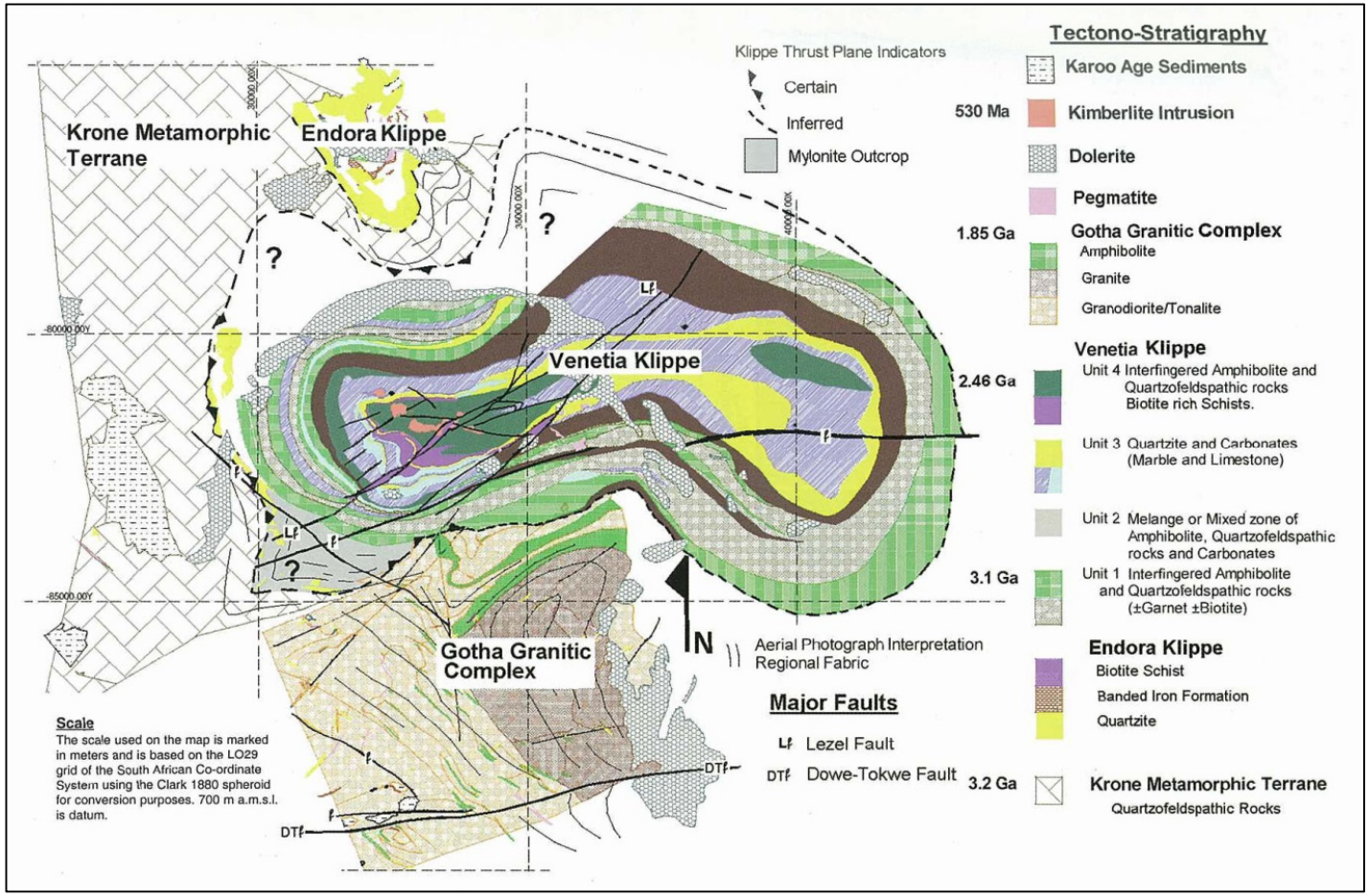


Figure 6.1. Geological map of the area around the Venetia kimberlite pipes. (Barton et al., 2003). Note that the present study area extends beyond limits of this map.

6.1.1. Interpretation of the ternary image of the radiometric data

A ternary Image or ternary ratio image provides the relative proportion of potassium, thorium and uranium response by assigning each channel to a given colour (potassium = red, thorium = green and uranium = blue). The relative proportion is useful for mapping the variations in the mineralogy of the surface materials and tends to show a strong correlation to geology and soils. Where the ternary image is very dark, there are low values in each of the channels, and in areas where the image is white, high values for all three channels exist. Bright colours indicate high concentrations of one or two of the elements.

The ternary image was compared to mapped geology (Figure 2.2 and Figure 6.1) and the various proportions displayed as different colours and brightness were interpreted accordingly. The very high concentrations of all three channels (white area in southwestern portion of Figure 6.2) were interpreted to be associated with the Gotha granodiorite. Directly east of this white area, the area with high K concentration (red) is interpreted to be caused by the Gotha granite. Areas with high U and Th concentrations (turquoise) in the south west seem to correlate with Karoo aged sediment deposits. Very low concentrations in all three channels in the south are contributed to dolerite intrusions or marble of the Venetia klippe. High concentrations of all three channels are seen in the south east of Figure 6.2, but it seems the concentration of K is slightly lower than that of K and Th, thus the slight yellow tinge to the colour. This is interpreted to be due to outcrops of the Malala Drift gneisses of the Beit Bridge Complex.

Very low concentrations of all three channels can be seen in the north of Figure 6.2 and this is attributed to the Tshipise and Red Rocks sediments of the Karoo.

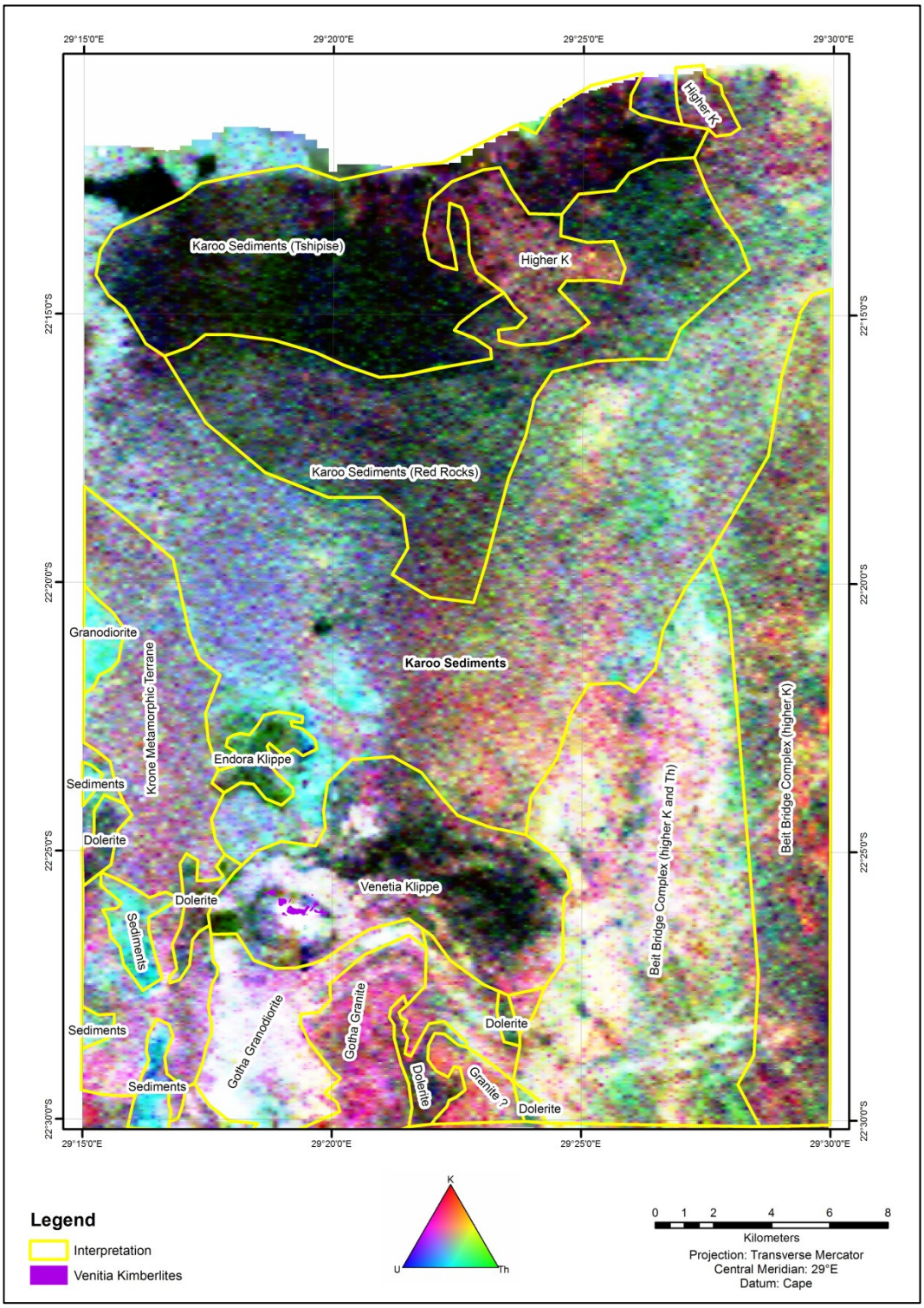


Figure 6.2. The interpretation of the ternary image. The interpreted geology is outlined in yellow. The Venetia kimberlites are shown as purple blobs in the western part of the area inferred to be the Venetia klippe.

6.1.2. Interpretation of the potassium channel radiometric data

The northern part of the study area is covered by Karoo sediments and the K values are low in this area (generally less than 88 counts) (Figure 6.3).The Karoo outcrops are mainly located on a topographic high area. In the southern part of the study area the K channel data is more complex than in the north (Figure 6.3) and this is due to the outcropping basement rocks. The area mapped as the Endora Klippe geological unit (A on Figure 6.3) has low (35 to 60 counts) potassium values. It is mostly comprised of quartzite. The area mapped as Venetia Klippe (B on Figure 6.3) is comprised of various geological lithologies and these seem to have differing K channel signatures. An area in the west of the klippe exhibits values of about 50 to 60 counts and correlates with mapped marble (C on Figure 6.3). A similar low area in the klippe (4 to 60 counts) is located to the south east of this anomaly (D on Figure 6.3) and correlates with an area covered in layers of marble, metaquartzite and dolerite. The Venetia pit (E on Figure 6.3) has very high K values (>120 counts). An area with high K values (±100 counts) curving around the north and east of the pit (F on Figure 6.3) is interpreted to be due to mine dumps in that area (see Figure 5.13).

The western part of the geological unit mapped as the Gotha Granitic Complex (G on Figure 6.3) in the southwest has K values of 88 counts and higher. These values are interpreted to be due to the K content of granodiorite. The area east of the granodiorite (H on Figure 6.3) has slightly lower values (88 to 120 counts) that is attributed to granite and a low in the between these two areas attributed to dolerite outcrops that correlate with it. Further east north-south striking areas (I on Figure 6.3) with values above 100 counts are interpreted to be due to the Messina suite granites and gneisses.

The areas east and west of the north-south striking topographic high (seeFigure 5.12) that divides the area in two have medium values between 70 and 90 counts. These are interpreted to be due to transportation of material from the topographic high areas both north (low K) and south (high K) via rivers (indicated on Figure 6.3).

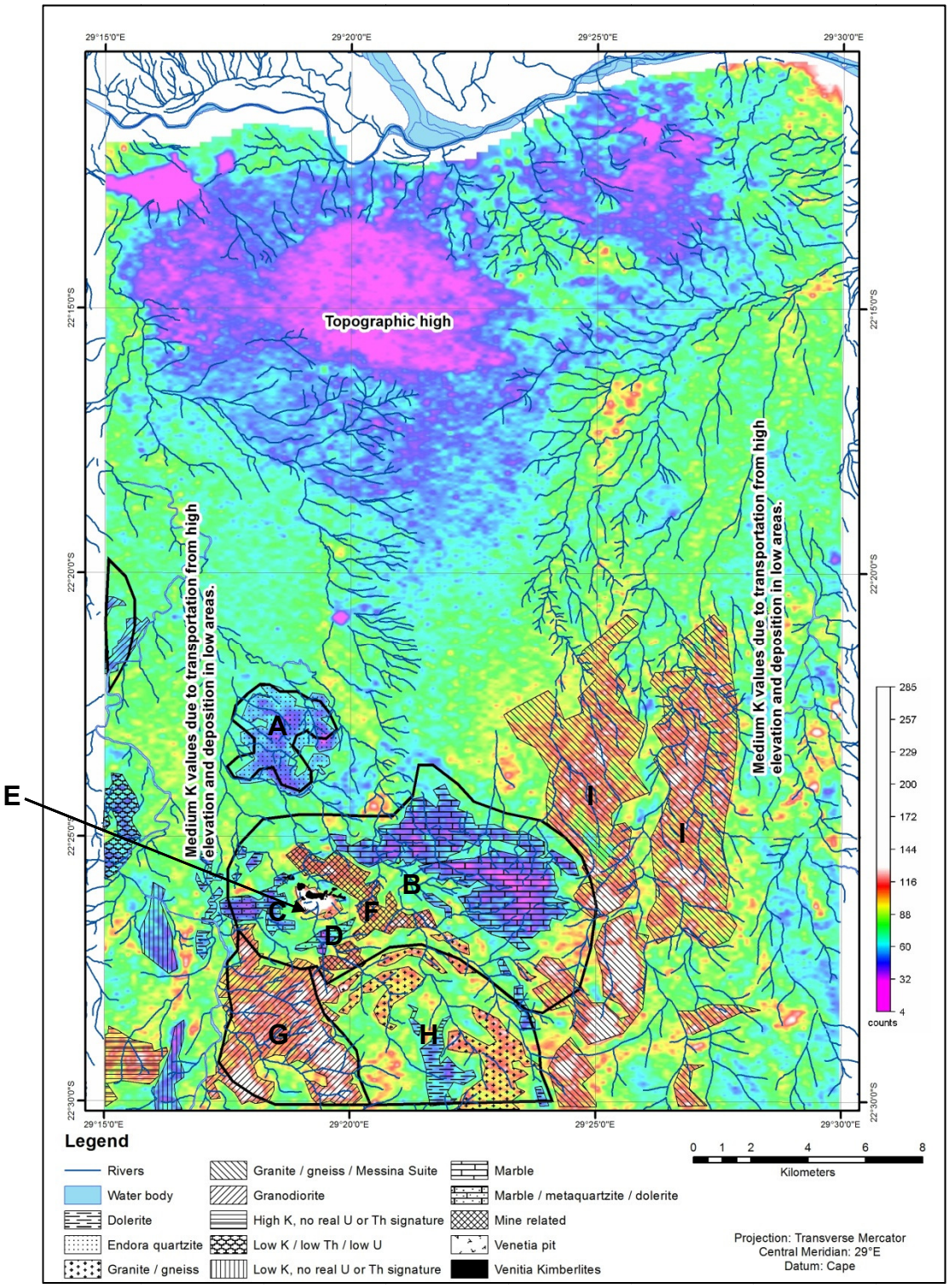


Figure 6.3. Interpretation of K channel radiometric data with the mapped geological units as thick black outlines. The rivers are indicated as navy blue lines and the interpreted geology as hatched areas.

6.1.3. Interpretation of the uranium channel data

The U channel data overlain with the mapped geological units is shown in Figure 6.4. The area is roughly divided into four north-south trending domains. The central zone with low values (17 to 30 counts) is located on the topographic high that runs through the area. To the east and west of this U low the medium values of 17 to 40 counts are attributed to the transportation of material from higher topographic areas to the valleys via rivers (indicated on the map). The very low values (< 17 counts) in the north are attributed to Karoo rocks and are located on a topographic high.

In the south the U values are more complex where the basement rocks outcrop. The very high values (>45 counts) in the southwest corresponds with the granodiorite of the mapped Gotha Granitic Complex. Directly east of the granodiorite the lower values between 20 counts and 40 counts are attributed to granite outcrops. North of the mapped Gotha granite the very low values (below 17 counts) are located on a topographic high. The Venetia pit corresponds with high U values (> 50 counts) in the west of the mapped Venetia Klippe unit. North and southeast of the pit similar high values are attributed to mine dumps and mine workings in the area (see Figure 5.13).

North of the Venetia Klippe low values below 20 counts are attributed to the quartzite of the mapped Endora Klippe. To the Far East the fourth north-south striking zone with values between 17 and 25 counts corresponds with scattered outcrops of aplite.

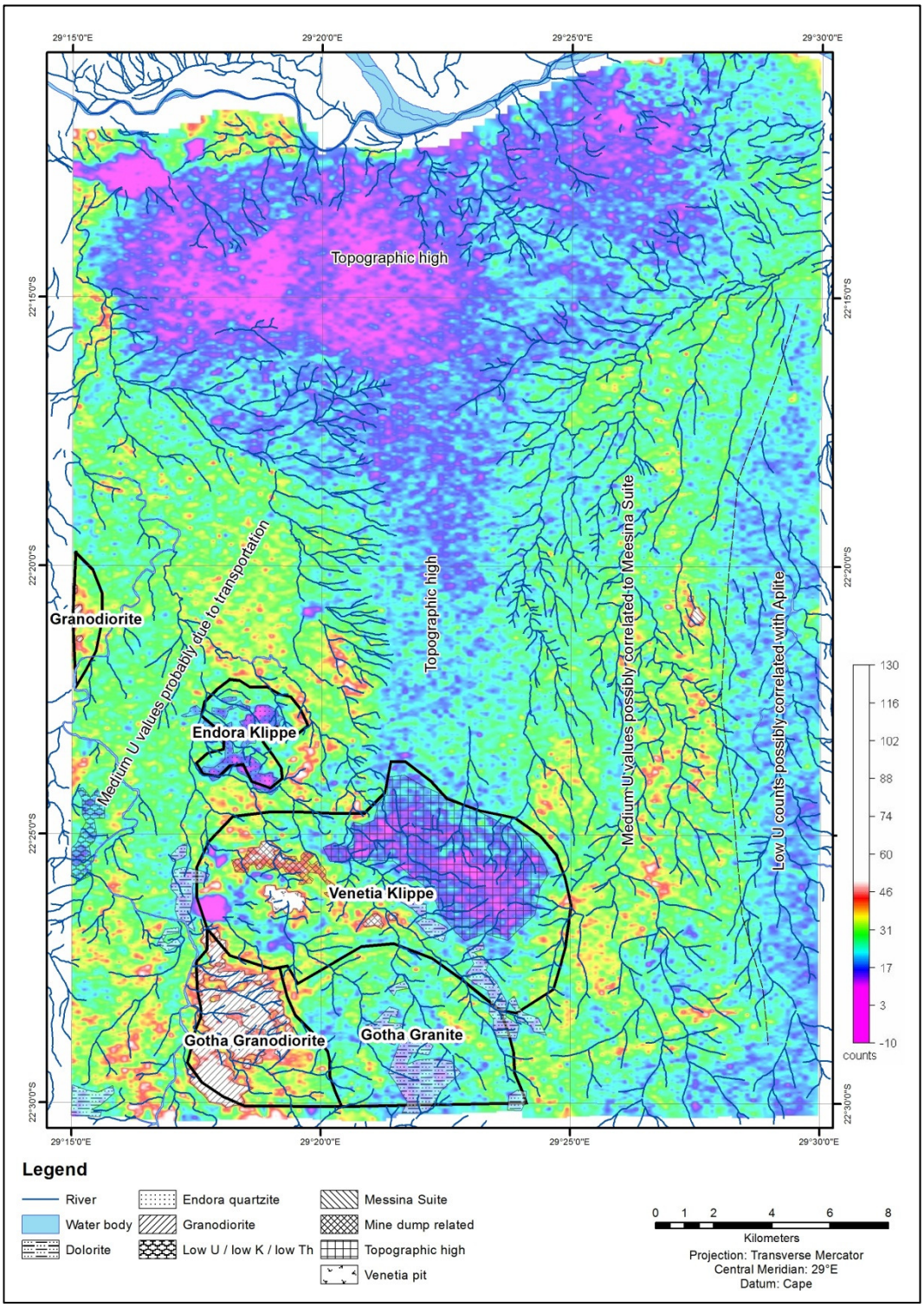


Figure 6.4. Interpretation of the U channel radiometric data. Some of the anomalies in the south correlate with known geology outcrops. Low values correlate to topographic highs and medium values could be caused by deposition in the valleys. Mapped geological units are shown in thick black outline.

6.1.4. Interpretation of the thorium channel radiometric data

The interpretation of the thorium channel data is very similar to the uranium channel data (Figure 6.5). Similar four north-south trending zones are identified. The central zone has values below 19 counts. It is located on a north-south trending topographic high. East and west of this ridge the Th values are between 15 and 28 counts and are attributed to transported material from topographically higher areas in the south and north. Values in the north of the area (covered by Karoo sediments) are low (below 15 counts),

In the south the basement lithologies have varied radiometric signatures. An area with elevated Th values (>30 counts) in the south west correlates with outcrops of granodiorite belonging to the mapped Gotha granitic complex. East of the granodiorite low values below 15 counts are attributed to outcropping granite and gneiss. There are also dolerite outcrops in this area, but they cannot be distinguished from the granite since both seem to have low Th values.

The mapped Venetia Klippe has low values in the west (10 to 13 counts) and east (< 13 counts) that are interpreted to be due to marble, metaquartzite and dolerite outcrops in the area. Medium to low values (13 to 19 counts) correlate with the mapped quartzite of the Endora Klippe.

Two narrow zones in the east strike north-south and have values above 30 counts. They correlate with outcrops of the Messina Suite of granites and gneisses. To the north higher values are attributed to transported Messina Suite material, moved there by the rivers indicated on the map (Figure 6.5).

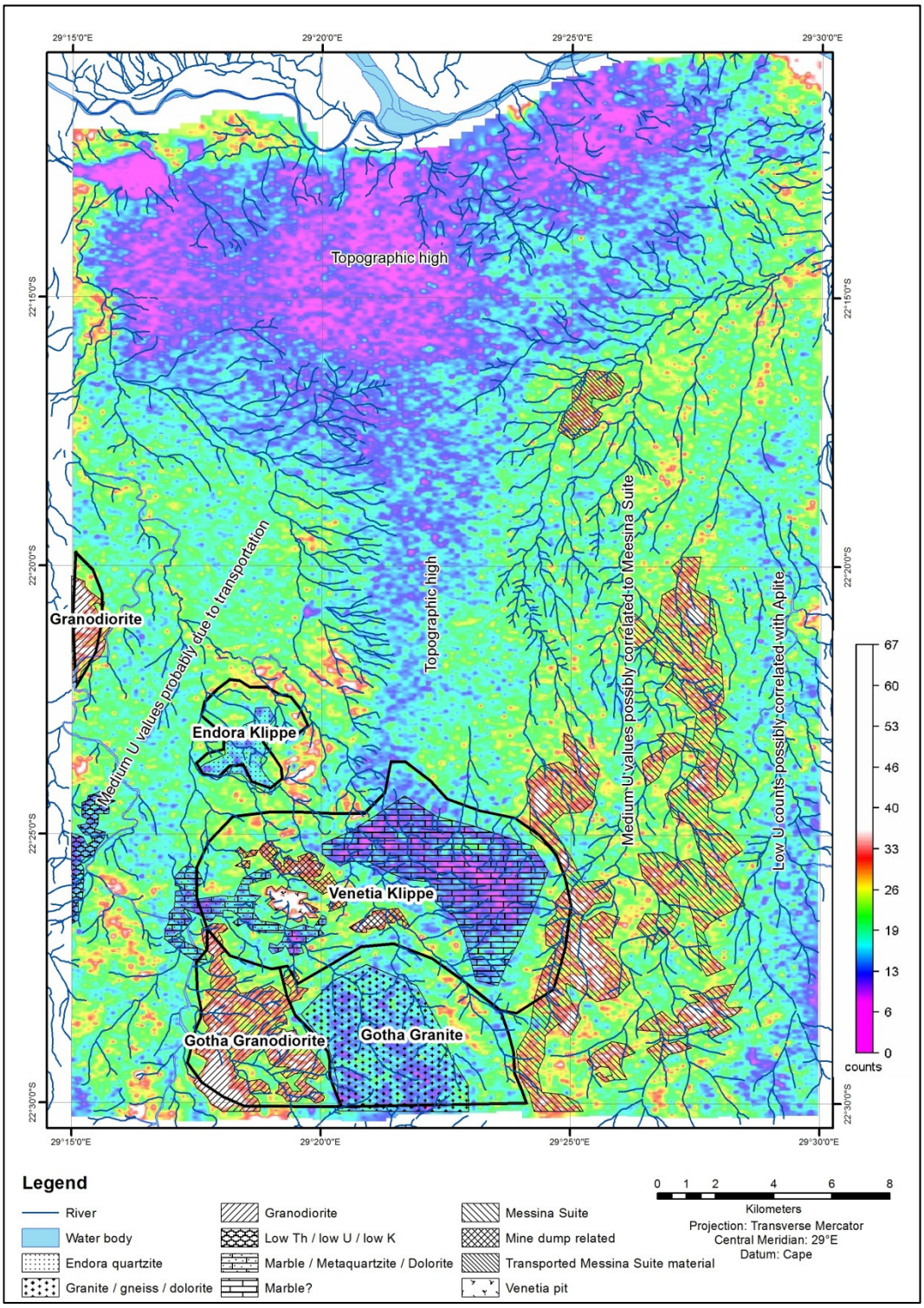


Figure 6.5. Interpretation of the Th channel radiometric data. Some of the anomalies in the south correlate with known geology outcrops. Low values correlate to topographic highs and medium to high values could be caused by transportation and deposition in the valleys. The mapped geological units are shown as thick black outline.

6.1.5. Interpretation of the total count radiometric data.

The interpretation of the total count data is shown in Figure 6.6. The northern part of the area is covered by Karoo sediments and is interpreted to consist of the Tshipise Member and Karoo sediments. These sediments are situated on a topographic high. On the western edge of the study area high TC values are attributed to granodiorite outcrops verified by J. M. Barton (personal communication, 2012).

In the south the low values in the centre is attributed to marble, metaquartzite and dolerite outcrops. The Venetia pit has high values. In the south west high values are attributed to granodiorite of the Gotha geological unit. Lower values east of the granodiorite are attributed to dolerite outcrops. The granites and gneisses of the Messina Suite are located in two north-south trending zones east of the Venetia Klippe. North of these outcrops a couple of areas with high values just south of the Karoo sediments are interpreted to be deposited there by the rivers indicated on the map.

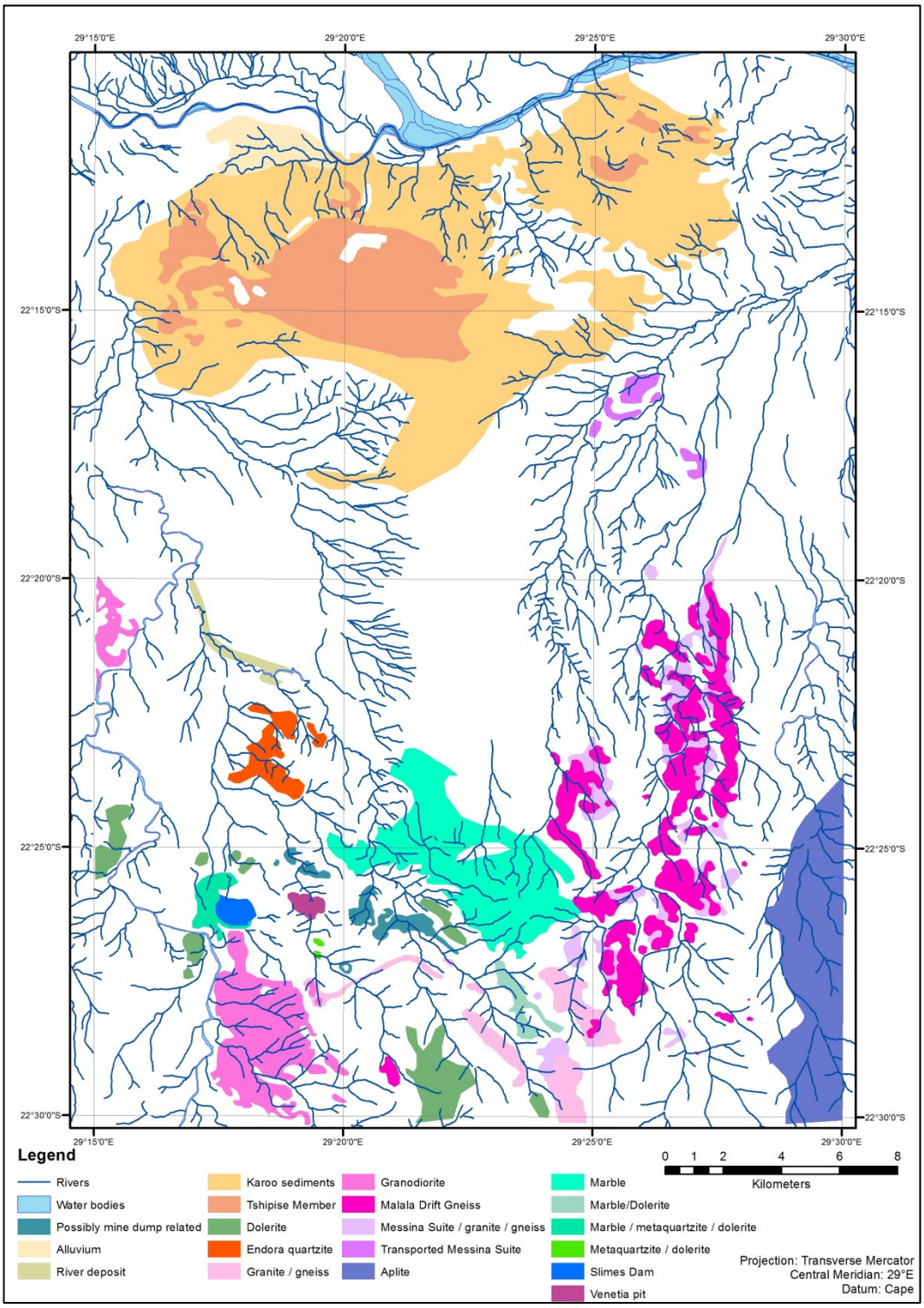


Figure 6.6. Interpretation of the total count radiometric data with the mapped geological units outlined in solid black.

6.1.6. Combining the radiometric interpretations

The geological and tectonic units defined and mapped by Barton et al. (2003) (Figure 6.1) around the Venetia kimberlite pipes are fairly closely mirrored using all three channels and the total count of the radiometric data (Figure 5.14 to Figure 5.17). The ~2.6 Ga granodioritic components have very high radiometric values while the ~3.2 Ga tonalitic to trondhjemitic components and ~2.6 Ga Gotha granite have low values (Figure 6.2 and Figure 6.3 to Figure 6.5). The rocks of Karoo Supergroup displays mostly low to very low radiometric values in all three channels (Th < 15 counts, U < 20 counts and K < 60 counts). Those of the Krone metamorphic terrane have elevated potassium and uranium values (Figure 6.3 and Figure 6.4) while the metasedimentary rocks of the Mount Dowe Group show more thorium and very little potassium (Figure 6.5 and Figure 6.3). The Venetia kimberlites also have elevated values in all three channels (Figure 6.3 to Figure 6.5). In the Venetia klippe, it is possible to distinguish individual lithologies from the total count radiometric data (Figure 6.6). Marble, limestone and quartzite of the Venetia klippe have low radiometric values (the central portion of the eastern lobe of the klippe). The Gotha Granitic Complex (Barnettt, 2005) consists of two separate intrusions, one granodioritic and one granitic in composition, that are clearly distinguished (Figure 6.3 to Figure 6.6). The Gotha granodiorite has elevated values in all three radiometric channels. Xenoliothic bands of amphibolite occur within the granodioritic intrusion. The Endora klippe, consisting of quartzite, banded iron formation and schist, has very low radiometric values (Figure 6.3 to Figure 6.6).

Very bright colours on the ternary image of the radiometric data (Figure 6.2), indicate high concentrations of the minerals. On the western side of the high elevation that runs north-south through the study area (see Figure 5.12) the rocks/soil seem to be enriched in uranium and thorium, displaying the aqua colour over the granodiorite, the Krone metamorphic terrane and east and northeast of the Endora klippe. The Gotha granodiorite and western part of the Venetia klippe is bright white, indicating high concentrations of all 3 radiometric minerals. The Gotha granite is enriched in potassium. The valley to the east of the topographic high is bright light yellow, indicating high concentrations of potassium and thorium. This spatial division is quite probably due to the

topography of the area caused by weathering and drainage. The highest elevation in the area is in the south, the Gotha granite with its high potassium concentration. The rivers leading down from the granite tend run to the east, into the valley enriched in potassium and thorium, more than uranium. The uranium and thorium enriched western valley gets sedimentation from rivers originating and running through the Gotha granodiorite and Venetia klippe, both enriched in those two elements. Figure 6.7 shows the final radiometric data interpretational map. New positions for the geological units are shown in black outline.

To conclude, the interpretation geological units ware overlain on the mapped geology in Figure 6.8 and are shown as red outlines over the image. In the Venetia klippe the radiometric data seem to follow the geology quite closely. It would seem that the radiometric signature of the area is controlled by the very radiometric Venetia klippe, Gotha granodiorite and Gotha granite outcrops. These rocks are weathered and deposited in the valleys east and west of the north-south trending topographic high and cause the concentrations we see there.

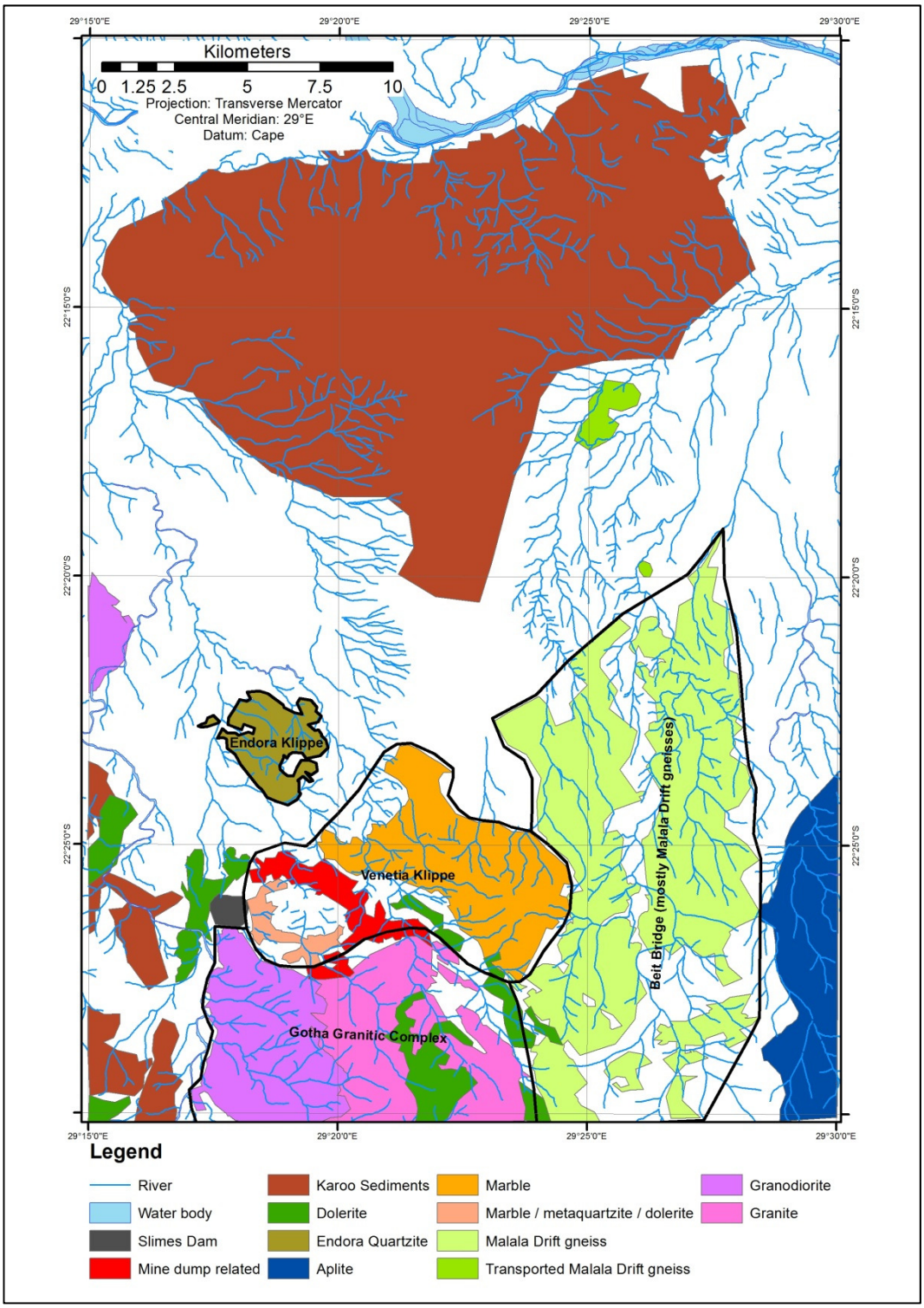


Figure 6.7. Final radiometric interpretational map. Interpreted boundaries for the geological units are shown in black outline.

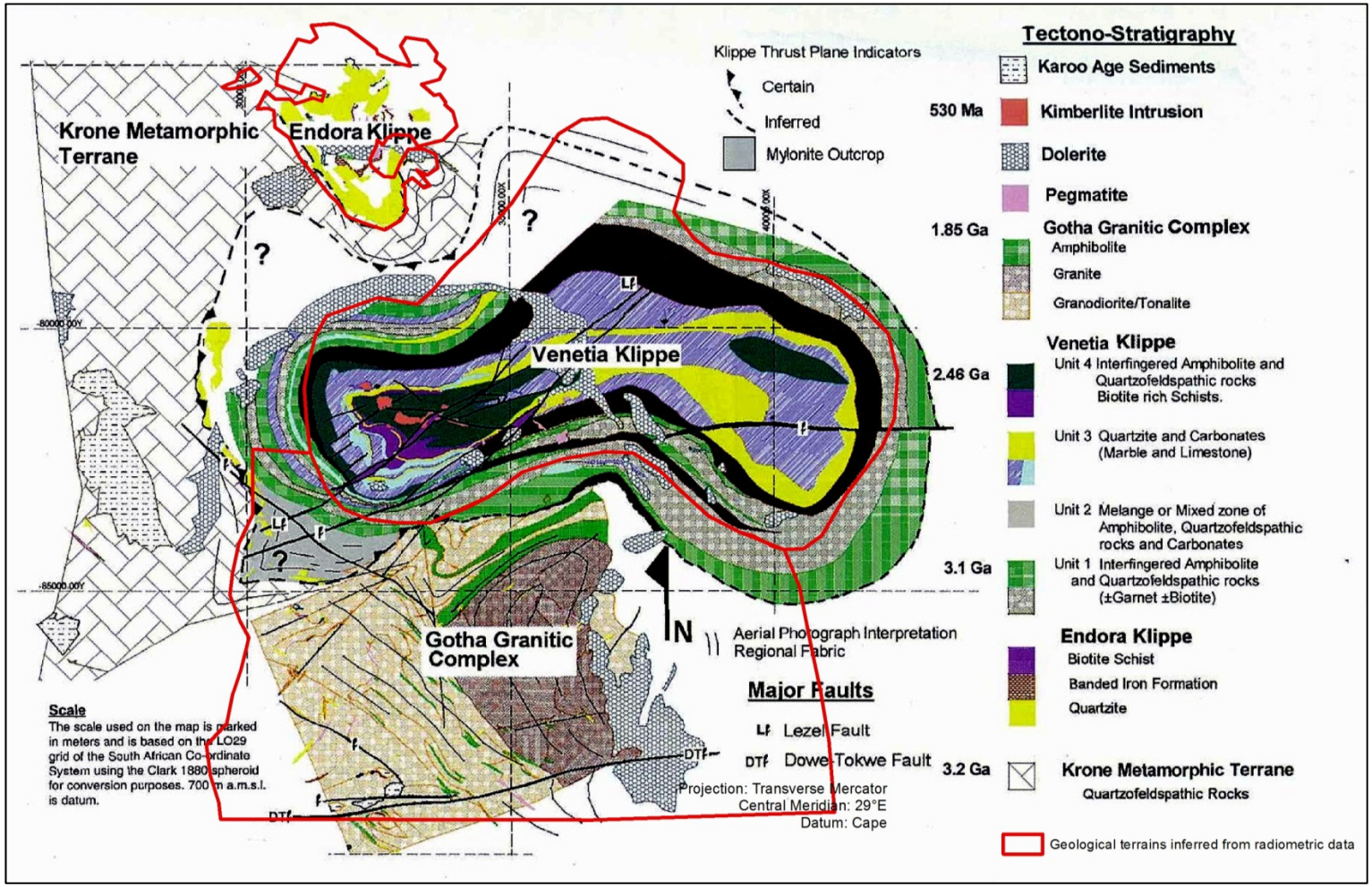


Figure 6.8. The geological units derived from radiometric data overlain in red on the high resolution mapped geology.

6.2. Magnetic data

This dissertation, being aimed at investigating the structures in the study area, focuses mainly on the lineaments, but some attention is paid to other magnetic anomalies.

6.2.1. Lineaments

Lineaments are common features in the graphical presentation of aeromagnetic datasets. In some cases, they represent dykes or veins with magnetic susceptibilities different, positively or negatively, from those of the surrounding lithologies. Negative anomalies are indicators of reversely polarised remanent magnetisation. Lineaments can also represent faults or fractures in the host rock containing either magnetic minerals, e.g. magnetite, to produce positive signatures or non-magnetic minerals, e.g. quartz or calcite, to produce relative negative or neutral signatures compared to the surrounding lithologies. In still other cases, lineaments represent the contact between lithologies with different magnetic susceptibilities. In most cases, lineaments are fairly straight but they also may be curved along contacts or by later deformation. Offsets in magnetic lineaments may be used to establish a chronology of intrusive or tectonic events.

The magnetic data (Figure 6.9) shows many linear features striking east to west (A), northeast to east-northeast (B), slightly to the east-southeast (C) and to the north-northwest (F). These lineaments are both positively and negatively magnetised (D) and in places it seems the lineaments can exhibit sections with positive magnetisation while in a different location on the same lineament exhibit negative magnetisation (E). This could be due to the lineament recording a reversal in the Earth's magnetic field or reactivation of the dyke at a different time. These lineaments are interpreted to be dolerite dykes, although outcrops are rare. This interpretation is based on the presence of the dolerite sills mapped in the Venetia area as well as dolerite dykes cutting through the Venetia pit. East-west trending dolerite dykes are also common intruding the Karoo sediments in the northern portion of the area. Boreholes drilled for coal exploration occasionally cut through dolerites and boreholes drilled at Venetia intersect multiple dolerite occurrences (Appendix II). It is unknown whether these are sills or dykes.

Although dykes do not intrude in perfectly straight lines and may seem displaced in many locations due to en-echelon displacement, the possible faults indicated in this dissertation show definite and large displacements in the lineaments and extend across more than one lineament at a time. These disruptions have been identified as possible faults where displacement of magnetic anomalies are obvious (a in Figure 6.9), or where magnetic bodies terminate abruptly against a 'straight line' (b). The sense of displacement on these faults are not always the same and this can be explained by a normal or thrust fault where the faulted dykes dip in different directions and the movement due to the fault (up or down) brings the dykes closer together on one side of the fault than on the other. A swarm of north-northwest trending disruptions of the east-northeast trending features is visible in the southern part of the area (c). These disruptions are faults based on mapping and interpretation done by Kurszlaukis and Barnettt (2003); Barnettt (2003); (2006). Lineaments further to the east (F) may be dykes or the edges of sills.

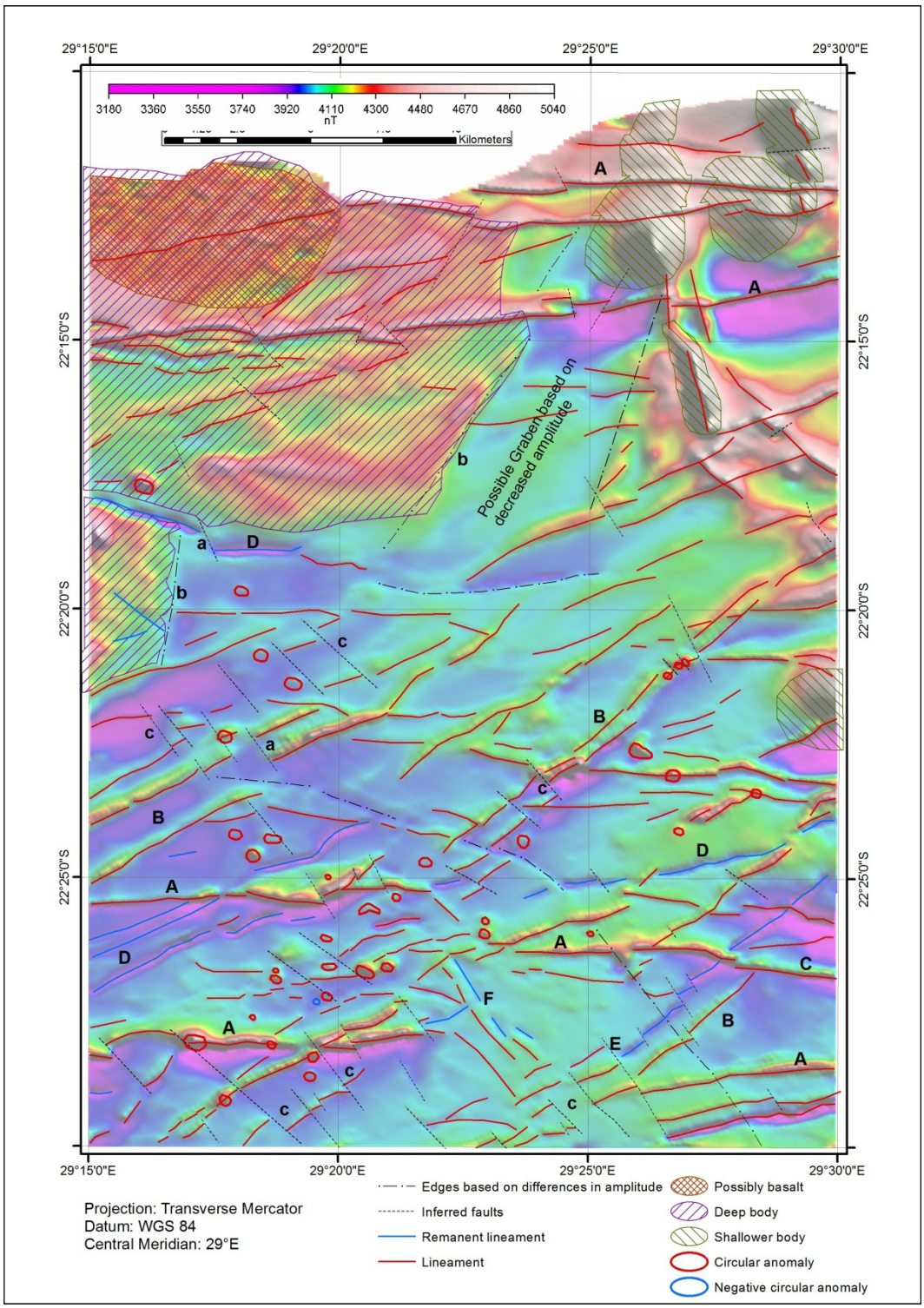


Figure 6.9. Qualitative interpretation of the total magnetic intensity data with IGRF removed, overlain on a faded image of the total field magnetic data. Features to note: E-W trending lineaments (A), ENE to NE trending lineaments (B), slightly ESE trending lineaments (C), negative lineaments (D), same lineament both positive and negative (E), NNW lineaments (F), horizontal displacements (a), abrupt linear edge to anomaly (b) and swarm of NNW trending disruptions (c).

In order to filter out high frequency data and only see regional effects, the data were upward continued to 500 m (Figure 6.10). This effectively moves the observer 500 m further away from the causative body of the anomaly, and therefore enhance deeper bodies relative to shallow bodies. An east-west trend (A) is visible in the north, and another in the south (A'). North of A there is clearly a higher amplitude signal than anywhere else in the study area (>5000 nT) with longer wavelenth. This area could be buried deeper. In Chapter 8 this will be discussed along with borehole data. A northeast trend (B) is visible in the centre of the area. An east south-east trend is visible in the east (C). A north-northeast trend seems to be indicated by magnetic lows in the south (D). There is a suggestion that some of the northeast trending lineaments are offset in a north-northwest direction, which could indicate faults (E). A magnetic high value in the north west could be attributed to a source body buried beneath the Karoo sediments. In the north east a very high amplitude (800 nT) anomaly could be attributed to a source body at depth.

The first vertical derivative of the magnetic data enhances the high frequency anomalies relative to the low frequency anomalies, and the result is that it eliminates the regional effects. The lineaments on this filtered dataset are much more clearly defined than on the total field magnetic data (Figure 6.11). A couple of lineaments that were not clear at all on the total magnetic field data were inferred from the first vertical derivative image. These are shown as thick black lines in the interpretation overlain on the first vertical derivative (Figure 6.11(a)) and to emphasise that they are not clear on the total magnetic field data, they are also overlain in an image of these data (Figure 6.11 (b)).

Formlines are lines usually drawn on digital terrain model data or satellite data by geologists. They merely outline forms seen in the data. On the second vertical derivative data they tend to highlight texture and trends in the data and can point to faults should the trends suddenly stop against a straight line. These formlines may in some cases improve an interpretation by delineating magnetic fabric that is not clear in the magnetic data alone. The formlines derived in this way are shown over the second vertical derivative data in Figure 6.12(a) and for comparison over the magnetic data in Figure

6.12 (b). The formlines did not highlight anything that was not derived from the magnetic data and first vertical derivative data.

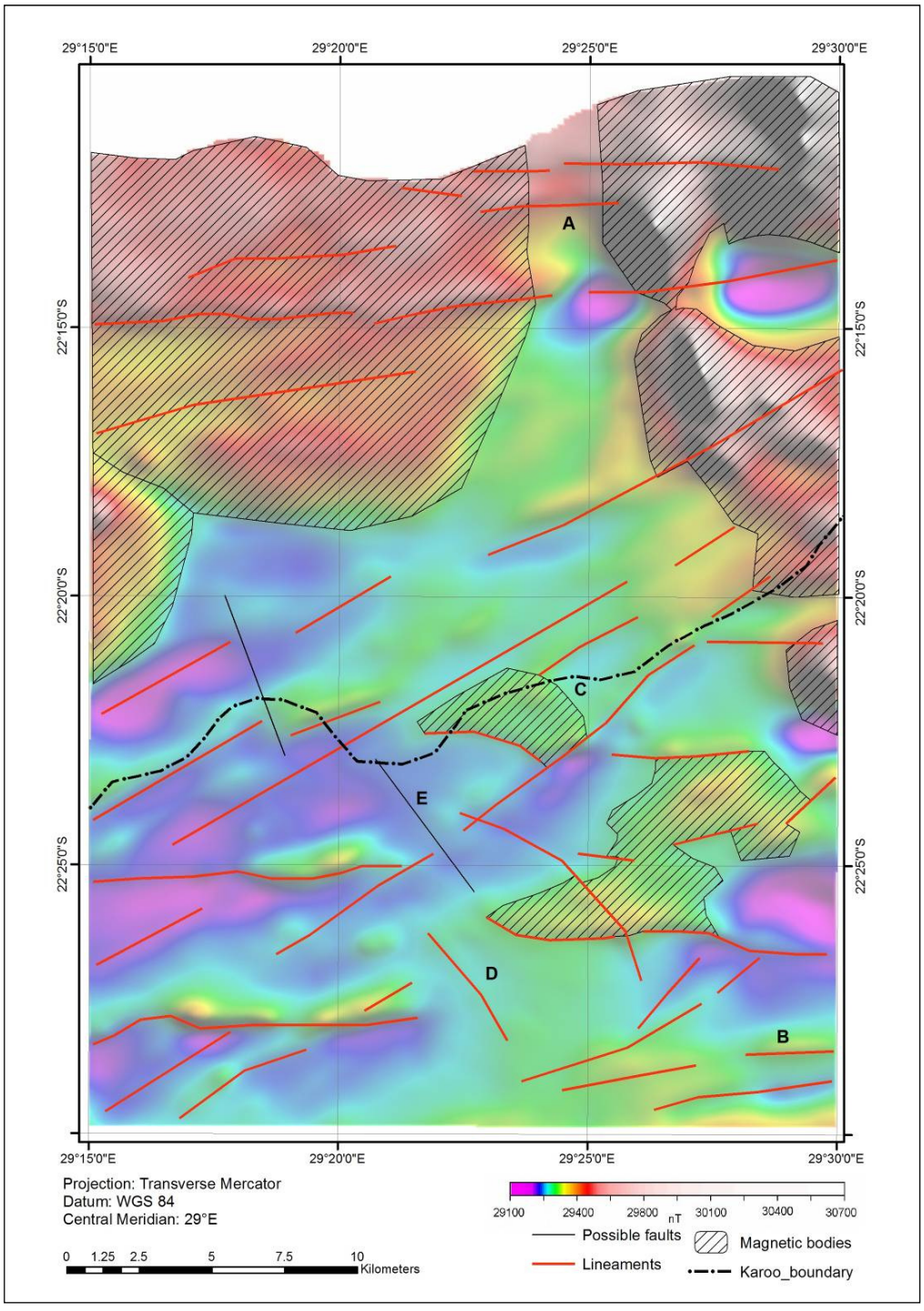


Figure 6.10. Interpretation of magnetic data upwards continued by 500 m overlain on a faded image of the upward continued data indicating deeper bodies. An east-west linear trend (A) in the north, east-west trend in the south (B), east-northeast trend through centre (C), north-northwest trending features (D) and north-northwest disruptions (E).

The analytical signal displays all anomalies as positive, and peaks of anomalies are symmetrical and occur directly over narrow bodies or the edges of broad bodies (Figure 6.13). A few dykes in the south-eastern corner of the area (A) were added, along with a dyke in the centre of the area (B) (see Figure 6.13). The other linear features are what seem to be faults (C) or part of the shear zone (D) trending to the north-northwest through the area. Although the data suggest cultural like markers indicative of a village or settlement, confirmation on Google Earth has indicated that there is no such village.

The automatic gain control filter represents both high and low amplitude data equally, thus enhancing features that would normally be obscured by bodies with high magnetic values. The thick black lines in Figure 6.14 (a) indicates features that were interpreted from this dataset that were not clear on the total field magnetic data (Figure 6.14 b).

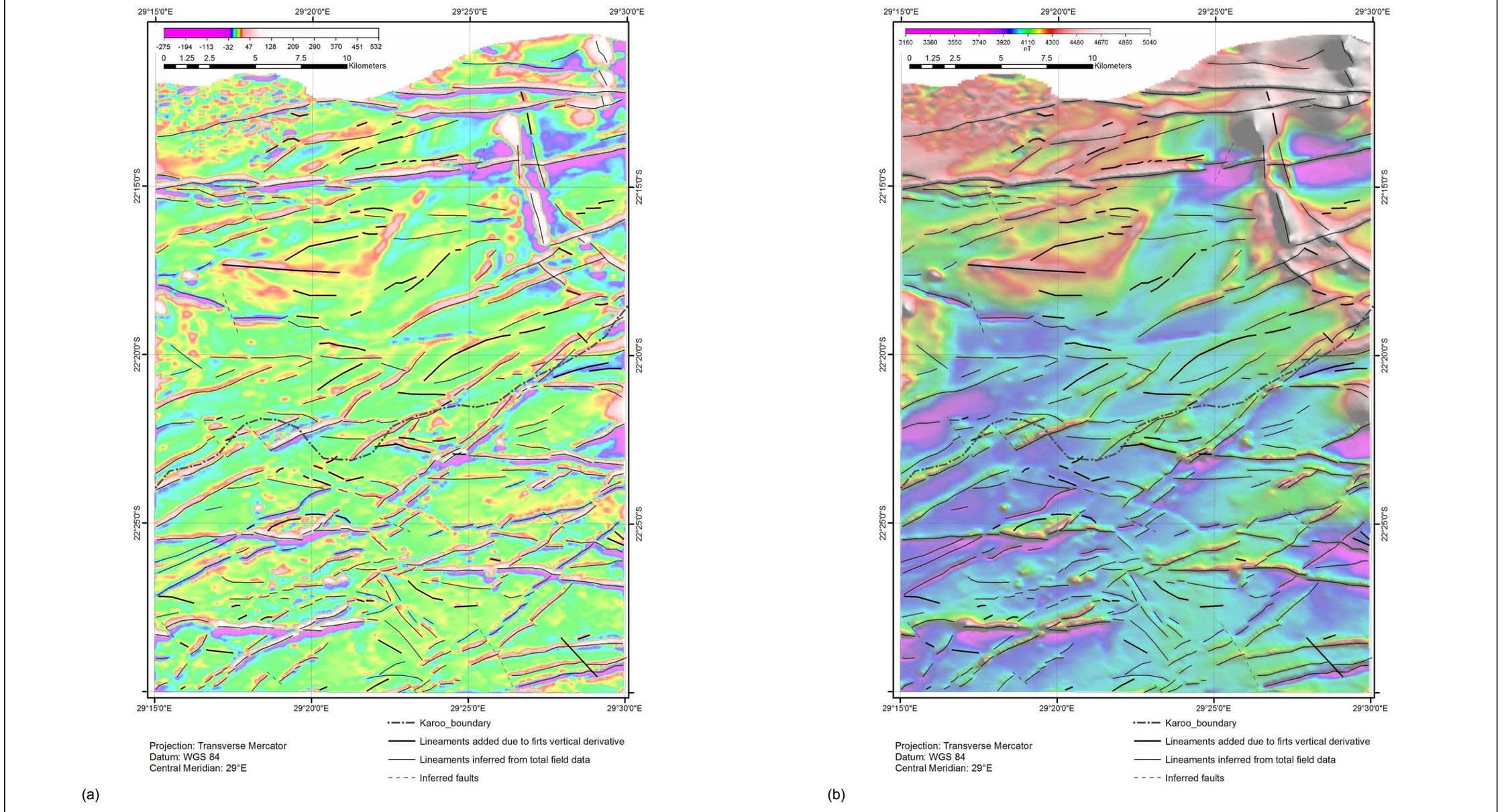


Figure 6.11. Lineaments inferred from both total field magnetic data and the first vertical derivative of the data overlain on (a) a faded image of the first vertical derivative of the data and (b) a faded image of the total field data. The thick black lines indicate the lineaments that were added from the interpretation of the first vertical derivative.

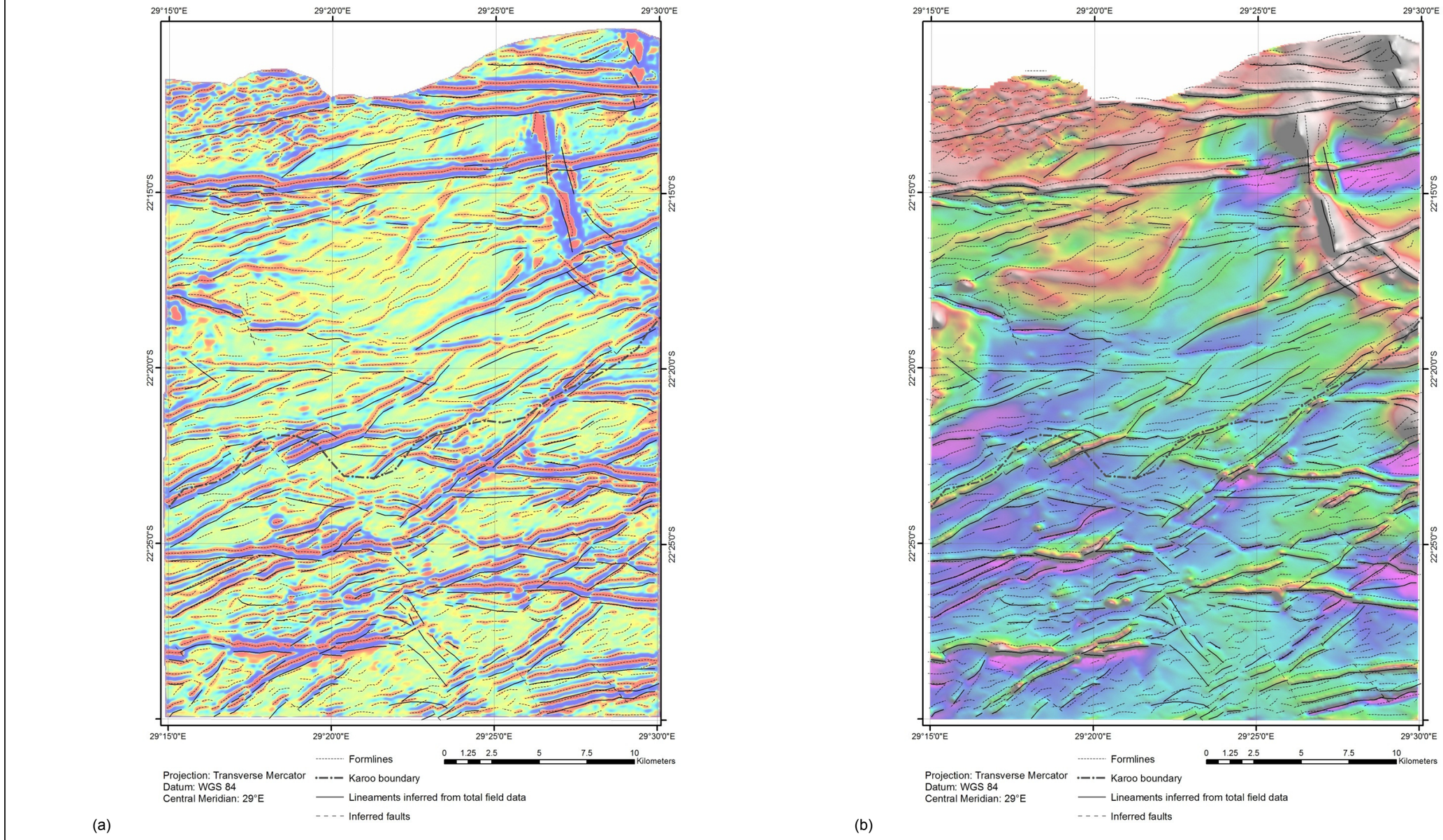
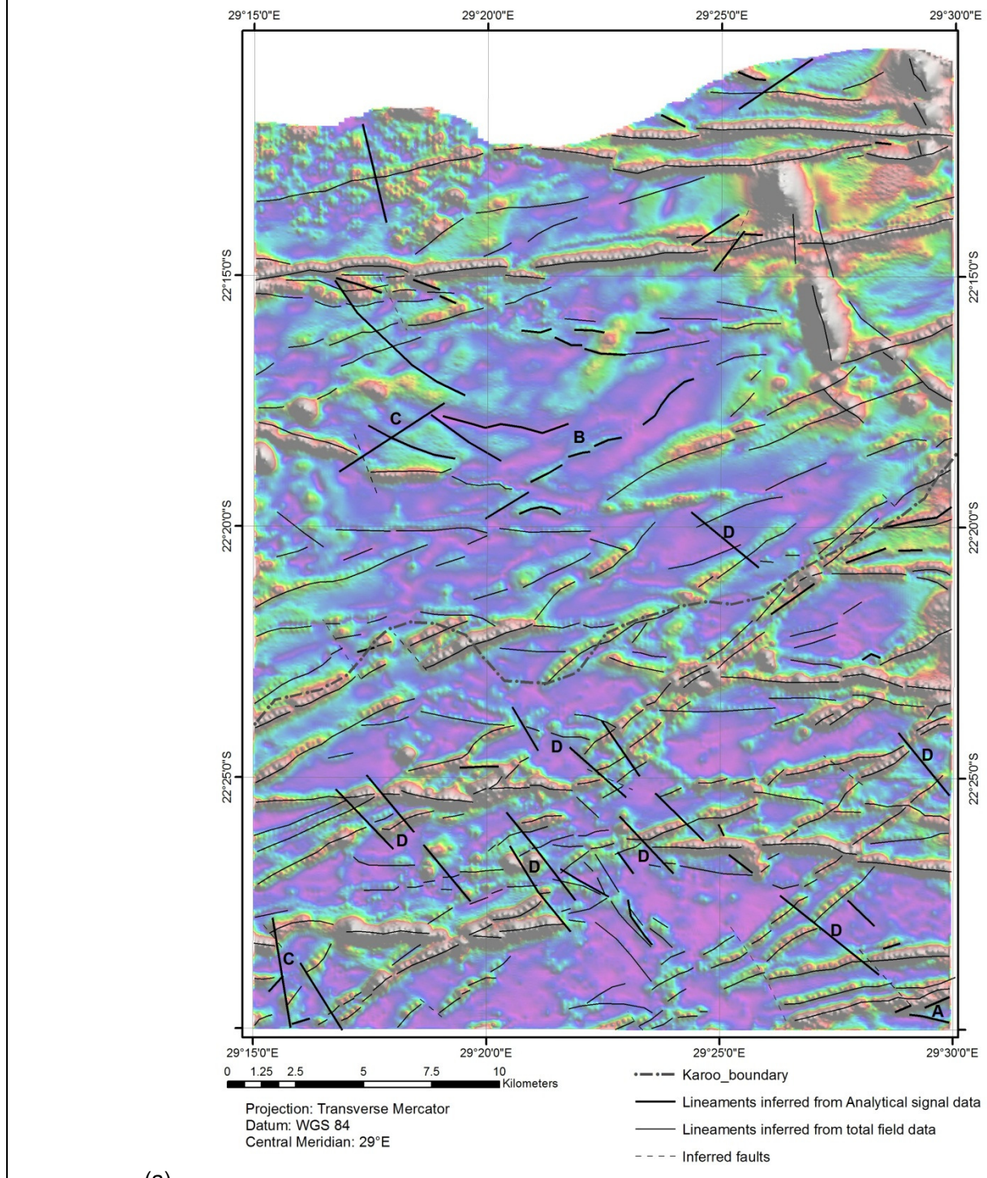
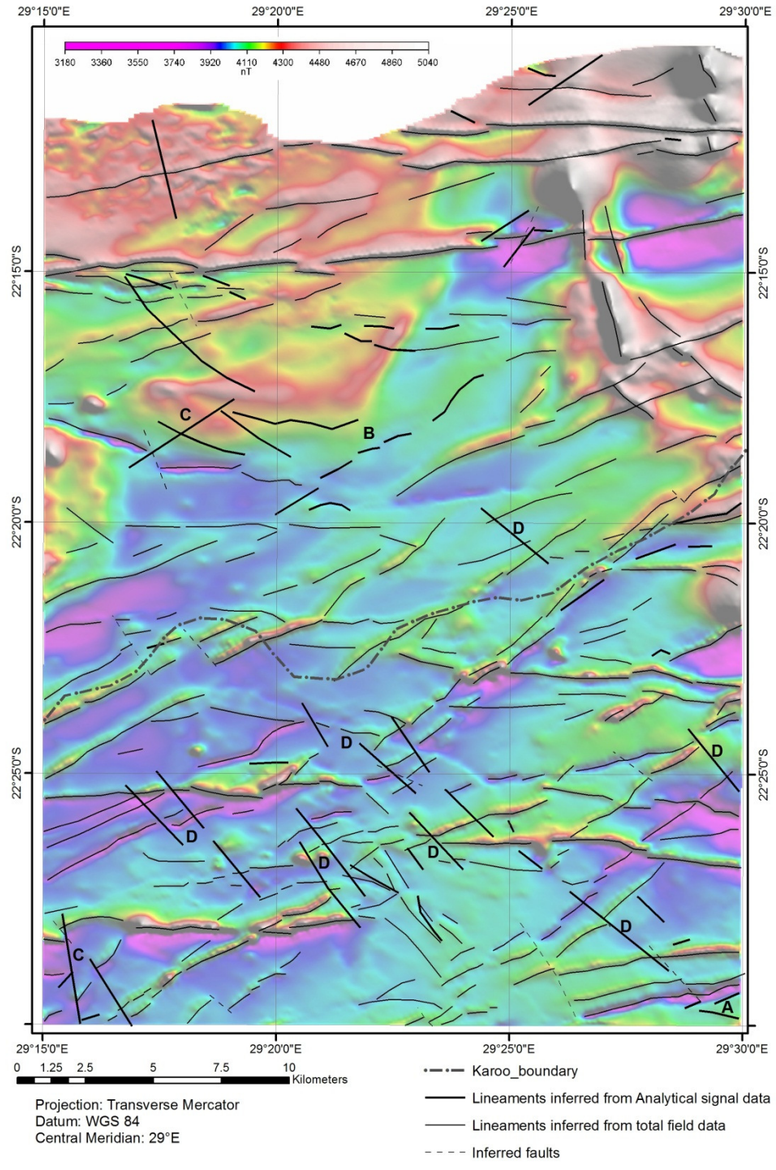


Figure 6.12. Formlines from second vertical derivative data over a faded image of the second vertical derivative data (a) and over a faded image of the magnetic data (b) for reference.

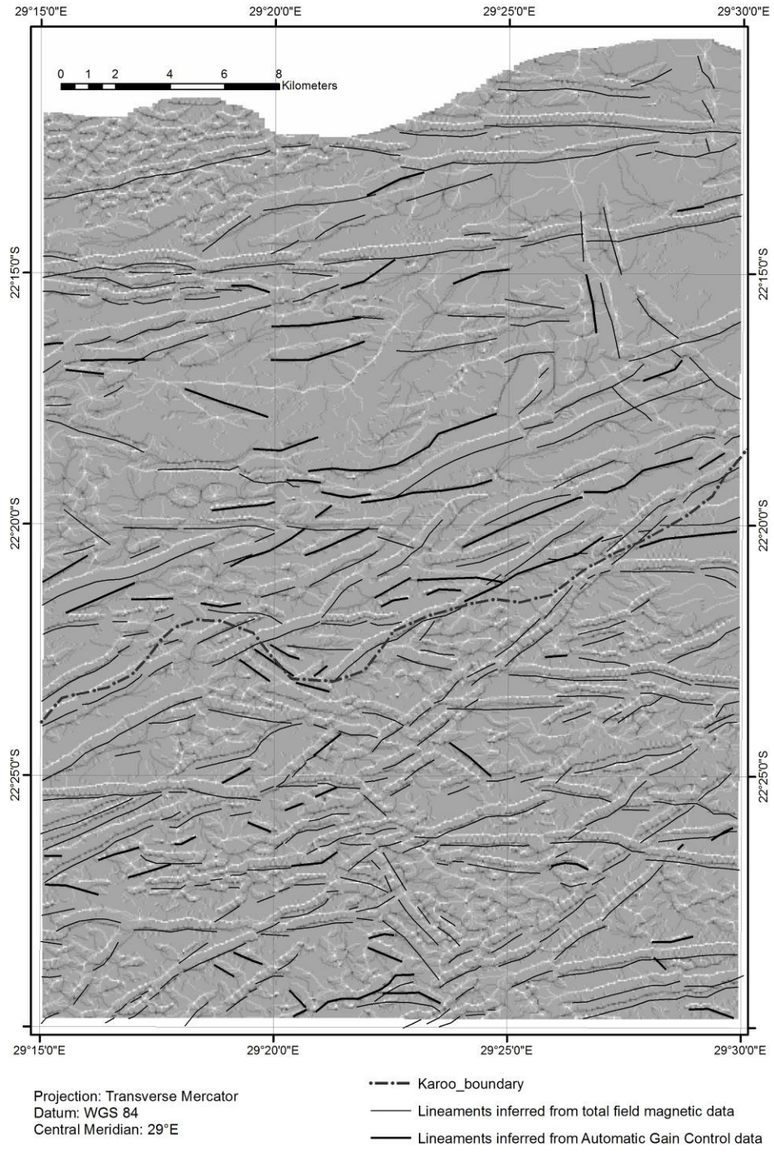


(a)

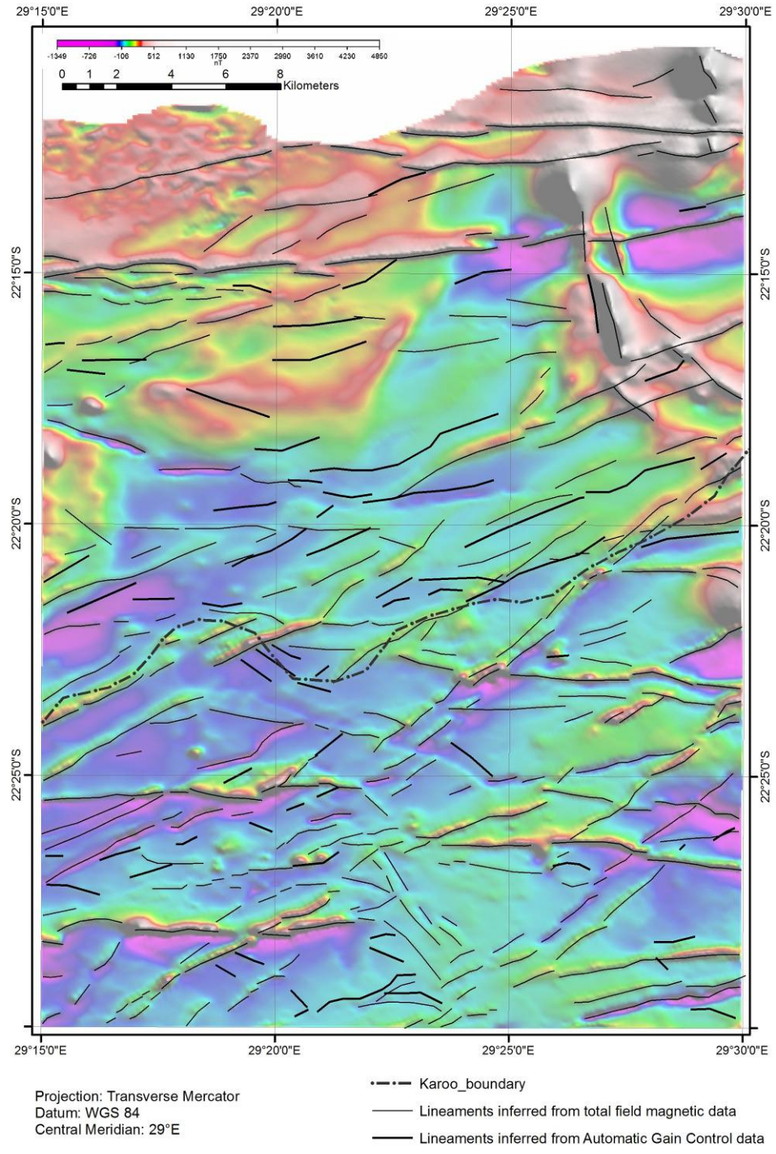


(b)

Figure 6.13. Lineaments inferred from both total field magnetic data and Analytical signal data. The thick black lines indicate the lineaments that are more obvious in the analytical signal data. (a) Shows the lineaments overlain on a faded image of the analytical signal data, while (b) shows them overlain on a faded image of the total magnetic field data. Features that are clearer on the analytical signal data than the total magnetic field data are: lineaments in southeast (A), northeast trending lineament (B), possible faults (C) and features that seem to be part of the north-northwest trending shear zone (D).



(a)



(b)

Figure 6.14 a and b. Lineaments inferred from both total field magnetic data and automatic gain control data. The thick black lines indicate the lineaments that are more obvious in the automatic gain control data. (a) Shows the lineaments overlain on a faded image of the analytical, while (b) shows the lineaments overlain on a faded image of the TMI data.

On the regional scale, lineaments can be used to define geographic domains or terrains. For example, Chernicoff (1984) identified 5 domains in the northern part of South Africa that correspond to areas defined by geology type rather than just lineament direction (Figure 6.15). Subsequently, Stettler et al. (1989) defined six domains based on lineament direction inferred from the regional magnetic data, in a portion of the same area. These domains may be correlated with distinct geological terranes (Figure 6.16 and Figure 6.17) Their domains 2 (Chernicoff) and F (Stettler) respectively correspond to the Beit Bridge Terrane of the Central Zone and Southern Marginal Zone of the Limpopo Belt respectively (Barton et al., 2006).

The strike directions of the lineaments (Figure 6.16 and Figure 6.17) on which these domains (Chernikoff, 1984 and Stettler et al., 1989) are based correspond very well with the strike directions of especially lineaments inferred in the Karoo portion of the study area (Figure 6.18). In the current study two domains are defined, one being restricted to the Karoo sediments and the second to the basement represented by the Beit Bridge rocks. More directions are visible in the current study due to higher resolution data and less aliasing of the data.

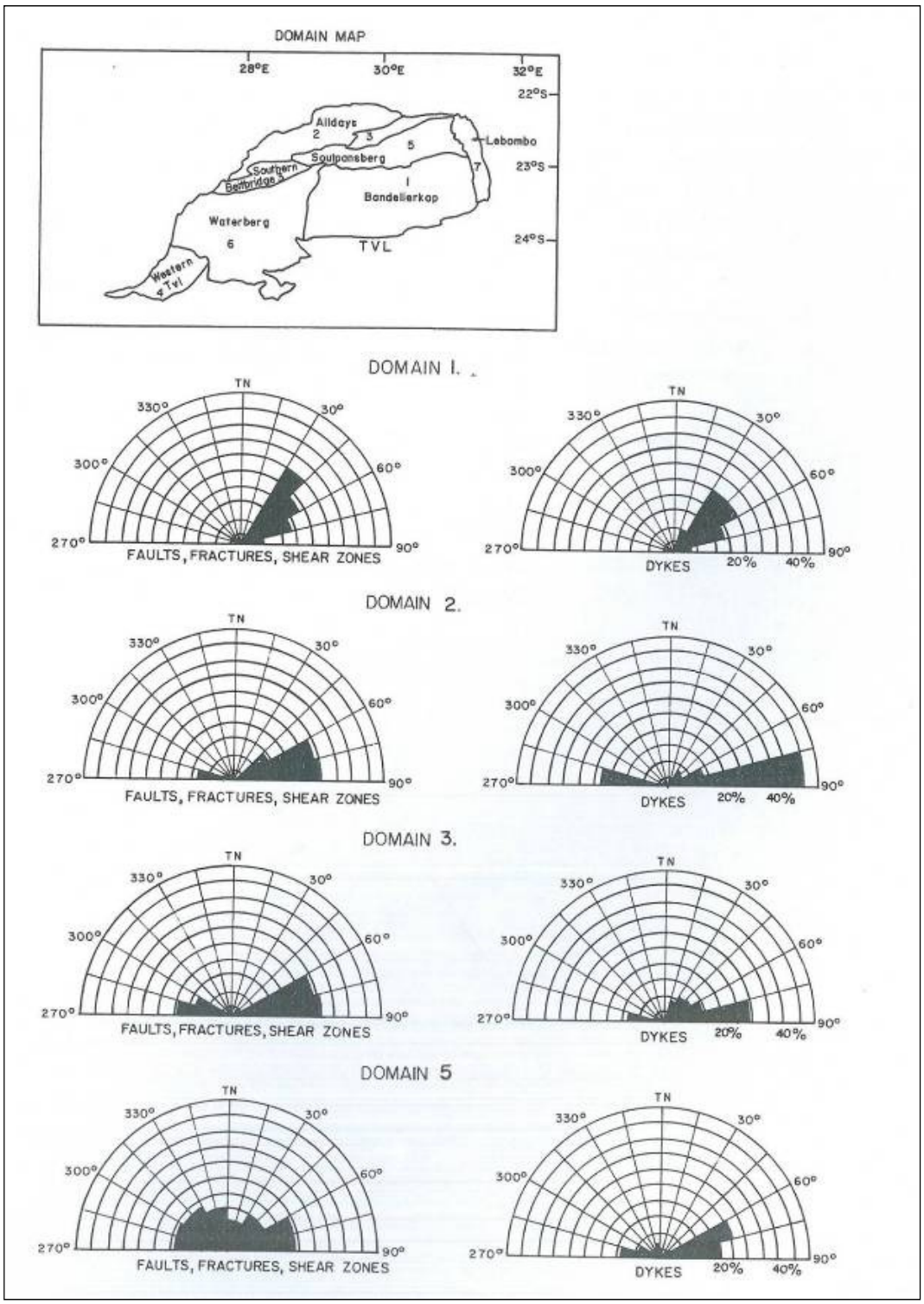


Figure 6.15. Principal strike directions of faults and lineaments and dykes as determined from geological maps and aerial photographs (Chernicoff, 1984). These domains were determined from geology type, rather than lineament direction.

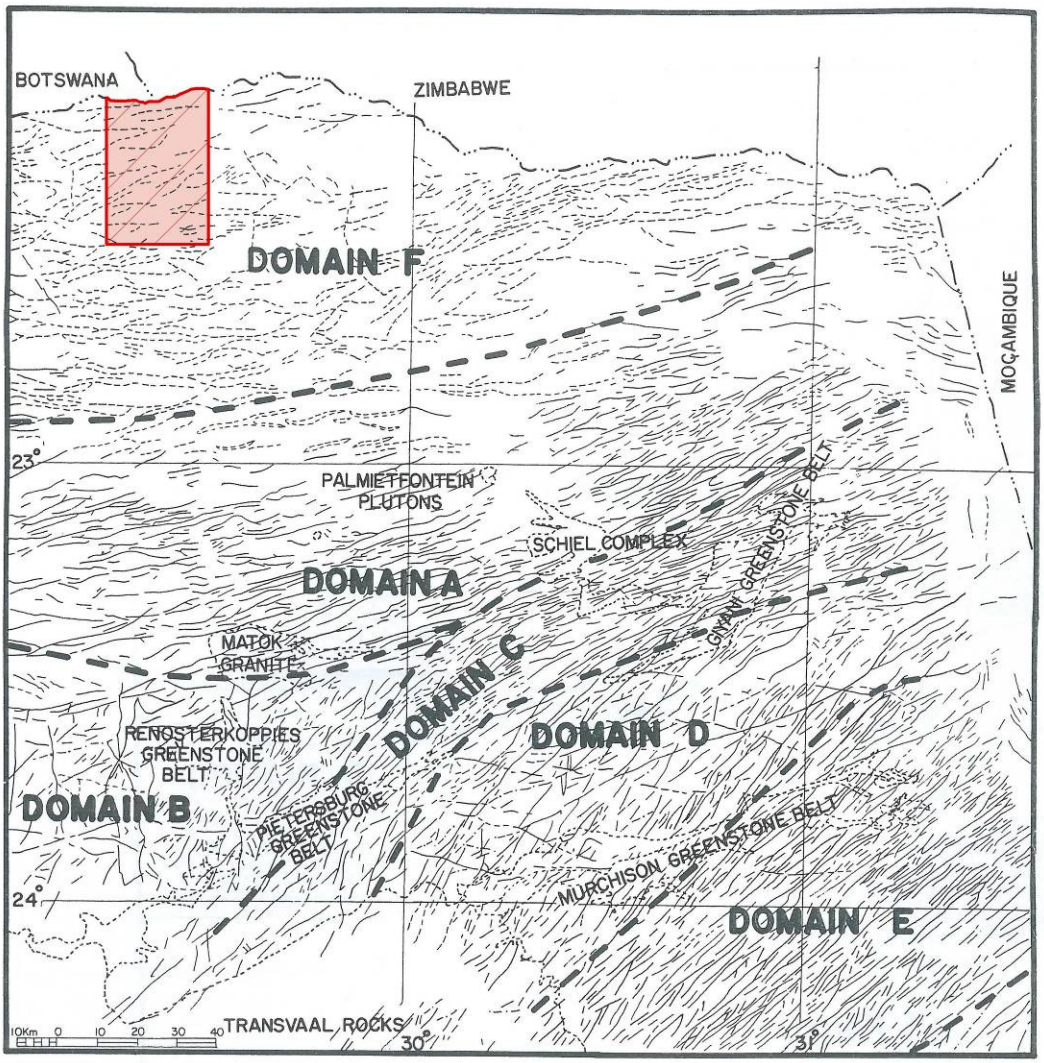


Figure 6.16. The aeromagnetic lineament map for the northern and northeastern Transvaal subdivided into six aeromagnetic lineament pattern domains based on lineament direction inferred from the regional magnetic data (Stettler et. al. 1989). The present study area is shown in red.

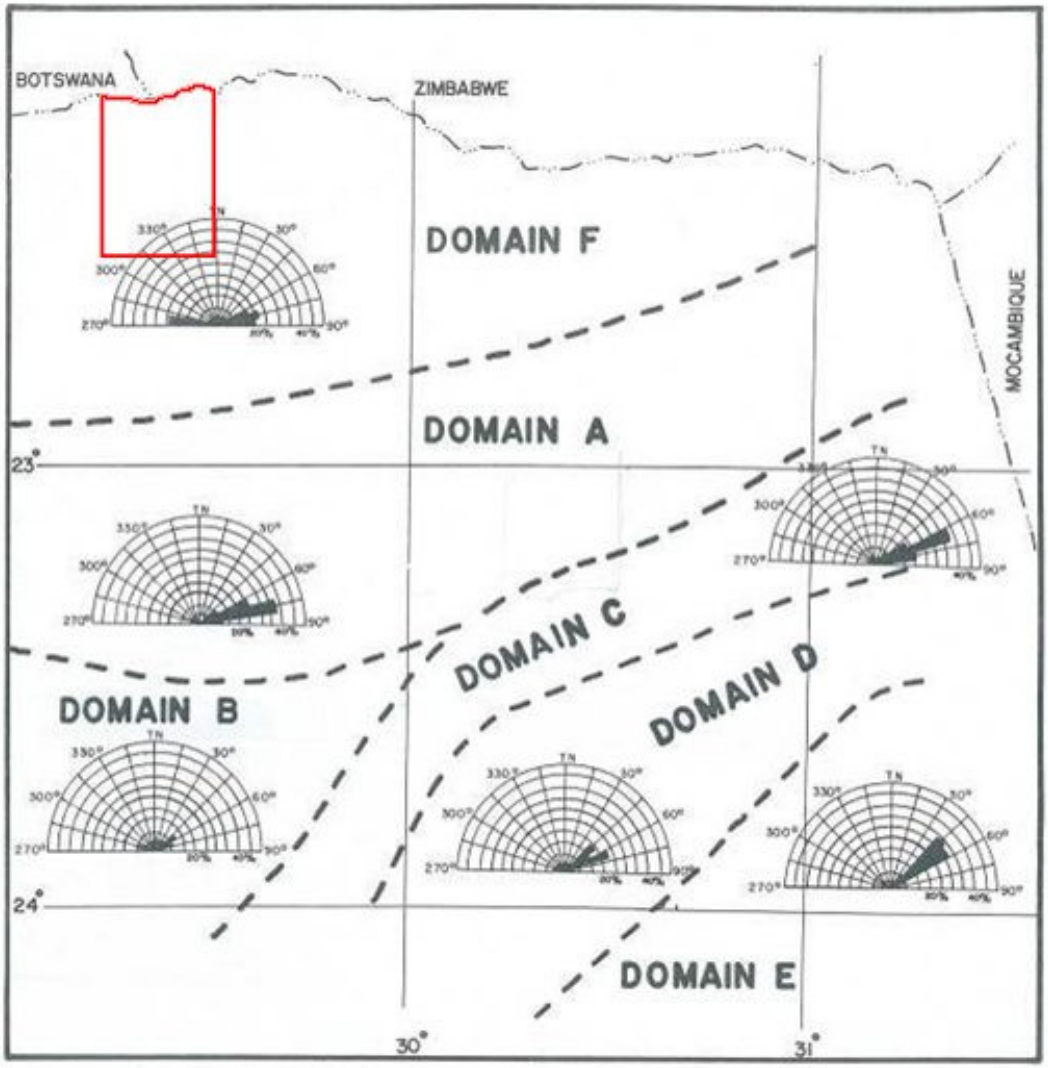


Figure 6.17. Rose diagrams depicting principal strike directions of magnetic lineaments in the individual pattern domains (Stettler et. al., 1989). Current study area shown in red.

From the indicated lineaments (Figure 6.9 to Figure 6.14), several groups of lineaments may be identified when their directions and number of lineaments are plotted on a rose diagram (Figure 6.18). These rose diagrams did not take the length of the lineaments into consideration, only number and direction. In addition, distinctly more lineaments occur in the basement than in the area covered by Karoo sediments and furthermore, some of the east to west and north-northwest trending lineaments are probably caused by a group of distinct dolerite dykes containing plagioclase phenocrysts several centimetres in length (Barton, personal communication, 2012). Because the study area has two distinct chronostratigraphic units, the largely Archaean basement exposed in the south and the

unconformably overlying late-Paleozoic Permian to Mesozoic (Jurassic) rocks of the Karoo Supergroup in the north, lineaments related to Mesozoic to recent processes may be identified as ones that are exposed in the Karoo. These Mesozoic and younger lineaments have primarily east to west trends with a small number trending to the northwest. In the older archean basement to the south, north-northwest and north-northeast trends predominate and east to west trends are less pronounced. In the Karoo rocks and basement, the north-northwest and north-northeast trending lineaments offset the east to west trending lineaments showing that they are younger. In addition, in the basement, the east to west, north-northeast and north-northwest trending lineaments offset the east-northeast and northwest trending lineaments, indicating that the latter are older.

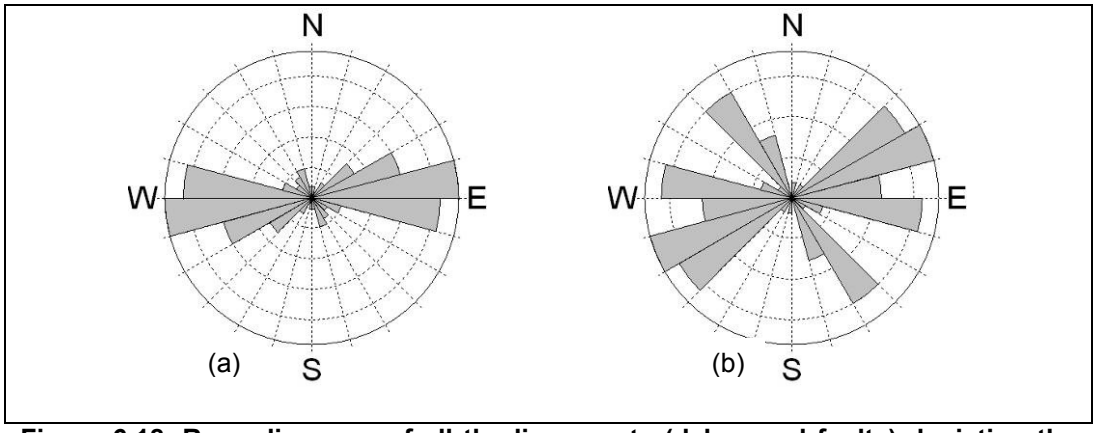


Figure 6.18. Rose diagrams of all the lineaments (dykes and faults) depicting the strike directions of lineaments in Karoo rocks (a) and basement rocks (b). In (b) the northwest trending lineaments are mostly faults.

Barnettt (2006) showed the major structural patterns (originally presented by Wilson, 1990) and their age relationships based on the SANABOZI data set. The early Proterozoic structures (Figure 6.19) corresponds well to the east-west to north-northeast striking directions of the inferred lineaments in the basement (Figure 6.18b). The younger Paleozoic structures (Figure 6.20) correspond with both the directions and locations of the inferred lineaments in the Karoo (Figure 6.18a). By comparing the interpretation of the SANABOZI data (black) and the new high resolution data (red), the aliasing in the older data is clearly visible (Figure 6.21). A, B and C are for reference to compare the lineaments from Barnettt (2006) to the ones from this study.

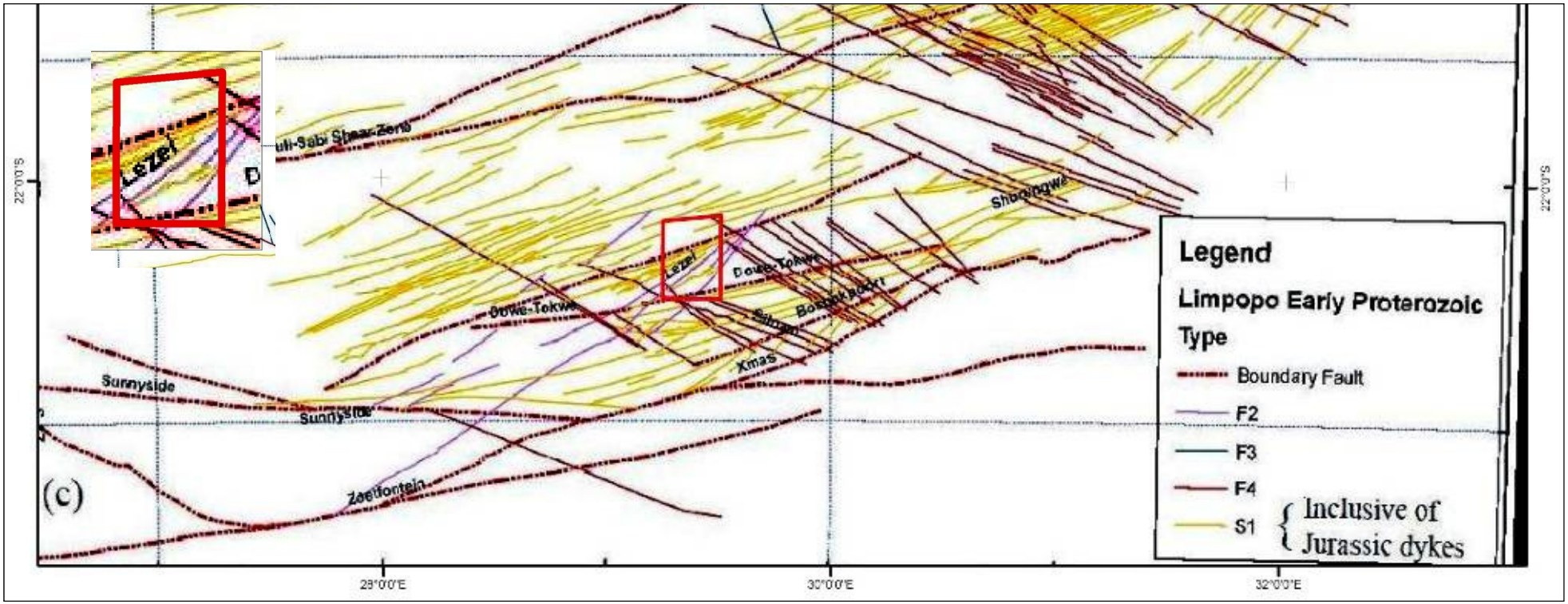


Figure 6.19. Structures interpreted to be early Proterozoic (2.5 Ga to 1.6 Ga) by Barnettt (2006). The current study area is shown in red and the insert shows an inflated image of the study area. F2 represent the oldest dykes and S1 the youngest.

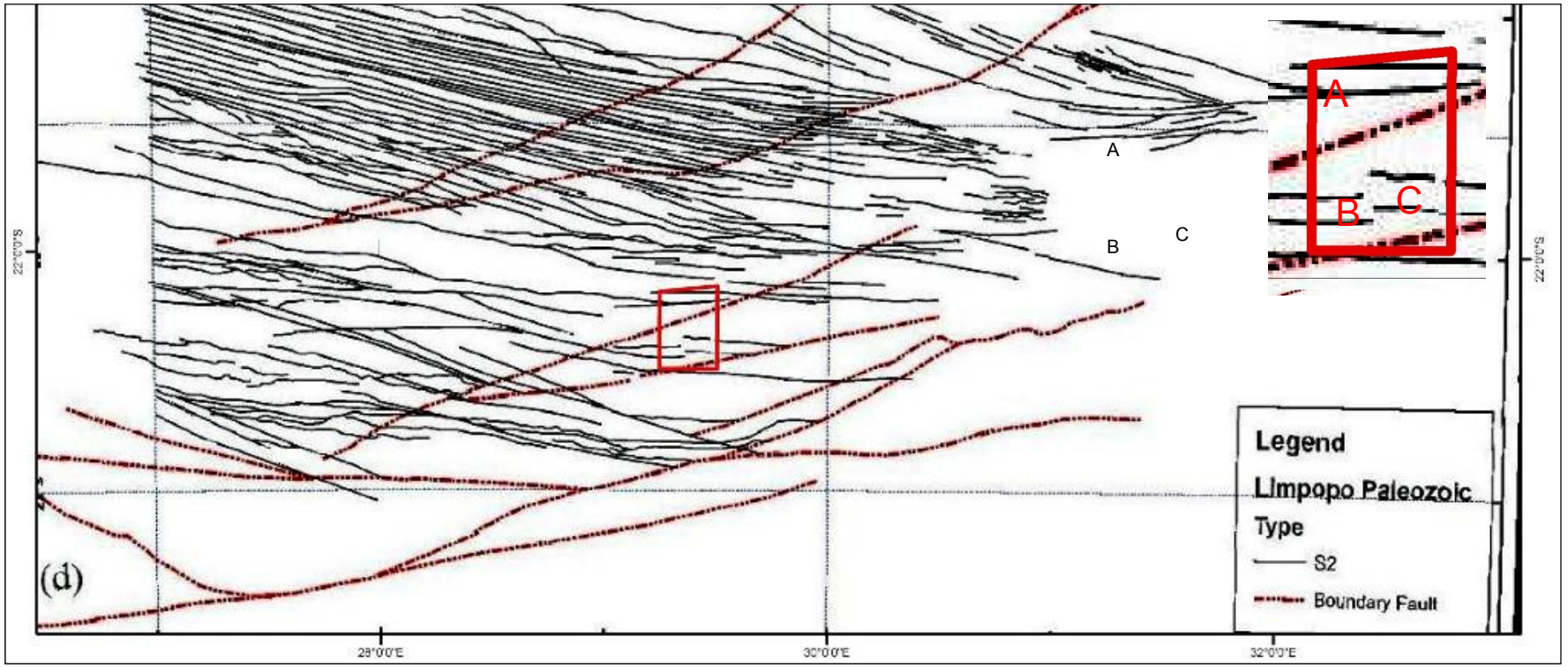


Figure 6.20. Structures interpreted to be (Paleozoic 542 Ma to 251 Ma) by Barnettt (2006). The current study area is shown in red and the insert shows an inflated image of the study area.

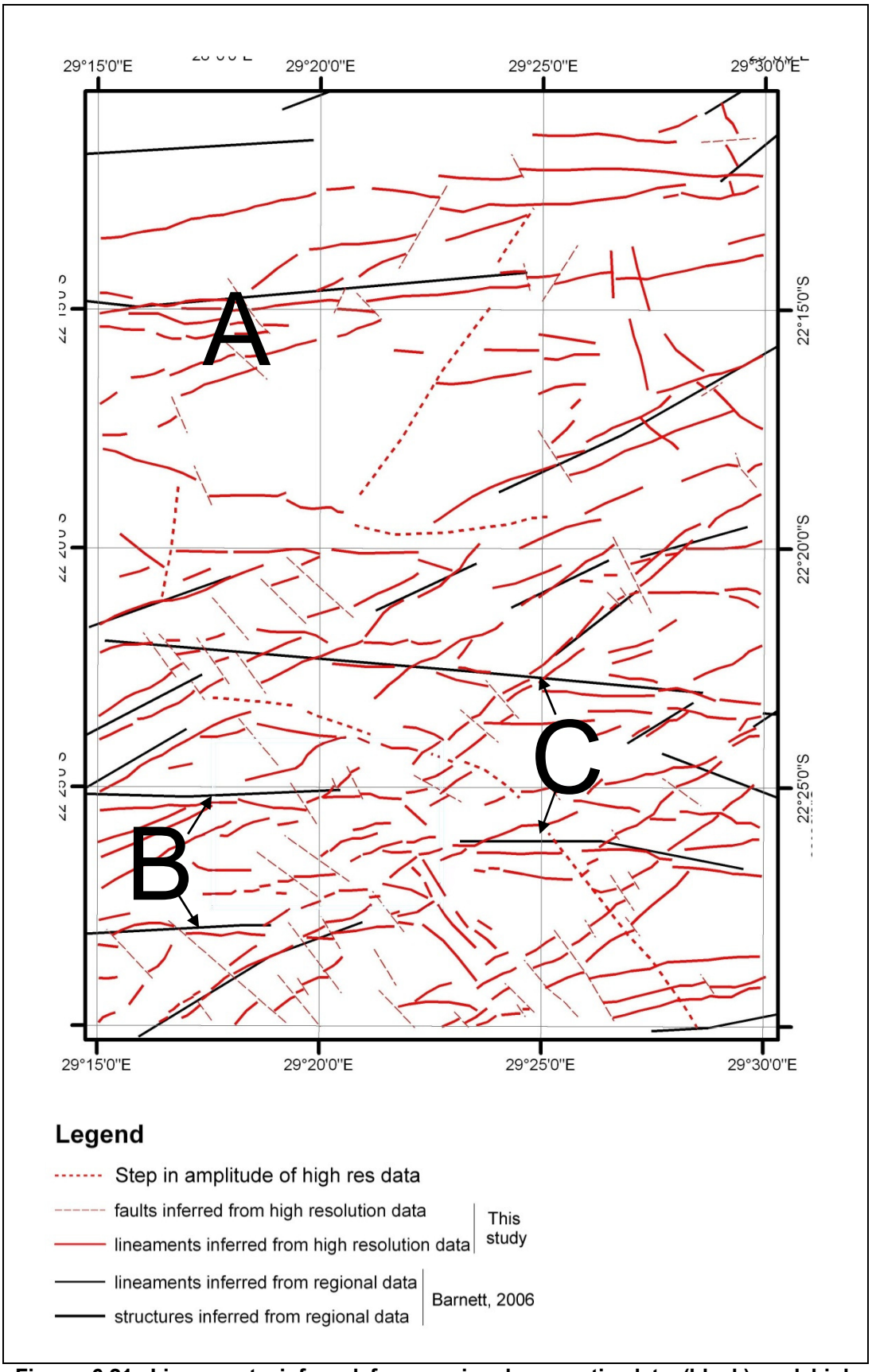


Figure 6.21. Lineaments inferred from regional magnetic data (black) and high resolution data (red) to compare with Barnettt (2006) lineaments. A, B and C indicate the lineaments inferred from regional data (black lines) correspond to lineaments in Figure 6.20.

6.2.2. Sills

There are many dolerite sills mapped based on outcrop in the area (Pretorius, 1996; Barton et al., 2003; Brandl, 2002). These are indicated in red hatched areas on Figure 6.22. Anomalies interpreted to be due to sills are indicated as outlines on Figure 6.22. No sills are mapped in the northern area covered by Karoo sediments and the magnetic anomalies seem to indicate larger bodies at depth and not sills close to the surface.

The sills edges of the sills are inferred from the mapped dolerite outcrops (A on Figure 6.22) where no clear sill edge can be inferred from the data. Where the TMI data and filtered data shows a clear anomaly that can be related to the edge of a sill, that was used to delineate the edge of the sill (B on Figure 6.22). In many cases the mapped outcrop and the magnetic anomaly coincided (C on Figure 6.22), but there are also some cases where it is clear that the sill/s are more complex than what can be delineated in this manner (D on Figure 6.22). It is difficult to determine which anomalies inferred as sill edges belong together, as there are many in the area surrounding Venetia and the edges are not forming complete enclosed ‘sills’.

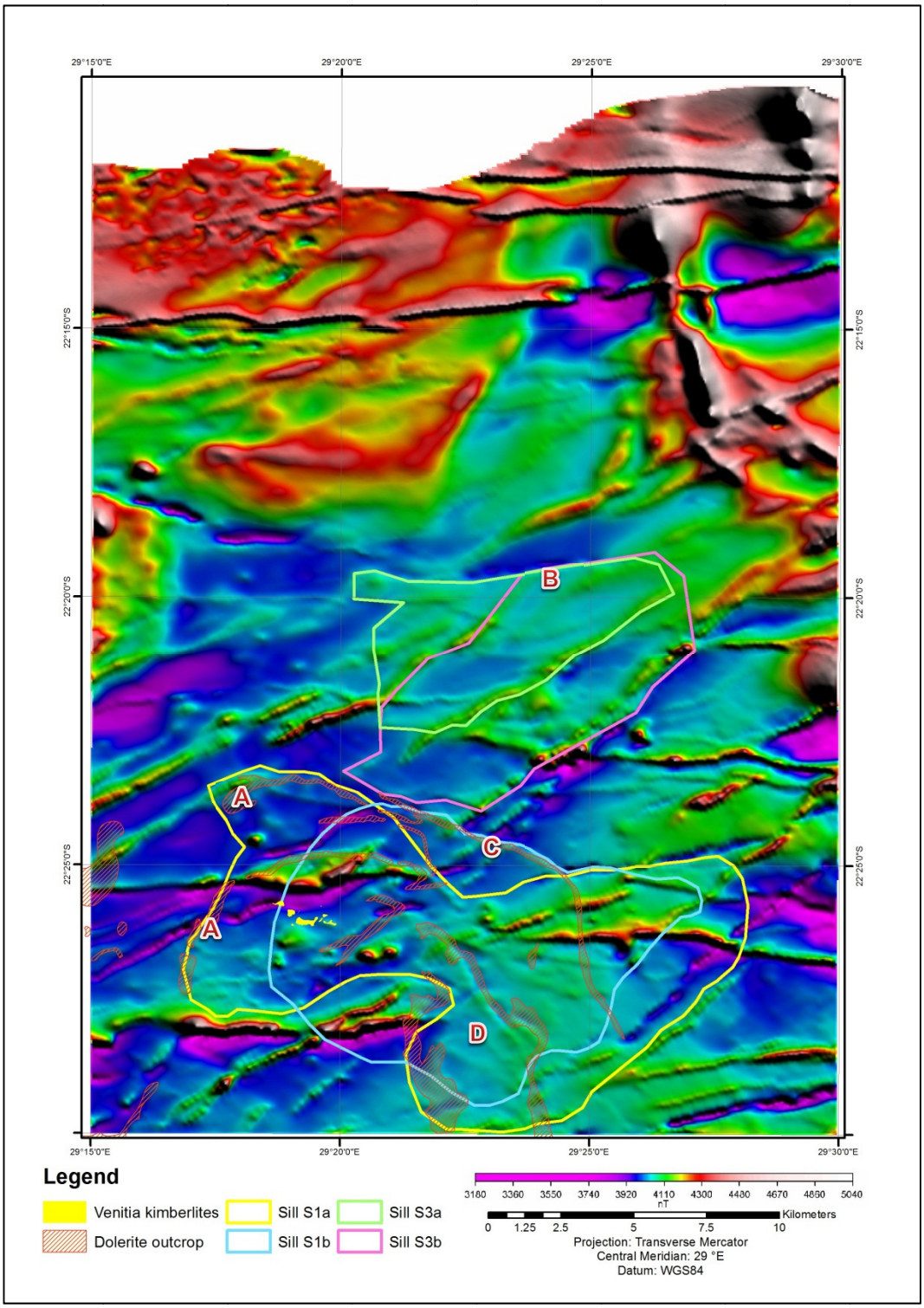


Figure 6.22. Dolerite sills inferred from the total field magnetic data in the southern portion of the magnetic data. The outline of the interpreted sill anomalies are based on spatial correspondence with outcrop and continuation of the magnetic anomaly from both the TMI image and enhanced filtered images and the mapped dolerite outcrops.

6.2.3. Circular and round magnetic anomalies

The aeromagnetic data from the study area indicate numerous magnetically positive and negative circular or rounded anomalies. Figure 6.23a is a zoomed-in view of some of the circular anomalies to show greater detail and Figure 6.23b shows their location on the current study area. The first vertical derivative of the magnetic data reveals some circular to round shaped bodies that are not clearly visible on the total field data. Figure 6.24a is a zoomed-in portion of the area to show the anomalies in greater detail. These anomalies have been interpreted from forward modelling results to be due to a plug-like source body. Figure 6.24b shows the location of inferred plugs overlain on a faded image of the first vertical derivative data of the study area.

The inferred plugs on the magnetic data are grouped into two elongated clusters, one having a north-northwest trend (dashed black lines on Figure 6.27) and the other a northeast to east-northeast trend. This latter trend correlates with the north-northeast trending faults and dykes. The Venetia kimberlite cluster is situated where these two elongated clusters cross (dark blue on Figure 6.22). It is also worthy to mention that most (if not all) plugs seem to plot where the north-northwest striking faults and fractures intersect the east-northeast trending dykes, the east to west trending dykes or both. Thus the intrusions appear to be taking advantage of local structural weaknesses as is also observed with kimberlite intrusions (Barnettt, 2006)

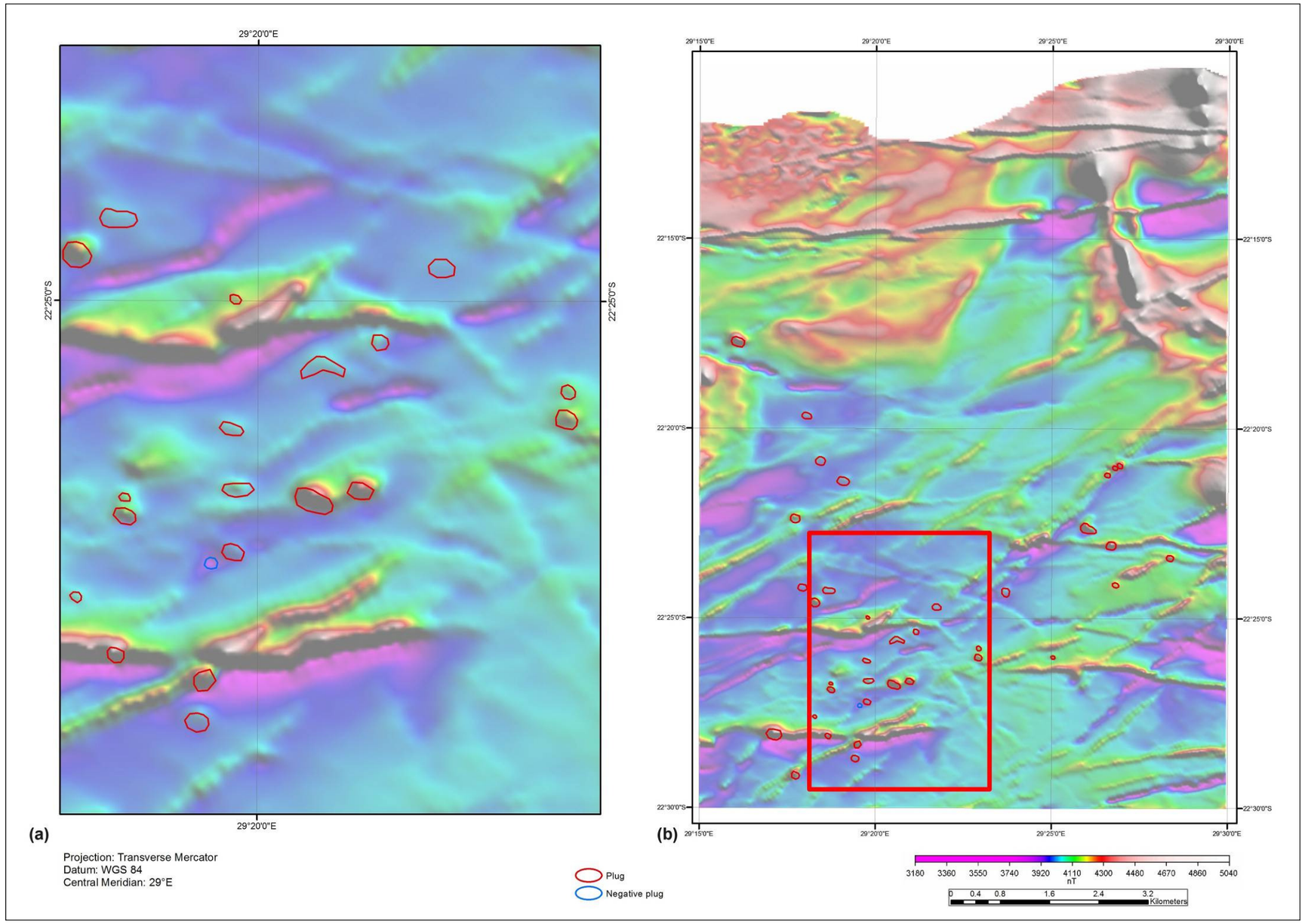


Figure 6.23. Plug shaped bodies inferred from total field magnetic data overlain on a faded image of the data. The extent of (a) is shown as a red rectangle on the study area (b).

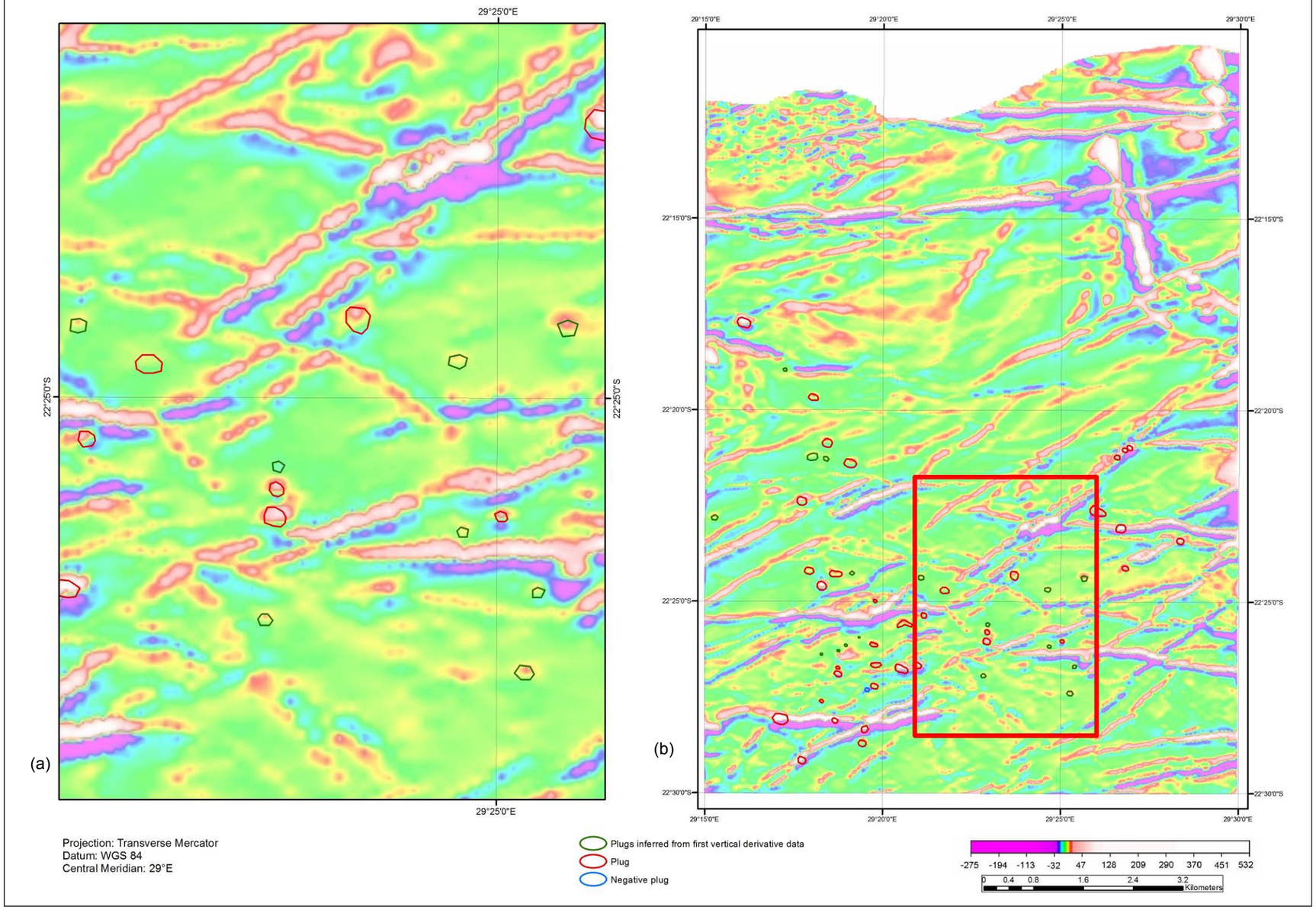


Figure 6.24. Plug shaped bodies inferred from the first vertical derivative data overlain on a faded image of the data. The extent of the zoomed in map on the left is shown as a red rectangle on the map of the study area (right).

It is interesting to note that although most of the Venetia kimberlite intrusions do not have a magnetic signature, it would seem that K4 and K5 coincide with an inferred positive plug shaped body (see Figure 6.25). Kimberlite clusters frequently have large variations in physical properties (especially susceptibility). Most of the pipes are quite small and fall between the 200 m line spacing interval. The positions of the kimberlite bodies are overlain on the analytic signal data, as this dataset shows the features clearest at this scale. It is also interesting to note that the K3, K2 and K1 bodies seem to be aligned in a northwest direction. Kurszlaukis and Barnettt (2003) interpreted a fault coinciding with this location and direction.

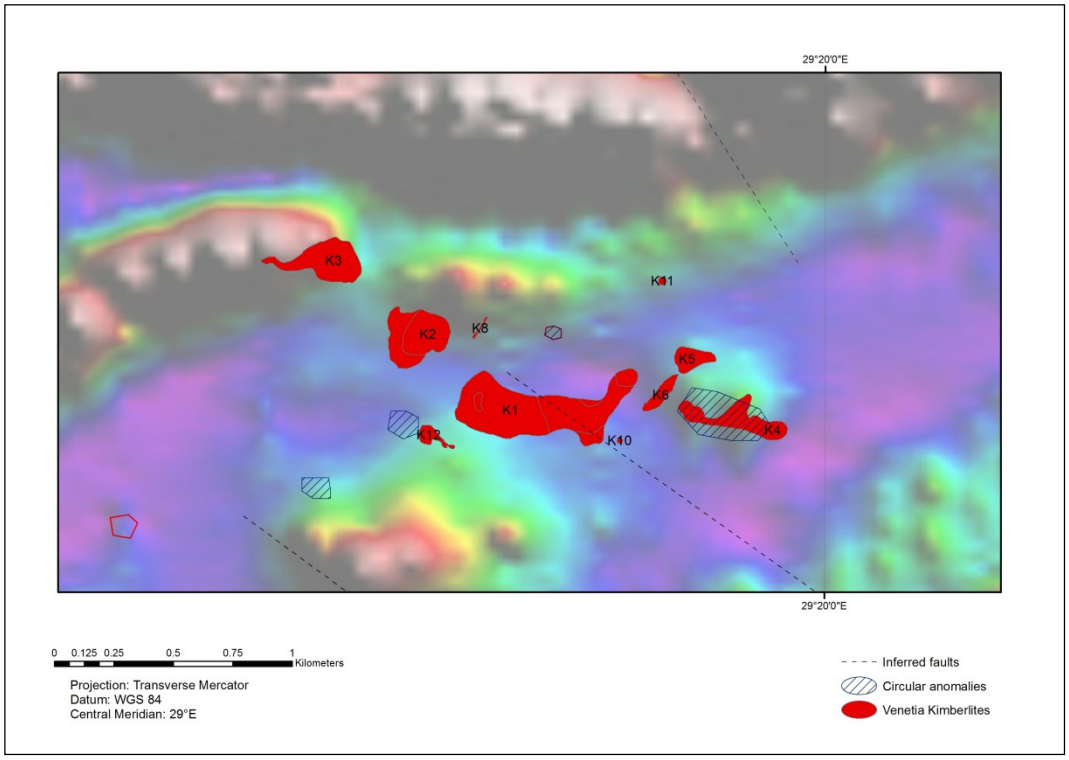


Figure 6.25. The Venetia kimberlite intrusions as well as structural features inferred from magnetic data overlain on a faded image of the analytical signal data.

The spatial distribution of any group of circular magnetic feature intrusions can be analysed with an unbiased geometrical examination of the distance and direction between each circular magnetic feature intrusions occurrence and all others in the area of

interest (Stubley, 2004) with the purpose of finding spatial / directional relationships in the intrusions. This is done by placing a plug (intrusion) on a common origin, while maintaining a consistent north, and plotting all others plugs relative to this origin. Then the process is repeated for every plug in the data set. This is called a translation diagram and was first used to determine interatomic distances in crystals, and in geology to determine strain from the distribution of objects in a rock (Patterson, 1934; 1935; Perutz, 1942; Fry, 1979). Further analysis is then done on the relations diagram by constructing a rose diagram recording the relationships in each radial sector (Vearncombe and Vearncombe, 1999; 2000).

A translations diagram or “Fry analysis” diagram was constructed based on the locations of the circular magnetic anomalies (Figure 6.26).

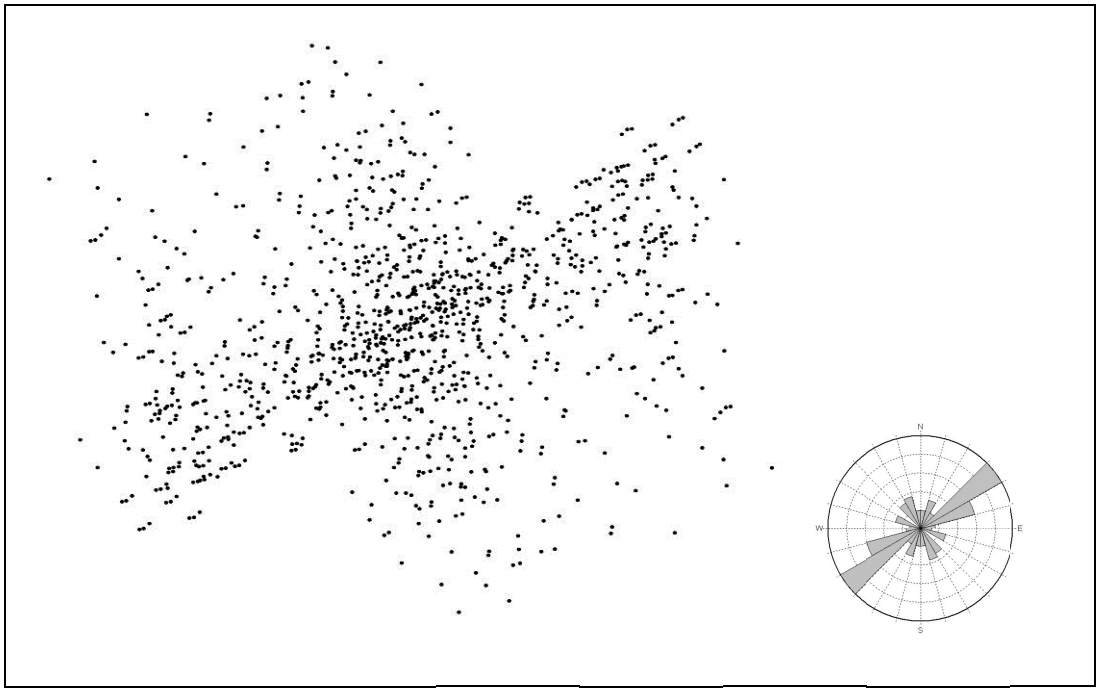


Figure 6.26. Translation diagram for all interpreted plugs and rose diagram with 15° radial sector angles showing preferred linear directions.

This analysis revealed that the plugs tended to be aligned on north-northwest and east-northeast trends (Figure 6.26). The rose diagram was created by manually placing a circle over the translations diagram with the centre of the circle on the centre of the

diagram, dividing the circle into 10° slices (much like a rose diagram) and counting the plugs in each slice to determine the percentage for that direction of the rose diagram.

6.2.4. Summary of magnetic interpretation

Figure 6.27 shows a summary of the distribution of the circular anomalies and lineaments. Note that the plugs are grouped in two elongated clusters, one aligned with the northeast trending dykes and the second aligned with the north-northwest striking zone of disruptions. The Venetia kimberlites also form part of the plugs that fall within these clusters. The majority of the plugs in the northeast trending cluster are located in the basement, while some of the plugs in the north-northwest striking cluster are located in the area covered by Karoo sediment.

The east-west trending dykes are younger than the northeast trending dykes (Barnettt, 2006). This appears to be confirmed by east-west trending dykes consistently cutting northeast trending dykes (A on Figure 6.27). The plugs (and most of the dykes) are covered by Karoo sediments and thus older than the Karoo sedimetation. Furthermore, the Venetia kimberlite (~520 Ma) intrudes two dolerite sills and thus these sills and possibly the plugs and dykes are older than the Venetia kimberlites.

The north-northwest trending zone of disruptions corresponds to a shear zone mapped on the farm Gotha south of the Venetia klippe (J.M. Barton, personal communication, 2009) and could be the northern extension of the shear zone.

A compilation of the interpreted magnetic bodies, lineaments and structures is shown in Figure 6.28. The map shows magnetic bodies at various depths in the northern part of the study area. These are indicated in shades of blue and dark blue hatching. The inferred small round anomalies are shown in dark red and inferred sills in the south are indicated with green hatching.

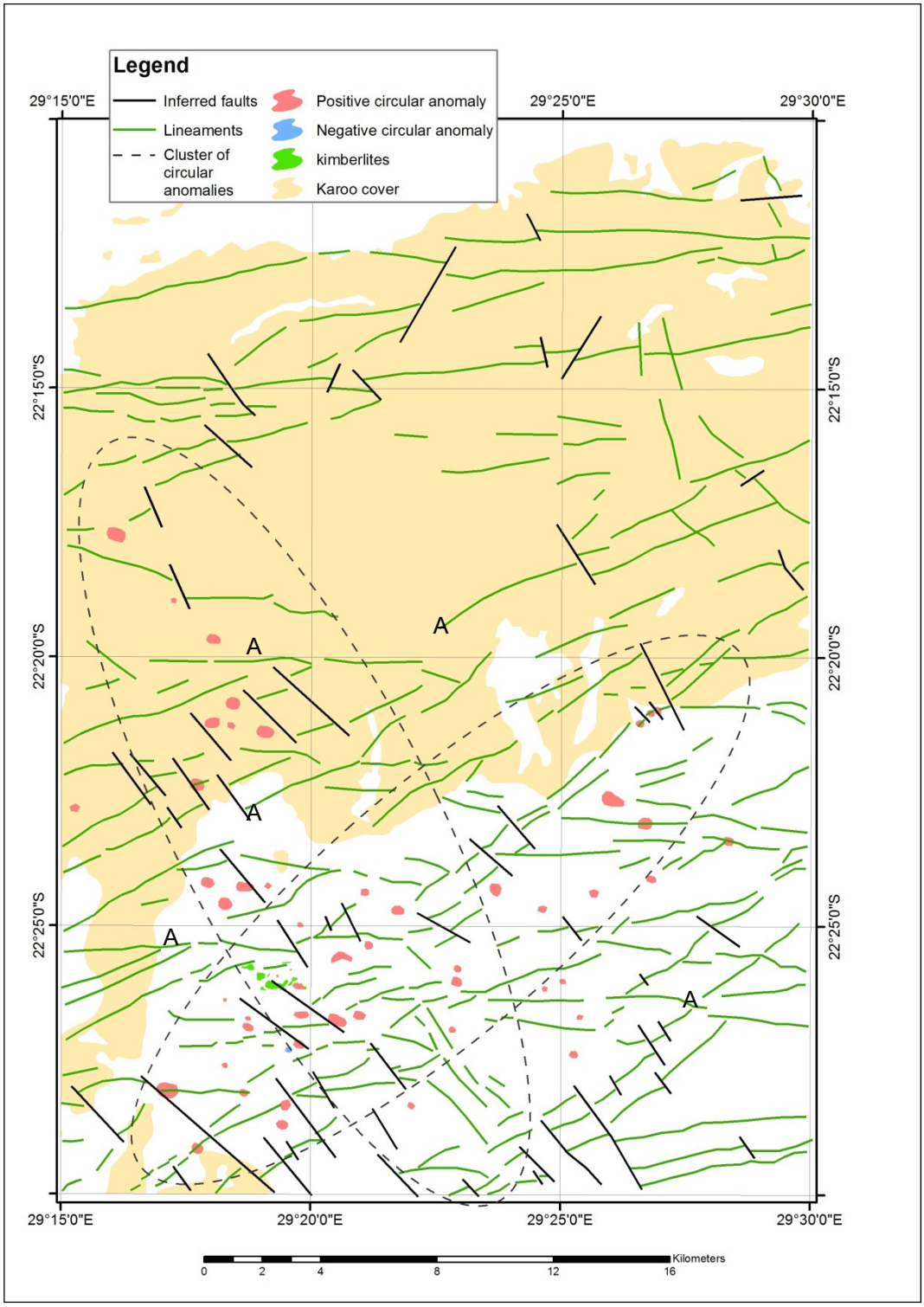


Figure 6.27. Distribution of plug-like bodies in relation to interpreted lineaments from both regional and high resolution data

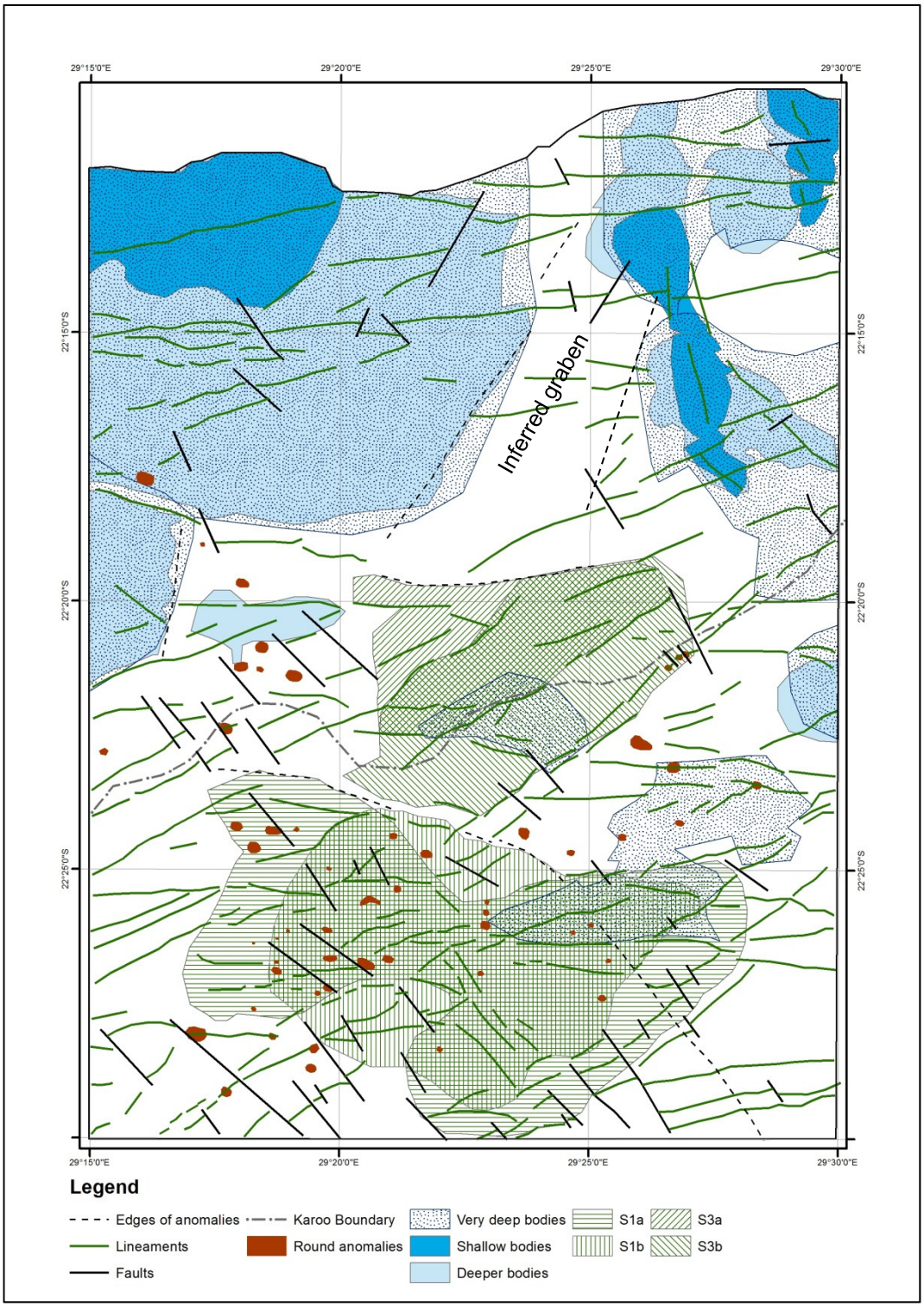


Figure 6.28. Compilation of the interpreted magnetic units and inferred dykes and faults from magnetic data and filtered magnetic data. S1a, S1b, S3a and S3b are inferred sills.

CHAPTER 7. Quantitative Interpretation

7.1. Preparing to model the magnetic anomalies

Magnetic data are ambiguous to model, since multiple variables influence the shape of the modelled anomaly and many different solutions can produce the same result. These variables are depth, susceptibility, shape and remanence. Depth affects the 'sharpness' of the anomaly. A very shallow body will cause a sharp short wavelength anomaly, while a deeper body will cause a longer wavelength anomaly. The magnetic susceptibility affects the amplitude of the anomaly, with larger susceptibilities resulting in larger anomalies. The remanent magnetic data influence the shape and size of the anomaly in many ways that will be discussed in the section **7.1.4** below. The geometry of the source also has an effect on the shape and size of the anomaly.

7.1.1. Modelling software

The profiles were modelled using the free 2.5D modelling software, Mag2DC (Cooper 1997). This software uses a Talwani type algorithm to calculate the anomaly. There may be up to 10 bodies in a model, each with up to 50 corners. Susceptibilities are measured in SI units and the anomaly in nT. Distances are measured in m or km. The software does both forward modelling and inversion to improve the fit of the calculated curve to the observed data. Inversion was used in the modelling once the fit of the calculated curve could no longer be improved manually.

7.1.3. Source body type and depth determination

The lineaments in the area are interpreted to be dolerite dykes. This is based on the fact that dolerite is present in the area in the form of outcropping dolerite sills (Figure 2.5). Further evidence is taken from core data from numerous boreholes drilled near Venetia that cut through dolerite and other boreholes drilled for coal exploration. The depths of the dykes are not precisely known, but it can be safely assumed that they are 50 m to 300 m deep based on the depths of boreholes drilled for coal exploration. These boreholes typically stop before they intersect dolerite (mostly when they encounter baked lithologies) since it is not favourable to coal grade.

Figure 7.1 shows the locations of boreholes in the study area overlain on the magnetic data. The depth to dolerite where encountered or the total depth of borehole is also shown on the map.

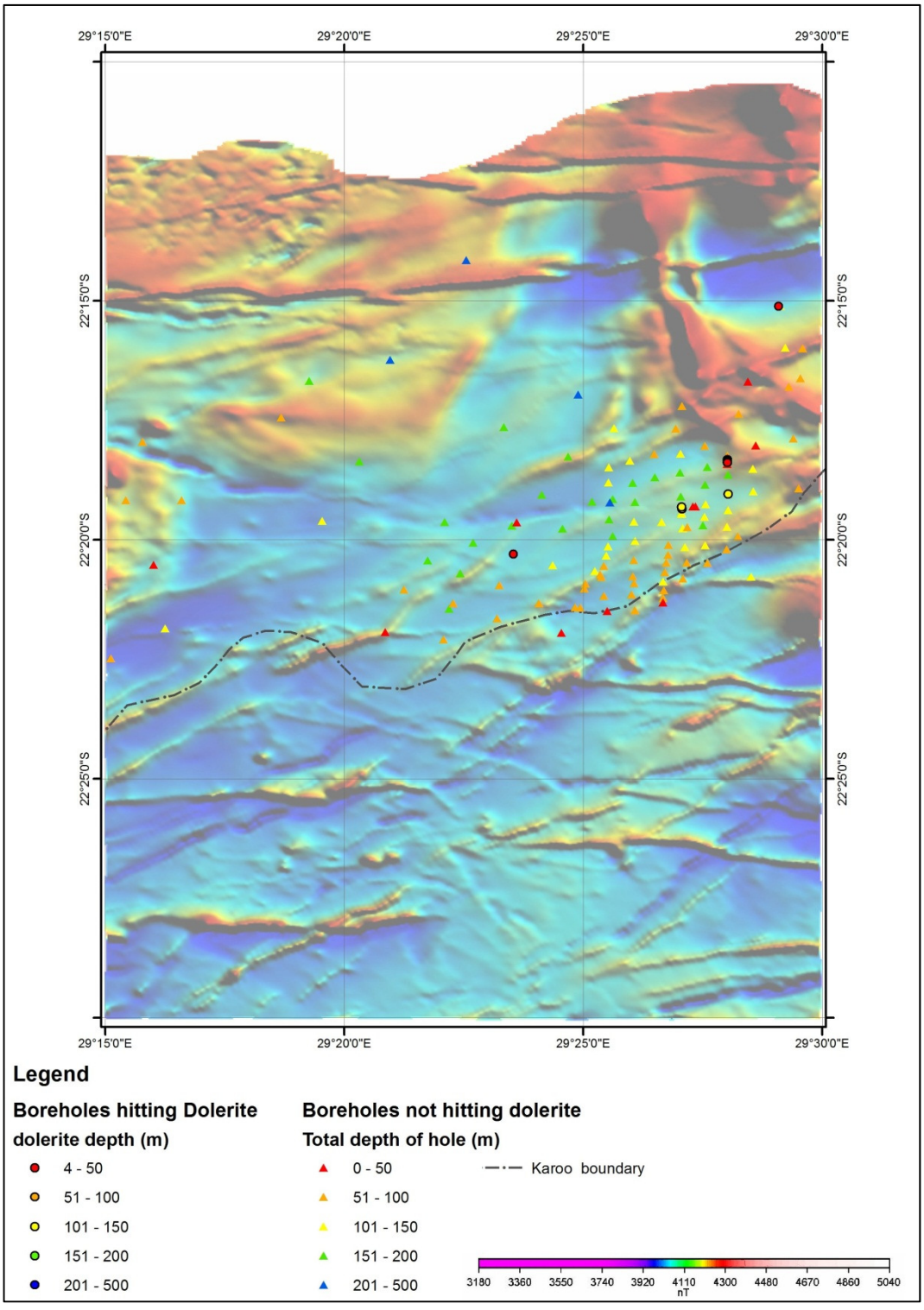


Figure 7.1. Borehole locations overlain on TMI image sunshaded from the north east at 45°. Triangles indicate boreholes that don't reach dolerite and circles indicate boreholes that intersect dolerite. Warm colours indicate shallow depth and cool colours deep depth.

It is clear that the majority of boreholes never encounter dolerite and the depths of these boreholes are mostly greater than 50 m. Many of these boreholes are near or above the magnetic anomalies caused by the dykes, thus the dykes are deeper than the total depth of the boreholes. The borehole logs used to create Figure 7.1 are included in Appendix II for completeness.

7.1.4. Physical Properties

The dykes in the area do not outcrop and as such their physical properties are unknown. In an attempt to constrain the range of physical properties, the entire range of susceptibility values for dolerite in South Africa (Maré and Tabane, 2004) was used as the available value range.

Magnetic susceptibility

Further complications to the modelling task are added with the large range of susceptibility values available for dolerite in South Africa (Maré and Tabane, 2004). These values range between 0.0000542 SI and 0.8574999 SI. There are, however no values for dolerite available near the study area. Thus there are no constraints available on the susceptibility.

The borehole logs for six boreholes located in a north-south trending line in the east of the study area (Figure 7.2) were available and are shown in Figure 7.3. Three of these boreholes encounter dolerite at a very shallow depth (± 5 m). Flight lines L565 and L570 cross the magnetic anomaly on which these boreholes are located (Figure 7.2). The data from these two flight lines will be modelled to better constrain the susceptibility values for dolerite in the area, since the depth is known.

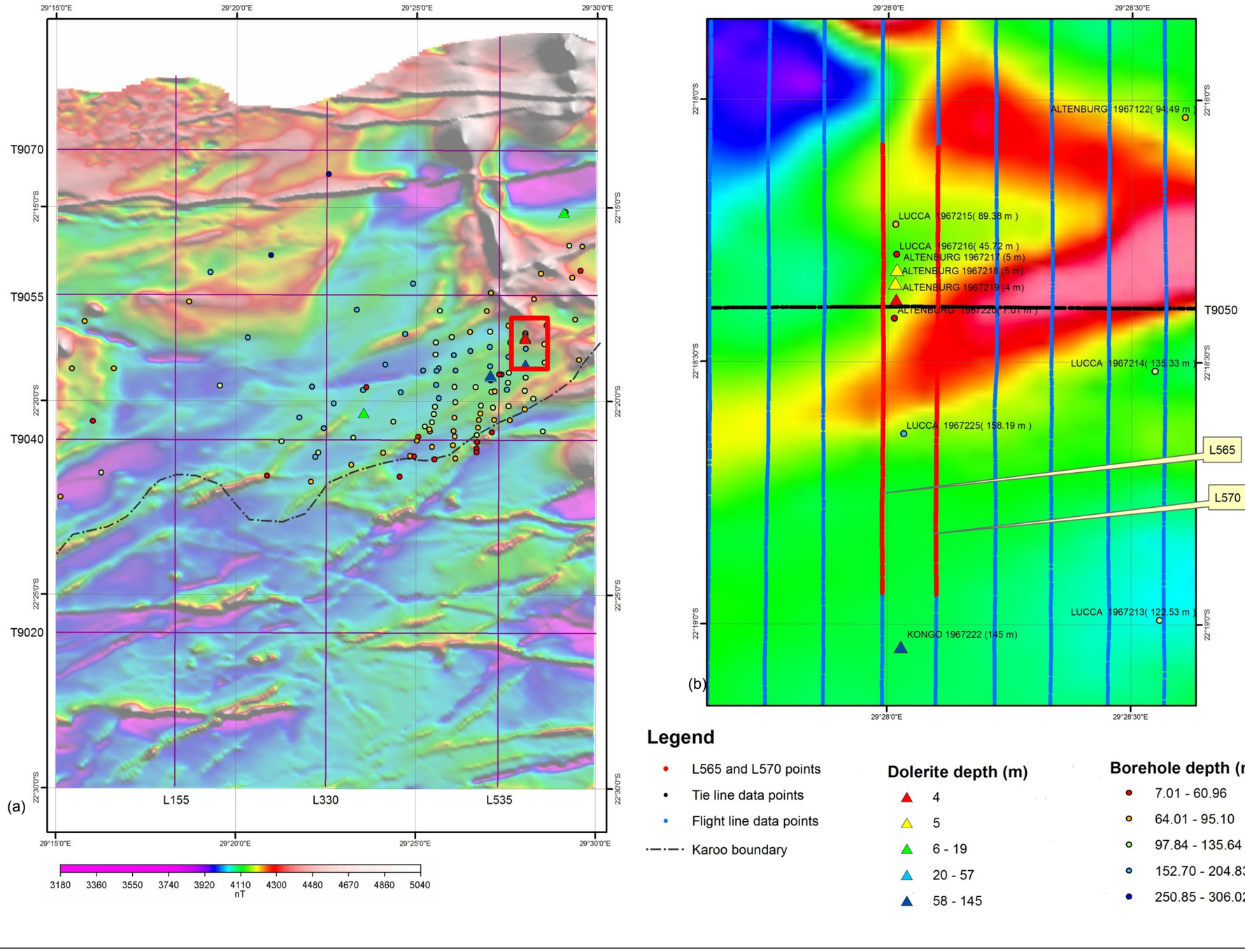


Figure 7.2. Total magnetic intensity data with the borehole locations and flight lines indicated (a): Triangles indicate boreholes that encounter dolerite. On the right (b) is a blow-up of the area around the boreholes (shown as red rectangle in map on left.). Portion of flight lines L565 (left) and L570 (right) that will be modelled are indicated in red and are either side of the row of boreholes that intersect dolerite.

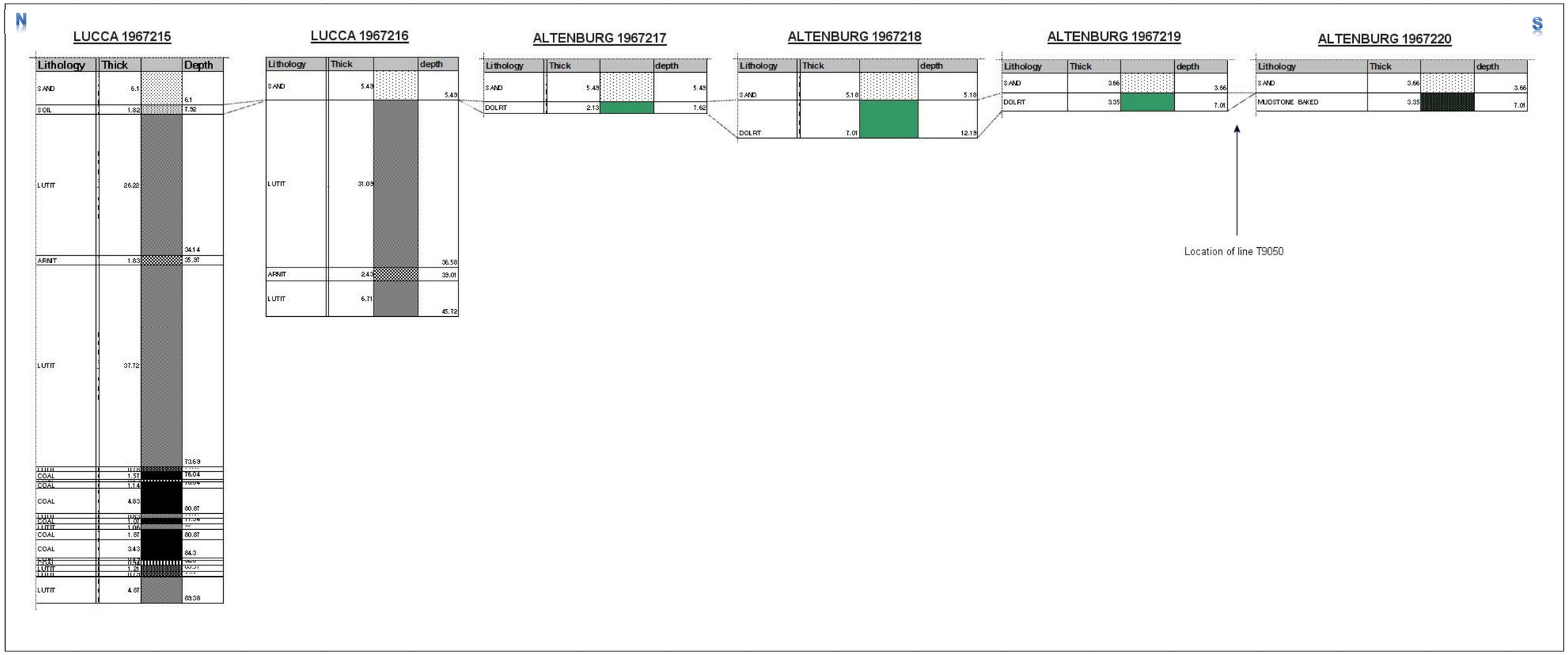


Figure 7.3. The logs for the 6 boreholes located on a north-south trending line of which 3 encounters dolerite (shown in green) at shallow depth. The thickness of the dolerite is unclear as drilling was stopped as soon as dolerite was encountered. (North is left and south is right). The location of tie line T9050 is indicated.

The profiles were modelled with susceptibility values 0.06 SI, 0.1 SI and 0.5 SI. The dolerite in the 3 boreholes is at least 3 meters thick. Figure 7.4 shows the model for a body with susceptibility of 0.5 SI. This results in a source body that is about 5 m deep and about 15 m thick in the north (where the boreholes are located).

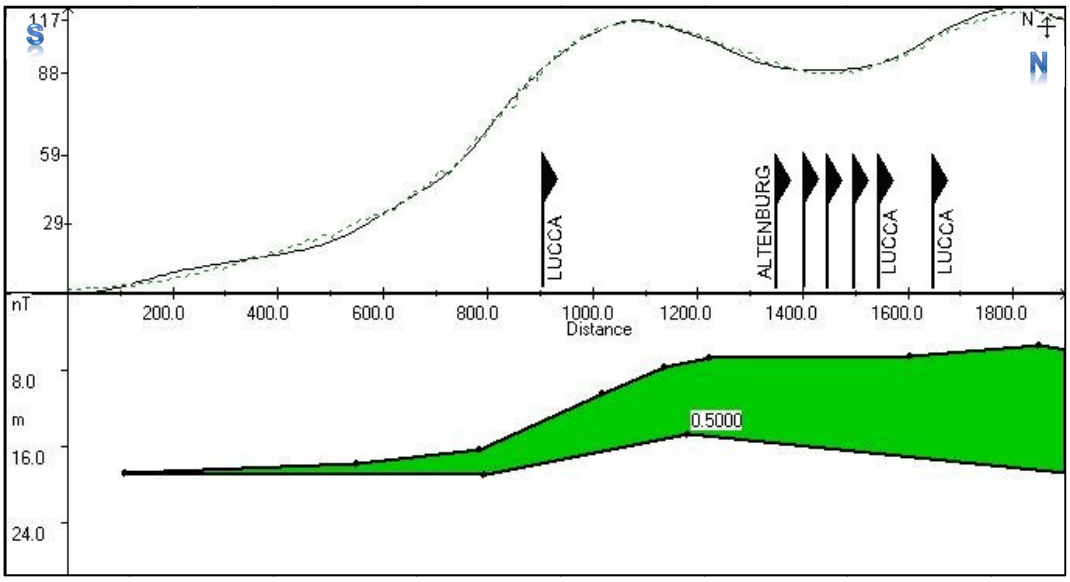


Figure 7.4. Flight line L565: A dolerite body modelled with a susceptibility of 0.5 SI, depth between 18 m and 5 m and thickness between a couple of cm and 15 m.

When the susceptibility is reduced to 0.1 SI, the required thickness of the body increases to about 35 m in the north (Figure 7.5 – note the depth scale). The southern part also needs to dip much steeper (120 m) for the calculated and measured fields to match.

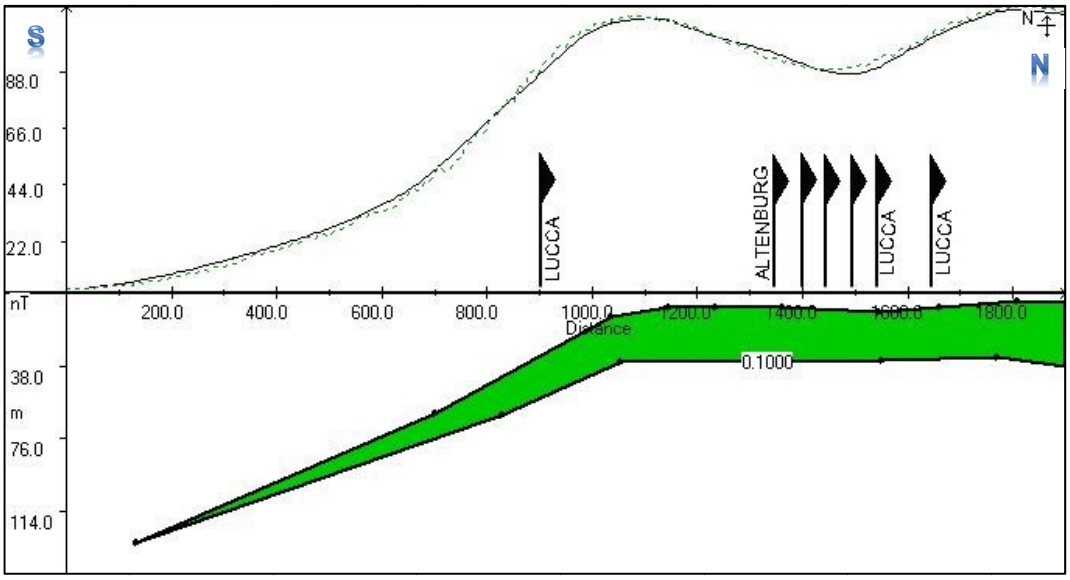


Figure 7.5. Flight line L565: A dolerite body modelled with a susceptibility of 0.1 SI, depth between 120 m and 5 m and thickness between a couple of cm and 35 m.

The susceptibility was lowered to 0.06 SI (Figure 7.6) and the resulting model shows a body at surface in the north and about 120 m at its deepest point in the south. The body is about 70 m thick where it is closest to the surface.

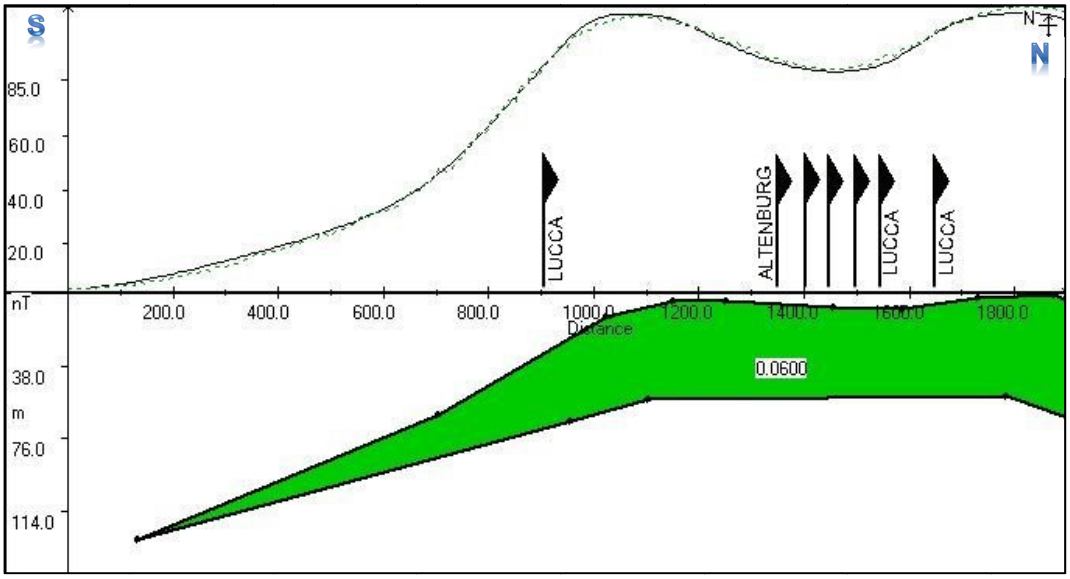


Figure 7.6. Flight line L565: A dolerite body modelled with a susceptibility of 0.06 SI, depth between 120 m and 0 m and thickness between a couple of cm and 70 m.

The flight line east of the row of boreholes is L570. A portion of this line was also modelled with susceptibilities 0.5 SI, 0.1 SI and 0.06 SI. These models are shown in Figure 7.7 to Figure 7.9. As with L565, the thickness of the source body increases from between 5 m and 16 m to between 30 m and 150 m with reduction in susceptibility. The depths at the shallowest points are all consistent with the borehole data and the thicknesses are all reasonable. Thus it would seem that for this particular dolerite body these values fall well within the range of susceptibility values that return reasonable modelling results.

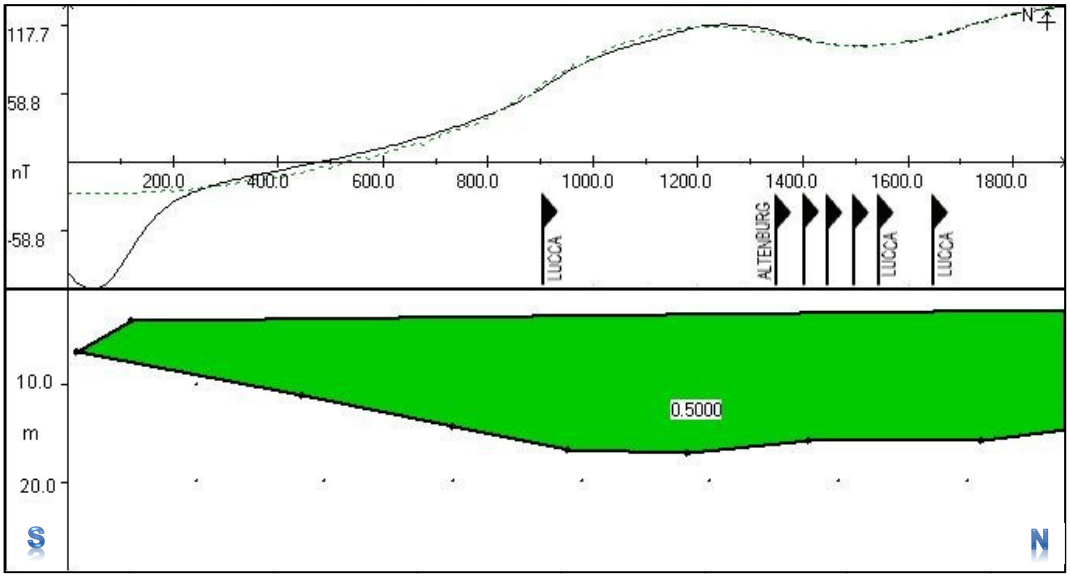


Figure 7.7. Flight line L570: A dolerite body modelled with a susceptibility of 0.5 SI, depth between 5 m and 3 m and thickness between 5 m and 16 m. The grid dots are spaced 10 m apart in depth.

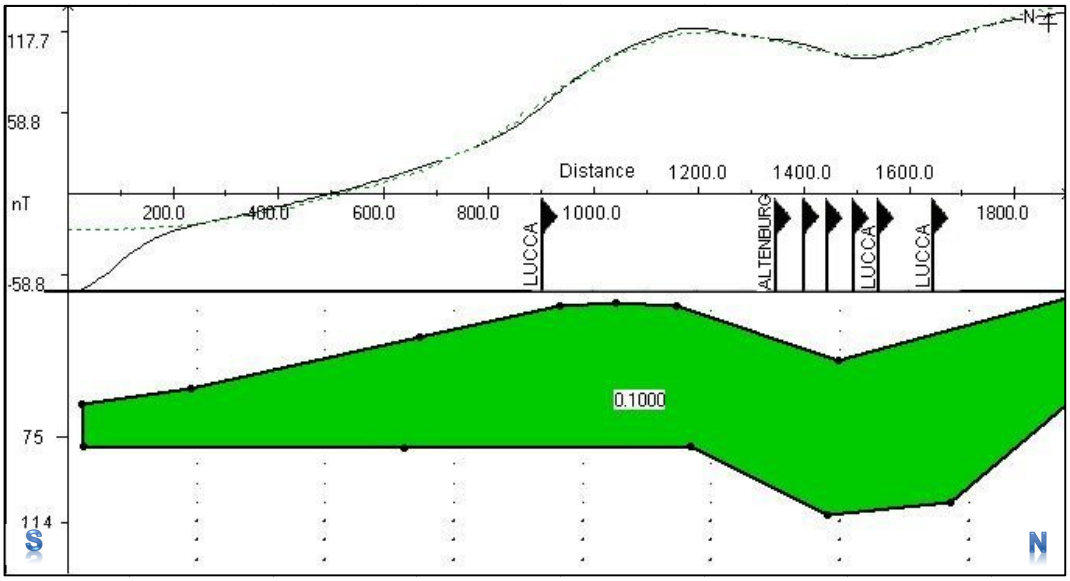


Figure 7.8. Flight line L570: A dolerite body modelled with a susceptibility of 0.1 SI, depth between 55 m and 3 m and thickness between 25 m and 60 m. The grid dots are spaced 10 m apart in depth.

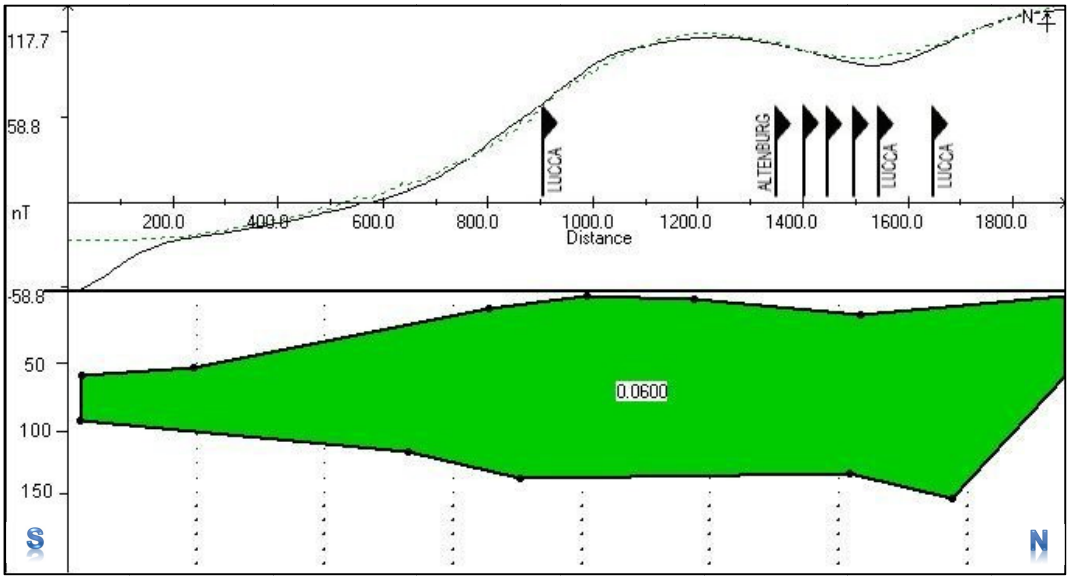


Figure 7.9. Flight line L570: A dolerite body modelled with a susceptibility of 0.06 SI, depth between 55 m and 3 m and thickness between 30 m and 150 m. The grid dots are spaced 10 m apart in depth.

7.2. Modelling of the linear magnetic anomalies

The objective of the modelling in Chapter 7 is to create closer constraints on the susceptibility values and depths to be used in Chapter 8 where the data from three flight lines; L155, L330 and L535 (Figure 7.10) and four tie-lines; T9020, T9040, T9055 and T9070 (Figure 7.10) will be modelled. The magnetic bodies (inferred dykes and plugs) that are intersected by these flight lines are labelled in Figure 7.10 and twenty-two short profiles were chosen across these labelled bodies. Data from the magnetic grid were extracted along these profiles and modelled in detail. Since the flight lines and tie-lines are very long, the models along them cannot be very detailed, thus the need for shorter, more detailed models across the relevant bodies.

The profile lines across many of the dykes are not as longs as one would like them to be, this is due to the fact that there are many dykes and they are quite close together. Before one can reach the background data, the influence of the next dyke is already visible. This is also the reason why many of the models have discrepancies on the edges – the effects of adjacent dykes on the observed data that cannot be modelled within the profile. In some instances a profile is taken across more than one dyke, purely because it is not possible to extract only the one dyke, they are way too close together. The profiles should ideally be perpendicular to the dyke, but since the dykes are not always parallel to each other, this is not possible, and the best average across all the dykes in the profile is chosen.

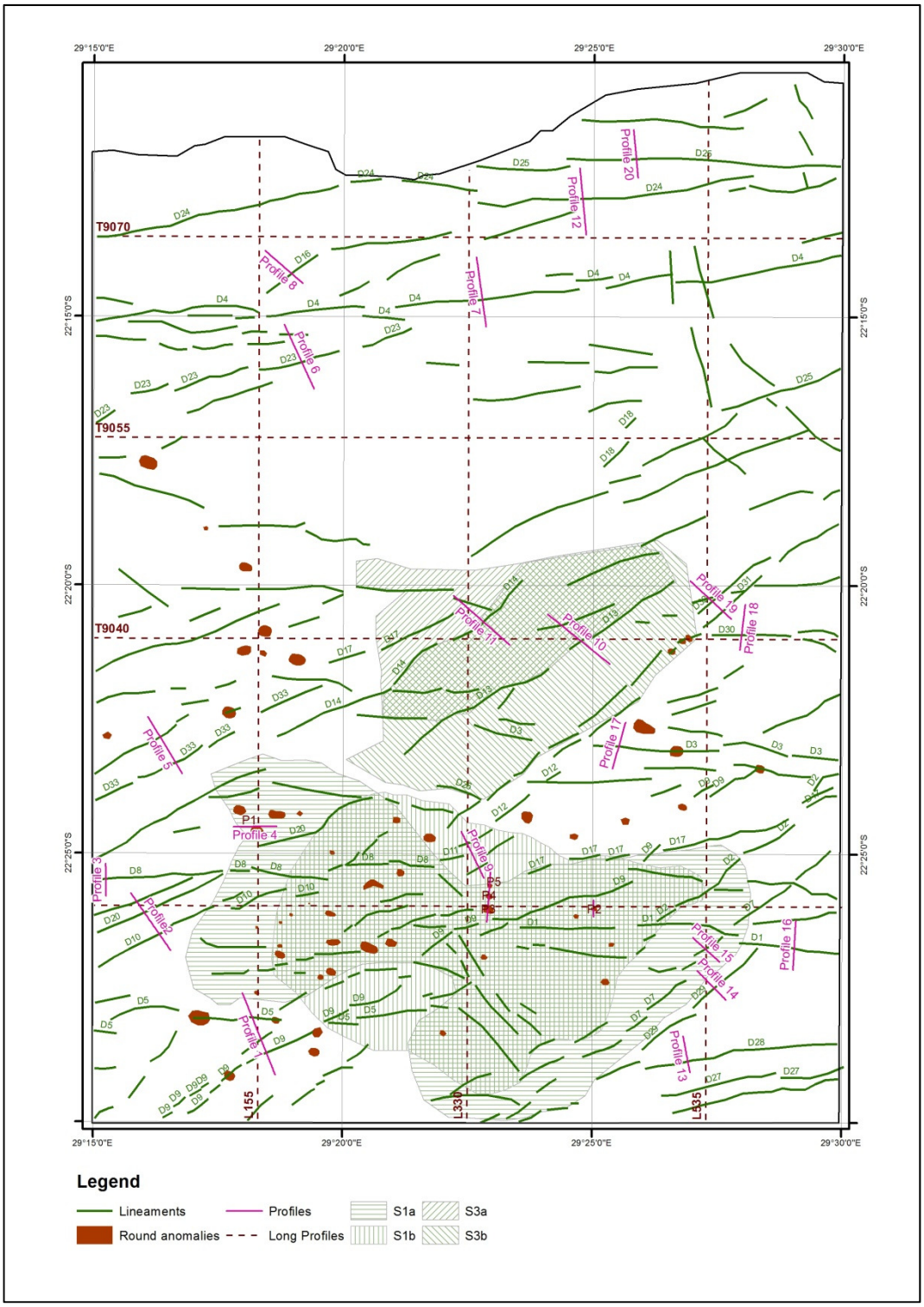


Figure 7.10. Locality map showing the locations of profiles 1 to 22, the locations of flight lines that will be modelled in chapter 8 and the inferred dykes, plugs and sills that are intersected by these profiles and flight lines.

7.2.1. Profile 1

Profile 1 (Figure 7.11) crosses the inferred dykes labelled D9 and D5 as well as the inferred sill labelled S1, from south to north. These features are intersected by flight line L155 in the southwestern part of the study area, and therefore the profile was chosen to be modelled. The northern D9 is clearer on the first vertical derivative data than on the TMI data.

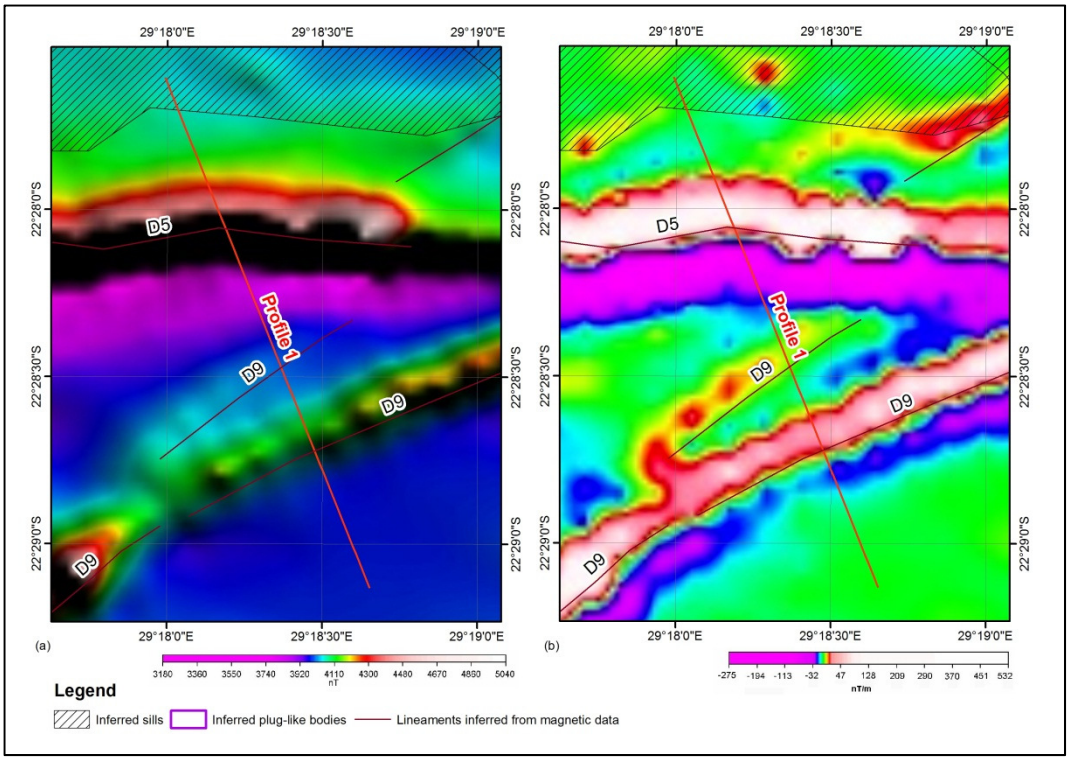


Figure 7.11. Profile 1 displayed over the magnetic TMI data (left) and the first vertical derivative data (right).

Inferred dyke D9 is modelled with a susceptibility of 0.03 SI and for the southern occurrence it has a depth of 19 m with thickness of 225 m, while the northern occurrence of D9 has a depth of 91 m and thickness of 120 m (see Figure 7.12). D5 has a susceptibility of 0.045 SI, a depth of 3 m and a width of 275 m. The inferred sill S1 is modelled with a susceptibility of 0.01 SI and a depth of 410 m. The dykes can all fit the data when modelled vertically.

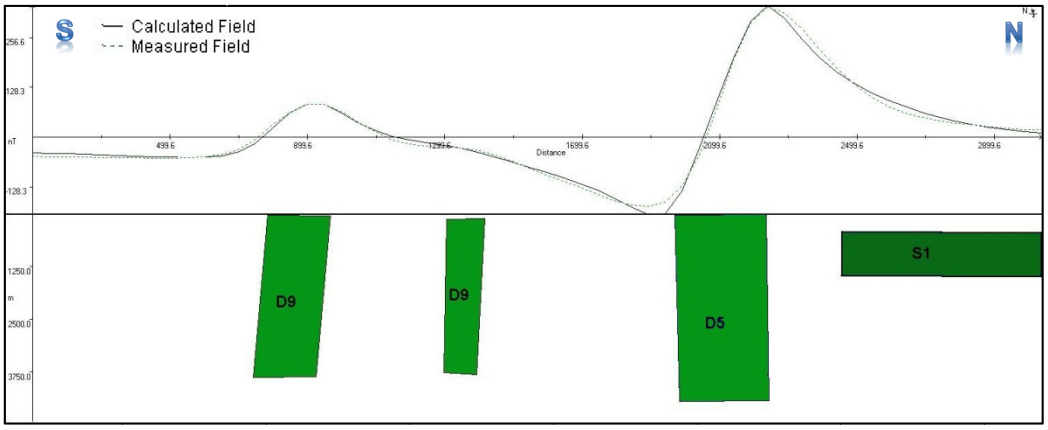


Figure 7.12. Profile 1: Model displaying dykes D9 and D5 as well as sill S1.

7.2.2. Profile 2

Figure 7.13 shows profile 2 striking northwest and crossing inferred dykes D10 and D20 as well as an unnamed dyke north of D20. On the left the profile is overlain on the magnetic data and on the right over the first vertical derivative data. A positive anomaly between D10 and D20 is visible on the first vertical derivative data. This body is not clear on the magnetic data.

The profile is modelled with three remanent dykes and a positively induced dyke between D10 and D20 (Figure 7.14). The remanent dykes have susceptibility of 0.01 SI. D10 is 65 m deep and 106 m wide while D20 is 94 m deep and 32 m wide. The unnamed dyke north of D20 has a depth of 125 m and width of 40 m. The positive dyke between D10 and D20 is modelled to have a susceptibility of 0.007 SI, width of 172 m and depth of 43 m. The remanence values for the three remanent dykes are given in Table 7.1.

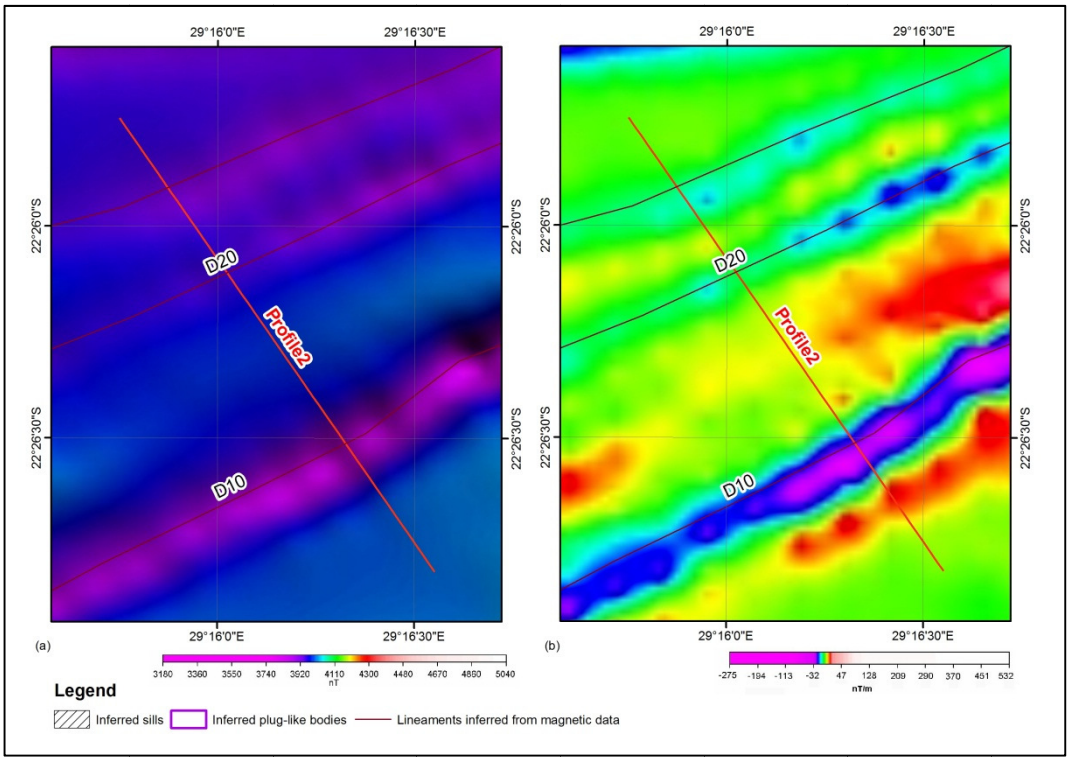


Figure 7.13. Profile 2 displayed over the magnetic TMI data (left) and the first vertical derivative data (right).

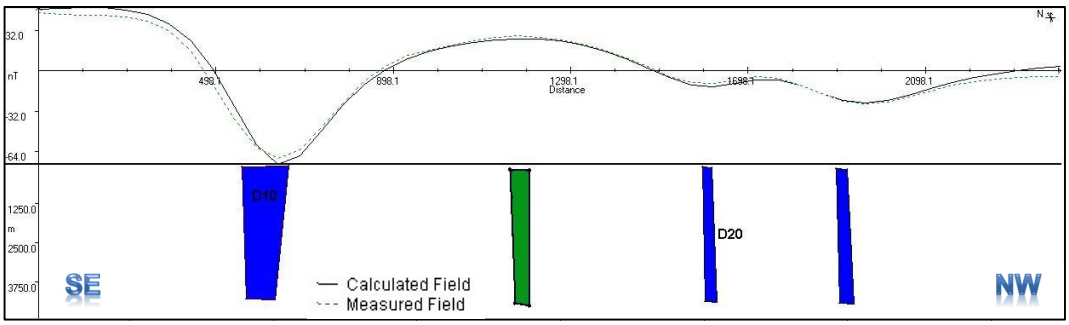


Figure 7.14. Profile 2: Model displaying remanent dykes D10 and D20 as well as two unnamed dykes, a positive dyke between D10 and D20 and a remanent dyke similar to D20 just north of D20.

7.2.3. Profile 3

Profile 3 is a north trending line across inferred dyke D8 (Figure 7.15). The east-west trending D8 is intersected by the southern portion of flight line L155 (Figure 7.10). It stops

just short of flight line L330 (Figure 7.10). The first vertical derivative data (on the right of Figure 7.15) shows a slight positive anomaly south of the dyke. This is not clear on the magnetic data.

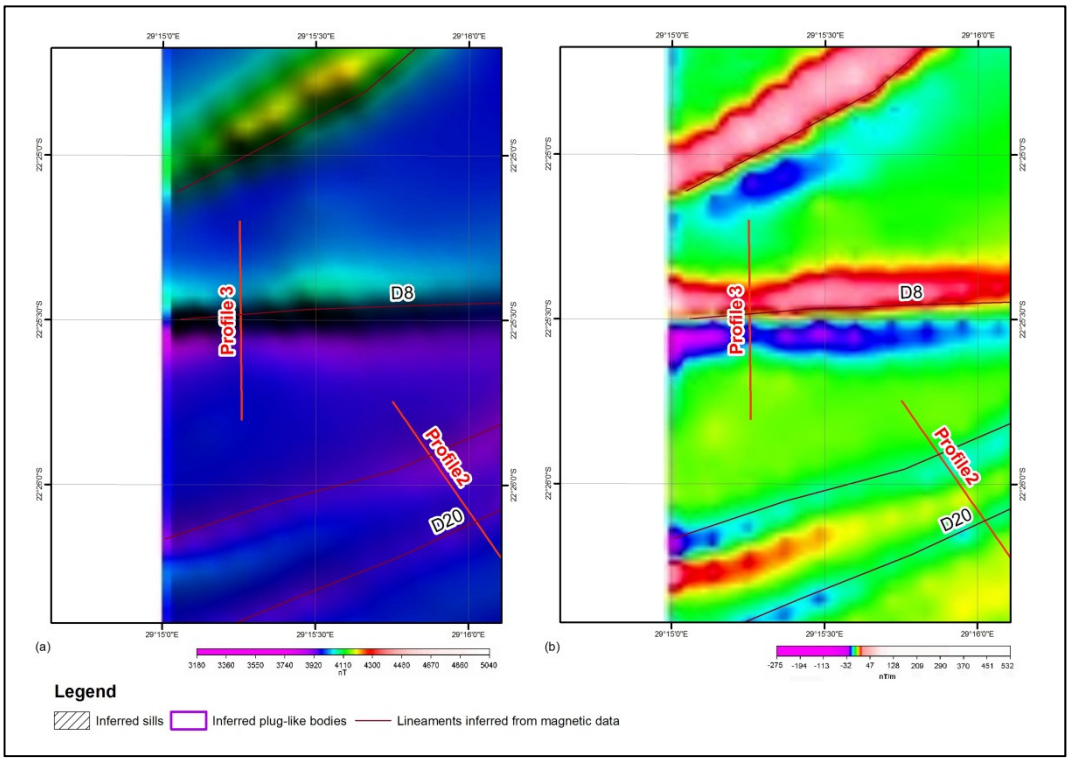


Figure 7.15. Profile 3, zoomed out to illustrate the proximity to dykes in north and the south.

The profile was not extended either north or south due to the proximity to other dykes. If the profile went any further north the influence of the dyke north of D8 would be very prominent on the observed data, the same for the dyke to the south (just north of D20 on Figure 7.15). Figure 7.16 shows the magnetic and first vertical derivative data directly around Profile 3.

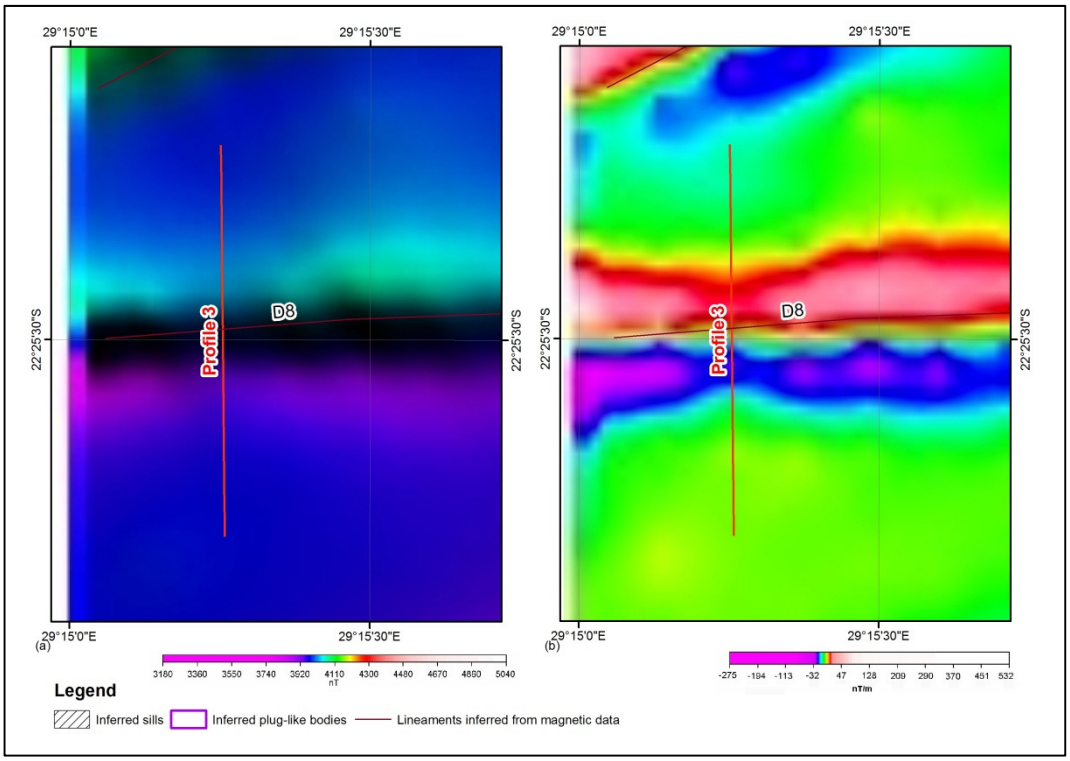


Figure 7.16. Profile 3 displayed over the magnetic TMI data (left) and the first vertical derivative data (right).

The model for profile 3 is shown in Figure 7.17. It consists of a vertical dyke, D8 with susceptibility 0.015 SI, depth 33 m and width 102 m. The discrepancy in the south is probably due to a body south of the dyke that reaches beyond the profile and is therefore not part of the model.

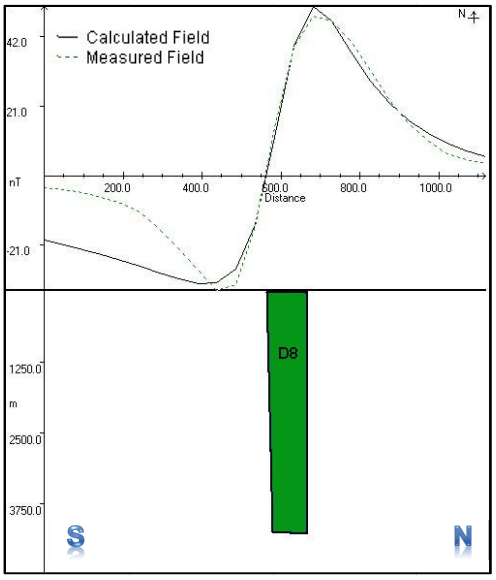


Figure 7.17. Profile 3: Model displaying inferred dyke D8. In the south a slight positive anomaly is visible on the first vertical derivative. This is probably the reason for the calculated and measured fields not matching in the south.

7.2.4. Profile 4

Profile 4 is an east to west striking profile across inferred plug P1 and sill S1. This plug, P1, falls on the southern portion of flight line L155 (Figure 7.10), and the physical properties obtained from this model will be used in chapter 8 to model the flight line. The first vertical derivative data (right hand side of Figure 7.18) does not show more detail than the magnetic data. The inferred sill S1 reaches ¾ of the way to the west.

The model for this profile can be seen in Figure 7.19. The inferred sill S1 has a susceptibility of 0.01 SI (as for profile 1) and is modelled to be 51 m deep. The inferred plug, P1 has a susceptibility of 0.06 SI, depth of 108 m and width of 200 m. It is modelled to dip towards the west.

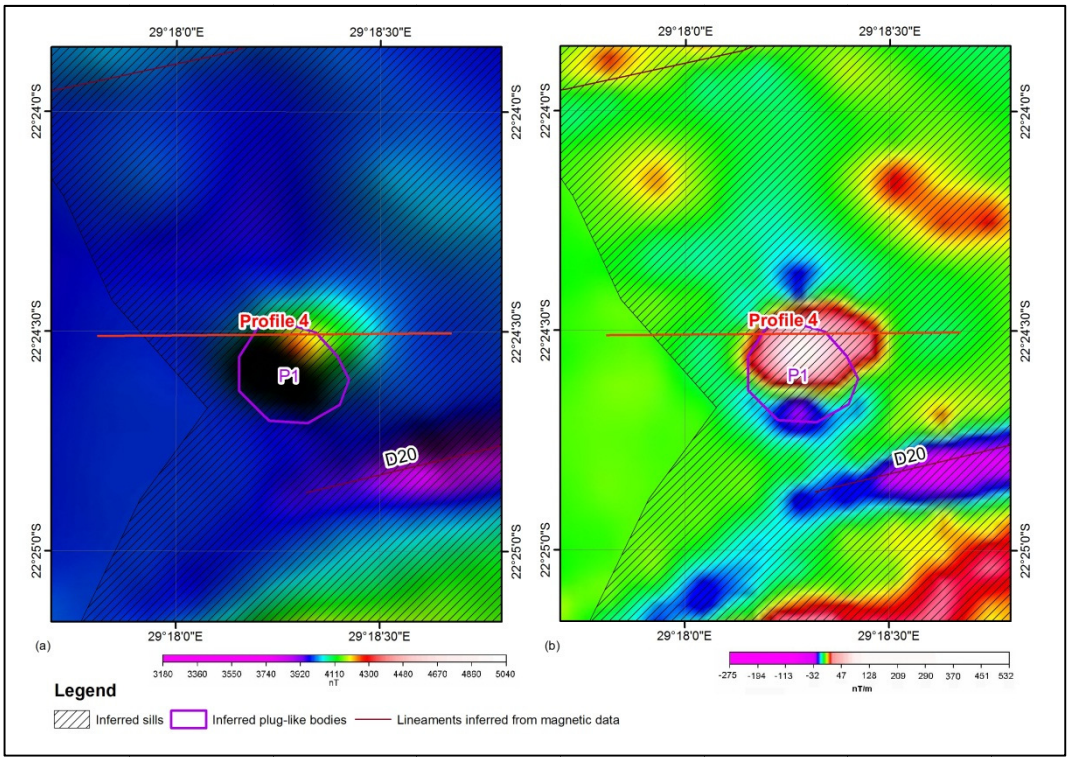


Figure 7.18. Profile 4 displayed over the magnetic TMI data (left) and the first vertical derivative data (right).

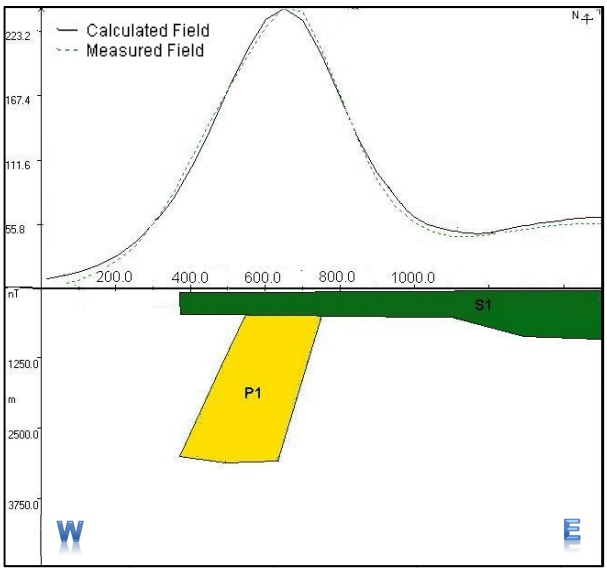


Figure 7.19. Profile 4: Model depicting P1 dipping to the west and S1 over the eastern portion of the profile. The offset between calculated and measured fields in the east is due to the sill extending beyond the profile and the model not.

7.2.5. Profile 5

Profile 5 is a north-northwest striking line across two inferred dykes, D33 in the south and an unnamed dyke in the north. There is a remanently magnetised dyke visible on the first vertical derivative data, just south of the profile (Figure 7.20). Flight line L155, which will be modelled in chapter 8 intersects this northeast trending dyke D33 in the south-eastern portion of the study area (Figure 7.10).

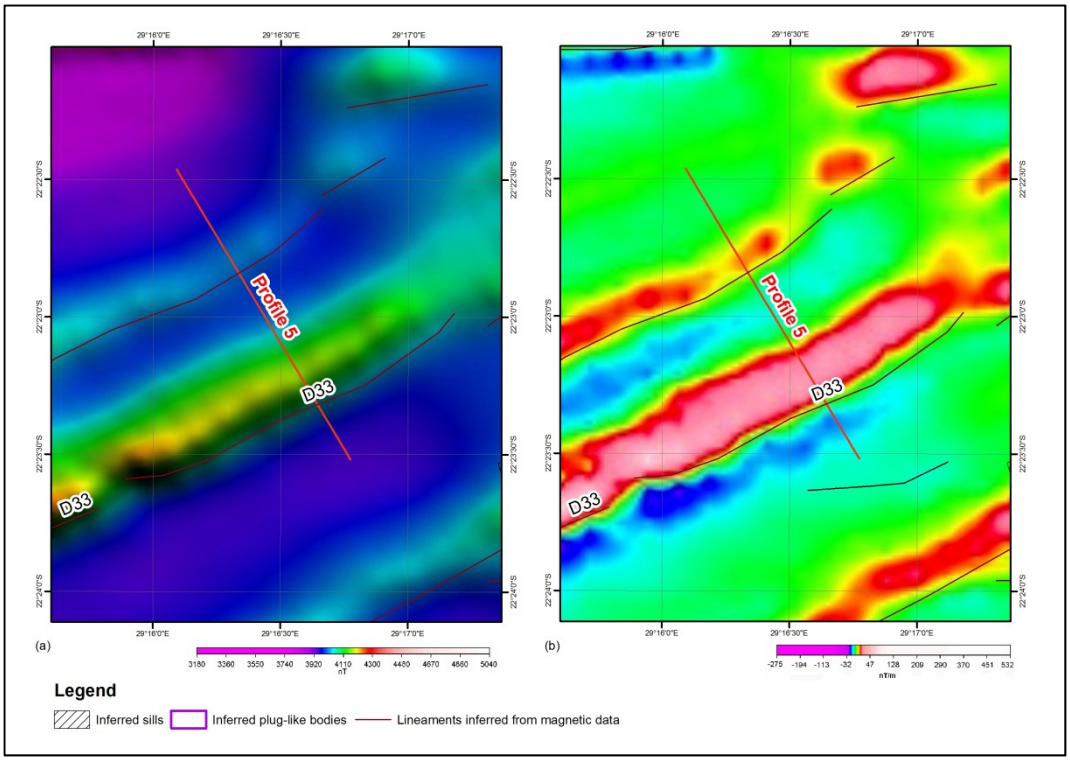


Figure 7.20. Locality map of profile 5 showing the proximity of a remanently magnetized dyke to the south east of the profile, indicated on the first vertical derivative data (b).

Figure 7.21 shows the profile overlain on the magnetic data (left) and the first vertical derivative (right). Both data images show the two dykes clearly.

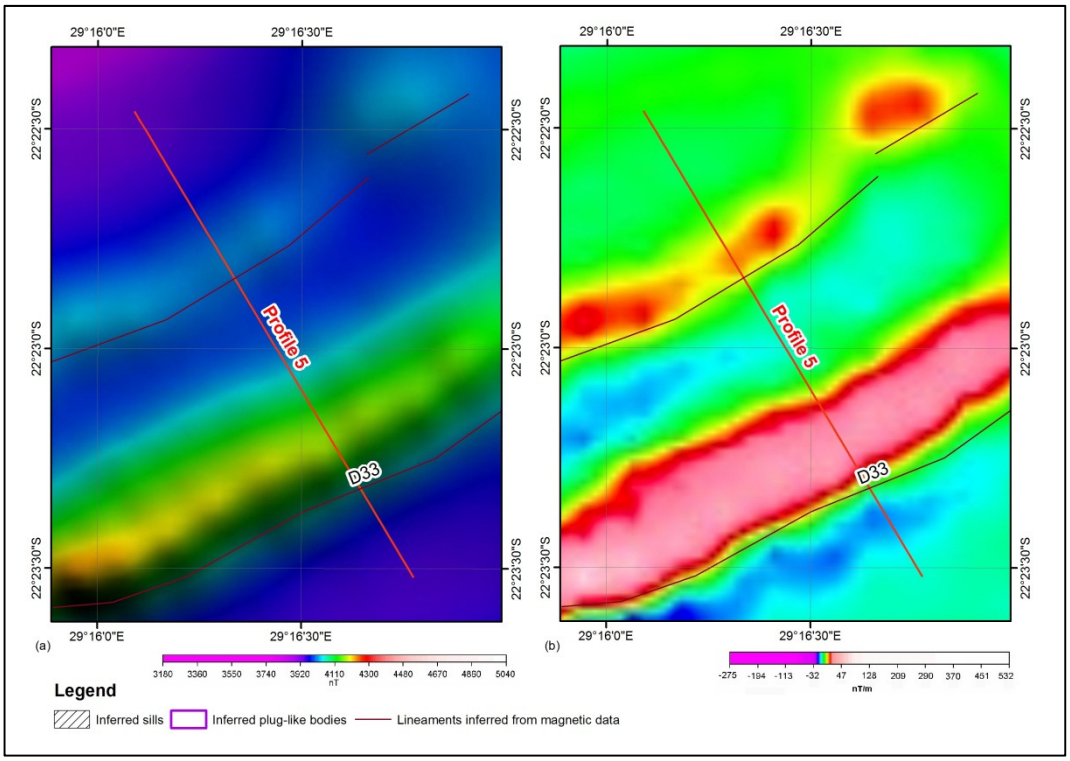


Figure 7.21. Profile 5 displayed over the magnetic TMI data (left) and the first vertical derivative data (right).

The model for profile 5 is shown in Figure 7.22 and comprises two almost vertical dykes. D33 is modelled as a 455 m wide dyke with susceptibility 0.02 SI that is 55 m below the surface. About 600 meters north of D33 another dyke is modelled with the same susceptibility, but quite a bit narrower at 125 m and at a depth of 130 m. The discrepancy between the modelled field and the observed field in the south is due to the effects of a remanently magnetised dyke just south of the profile (see Figure 7.20).

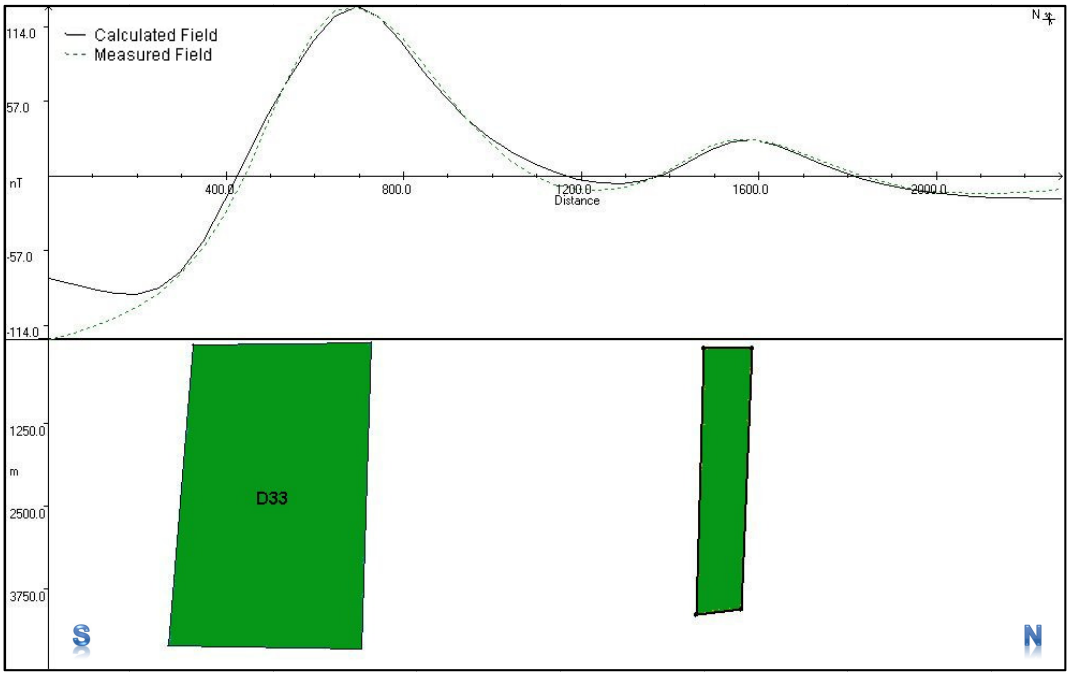


Figure 7.22. Profile 5: Model depicting inferred dyke D33 and an unknown dyke just north of it.

7.2.6. Profile 6

Profile 6 is a north-northwest trending line across the inferred dyke labelled D23 in Figure 7.10. On the magnetic data (Figure 7.23a) it seems to cross only D23 and another dyke north of D23. On the first vertical derivative data (Figure 7.23b), however, it is clear that there is another dyke south of D23 as well as a remanently magnetised dyke north of D23.

This profile was extracted and modelled to provide susceptibility values for the modelling of flight line L155 that intersects D23, an east-northeast trending dyke, in the northern part of the study area (Figure 7.10).

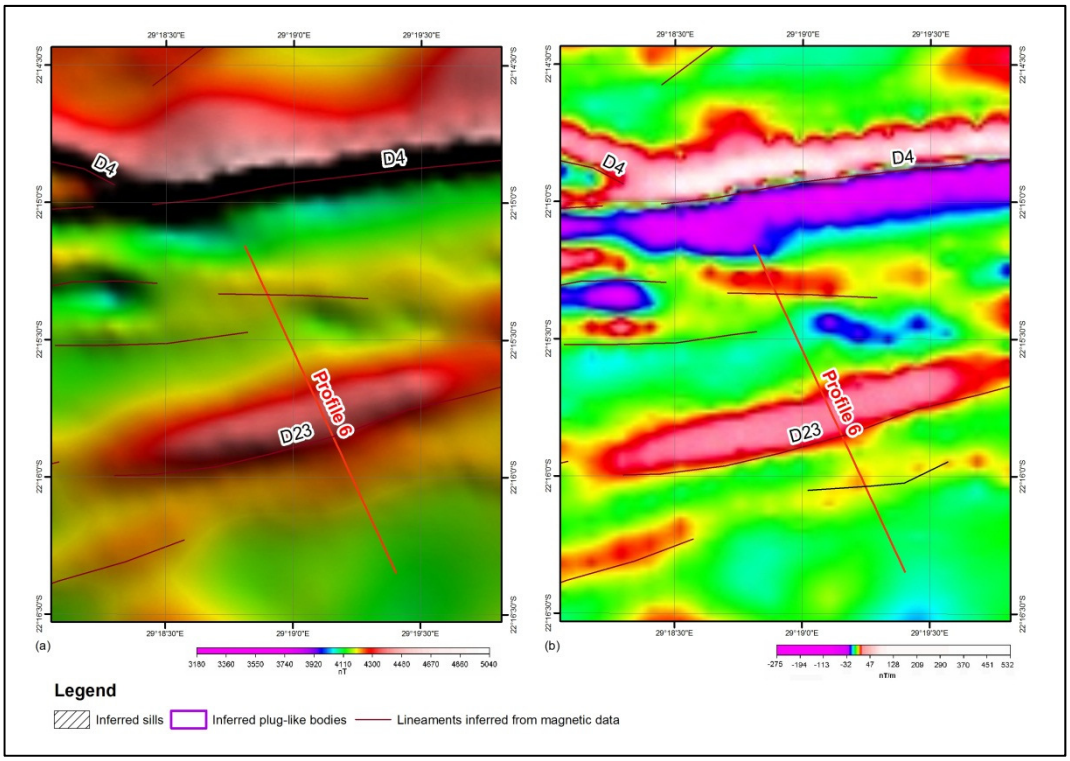


Figure 7.23. Location map of profile 6 showing the proximity of D4 to the northern end of the profile.

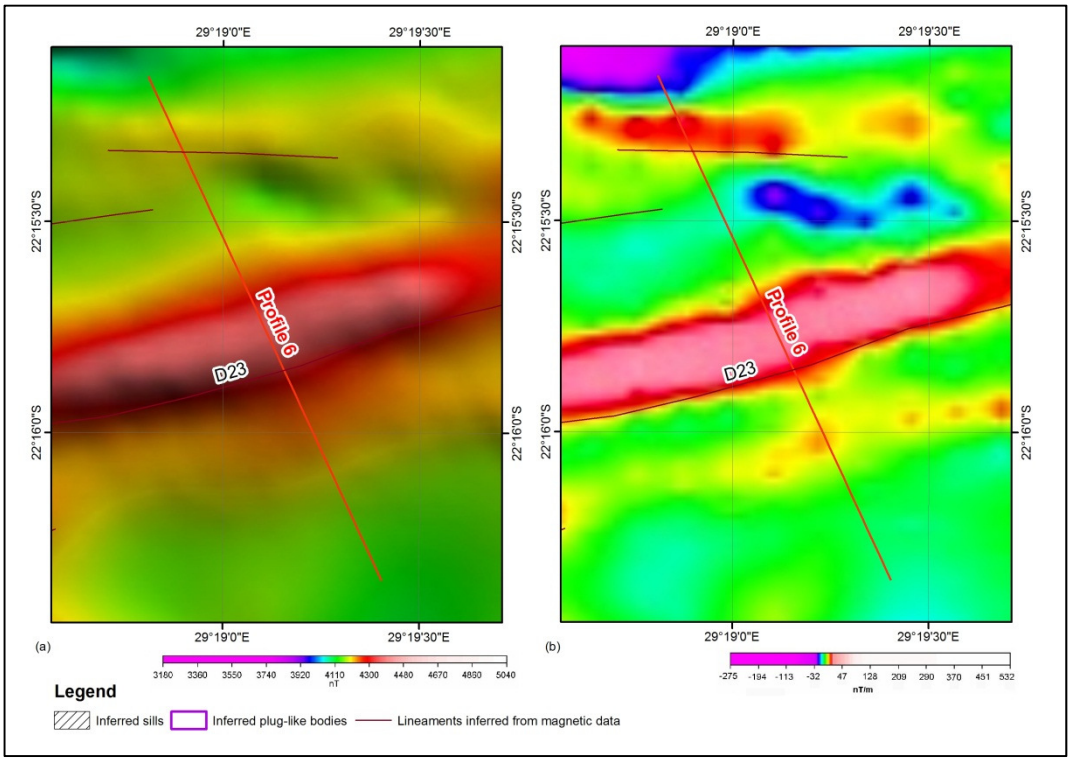


Figure 7.24. Profile 6 displayed over the magnetic TMI data (a) and the first vertical derivative data (b).

The model for profile 6 is shown in Figure 7.25. South of D23 is a broad dyke with a susceptibility of 0.0635 SI, a depth of 408 m and a width of 268 m. Dyke D23 is a near-vertical dyke with a susceptibility of 0.1 SI at 217 m depth and it is modelled to be 49 m wide. The remanently magnetised dyke north of D23 has a susceptibility of 0.0075 SI, is 452 m deep and 72 m wide. The discrepancy in the northern edge of the profile is due to the influence of the nearby dyke D4 just north of the profile (Figure 7.23).

The remanence values for the dyke north of D23 on profile 6 are given in Table 7.1

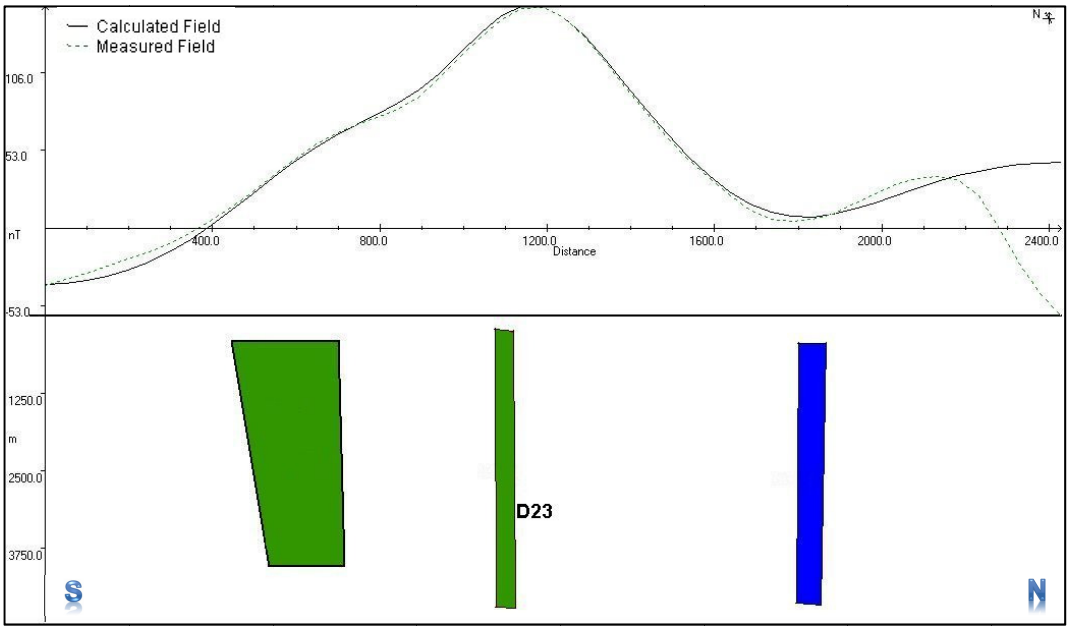


Figure 7.25. Profile 6: Model depicting dyke D23 and two dykes, one south and a remanent one north of it.

7.2.7. Profile 7

Profile 7 is located in the north and centre of the study area. It was chosen to model dyke D4, an east-west trending dyke that is intersected by flight lines L155, L330 and L535 (Figure 7.10). On the magnetic data (Figure 7.26a) it appears that the profile only cuts

across D4, but on the first vertical derivative (Figure 7.26b) a second dyke north of D4 is more apparent.

Dyke D4 is modelled as a 361 m wide near-vertical dyke at 44 m deep with a susceptibility of 0.038 SI (Figure 7.27). The second dyke north of D4 is much deeper at 574 m and only 36 m wide. It has a susceptibility of 0.01 SI in this model.

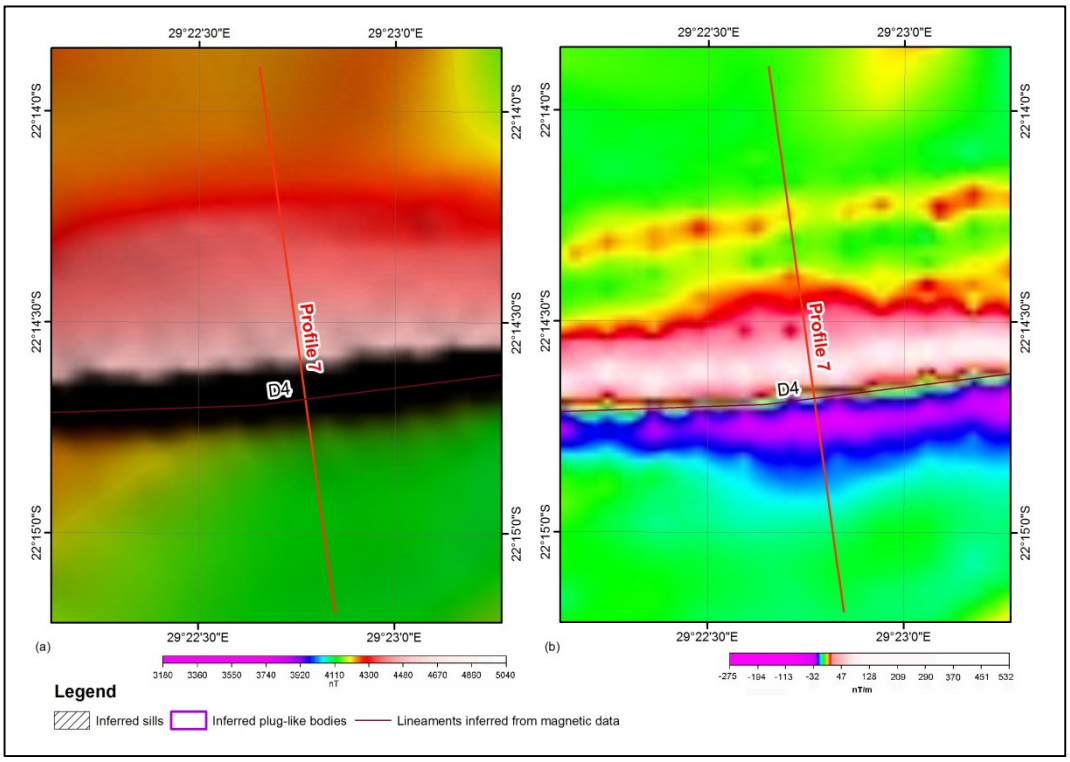


Figure 7.26. Profile 7 displayed over the magnetic TMI data (a) and the first vertical derivative data (b).

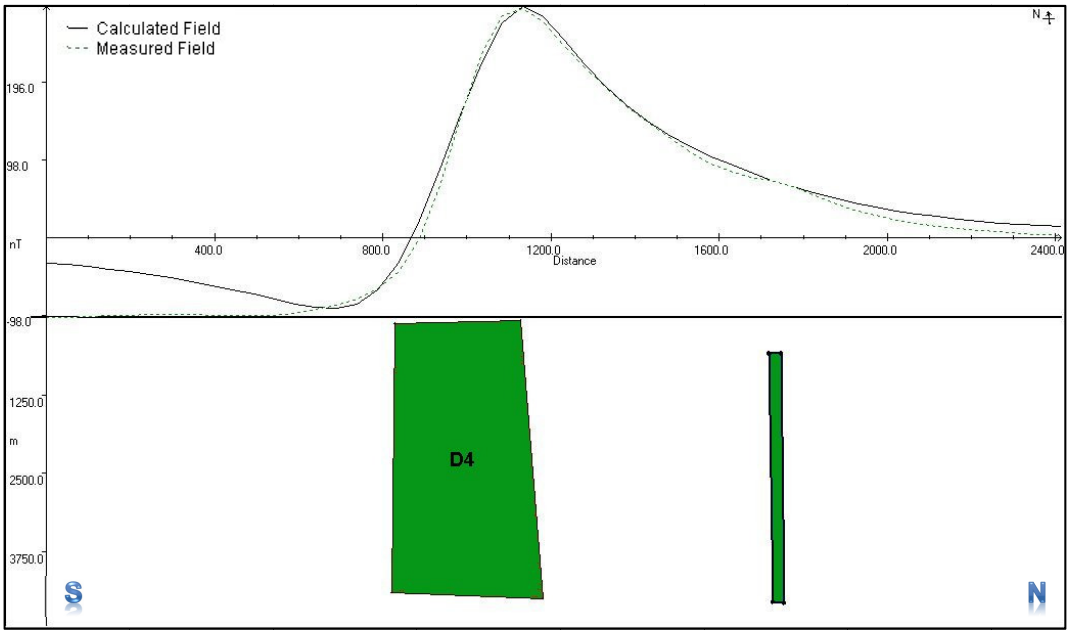


Figure 7.27. The model of profile 7 showing D4 and a second dyke north of D4.

7.2.8. Profile 8

Profile 8, a northwest trending profile in the north-western portion of the study area (Figure 7.10), was chosen to model dyke D16, which will feature in the modelling of L155 in chapter 8. At first glance it seems that there are only two northeast trending dykes intersected by profile 8, but on closer inspection of both the magnetic data (Figure 7.28a) and the first vertical derivative data (Figure 7.28b), it appears that there may be a remanently magnetised plug located between the two dykes.

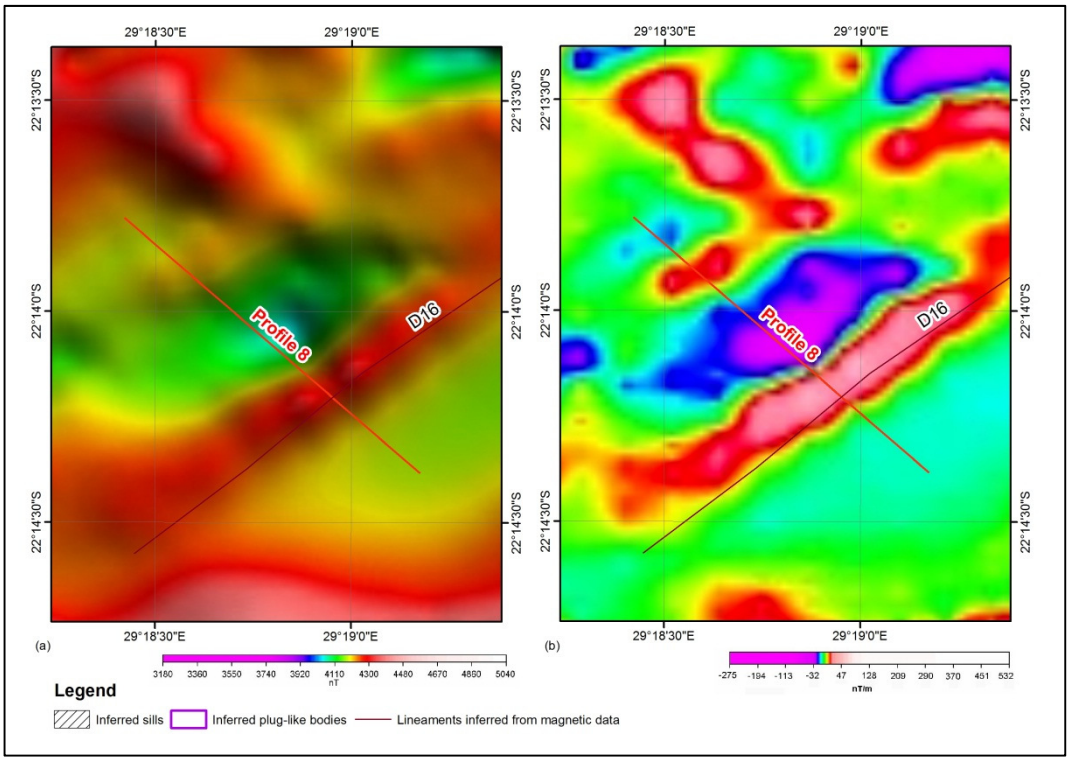


Figure 7.28. Profile 8 displayed over the magnetic TMI data (a) and the first vertical derivative data (b).

Dyke D16 is modelled as a slightly northwest dipping dyke (Figure 7.29) with susceptibility of 0.0315 SI, a depth of 39 m and width of 267 m. The remanently magnetised plug-like body just northwest of D16 has susceptibility of 0.01 SI, 42 m in diameter and is 124 m deep. The remanence values for this plug are given in Table 7.1. The second dyke on the profile has a susceptibility of 0.01, is 28 m deep and 310 m wide.

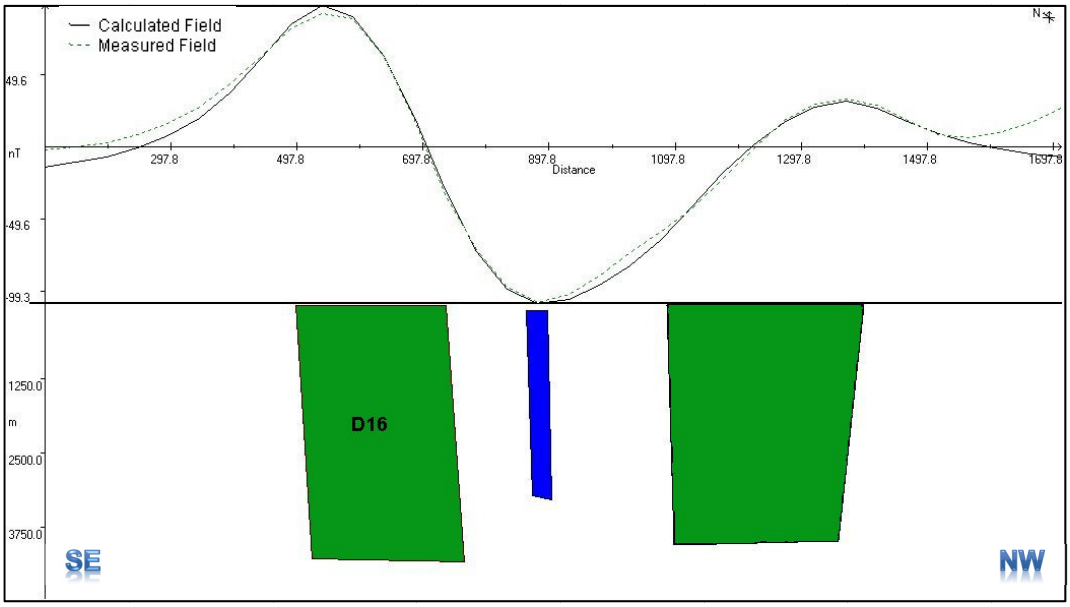


Figure 7.29. The model of profile 8 showing dyke D16, a remanent plug and another dyke north of it.

7.2.9. Profile 9

Profile 9 intersects two northeast trending dykes, one of which is labelled D12 (Figure 7.10). It also cuts across the very tip of the east-west trending remanently magnetised dyke, D11. Figure 7.30 is a locality map showing the proximity of the edge of a sill and a northeast trending, unnamed dyke to the northern edge of the profile.

All three dykes are visible on the magnetic data (Figure 7.31a), but the effect of D11 is clearer on the first vertical derivative data (Figure 7.31b). The flight line L330 cuts across D16 in the southern central portion of the study area.

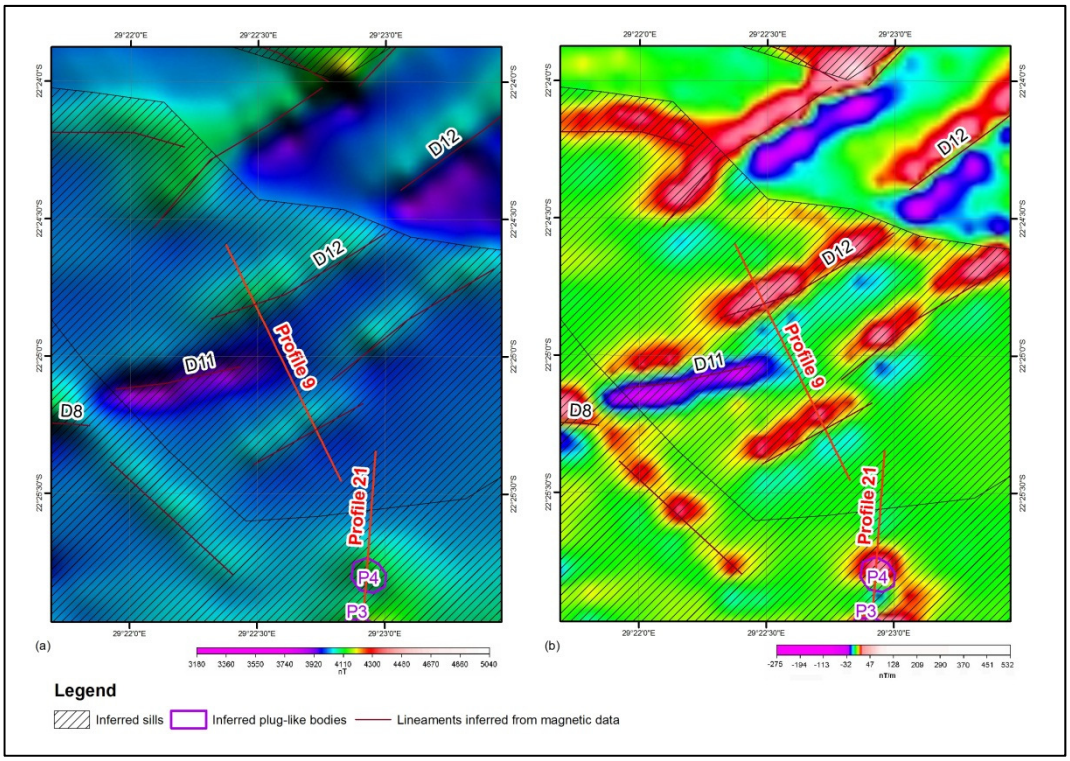


Figure 7.30. Locality of profile 9 showing the proximity of the edge of a sill and a northeast trending dyke in the north as well as the effect of the plug P4 in the south.

Both positive anomalies on profile 9 are modelled as dykes with a susceptibility of 0.02 SI. D12 is shallower, at 21 m deep while the second dyke is 45 m deep and D12 is 190 m wide, while the southern dyke is 96 m wide. The remanently magnetised dyke has a susceptibility of 0.01 SI, is 75 m deep and 36 m thick. The remanence values are given in Table 7.1. The discrepancy in the north between the measured field and the calculated field is due to the negative portion of the anomaly created by the northeast trending dyke and the discrepancy in the south is due to the effects of plug P4 on the measured field.

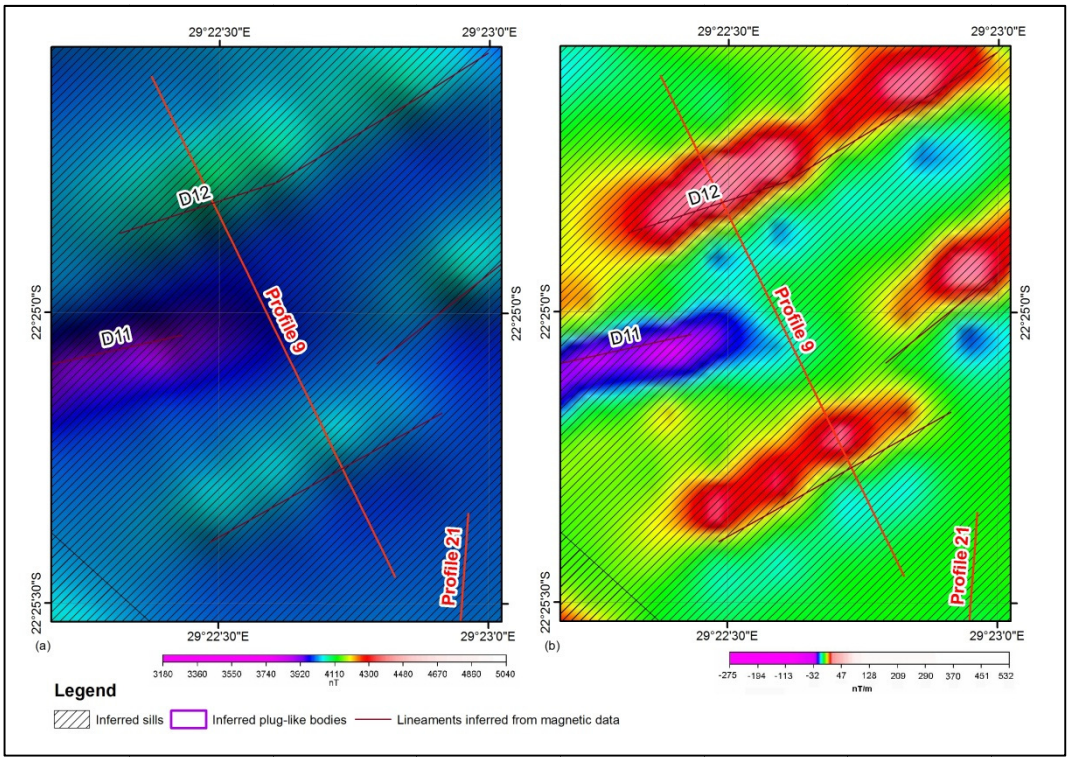


Figure 7.31. Profile 9 displayed over the magnetic TMI data (a) and the first vertical derivative data (b).

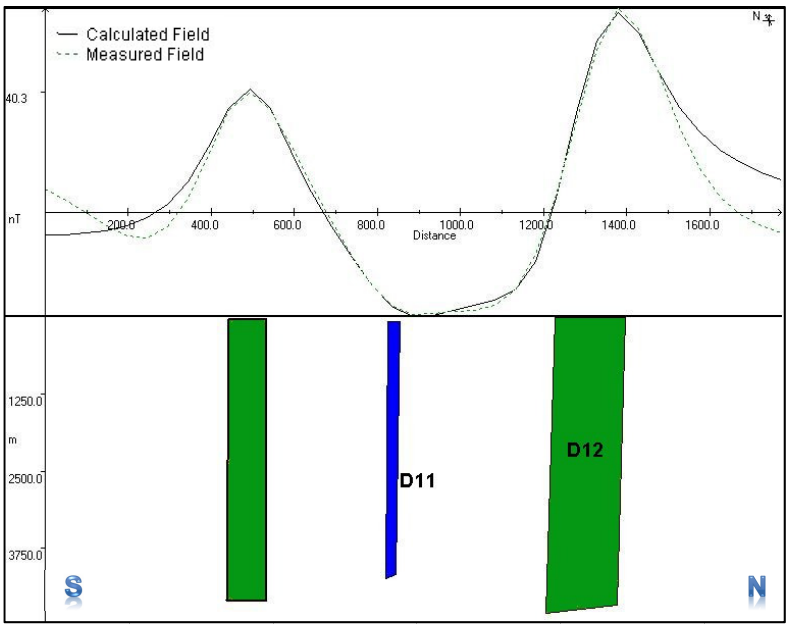


Figure 7.32. The model of profile 9 showing the remanent D11, D12 and a third dyke south of D11.

7.2.10. Profile 10

Profile 10 was chosen to model D13, a northeast trending dyke that intersects tie-line T9040. On both the magnetic data (Figure 7.33a) and the first vertical derivative data (Figure 7.33b) two dykes are visible. A body to the southeast of D13 can also be distinguished on both, but is clearer on the first vertical derivative.

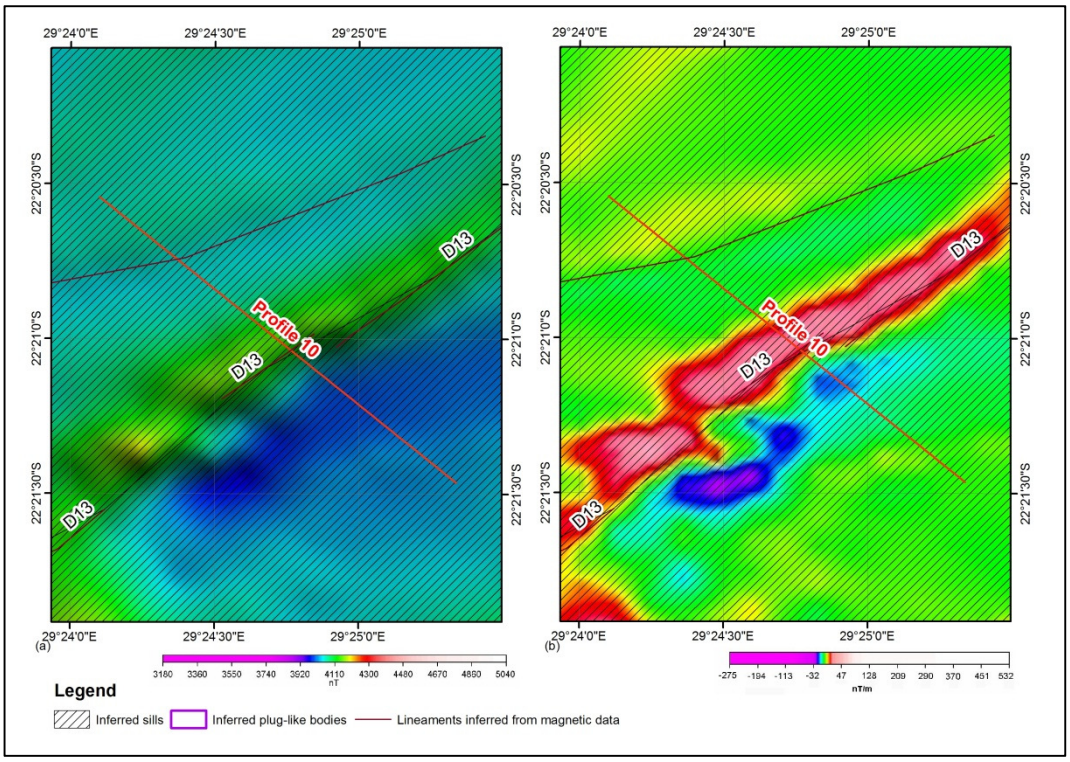


Figure 7.33. Profile 10 displayed over the magnetic TMI data (a) and the first vertical derivative data (b).

The dyke D13 is modelled (see Figure 7.34) with susceptibility 0.01 SI, depth 24 m and 381 m width. The magnetic body southeast of D13 has a susceptibility of 0.012 SI and is modelled to be 287 m deep and 317 m wide. The dyke northwest of D13 has a susceptibility of 0.0315 SI, depth of 155 m and width of 78 m.

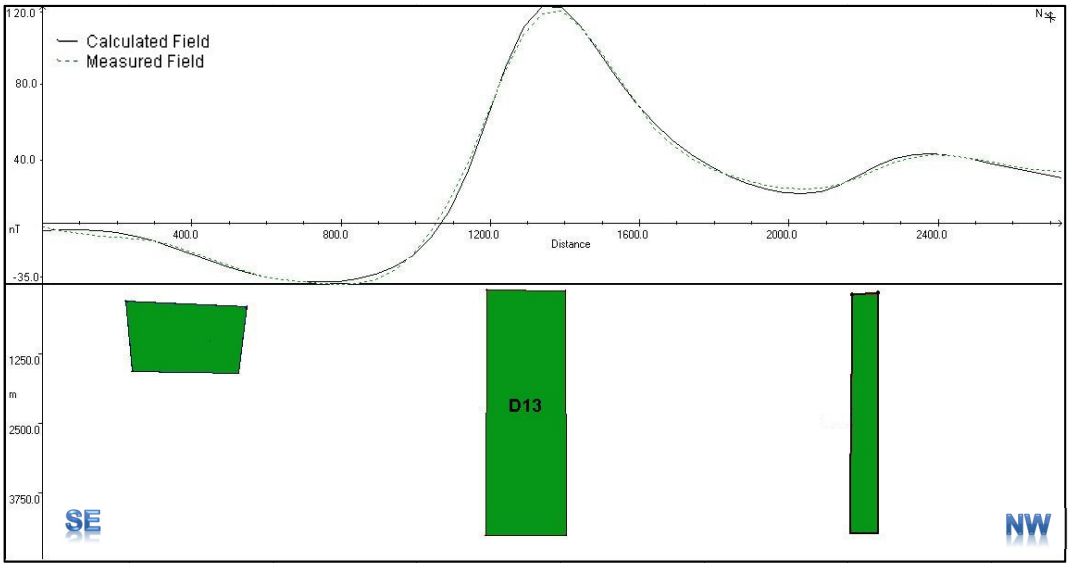


Figure 7.34. Profile 10 modelled with D13 in the centre, a magnetic body to the southeast and a dyke northwest of it.

7.2.11. Profile 11

Profile 11 is a northwest trending line across dyke D14. Dyke D14 is transected by flight line L330 and tie-line T9040 (see Figure 7.10). Subtle anomalies northwest and southeast of D14 is visible on the magnetic data (Figure 7.35a). These anomalies are more pronounced on the first vertical derivative data (Figure 7.35b).

The profile is modelled with three dykes; D14 and two dykes either side of it, as showed in Figure 7.36. D14 has a susceptibility of 0.03 SI, is 80 m deep and 272 m wide. The dyke to the northwest has a susceptibility of 0.01 SI, a depth of 163 m and width of 315 m, while the susceptibility of the dyke in the southeast is 0.013 SI. The dyke is 138 m deep and 165 m wide.

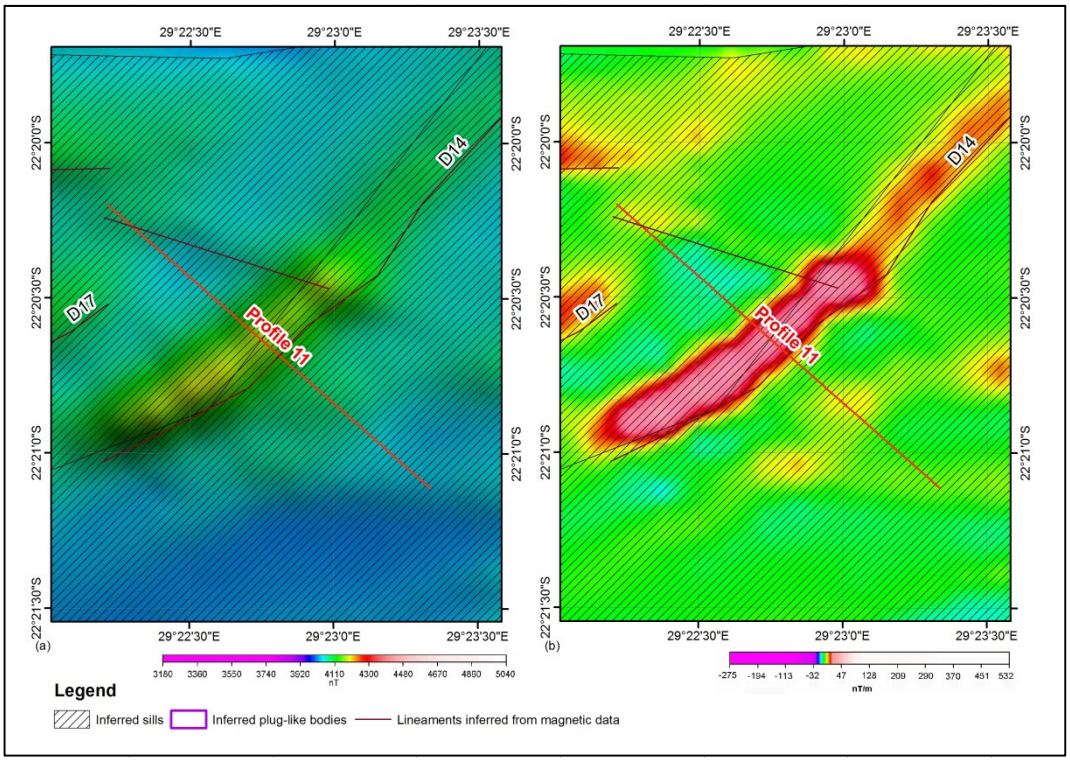


Figure 7.35. Profile 11 displayed over the magnetic TMI data (a) and the first vertical derivative data (b).

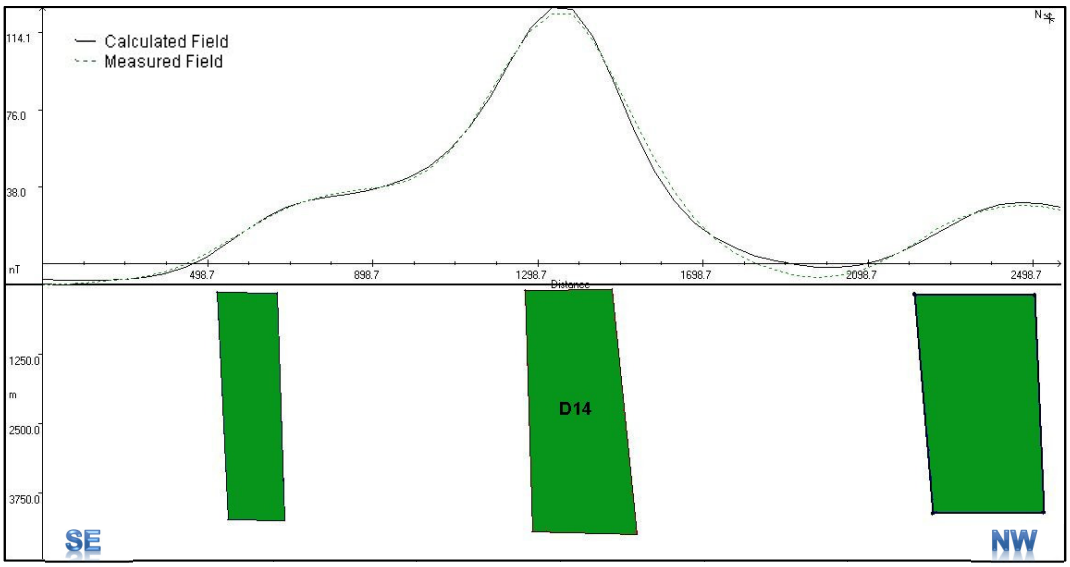


Figure 7.36. Model of profile 11 showing D14 with a dyke on either side of D14.

7.2.12. Profile 12

The north striking profile 12 was selected to model dyke D24, since both flight line L330 and L535 intersect this dyke in the northern part of the study area (Figure 7.10). The southern end of the profile almost touches what seems to be a negatively magnetised dyke on the first vertical derivative data ((b) on Figure 7.37).

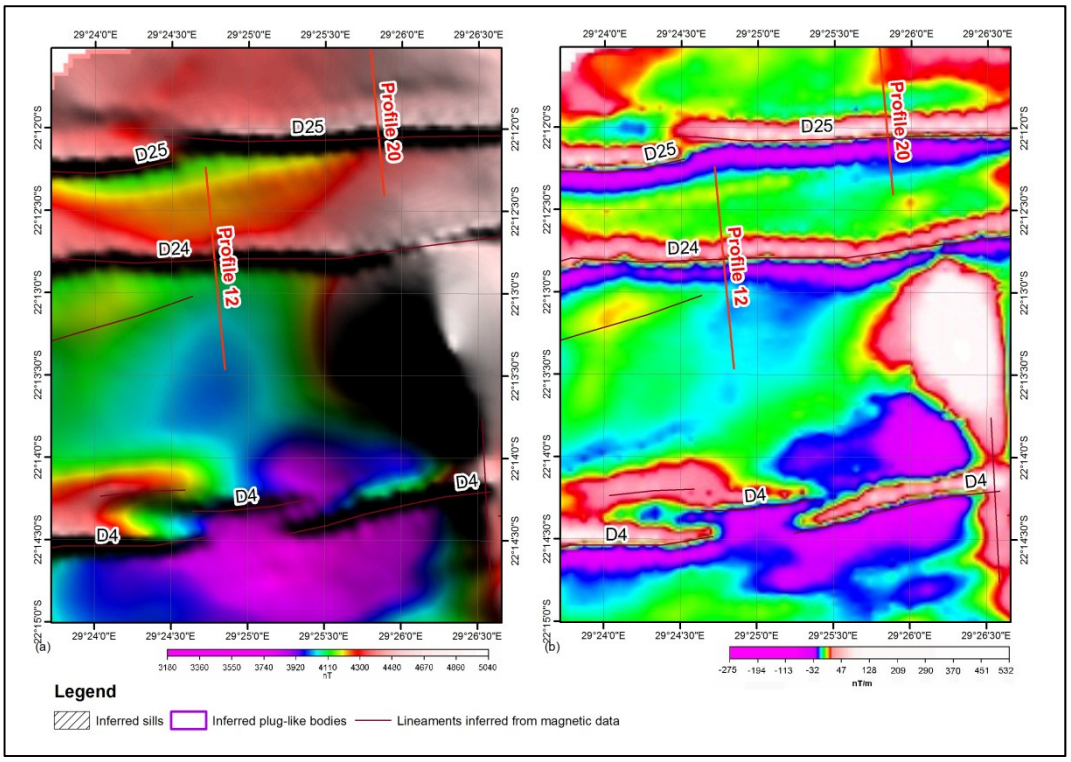


Figure 7.37. Locality map of profile 12 showing the proximity of D25 in the north and what appears to be a remanent dyke on the first vertical derivative data (b).

Dyke D24 is an east-west striking dyke that extends from the west to east of the study area. On the magnetic data (Figure 7.38a) D24 is very clear. A dyke located to the south of D24 is visible on both the magnetic data and the first vertical derivative (Figure 7.38b). To the north of D24 a dyke is visible on the first vertical derivative data.

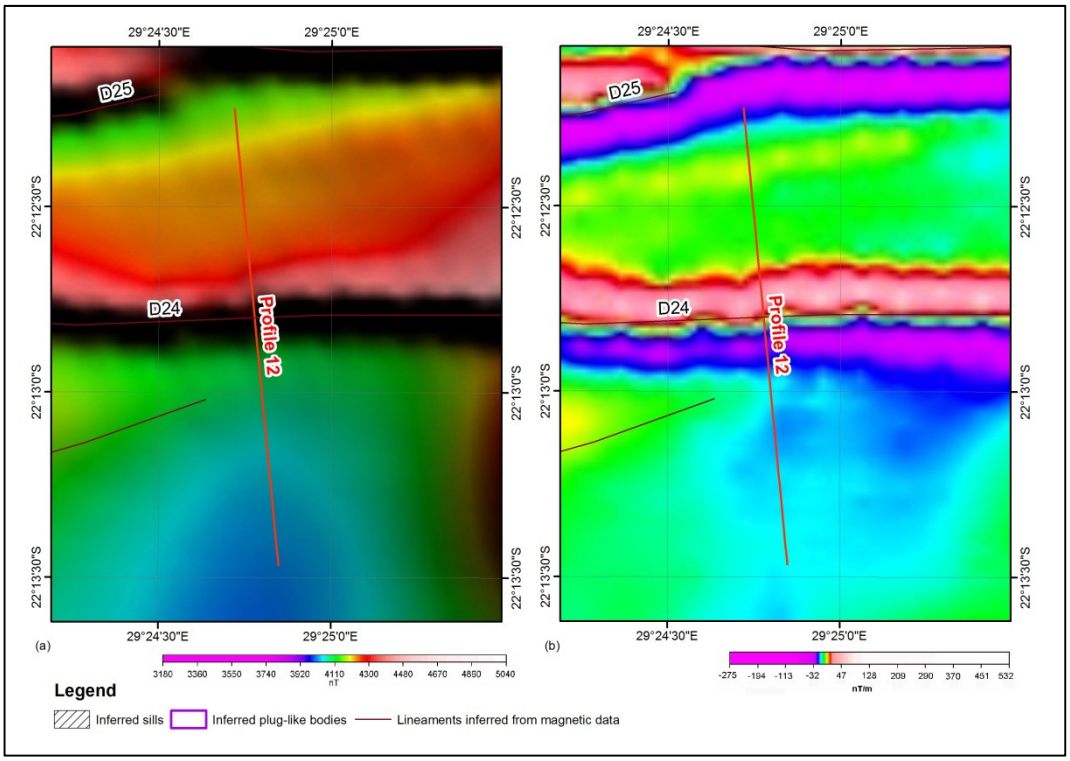


Figure 7.38. Profile 12 displayed over the magnetic TMI data (a) and the first vertical derivative data (b).

The model for profile 12 is shown in Figure 7.39. The dyke to the south of D24 has a susceptibility of 0.018 SI, depth of 271 m and is 190 m wide. D24 has a susceptibility of 0.03 SI and is 53 m deep with a width of 229 m. To the north of D24 a dyke with susceptibility 0.029 SI, depth of 278 m and width of 164 m was modelled. The discrepancy in the south is due to the negatively magnetised dyke near the southern end of the profile.

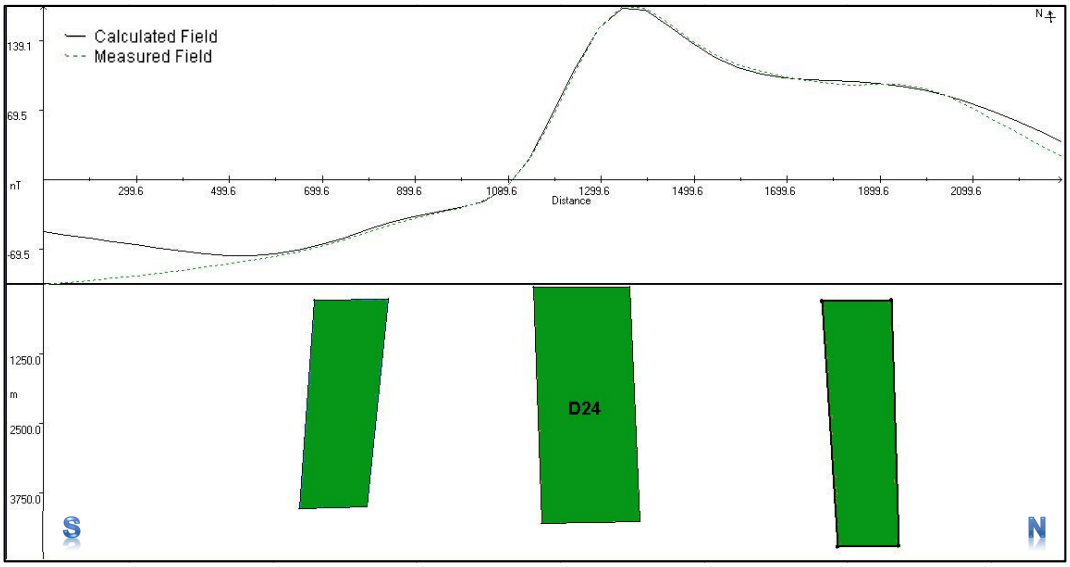


Figure 7.39. The model for profile 12 showing D24 with a dyke on either side of D24.

7.2.13. Profile 13

Profile 13 is located in the southeast of the study area (Figure 7.10). It crosses inferred dyke D28, a dyke that is intersected by flight line L535. Dykes D29 and D27 to the north and south of D28 are visible (Figure 7.40) and it is clear that the profile could not be made longer in either direction without the influence of the adjacent dykes becoming too prominent.

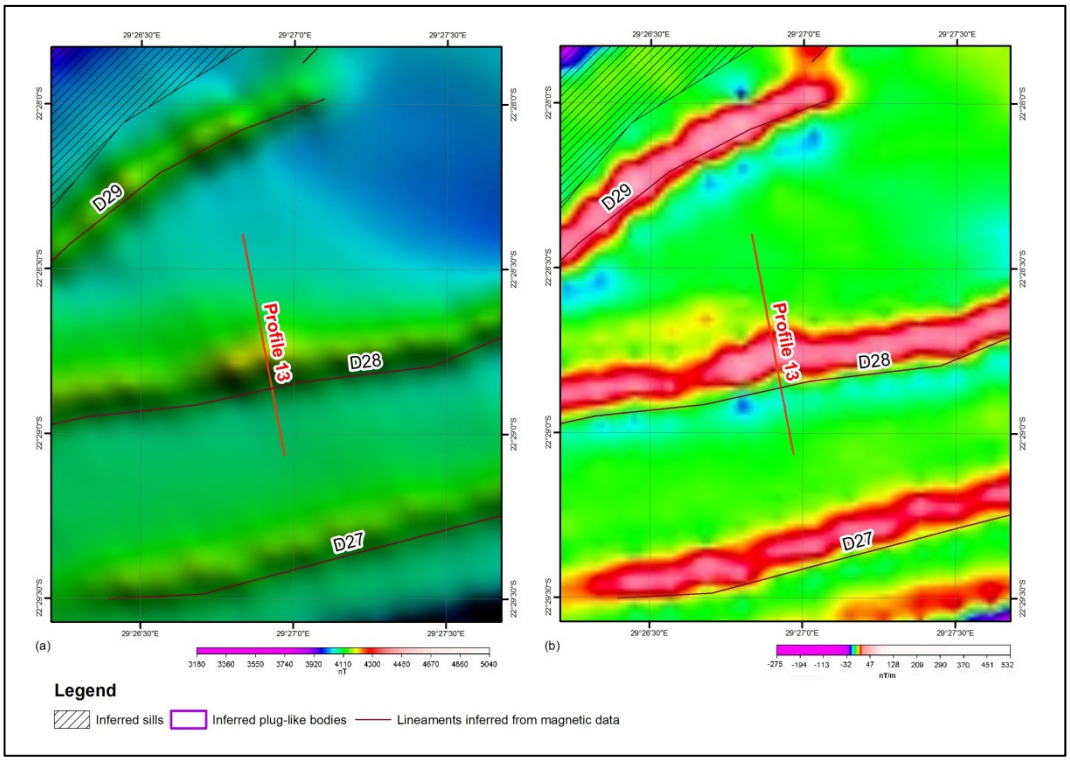


Figure 7.40. Locality map of Profile 13 showing the proximity to D29 in the north and D27 in the south.

A single dyke is visible on both the magnetic data (Figure 7.41a) and the first vertical derivative data (Figure 7.41b). The profile is modelled with a single dyke, D28, having susceptibility of 0.0325 SI, depth of 81 m and a width of 85 m.

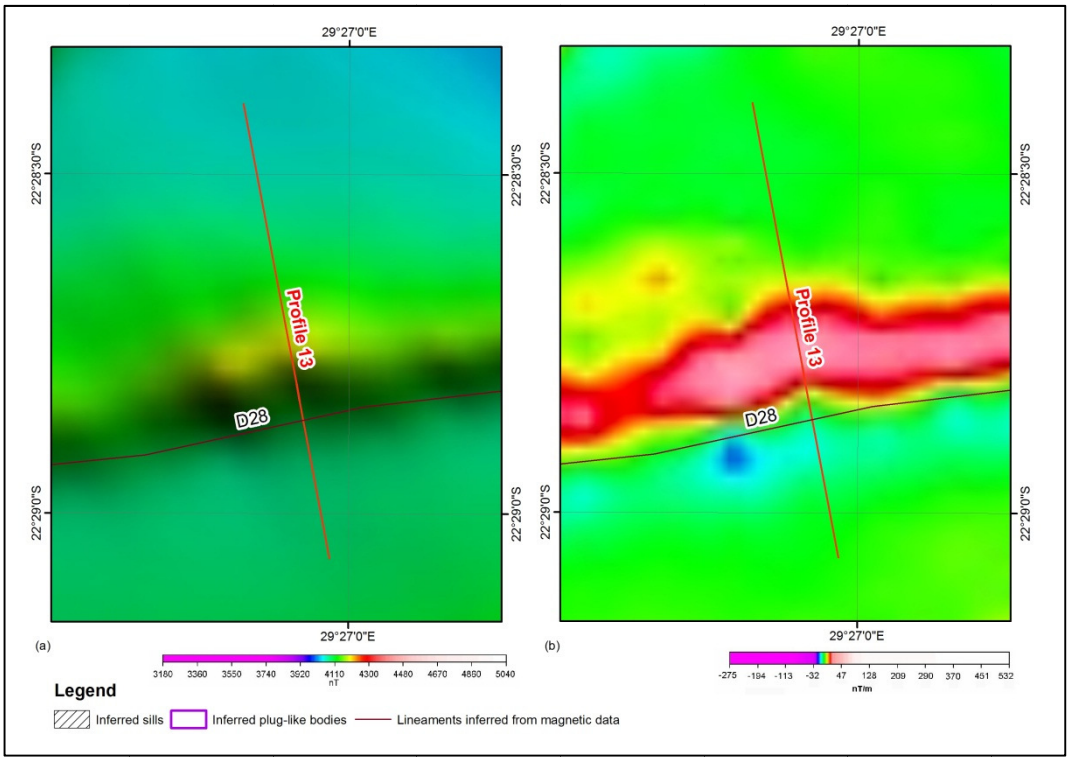


Figure 7.41. Close-up of Profile 13 displayed over the magnetic TMI data (a) and the first vertical derivative data (b).

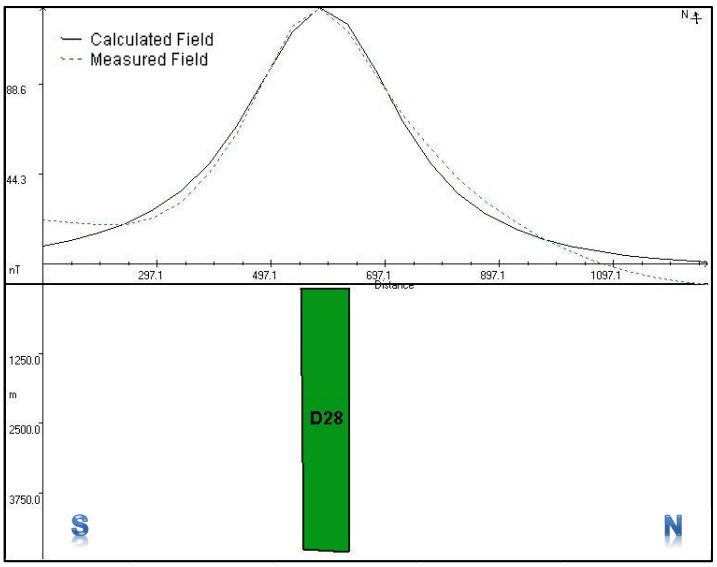


Figure 7.42. Model of profile 13 showing dyke D28.

7.2.14. Profile 14

Flight line L535 intersects inferred northeast dyke D29 in the southeast of the study area (see Figure 7.10) and profile 14 was selected to model the dyke. On the magnetic data (Figure 7.43a) only the one dyke is visible but on the first vertical derivative data (Figure 7.43b) a subtle magnetic anomaly is visible in the southeast.

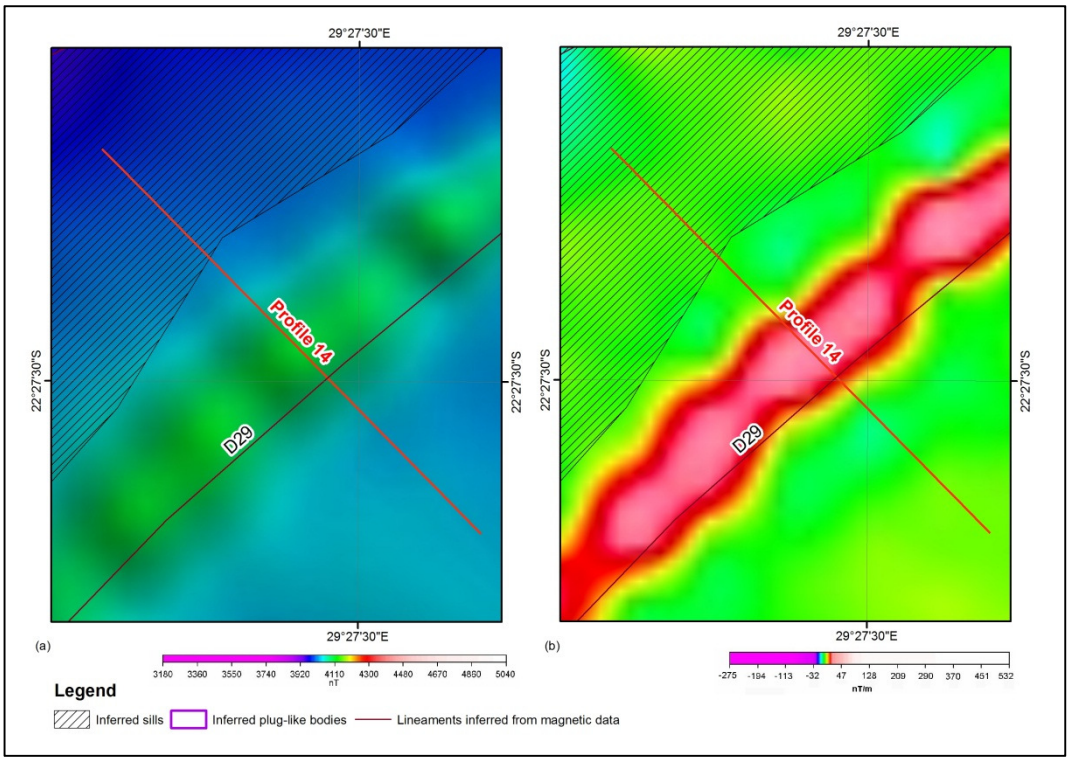


Figure 7.43. Profile 14 displayed over the magnetic TMI data (a) and the first vertical derivative data (b).

The data are modelled with two bodies, D29 and a small body in the southeast (Figure 7.44). The body in the southeast has a susceptibility of 0.01 SI. It is 201 m deep and 107 m wide. D29 is a southeast dipping dyke with a susceptibility of 0.039 SI, depth of 29 m and width of 159 m.

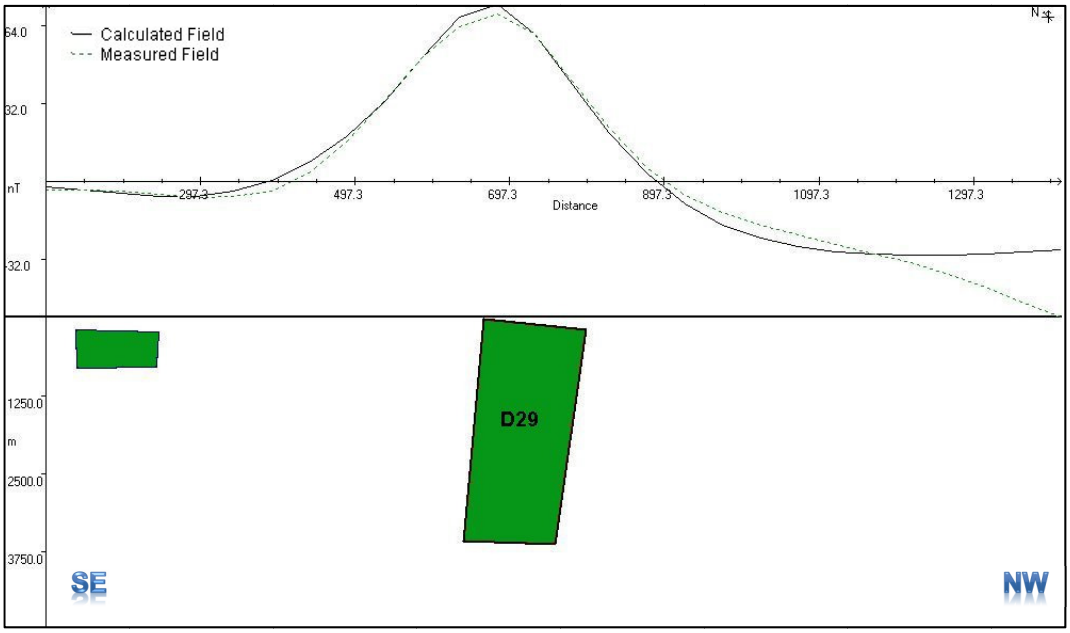


Figure 7.44. The model of profile 14 showing a body in the south and the dyke D29.

7.2.15. Profile 15

Profile 15 is a northwest trending line across a remanently magnetised dyke D7. Flight line L535 and tie-line T9020 both intersect D7 (see Figure 7.10). The proximity of D29 in the southeast (Figure 7.45) and D1 in the northwest makes it not feasible to have the profile extending any further in any direction.

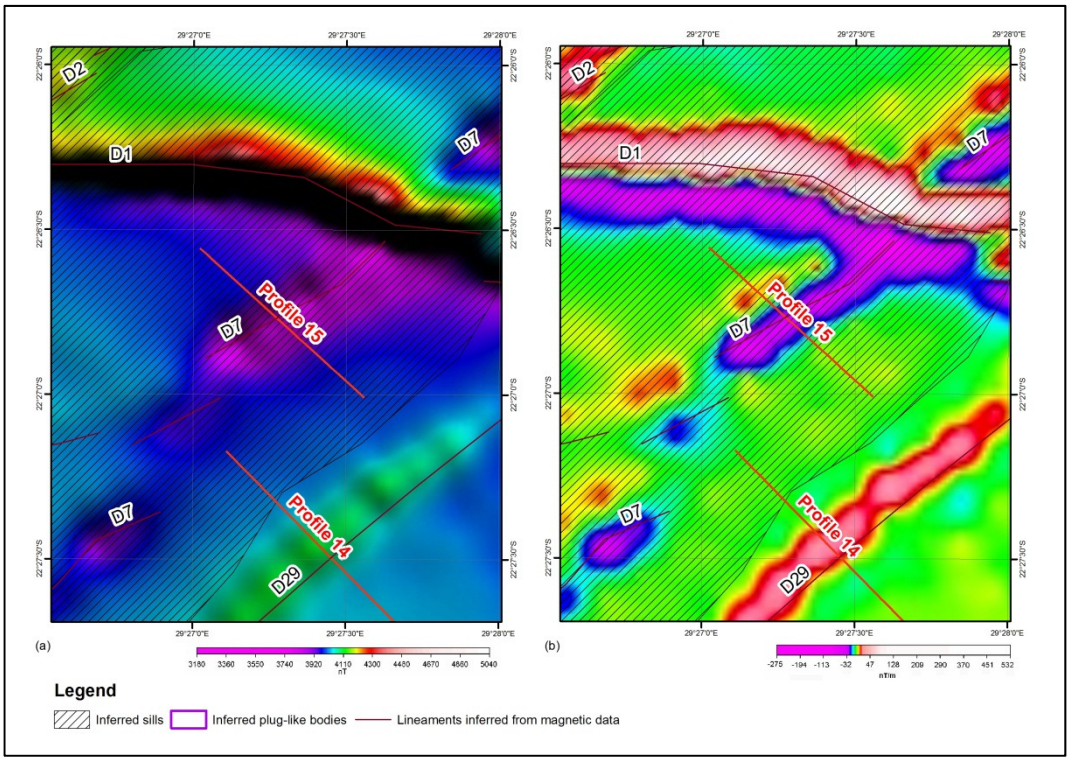


Figure 7.45. Locality map of Profile 15 showing the proximity of D1 in the northwest and D29 in the southeast.

On the magnetic data in the close-up of profile 15 (Figure 7.46a), only a remanently magnetised northeast trending dyke is visible, but on the first vertical derivative data (Figure 7.46b) a positive anomaly is visible north of D7. A slight magnetic anomaly to the southeast could be due to a magnetic body.

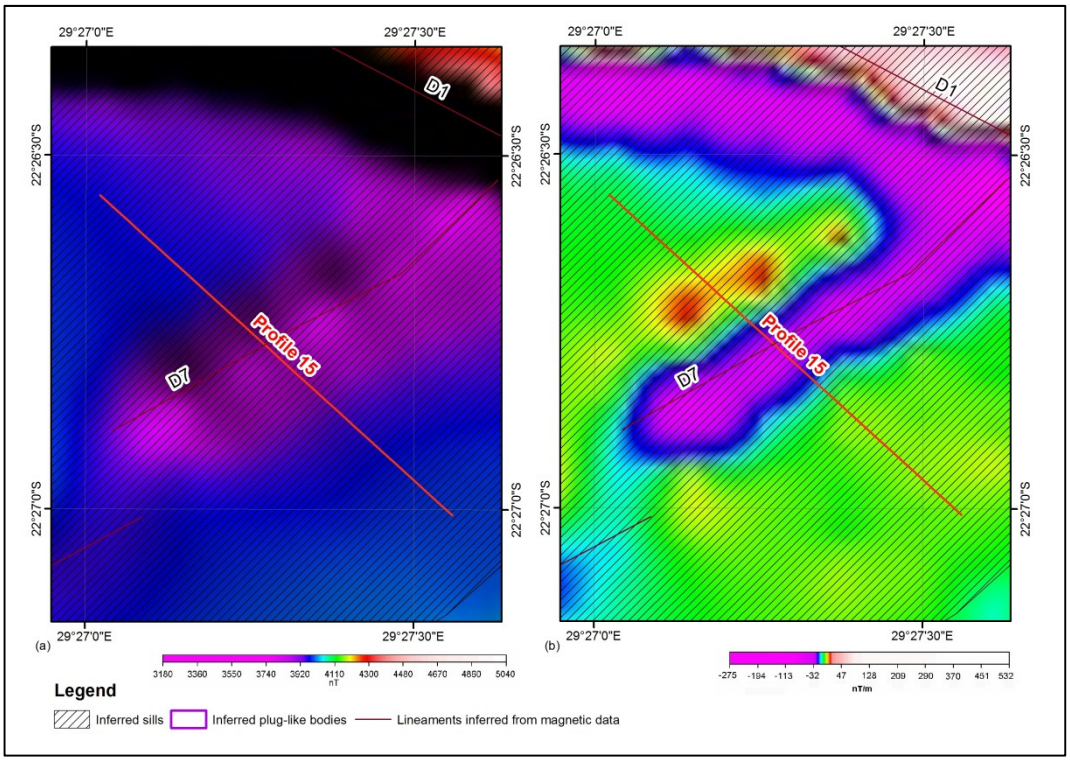


Figure 7.46. Profile 15 displayed over the magnetic TMI data (a) and the first vertical derivative data (b).

The model of profile 15 is given in Figure 7.47. D7 is modelled with a susceptibility of 0.2 SI. It is 73 m deep and 40 m wide. The dyke northwest of D7 is modelled with a susceptibility of 0.01 SI, depth of 19 m and width of 36 m. A body is modelled to the southeast of D7 with susceptibility 0.03 SI, depth of 238 m and width of 360 m. The remanence values for D7 are listed in Table 7.1.

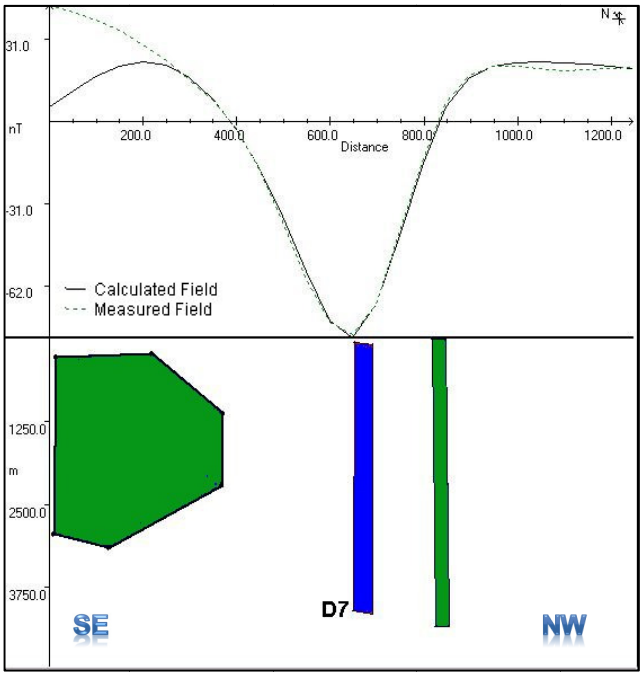


Figure 7.47. Model of profile 15 showing a magnetic body is the southest, D7 and another dyke in the northwest.

The misfit in the south-eastern part of the model is due to the body not being modelled beyond the reach of the profile while the anomaly extends further southeast. As mentioned earlier, the profile cannot be extended in the southeast due to D29 being very close to the end of the profile.

7.2.16. Profile 16

Profile 16 is a north trending line across dyke D1, an east-west trending dyke in the south east of the study area. Flight line L535 intersects D1 in the south (see Figure 7.10). On the magnetic data (Figure 7.48a) and the first vertical derivative data (Figure 7.48b) D1 is visible as a positive anomaly.

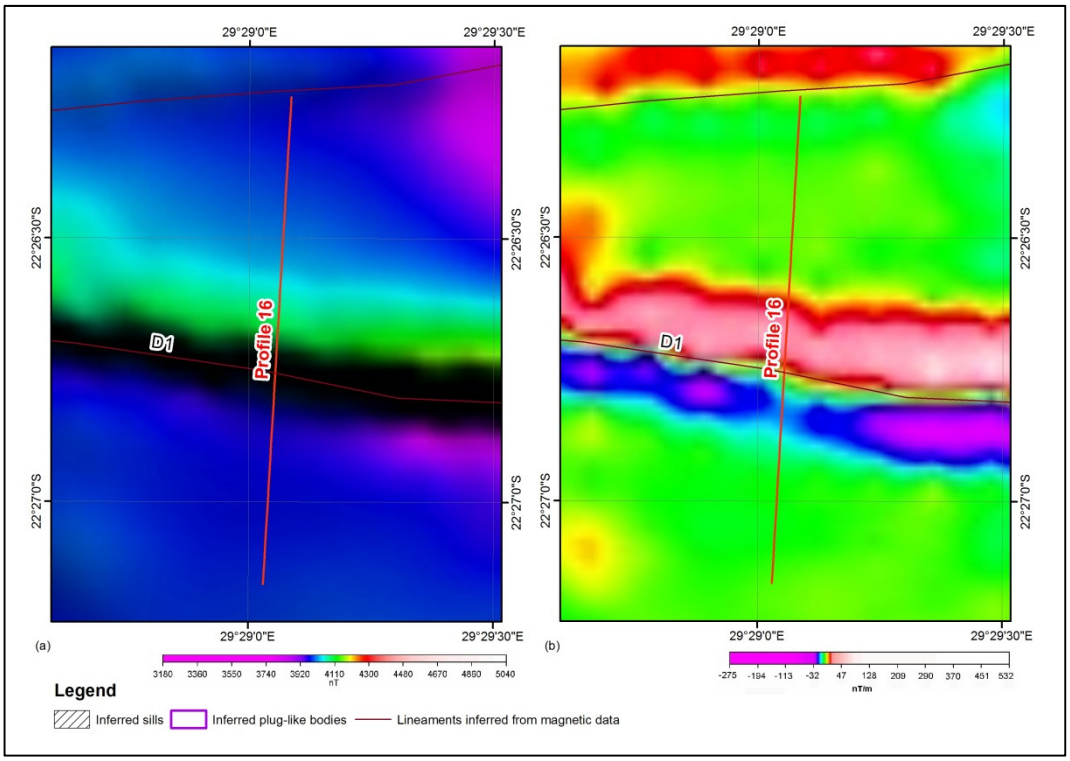


Figure 7.48. Profile 16 displayed over the magnetic TMI data (a) and the first vertical derivative data (b).

The model for D1 on profile 16 is shown in Figure 7.49. The dyke is modelled with a susceptibility value of 0.029 SI, a depth of 40 m and a width of 181 m.

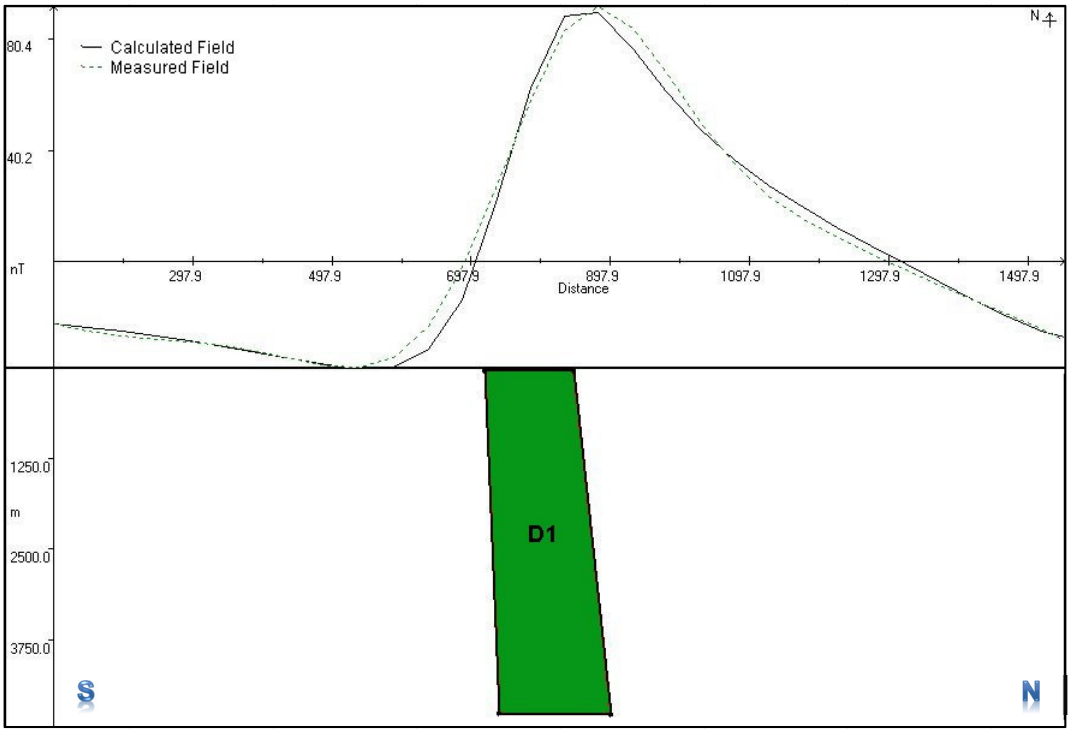


Figure 7.49. The model for profile 16 showing D1

7.2.17. Profile 17

This profile is a north-northeast trending line in the southeast of the study area (see Figure 7.10). It was chosen to model dyke D3, an east-west trending dyke that is intersected by both L330 and L535. The profile length is restricted by the proximity of dykes to the north and south of D1. The direction of the profile is also not 100% perpendicular to the dyke, as this would have resulted in an even shorter profile.

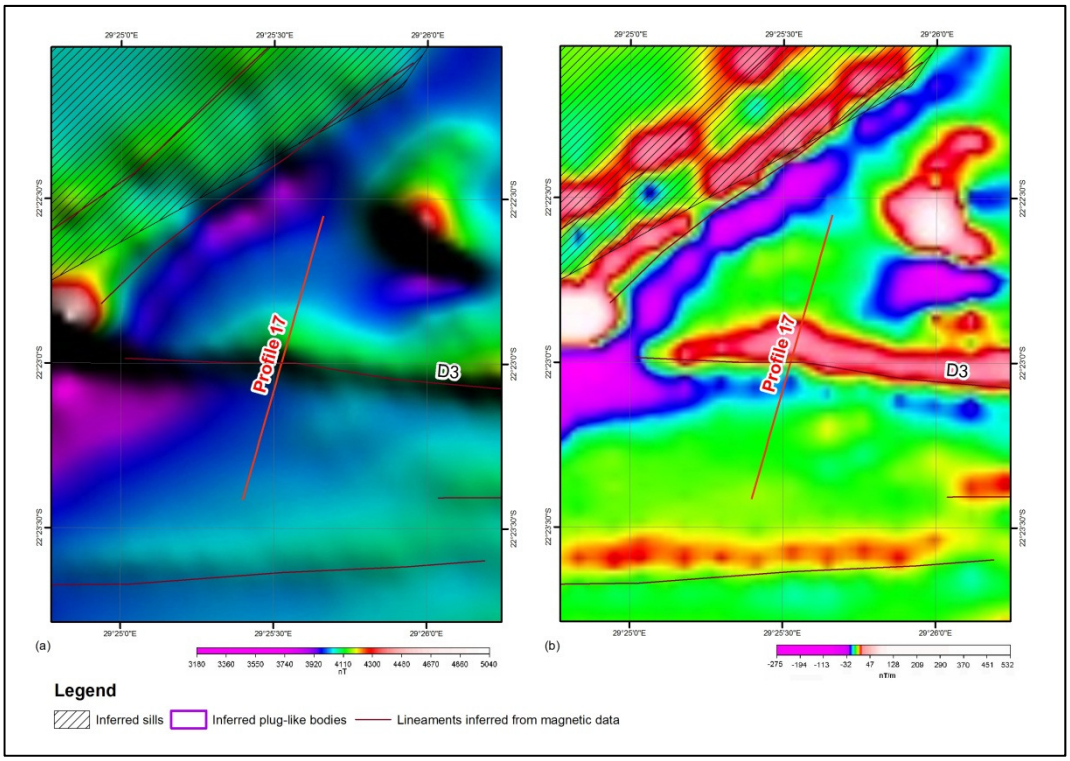


Figure 7.50. Locality map of profile 17 showing the proximity to dykes in the north and south.

On the magnetic data (Figure 7.51a) only the dyke is clearly visible, but on the first vertical derivative (Figure 7.51b), the effect of another dyke in the north is visible.

The model for the profile is shown in Figure 7.52. The misfit in the northeast is due to the effect of the dyke north of profile 17. D3 is modelled with a susceptibility of 0.015 SI, depth of 3 m and width of 182 m.

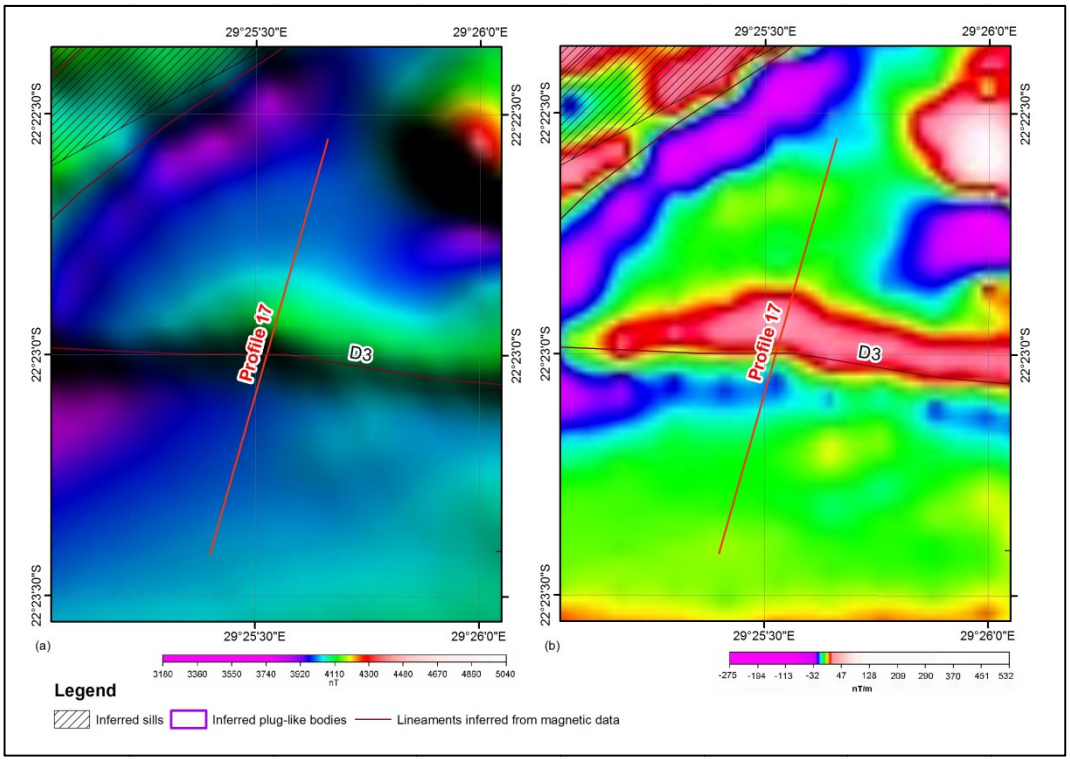


Figure 7.51. Profile 17 displayed over the magnetic TMI data (a) and the first vertical derivative data (b).

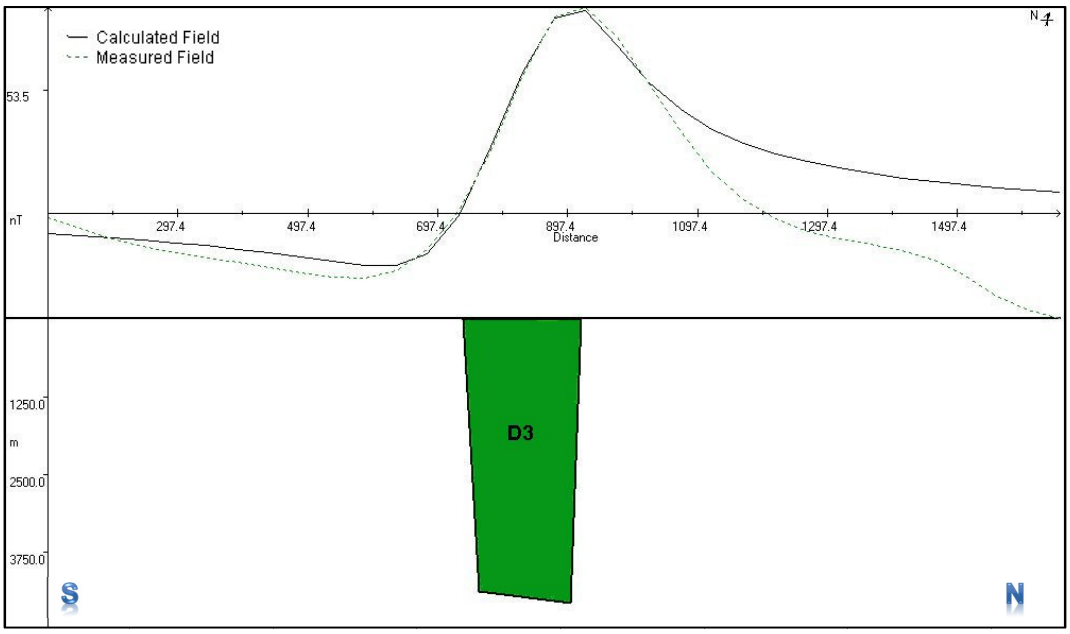


Figure 7.52. The model of D3 on profile 17.

7.2.18. Profile 18

Profile 18 intersects the inferred east-west striking dyke D30. This dyke affects L535 in the centre and east of the study area (Figure 7.10). On the magnetic data D30 looks like a large wavelength anomaly, but on the first vertical derivative data a second, northeast trending dyke is visible.

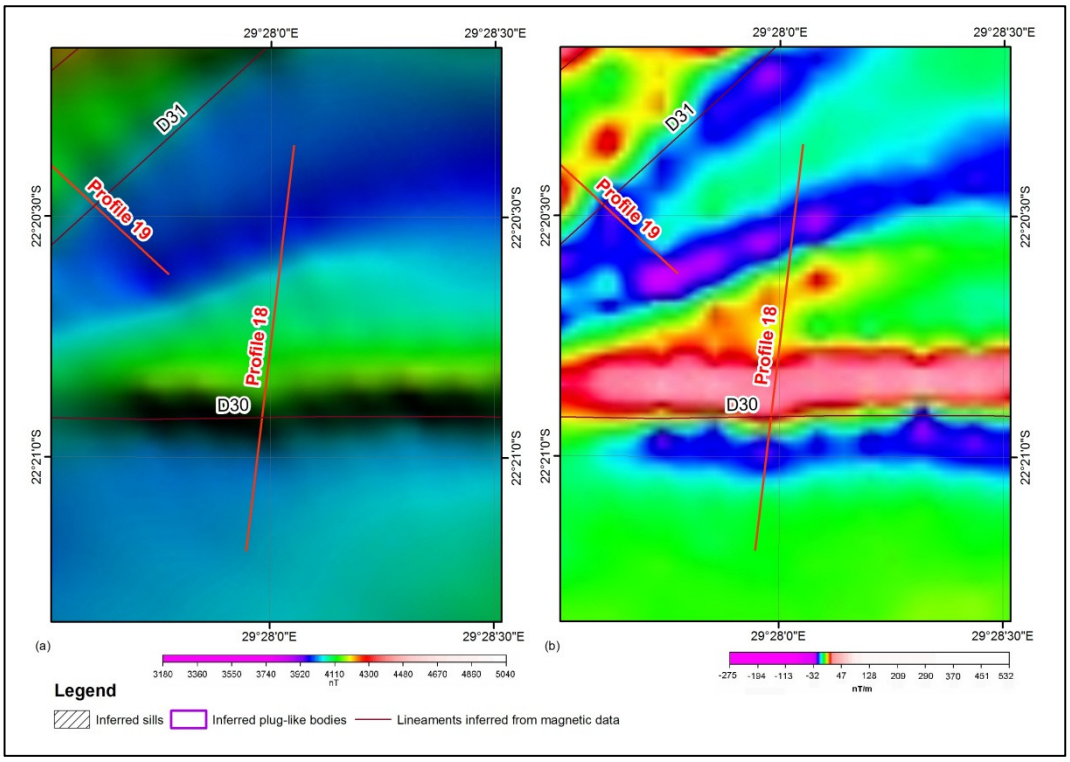


Figure 7.53. Profile 18 displayed over the magnetic TMI data (a) and the first vertical derivative data (b).

Figure 7.54 shows dyke D30 modelled with susceptibility of 0.0341 SI, at a depth of 56 m and with a width of 125 m. North of D30 is a dyke with a susceptibility of 0.01 SI, width of 60 m and depth of 162 m. The remanently magnetised dyke has a susceptibility value of 0.01 SI, depth of 106 m and width of 163 m. The remanence values are listed in Table 7.1.

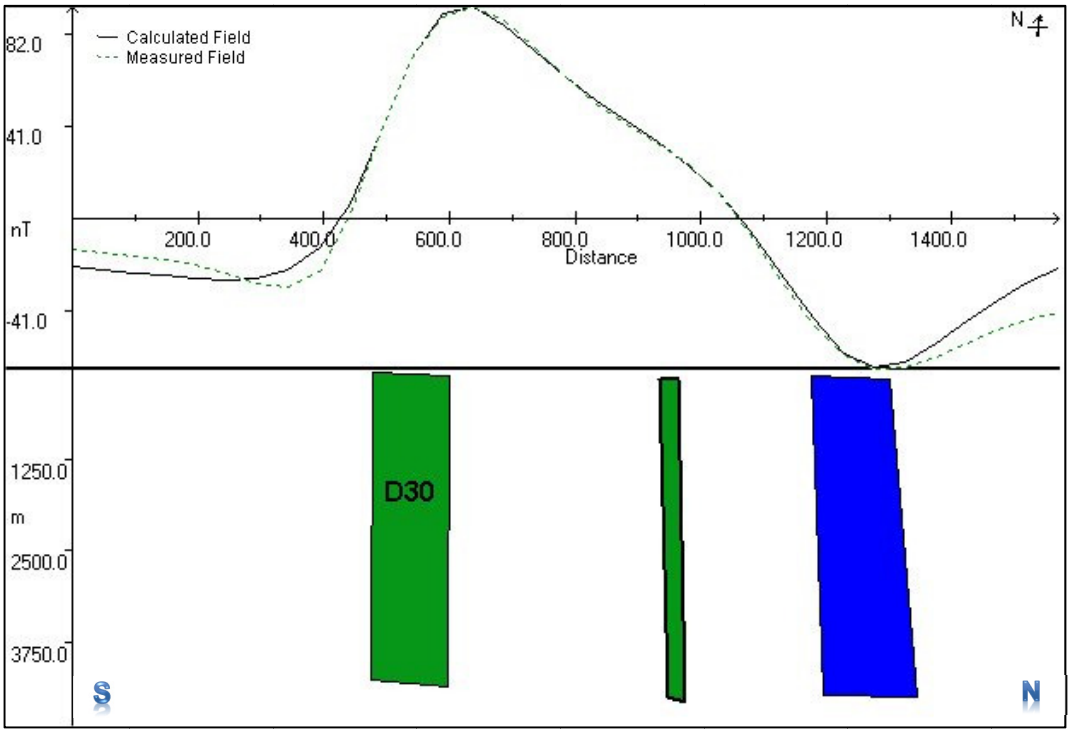


Figure 7.54. The model of the data showing dyke D30 to the south and a remanent dyke to the north and a third dyke in between them.

7.2.19. Profile 19

Profile 19 crosses dykes D31 and D32, two parallel northeast trending dykes that are intersected by flight line L535 and tie-line T9020 (Figure 7.10). Figure 7.55 shows the profile over the magnetic data (a) and the first vertical derivative data (b). Two northeast trending dykes are visible, D31 in the south and D32 in the north.

The two dykes on profile 19 were modelled and the model is shown in Figure 7.56. In this model D31 has susceptibility of 0.0345 SI, depth of 96 m and width of 113 m and D32 has susceptibility of 0.048 SI, depth of 236 m and width of 295 m.

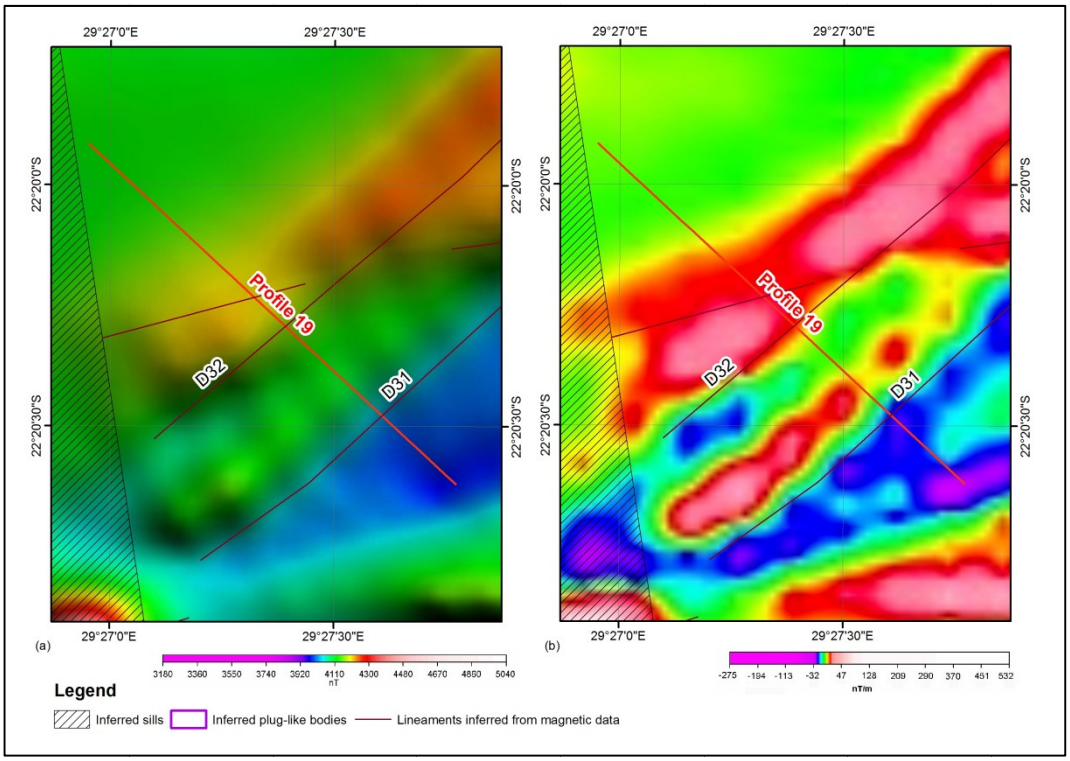


Figure 7.55. Profile 19 displayed over the magnetic TMI data (a) and the first vertical derivative data (b).

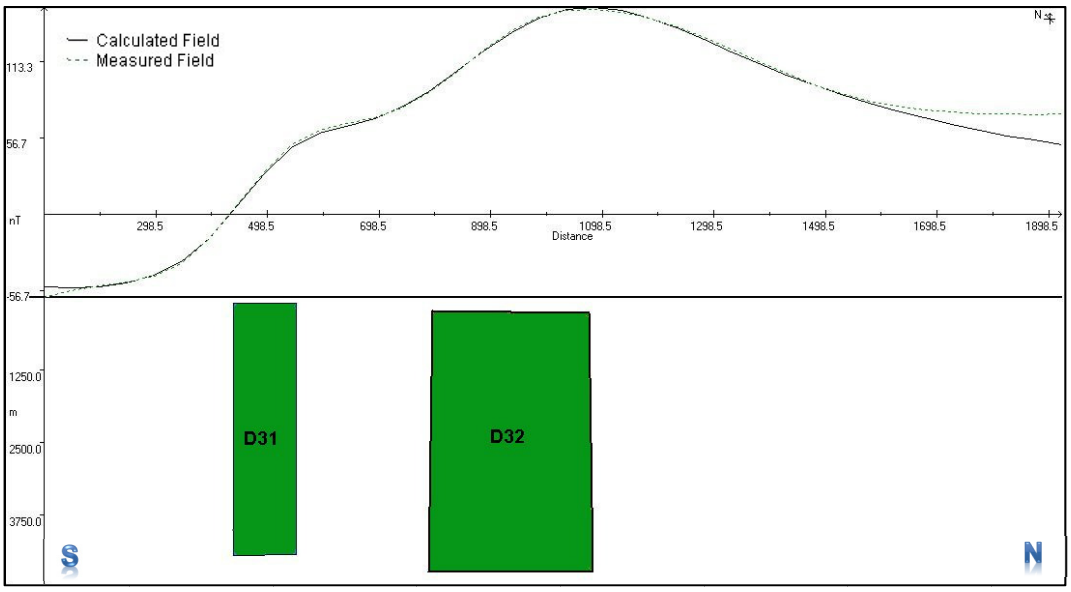


Figure 7.56. The model of profile 19 showing D31 and D32 just north of D31.

7.2.20. Profile 20

Profile 20 is located in the northeast of the study area (Figure 7.10). It transects inferred dyke D25, a dyke that is crossed by flight line L535. The profile is displayed in Figure 7.57 over the magnetic data (a) and the first vertical derivative data (b). On the magnetic data only D25 is visible, but on the first vertical derivative a negative linear anomaly is visible directly north of D25.

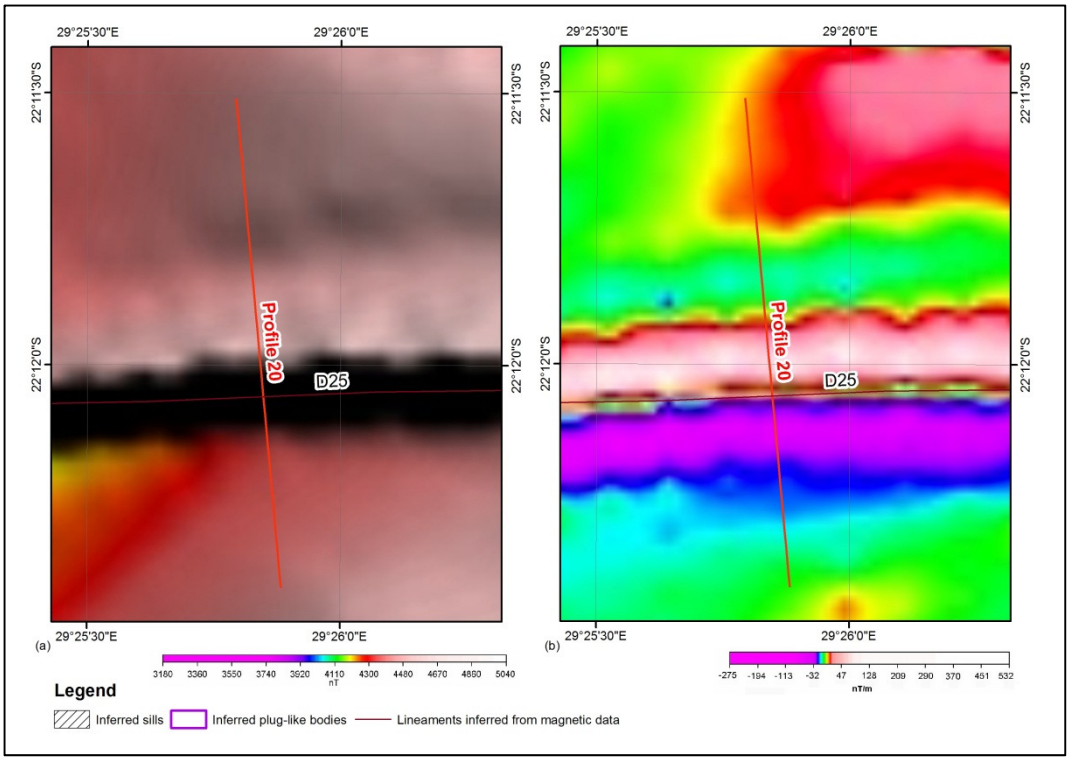


Figure 7.57. Profile 20 displayed over the magnetic TMI data (a) and the first vertical derivative data (b).

The model of profile 20 is shown in Figure 7.58. Dyke D25 is located to the south and is modelled with a susceptibility of 0.047 SI, at a depth of 45 m and width of 180 m. The remanently magnetised body north of D25 represents the negative anomaly seen on the first vertical derivative data. It has susceptibility of 0.0002 SI, depth of 139 m and width of 227 m. The remanence values for this body are listed in Table 7.1.

.

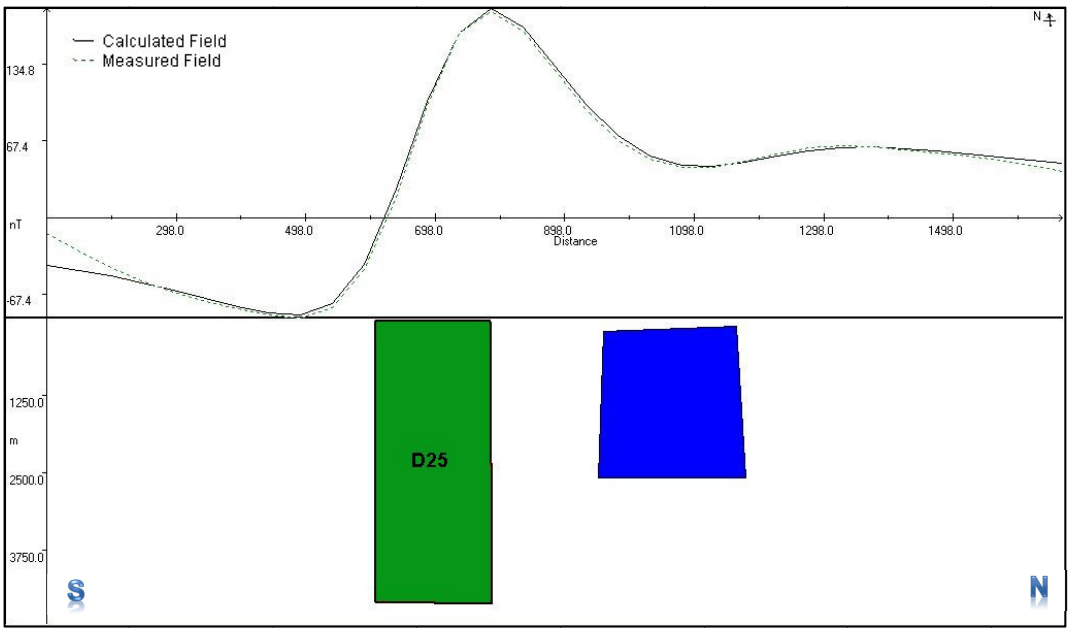


Figure 7.58. The model of profile 20 with D25 to the south and a remanent body to the north.

7.2.21. Profile 21

Profile 21 is located in the south of the study area and crosses two plugs, P3 and P4. P3 is traversed by tie-line T9020 (see Figure 7.10). Figure 7.59 shows the profile overlain on the magnetic data (a) and the first vertical derivative data (b). The two positive round anomalies are clearly visible on both datasets.

The model of the data is displayed in Figure 7.60. P3 is a thicker plug, with susceptibility of 0.76 SI, depth of 124 m and width of 181 m. P4, with the same susceptibility as P3 is thinner with a width of 67 m and depth of 76 m. The strike lengths of the plugs were constrained by the modelling software to be 100 m.

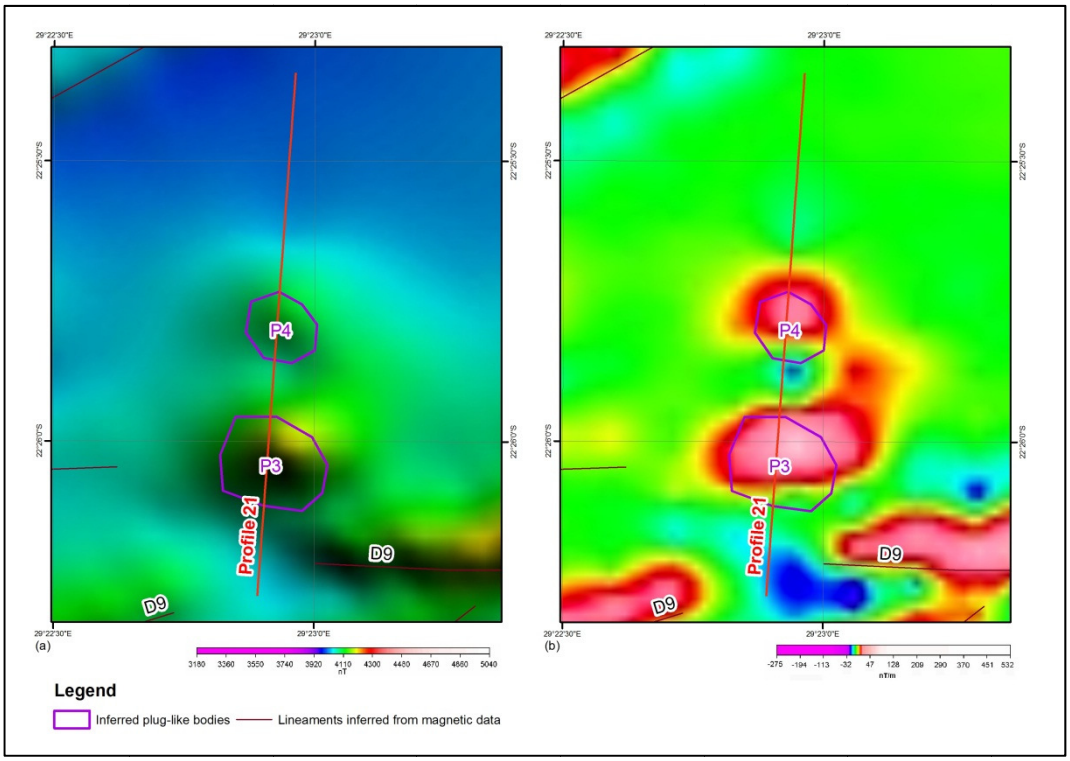


Figure 7.59. Profile 21 displayed over the magnetic TMI data (a) and the first vertical derivative data (b).

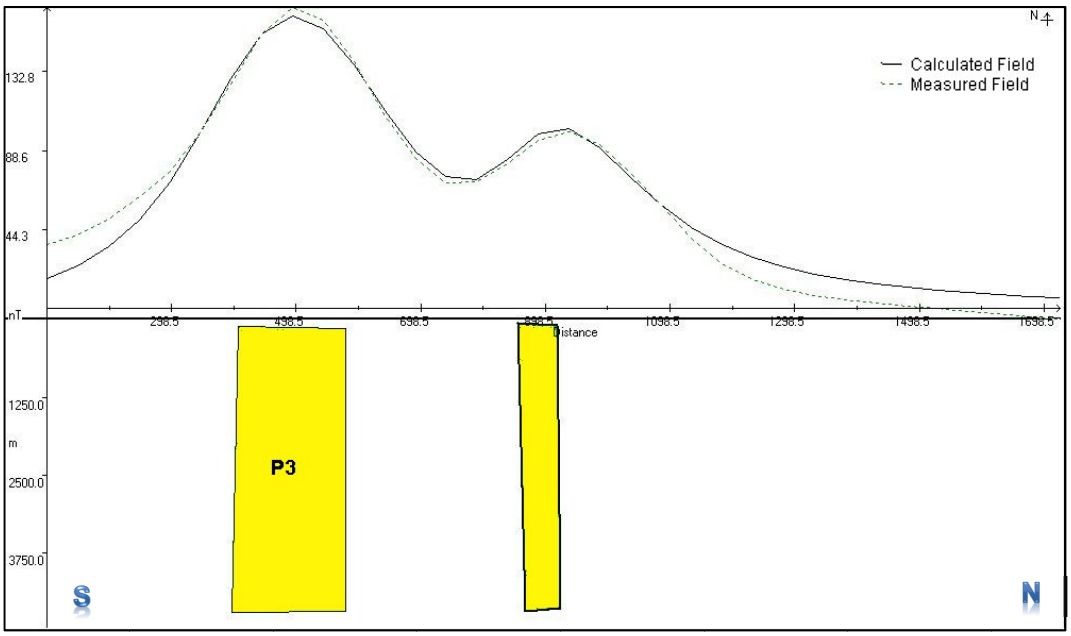


Figure 7.60. The model of the data showing P3 and P4.

7.2.22. Profile 22

The final profile is across the plug P2 to the east of profile 21 (Figure 7.10). The profile was not extended to either the north or south as this would have crossed D9 in the north and D1 in the south (Figure 7.61).

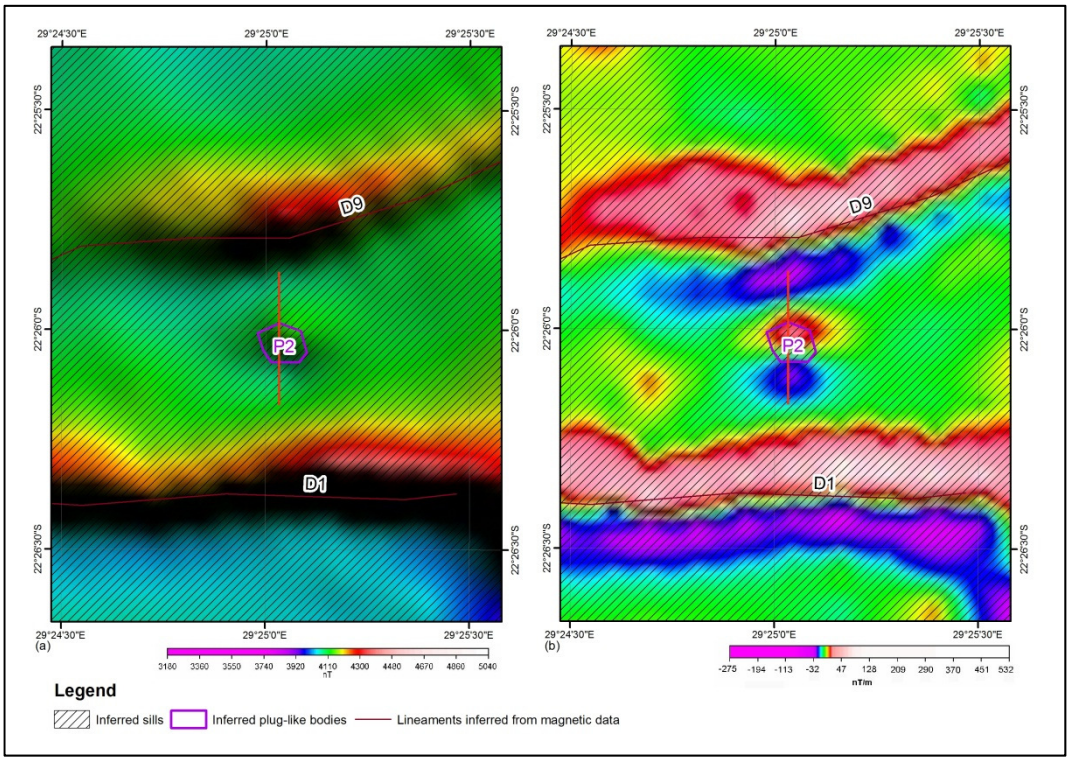


Figure 7.61. Locality map showing profile 22 and the proximity to D9 in the north and D1 in the south.

The profile is displayed over the magnetic data in Figure 7.62a as well as the vertical derivative data (Figure 7.62b). The plug is visible on both datasets, but it is much clearer on the first vertical derivative.

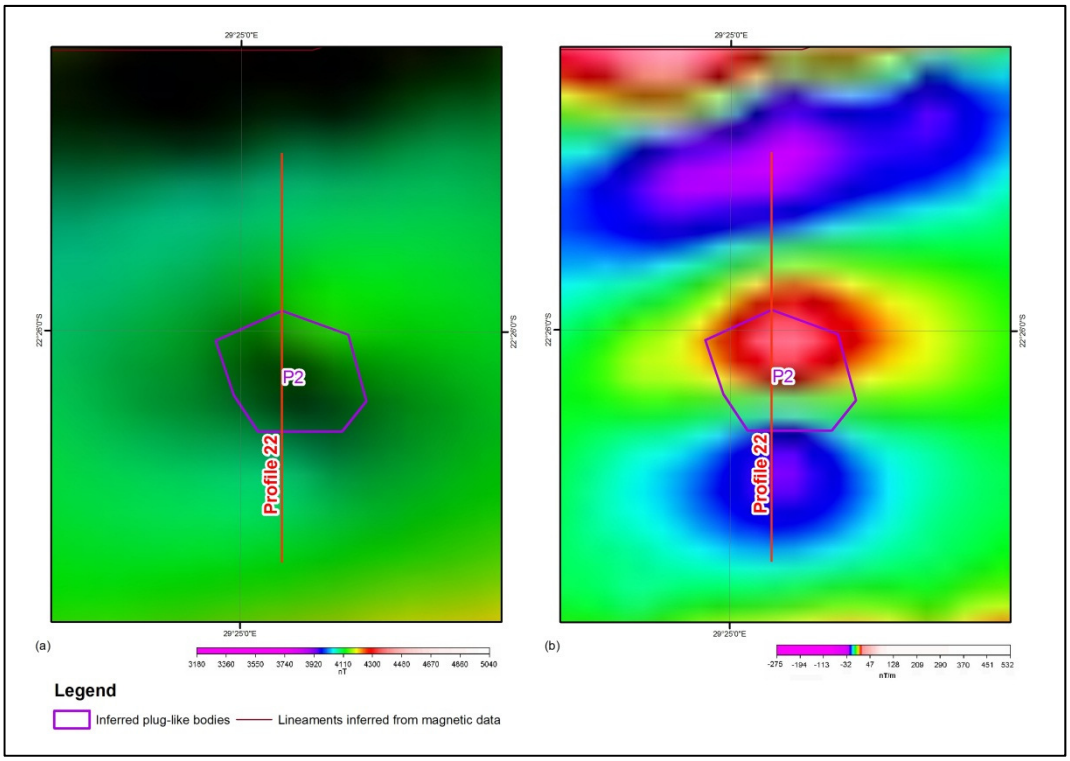


Figure 7.62. Profile 22 displayed over the magnetic TMI data (a) and the first vertical derivative data (b).

The model for the data is shown in Figure 7.63 and displays the plug P2 with a susceptibility of 0.055 SI, depth of 22 m and width of 94 m. The misfit to the north is due to the effect of the dyke (D9 - Figure 7.10) on the very edge of the profile. The strike length was constrained by the modelling software to be 100 m.

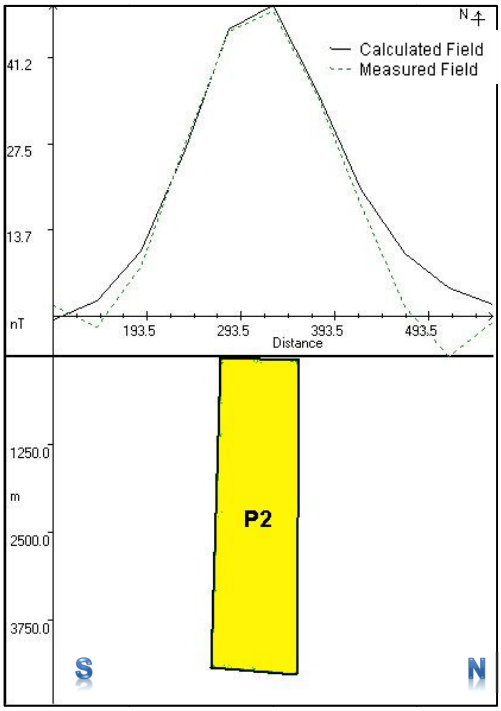


Figure 7.63. Model of the data showing the plug P2.

Table 7.1. Modelled remanence values.

Dyke	Intensity	Inclination	Declination
D7	574.7	90	318.8
D10	1690.8	10.5	231.9
D20	878.9	11.8	244.5
D11	80	90	220
North of D20 (profile2)	777.1	19.0	233.2
North of D23 (profile 6)	626.7	18.6	11.6
North of D25 (profile 20)	172.3	10.3	63.6
North of D30 (profile 18)	100	90	-360
Remanent plug (profile 8)	709.1	26.7	244.6

7.3. Euler Deconvolution

Euler deconvolution indicates portions of the data that are of interest to the interpreter. It does not use a particular geological model but rather uses a range of elementary magnetic or gravity distributions as the source of the anomalies (Cooper, 2004i).

According to Reid et al. (1990) a function $f(x, y, z)$ is homogenous of degree N if

$$f(tx, ty, tz) = t^N f(x, y, z)$$

If this function is homogenous of degree N then it satisfies Euler's equation.

Euler's equation is given by Blakely (1995) as:

$$r.\nabla f = -Nf$$

Where N is the structural index, an index that corresponds to the decay in amplitude of the field with distance (Cooper, 2004i).

Table 7.2. Structural index values based on the shape of the causative body. (Cooper, 2004i)

Magnetic body shape	Structural Index
Sphere	3
Pipe	2
Horizontal cylinder	2
Dyke	1
Sill	1
Contact	0

The solutions cluster around the vertical edges of causative bodies.

Euler deconvolution was applied to the profiles extracted for modelling using the freeware program Euler.exe (Cooper, 2002).

7.3.1. Profile 1

Profile 1 is a north-northwest trending profile across dyke D9 in the south and D5 in the north. There are two occurrences of D9 on the profile, an anomaly to the south and a lower amplitude anomaly north of it. The profile was modelled in section 7.2.1 with three dykes and a sill (S1) in the north. Euler processing using a structural index (SI) of 1 and window size of 9 results in clusters that could point to four possible bodies, as indicated in Figure 7.64.

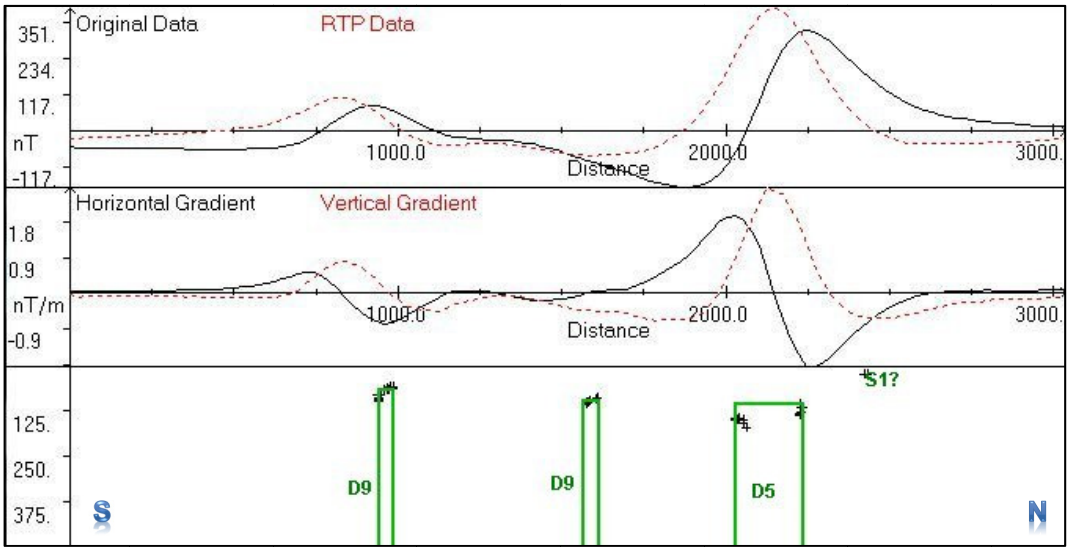


Figure 7.64. Euler results for profile 1 with the inferred bodies shown in green.

The southern D9 is at 40 m depth and about 50 m wide, the northern D9 is about 90 m deep and 50 m wide. Dyke D5 is 100 m deep and 250 m wide while the cluster of points that could indicate the edge of the sill S1 is at ±10 m deep.

7.3.2. Profile 2

Profile 2 is a north-northwest trending profile across dyke D10 in the south, D20 in the north and an unnamed remanently magnetised dyke north of D20. The profile was modelled in section 7.2.2 with four dykes, the three remanent dykes visible on the magnetic data and an additional positively magnetised unnamed dyke, visible on the first vertical derivative data, between D10 and D20. Euler processing using a SI of 1 and window size of 9 results in clusters that could point to four possible bodies, as indicated in Figure 7.65.

D10 seems to be located at depth ±60 m with a width of ±100 m and D20 is ±100 m deep and ± 75 m wide. The unnamed positively magnetised dyke between D10 and D20 is located at a depth of about 50 m and has a width of about 100 m, while the remanently magnetised unnamed dyke north of D20 is at ±60 m depth and has a width of ±100 m.

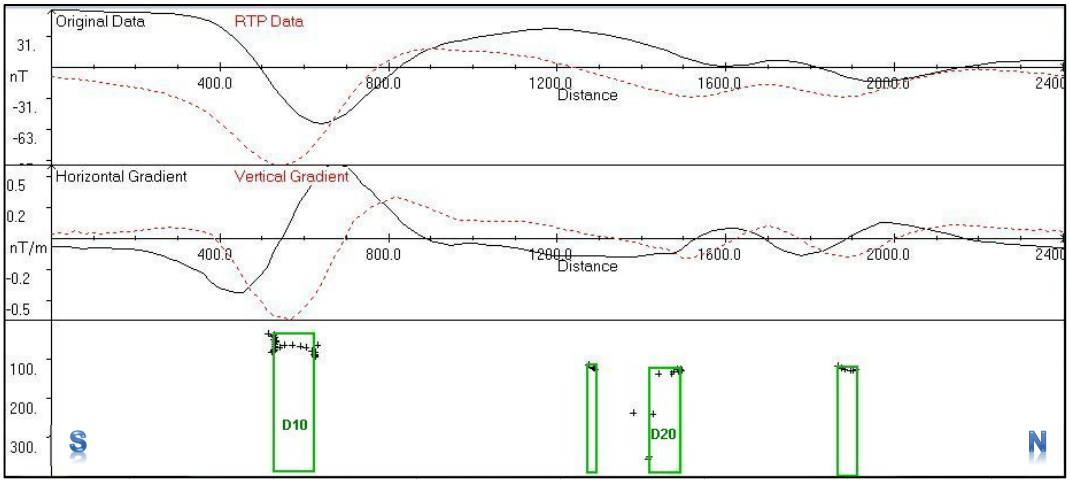


Figure 7.65. Euler results with inferred bodies in green.

7.3.3. Profile 3

Profile 3 is a north-south trending profile across dyke D8. The profile was modelled in section 7.2.3 with one dyke. Euler processing using a SI of 1 and window size of 9 resulted in clusters indicating a body as shown in Figure 7.66. The dyke D8 is located at a depth of about 35 m and is about 150 m wide.

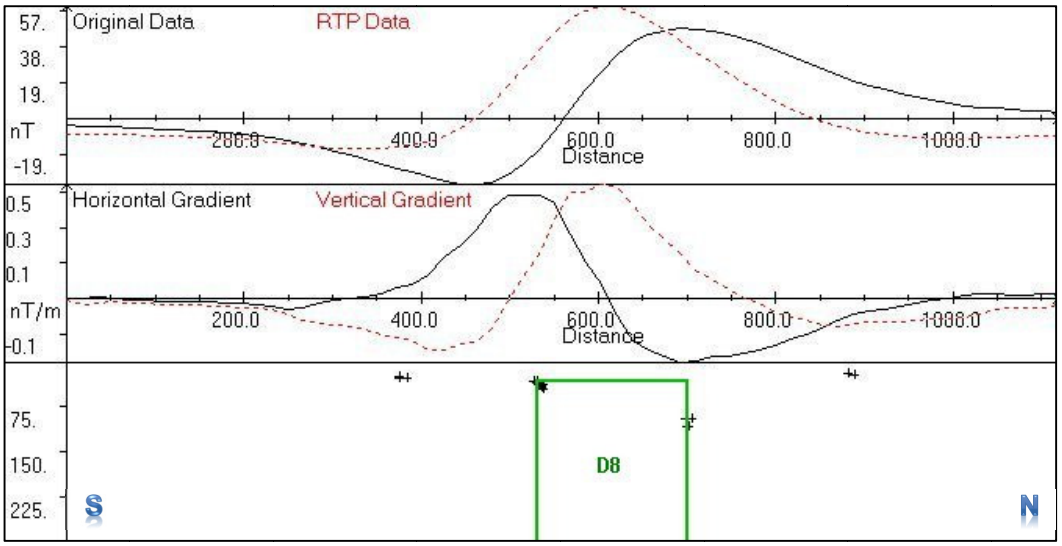


Figure 7.66. Euler deconvolution results for profile 3 with the inferred body shown in green.

7.3.4. Profile 4

Profile 4 is an east-west trending profile across plug P1. The profile was modelled in section 7.2.4 with one plug. Euler processing using a SI of 2 and window size of 9 resulted in clusters indicating bodies as shown in Figure 7.67. The plug P1 is located at a depth of about 186 m and is about 200 m wide.

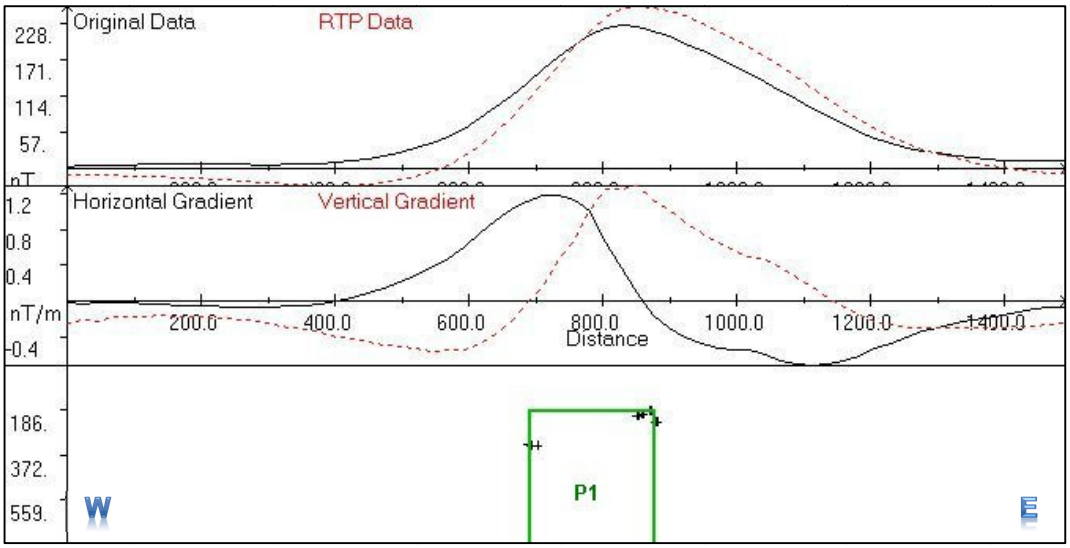


Figure 7.67. Euler deconvolution results for profile 4 with the inferred body shown in green.

7.3.5. Profile 5

Profile 5 is a north-northwest trending profile across dyke D33 and an unnamed dyke north of D33. The profile was modelled in section 7.2.5 with two positively magnetised dykes. Euler processing using a SI of 1 and window size of 11 resulted in clusters indicating bodies as shown in Figure 7.68.

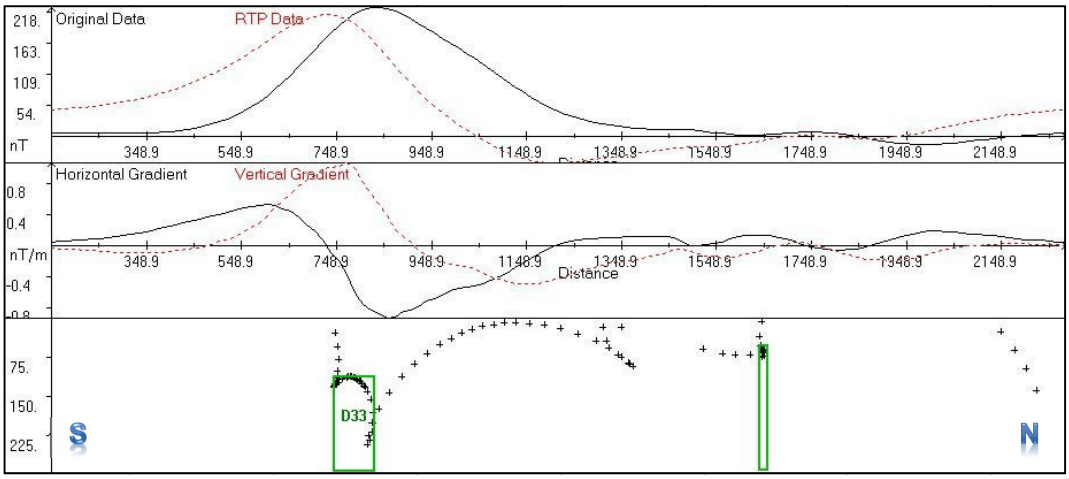


Figure 7.68. Euler deconvolution results for profile 5 with the inferred locations of the dykes shown in green.

The dyke D33 is located at a depth of about 100 m and is about 100 m wide. The unnamed dyke is located at a depth of about 40 m and is about 25 m wide.

7.3.6. Profile 6

Profile 6 is a north-northwest trending profile across dyke D23 and two unnamed dykes, one either side of D23. The profile was modelled in section 7.2.6 with two positively magnetised dykes and a remanently magnetised dyke north of D23. Euler processing using a SI of 1 and window size of 15 resulted in clusters indicating three possible bodies as shown in Figure 7.69.

The dyke south of D23 is at ±550 m depth and is about 70 m wide. D23 is at 410 m depth and is ±100 wide while the unnamed dyke north of D23 is about 380 m deep and 75 m wide.

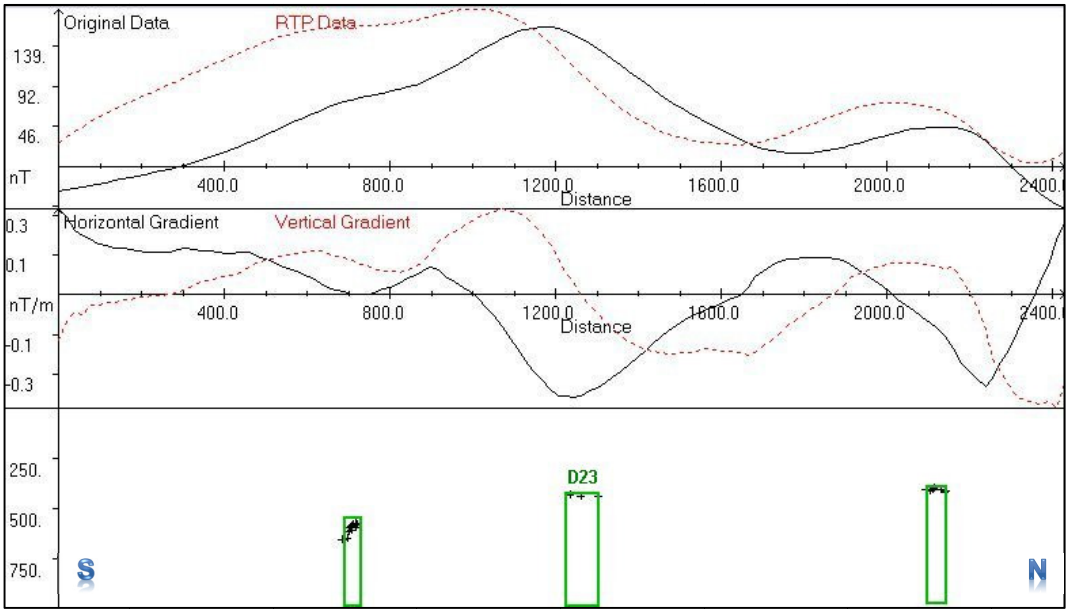


Figure 7.69. Results from Euler deconvolution over profile 6 with the possible 3 bodies shown in green.

7.3.7. Profile 7

Profile 7 is an almost north-south trending profile across dyke D4 and an unnamed dyke north of D4. The profile was modelled in section 7.2.7 with two positively magnetised dykes. Euler processing using a SI of 1 and window size of 9 resulted in clusters indicating two possible bodies as shown in Figure 7.70.

The dyke D4 seems to be at depth ± 50 m and about 130 m wide. The unnamed dyke to the north is deeper at about 600 m and is about 30 m wide.

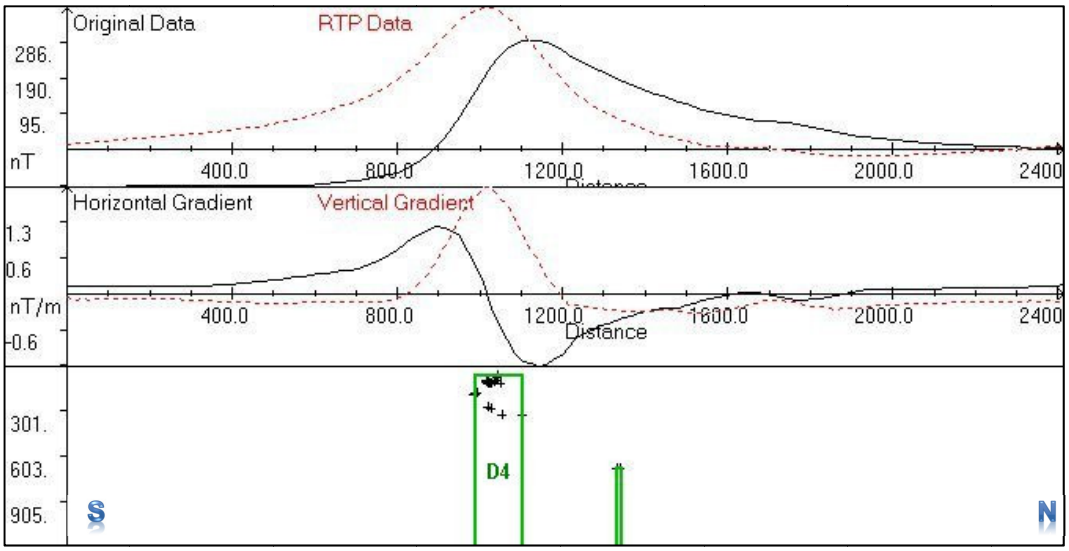


Figure 7.70. Euler deconvolution results for profile 7 with the inferred bodies shown in green.

7.3.8. Profile 8

Profile 8 is a northwest trending profile across dyke D16, an unnamed round anomaly and an unnamed dyke in the north. The profile was modelled in section 7.2.8 with two positively magnetised dykes and a remanent plug. Euler processing using a SI of 1 for the dykes and 2 for the plug with a window size of 9 resulted in clusters indicating the three bodies as shown in Figure 7.71.

Dyke D16 according to Euler processing is at about 50 m depth and is about 300 m wide. The remanently magnetised plug is about 30 m deep and 210 m in diameter. The positively magnetised unnamed dyke north of the plug is about 30 m deep and 250 m wide.

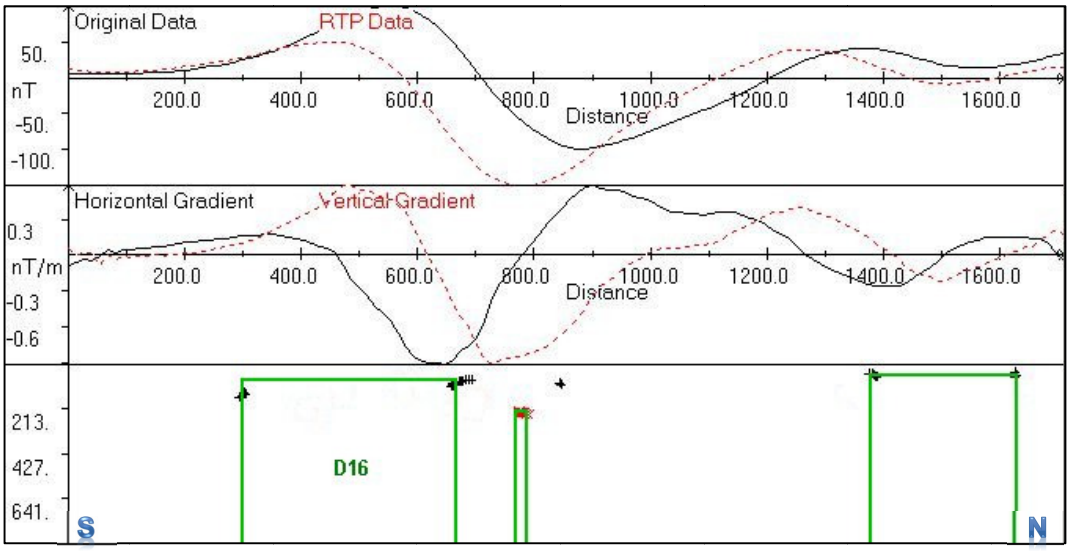


Figure 7.71. Euler deconvolution results for profile 8 showing three inferred bodies shown in green. The black clusters are for SI = 1 and the red cluster for SI = 2.

7.3.9. Profile 9

Profile 9 is a north-northwest trending profile across dykes D11 and D12 and an unnamed dyke south of D11. The profile was modelled in section 7.2.9 with two positively magnetised dykes and a remanent dyke. Euler processing using a SI of 1 with a window size of 7 resulted in clusters indicating the three bodies as shown in Figure 7.72.

D12 is located about 15 m depth and is about 150 m wide. D11 about 110 m deep and 20 m wide and the unnamed dyke to the south is 50 m deep and 60 m wide.

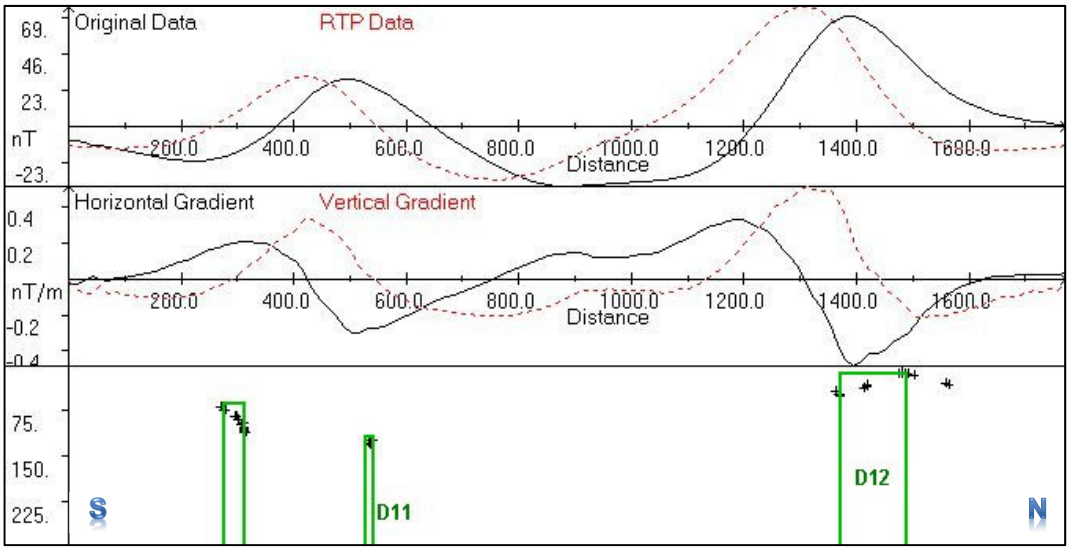


Figure 7.72. Euler deconvolution results for profile 9 with the inferred bodies shown in green.

7.3.10. Profile 10

Profile 10 is a north-northwest trending profile across dyke D13 and an unnamed dyke north of D13. The profile was modelled in section 7.2.10 with two positively magnetised dykes and a positively magnetised body to the south. Euler processing using a SI of 1 with a window size of 7 resulted in clusters indicating the edges of three bodies as shown in Figure 7.73.

The clusters of results in the south seems to indicate a body at 150 m depth with a width of 310 m. D13 seems to be located at a depth of about 100 m with a width of about 300 m and the unnamed dyke in the north seems to be at 160 m depth with a width of about 40 m.

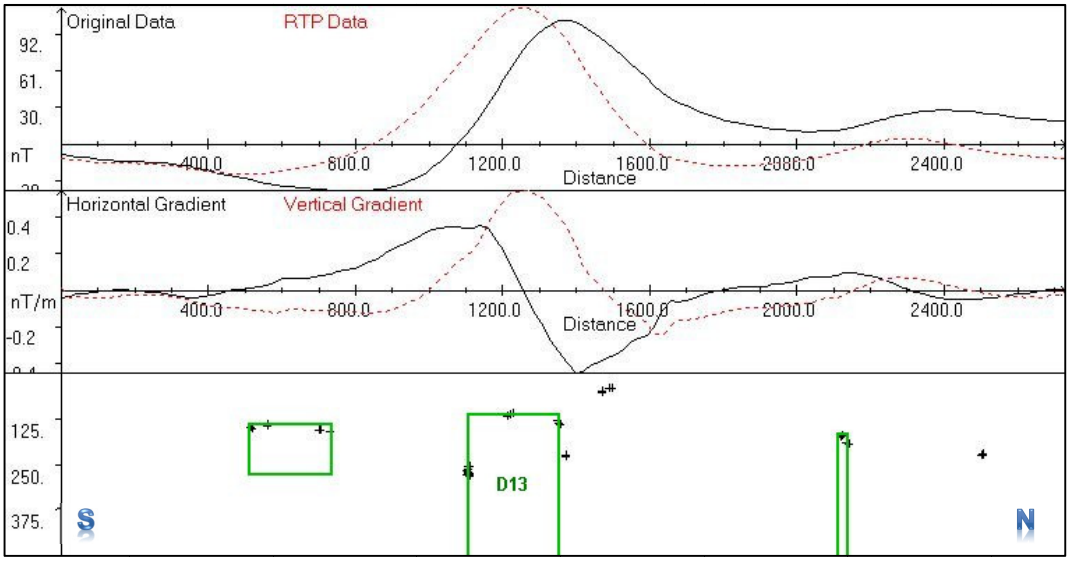


Figure 7.73. Euler deconvolution results for profile 10 with the three bodies shown in green.

7.3.11. Profile 11

Profile 11 is a northwest trending line across dyke D14 and was modelled in section 7.2.11 with three positively magnetised dykes. Figure 7.74 shows the results of Euler processing with SI of 1 and a window size of 9 over the northwest trending profile 11, intersecting dyke D14 and two unnamed dykes, one either side of D14.

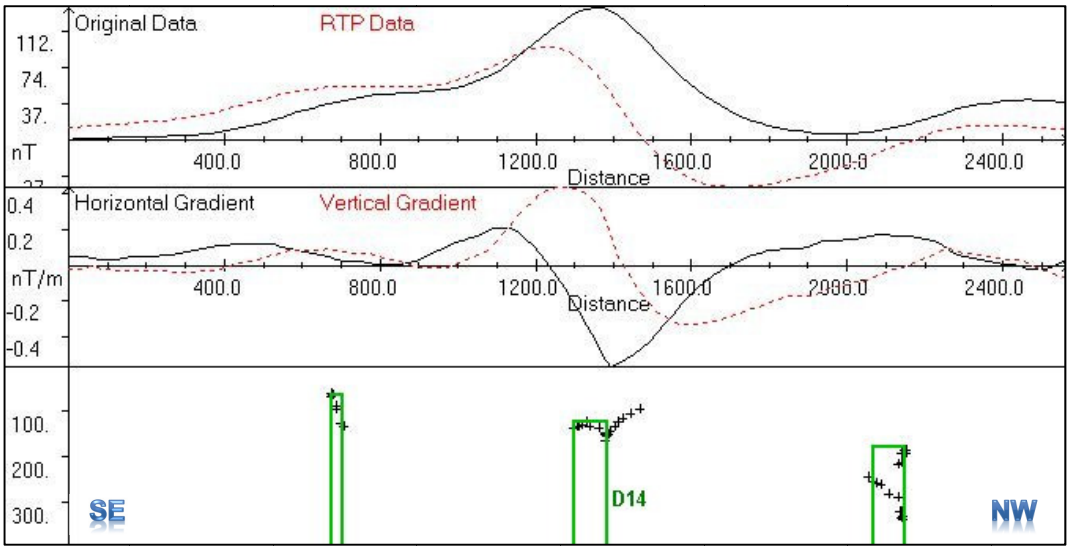


Figure 7.74. Euler deconvolution results for profile 11 with clusters of results indicating three bodies shown in green.

The clusters of data points indicate three bodies as shown in green in Figure 7.74. The dyke southeast of D14 is about 50 m deep and 50 m wide, while the dyke northwest of D14 is ± 150 m deep and ± 100 m wide. Dyke D14 is about 100 m deep and 110 m wide.

7.3.12. Profile 12

Profile 12 is an almost north-south trending profile intersecting dyke D24 and one dyke either side of D24. The profile was modelled in section 7.2.12 with three positively magnetised dykes. The Euler results over profile 12 using SI 1 and window size 9 are shown in Figure 7.75.

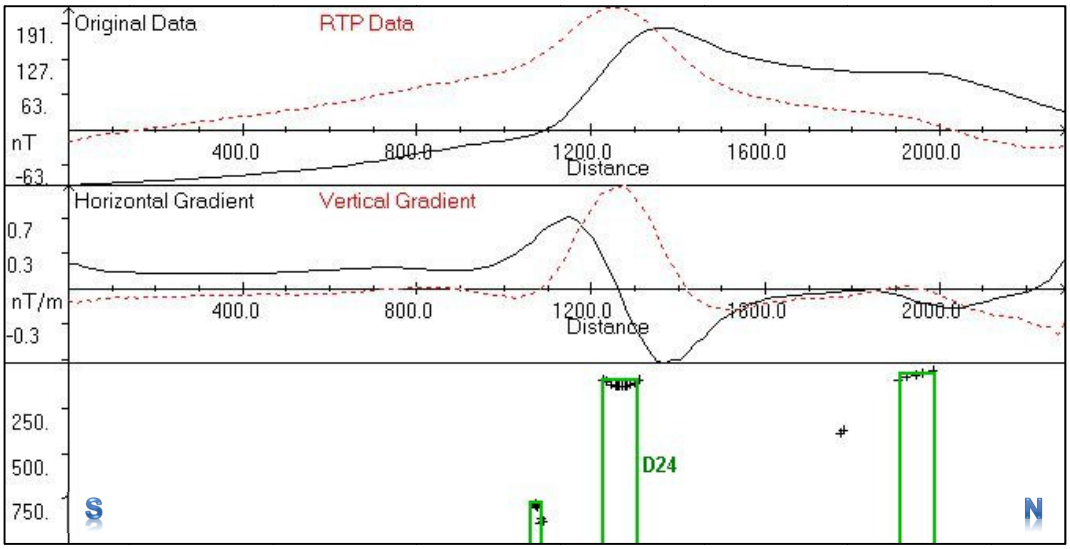


Figure 7.75. Euler deconvolution results for profile 12 with SI of 1 and window size 9. The inferred bodies are shown in green

The body south of D24 is at a depth of ± 750 m and is about 50 m wide. Dyke D24 is at ± 50 m depth with a width of ± 100 m and the dyke north of D24 is about 30 m deep and 100 m wide.

7.3.13. Profile 13

Profile 13 is almost north-south trending and crosses dyke D28. It was modelled with a single dyke in section 7.2.13. Euler deconvolution was applied to the profile data using SI 1 and a window size of 11. The results are shown in Figure 7.76.

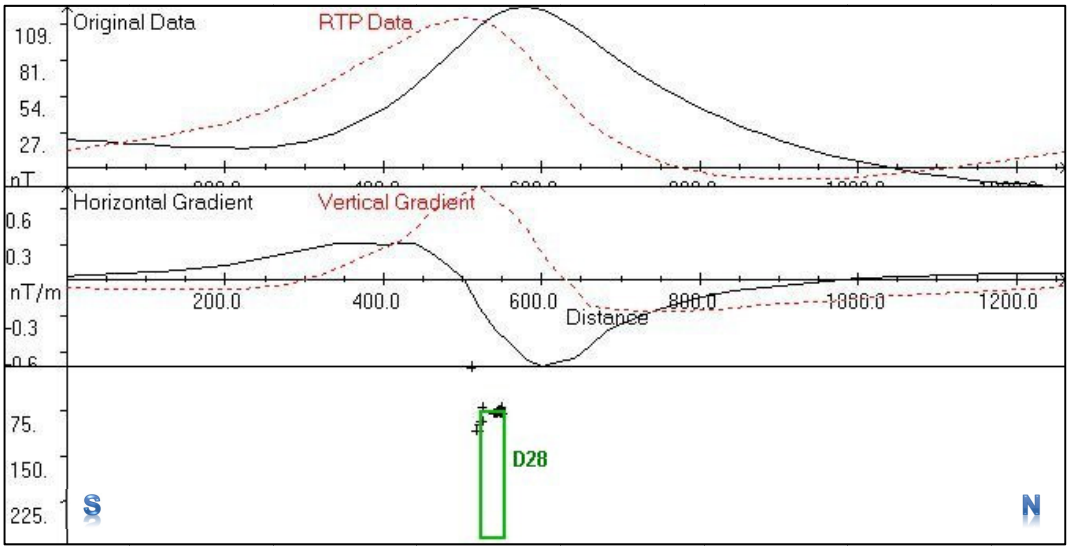


Figure 7.76. Euler deconvolution results for profile 13 with SI = 1 and window size 11. The dyke is shown in green.

According to the results the dyke D28 is at depth of about 70 m and has a width of about 50 m.

7.3.14. Profile 14

Profile 14 is a northwest trending line across dyke D29. It is modelled in 7.2.14 with a dyke (D29) and an unnamed body to the southeast of D29. The results from Euler deconvolution using an SI value of 1 and a window size of 7 is shown in Figure 7.77. The dyke D29 seems to be about 30 m deep and 80 m wide.

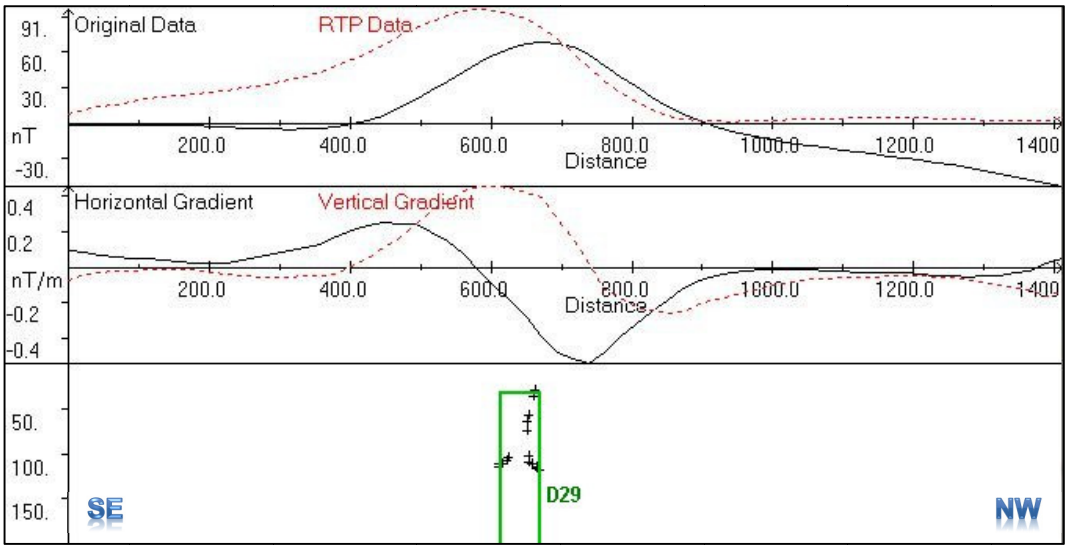


Figure 7.77. Results of Euler deconvolution for profile 14, using SI of 1 and a window size of 7. The dyke D29 is shown in green.

7.3.15. Profile 15

Profile 15 is also a northwest trending line across dyke D7. The profile was modelled in section 7.2.15 with two dykes, a remanently magnetised D7 and a positively magnetised unnamed dyke northwest of it. The results of Euler deconvolution is shown in Figure 7.78. A window size of 7 was used along with an SI of 1.

According to the Euler results, D7 is at a depth of about 80 m and has a width of about 30 m while the dyke to the northwest is about 110 m deep and 15 m wide.

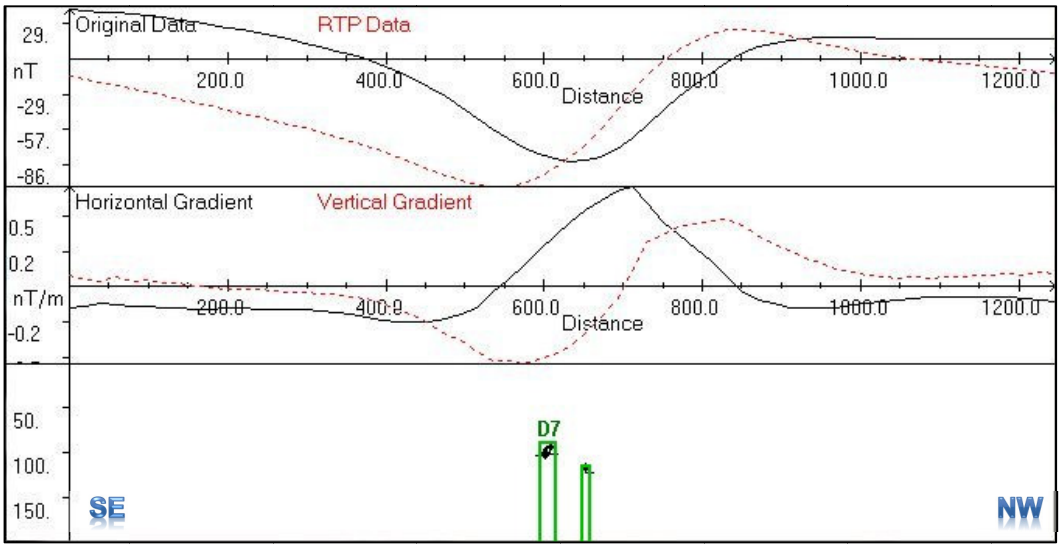


Figure 7.78. Euler deconvolution results using an SI value of 1 and a window size of 7. The positions of the bodies are shown in green.

7.3.16. Profile 16

Profile 16 is a north-south trending line across dyke D1. The profile was modelled in section 7.2.16 with a single dyke, D1. The results of the Euler deconvolution are shown in Figure 7.79 using an SI value of 1 with a window size of 7. The depth of D1 is ± 70 m and the width about 130 m.

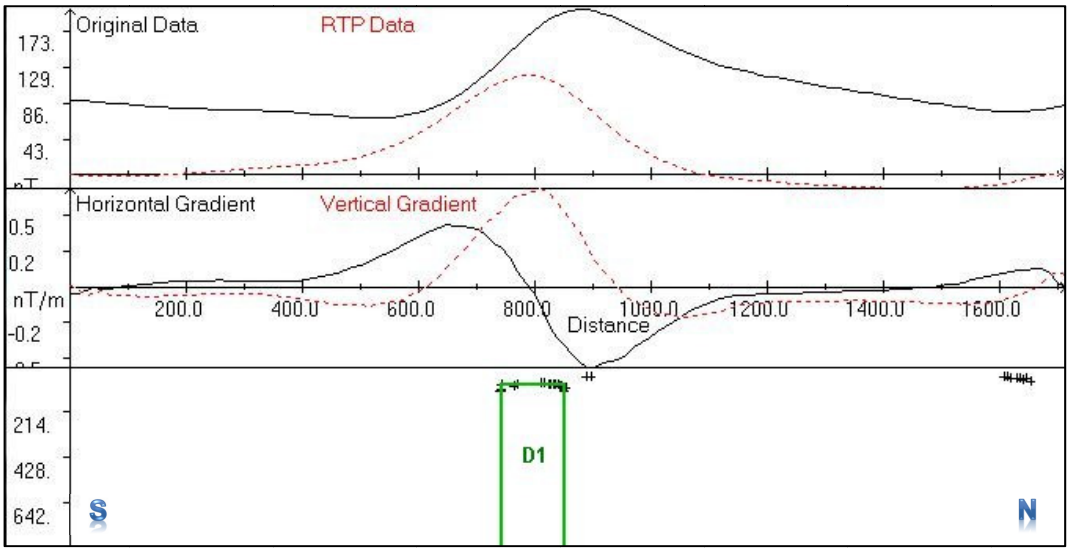


Figure 7.79. Euler deconvolution results for profile 16 using SI 1 and a window size of 7. The position of the dyke is shown in green.

7.3.17. Profile 17

Profile 17 is a north-northeast trending line across dyke D3. The profile was modelled with a single positively magnetised dyke in section 7.2.17. Euler deconvolution was applied to the profile data usning SI 1 and a window size of 11. The results are shown in Figure 7.80.

According to the Euler results it seems the dyke is at a depth of about 10 m and is about 110 m wide.

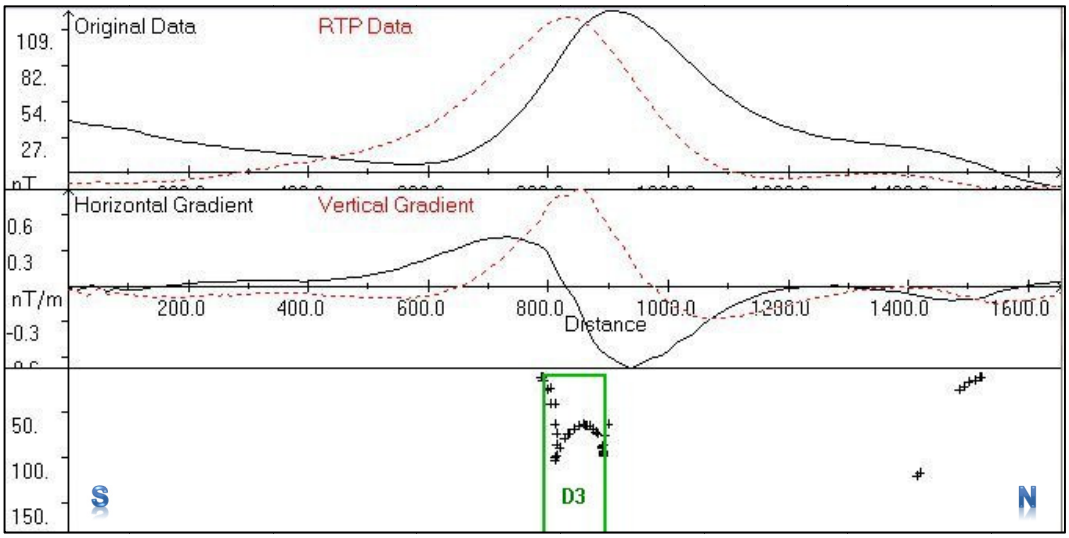


Figure 7.80. Results of Euler deconvolution for profile 17 using SI 1 and a window size of 11. The position of dyke D3 is shown in green.

7.3.18. Profile 18

Profile 18 is an almost north-south trending line across dyke D30. It is modelled in section 7.2.18 with dyke D30 and two dykes north of it, the furthest north one being remanently magnetised. Euler deconvolution was applied to the profile data and the results of using SI 1 and a window size of 9 are shown in Figure 7.81.

According to the Euler results, dyke D30 is about 75 m deep and 130 m wide, the dyke directly north of D30 is about 500 m deep and 20 m wide and the remanently magnetized dyke in the north is about 200 m deep and 150 m wide.

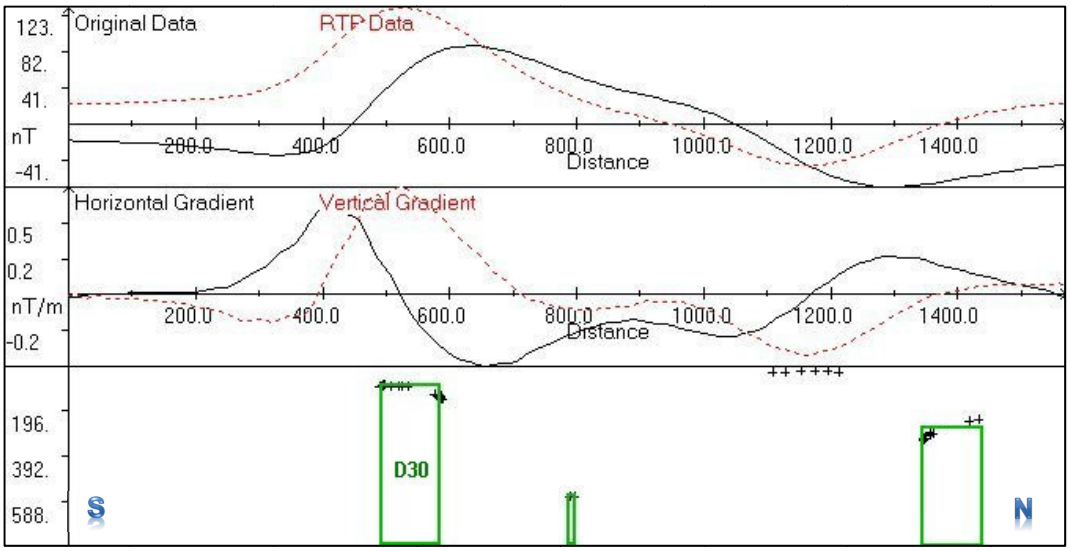


Figure 7.81. Euler deconvolution results of profile 18 with SI 1 and window size 9. Dykes are shown in green.

7.3.19. Profile 19

Profile 19 is a northwest trending line across dyke D31 and D32. It is modelled in section 7.2.19 with two dykes close to each other. Euler deconvolution was applied to the profile data and the results of using SI 1 and a window size of 11 are shown in Figure 7.82.

According to the Euler results, dyke D31 is about 80 m deep and 25 m wide and dyke D32 in the north west is about 240 m deep and 150 m wide.

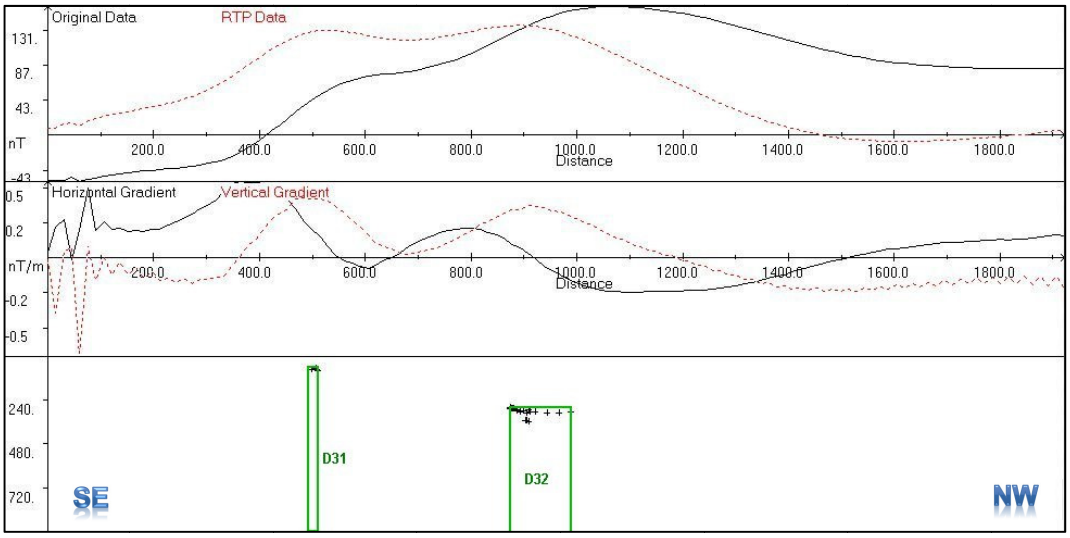


Figure 7.82. Euler deconvolution results for profile 19 using SI 1 and window size 11. The two dykes are shown in green.

7.3.20. Profile 20

Profile 20 trends north-south and intersects dyke D25. It was modelled with a positively magnetized dyke (D25) and a remanently magnetised body to the north in section 7.2.20. Euler deconvolution was applied to the profile data and the results when using SI 1 and window size 9 are shown in Figure 7.83.

According to the Euler results, D25 is about 40 m deep and 180 m wide while the body to the north of D25 seems to be at a depth of about 20 m. Since the is only a single cluster on the one end of the anomaly it is unclear how wide the body is. The body to the south is at a depth of about 125 m and could be about 100 m wide if the second cluster of points to the far south indicates a vertical edge to this body.

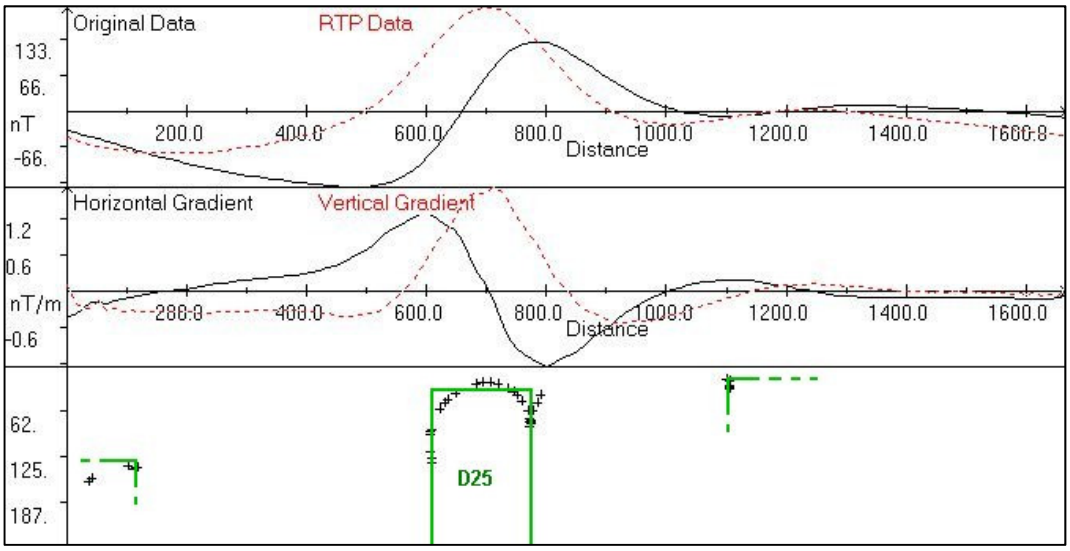


Figure 7.83. Euler deconvolution results for profile 20 using SI 1 and window size 9. D25 is shown in solid green outline and the possible edges of two other bodies are shown is green dashes.

7.3.21. Profile 21

Profile 21 trends north-south and intersects two plugs, P3 and P4. It was modelled with two plugs in section 7.2.21. Euler deconvolution was applied to the profile data and the results when using SI 2 and window size 9 are shown in Figure 7.84.

According to the Euler results, P3 is about 120 m deep and 90 m wide. The plug to the north, P4 is about 80 m deep and 70 m wide.

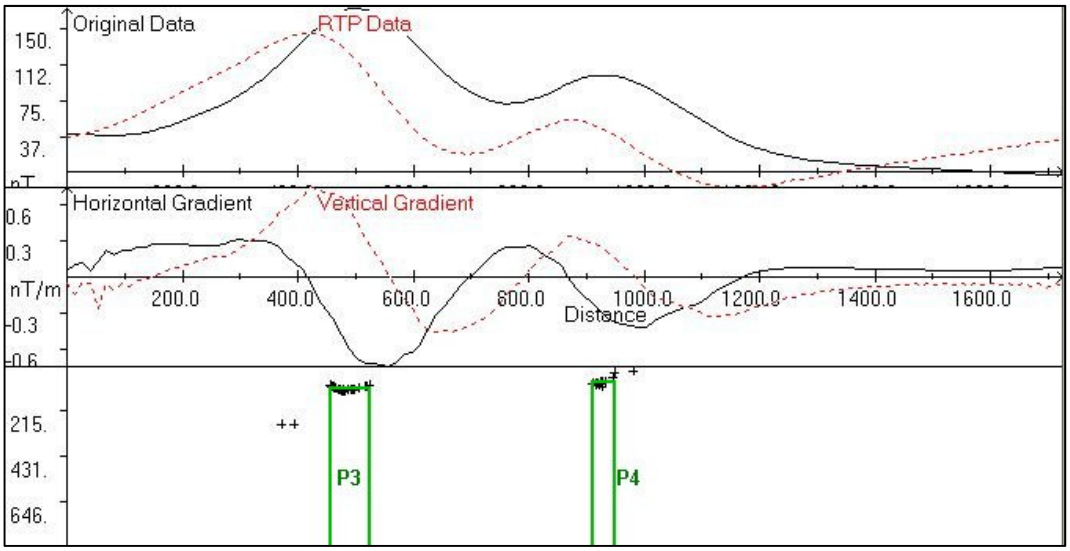


Figure 7.84. Euler deconvolution results for profile 21 using window size 9 and SI 2. The two plugs are shown in green.

7.3.22. Profile 22

Profile 22 is a north-south trending line across plug P2. It was modelled in section 7.2.22. Euler deconvolution was applied to the profile data and the results when using an SI value of 2 and window size of 7 are shown in Figure 7.85.

The depth of the plug according to the Euler results is about 20 m and the width about 150 m.

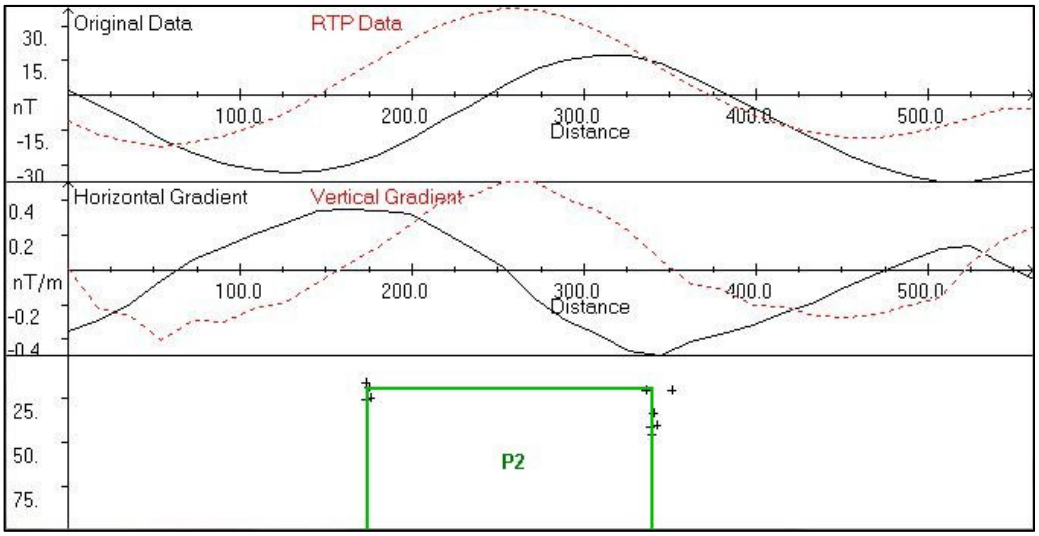


Figure 7.85. Euler deconvolution for profile 22 with SI 2 and window size 7. Plug position is shown in green.

7.5. Conclusion of quantitative interpretation

Twenty-two profiles were extracted from the data in specific locations across dykes that will be modelled in chapter 8. Euler deconvolution was also applied to the profile data and compared to the depth and width values obtained by the modelling. The values are compared and listed in Table 7.3. The cells coloured blue indicate a difference in value between modelled and Euler of less than 30%. Cells in red indicate a difference in value of more than 60%. It would seem that in most cases the modelled depths and widths compare quite favourably with the values obtained from Euler deconvolution.

Table 7.3. Comparison between modelled body depth and width and values inferred from Euler deconvolution results. Cells in red indicate a difference in value of more than 60%. It would seem that in most cases the modelled depths and widths compare quite favourably with the values obtained from Euler deconvolution.

Profile	Body	Modelled depth (m)	Euler depth (m)	Modelled width (m)	Euler width (m)
1	D9 (south)	19	40	225	50
	D9 (north)	91	90	120	50
	D5	3	100	275	250
	S1	410	10	n/a	n/a
2	D10	65	60	106	100
	Unnamed	43	50	172	100
	D20	94	100	32	30
	Unnamed	125	120	40	50
3	D8	33	35	102	150
4	P1	108	186	200	200
5	D33	455	100	55	100
	Unnamed	125	40	130	25
	Unnamed (S)	408	550	268	70

Profile	Body	Modelled depth (m)	Euler depth (m)	Modelled width (m)	Euler width (m)
6	D23	217	410	49	100
	Unnamed (N)	452	380	72	75
7	D4	44	50	361	130
	Unnamed (N)	574	600	36	30
8	D16	39	50	267	300
	Plug	42	30	124	210
	Unnamed	28	30	310	250
9	Unnamed	45	50	96	60
	D11	75	110	36	20
	D12	21	15	190	150
10	Unnamed (S)	287	150	317	310
	D13	24	100	381	300
	Unnamed (N)	155	160	78	40
11	Unnamed (S)	138	50	165	50
	D14	80	100	272	110
	Unnamed (N)	163	150	315	100
12	Unnamed (S)	271	750	190	50
	D24	53	50	229	100
	Unnamed (N)	278	30	164	100
13	D28	81	70	85	50
14	D29	29	30	159	80
15	D7	73	80	40	30
	Unnamed (N)	19	110	36	15
16	D1	40	70	181	130
17	D3	3	10	182	110
	D30	56	75	125	130

Profile	Body	Modelled depth (m)	Euler depth (m)	Modelled width (m)	Euler width (m)
18	Unnamed 1	60	20	162	500
	Unnamed 2	106	200	163	150
19	D31	96	80	113	25
	D32	236	240	295	150
20	D25	45	40	180	180
	Unnamed	139	20	227	Unknown
21	P3	124	120	181	180
	P4	67	70	76	80
22	P2	22	20	94	150

CHAPTER 8. Modelling of cross sections through the study area

In order to combine all the information collected and interpreted in this study in an approximate 3D sense, cross-sections were modelled from aeromagnetic flight line data along 7 traverses crossing the area (Figure 8.1). Three cross sections run north-south along flight lines from west to east L155, L330 and L353. East-west trending cross sections were constructed from south to north along tie-lines T9020, T9040, T9055 and T9070. Information utilised in the modelling of the traverse includes boreholes drilled in the area (Appendix II) and the traverses modelled in Chapter 7 in addition to the qualitative interpretations in Chapter 6 and the outcrop information summarized in Chapter 3. Flight lines are used, as opposed to gridded data, as they preserve more detail than the gridded data do.

According to Maré and Tabane (2004) there are 3 separate remanence values for rocks of the Beit Bridge Terrane recorded at the same location (22.5° South and 28.5° East) to the west of the study area. (Table 8.1). Because it is not certain whether the basement in the study area is composed of any one or a combination of one or more of the Beit Bridge Terrain rocks given Table 8.1, a value of R_dec = 357.2º and R_inc = -66.4º with intensity ranging between 300 nT and 800 nT was used as an average basement value and those values fitted the data best. Where basement is modelled to consist of higher concentrations of either group 1 or 2 gneisses, they are shown as BB1 and BB2 in the above mentioned figures.

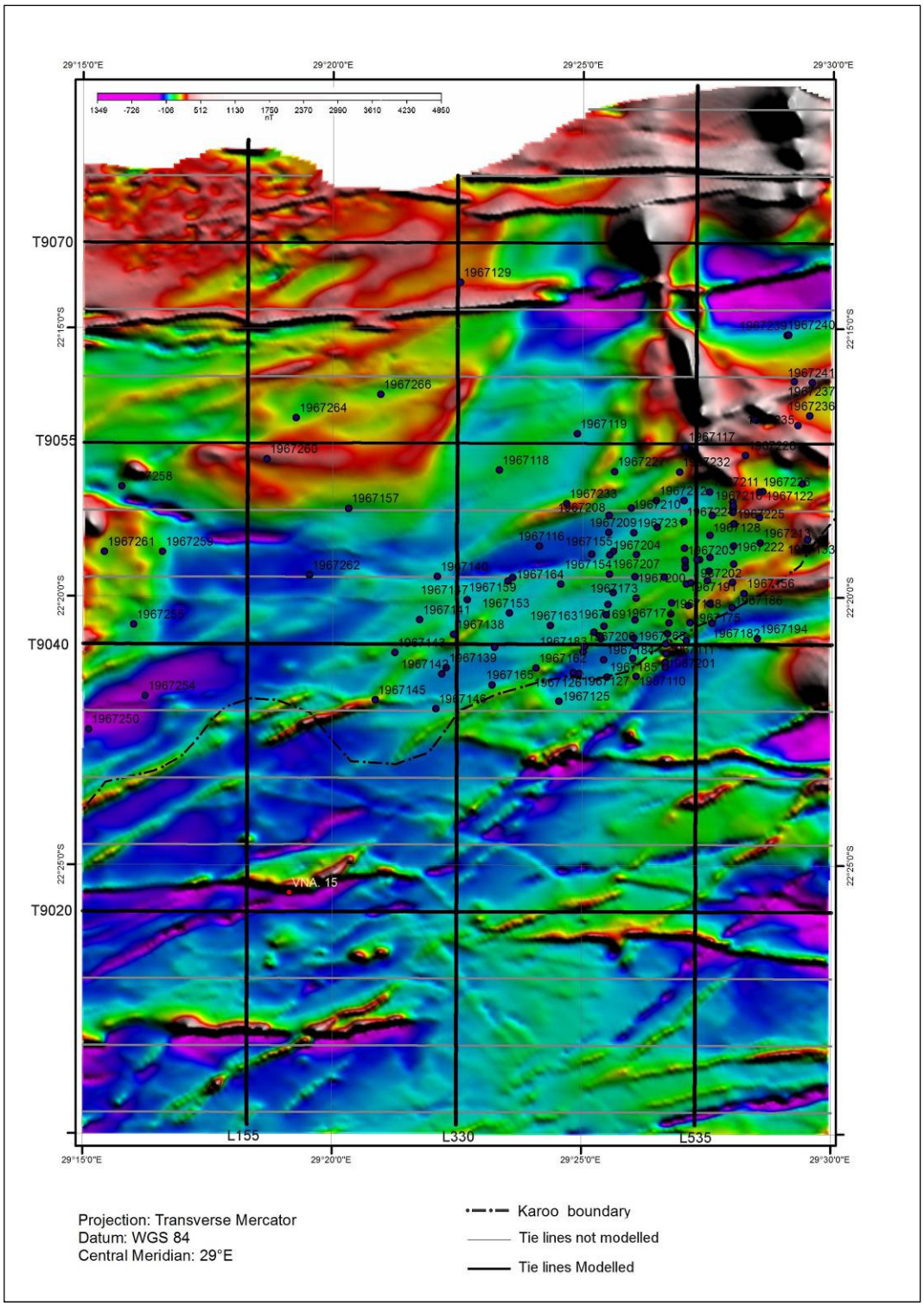


Figure 8.1. Location of flight lines and tie-lines used in modelling, as well as the boreholes used in the modelling.

Table 8.1. Physical properties for Beit Bridge gneisses (Maré and Tabane, 2004).

Lithology	Remanent Declination	Remanent Inclination	Lat	Lon
Beit Bridge gneiss A	352.1	60	-22.5	28.5
Beit Bridge gneiss B	41.1	-6.5	-22.5	28.5
Beit Bridge gneiss C	357.2	-66.4	-22.5	28.5

In an effort to map the topography of the basement under the Karoo rocks and the Karoo itself, the borehole logs of boreholes drilled in the area for coal exploration were used. Since most of these boreholes do not go deep enough to penetrate the basement, they cannot be used to determine depth to basement, but they do shed light on the direction of dip in the Karoo as well as possible vertical displacement of Karoo layers that may indicate post Karoo faulting. A list of the boreholes used in the modelling is given in Table 8.2. For the complete borehole logs, see Appendix II. The boreholes are not equally distributed throughout the region, in many areas there are few constraints on the modelling. The solutions used to model the 7 traverses are shown in Table 8.3. Where the body was modelled in chapter 7, the values determined there are used.

According to Dr. Gunther Brandl (personal communication, 2012, Brandl, 1995, Brandl, 2007), the stress field in the study area has remained virtually unchanged since 2.0 Ga. This stress field is extension in a north-south direction, and thus faults that are roughly perpendicular to this stress field will be normal faults.

Table 8.2. Boreholes used in the modelling.

Borehole Label	Borehole	Borehole ID	Depth (m)	Elevation (m)
BH1	Venetia 15	2000179	267.35	666.0
BH2	Lizzulea	1967262	108.20	579.9
BH3	Hartbeestfontein	1967157	154.53	586.3
BH4	Faure	1967260	89.92	573.8
BH5	Faure	1967264	178.61	589.3
BH6	Luna	1967146	74.07	648.3
BH7	Luna	1967142	156.67	642.6
BH8	Oriental	1967139	99.06	642.0
BH9	Oriental	1967138	160.63	638.4
BH10	Coila	1967147	186.23	635.1
BH11	Luna	1967140	185.93	633.6
BH12	Sardinia	1967118	185.32	610.3
BH13	La Reve	1967129	306.02	603.3
BH14	Kongo	1967180	58.00	631.5
BH15	Kongo	1967175	86.87	618.8
BH16	Schietfontein	1967177	104.98	613.5
BH17	Schietfontein	1967191	104.98	606.2
BH18	Lucca	1967210	112.78	581.0
BH19	Lucca	1967211	93.57	577.9
BH20	Lucca	1967117	88.70	565.3
BH21	Patricia	1967255	37.19	578.4
BH22	Luna	1967143	99.06	635.2
BH23	Coila	1967137	98.76	641.3
BH24	Schietfontein	1967183	85.65	641.7
BH25	Schietfontein	1967171	69.49	637.9

Borehole Label	Borehole	Borehole ID	Depth (m)	Elevation (m)
BH26	Kongo	1967179	60.10	634.1
BH27	Kongo	1967194	120.40	639.6
BH28	Lucca	1967119	203.30	572.6
BH29	Lucca	1967228	67.49	565.4

Table 8.3. Table of physical properties values used in the modelling of the flight lines and tie-lines.

Body label	Description	Susceptibility (SI)	Remanent Intensity (A/m)	Remanent Inclination (°)	Remanent Declination (°)
D1		0.029	0	0	0
D2		0.015	0	0	0
D3		0.01 - 0.015	0	0	0
D4		0.03 - 0.0378	0	0	0
D5	Negative	0.01	357.2	-66.4	0
D6		0.0665	0	0	0
D7	Negative	0.2	480	90	220
D8		0.015	0	0	0
D9		0.287 - 0.03	0	0	0
D10	Negative	0.198	80	90	220
D11	Negative	0.025	80	90	220
D12		0.02	0	0	0
D13		0.01	0	0	0
D14		0.03	0	0	0
D15		0.03	0	0	0
D16		0.0315	0	0	0
D17	Negative	0.19	480	90	220
D18		0.01	0	0	0
D19		0.01	0	0	0
D20	Negative	0.01	80	90	220
D21		0.027	0	0	0
D22		0.15	0	0	0
D23		0.1	357.2	-66.4	0
D24		0.03	0	0	0
D25		0.047	0	0	0
D26		0.03	0	0	0
D27		0.0345	0	0	0
D28		0.0325	0	0	0
D29		0.039	0	0	0
D30		0.0341	0	0	0

Body label	Description	Susceptibility (SI)	Remanent Intensity (A/m)	Remanent Inclination (°)	Remanent Declination (°)
D31		0.0345	0	0	0
D32		0.048	0	0	0
D33		0.01	0	0	0
S1		0.01 -0.019	0	0	0
S3		0.03	0	0	0
BB1	Beit Bridge A	0.01	300 - 800	350	60
BB2	Beit Bridge B	0.1	300 - 800	357.2	-66.4
B1	Basalt	0.03	0	0	0
B2		0.02	0	0	0
B3		0.18	0	0	0
P1		0.06	0	0	0
P2		0.055	0	0	0
P3		0.076	0	0	0

8.1. North-south cross sections

8.1.1. Flight line L155

Flight line L155 (Figure 8.1) is a north-south trending flight line that starts in the south and covers basement rocks, passes west of the Venetia kimberlite pipes, crosses over one of the plug-shaped anomalies and continues over Karoo rocks towards the north. Simplified logs of boreholes that are adjacent to L155 are shown in Figure 8.2. The coal seams are used as markers and it is clear that the seams dip to the north as far as Hartebeestfontein and then the seams are vertically displaced upward by a normal fault but maintain a northward dip .

Figure 8.3 shows the magnetic model for this line. The locations of the boreholes are indicated on the image. The basement can be modelled as containing some sills (S1 on Figure 8.3) and various dykes, both positively (D4, D5, D8, D9, D16, D23 and D33) and negatively magnetised (D10) and a plug-shaped body (P1 in yellow on Figure 8.3). Borehole BH1 (Figure 8.3) intersects dolerite (shown in red and labelled as ‘Dolorite’ on Figure 8.2) at 42 m. This intersection has been modelled as a sill, the extent of which was determined from the qualitative interpretation in Figure 6.22.

The Karoo thickens towards the north. Four boreholes penetrating the Karoo (BH2 - BH5) are indicated on Figure 8.3. Three faults are modelled in the north of the profile; two are shown as faults and D4 is modelled to intrude into the northern most fault. In the far north a possible basalt intrusion used to model the mottled effect (indicated as basalt in Figure 6.9) in the north western part of the aeromagnetic data. Beit Bridge Gneisses 1 (BB1) and 2 (BB2) are modelled beneath the Karoo.

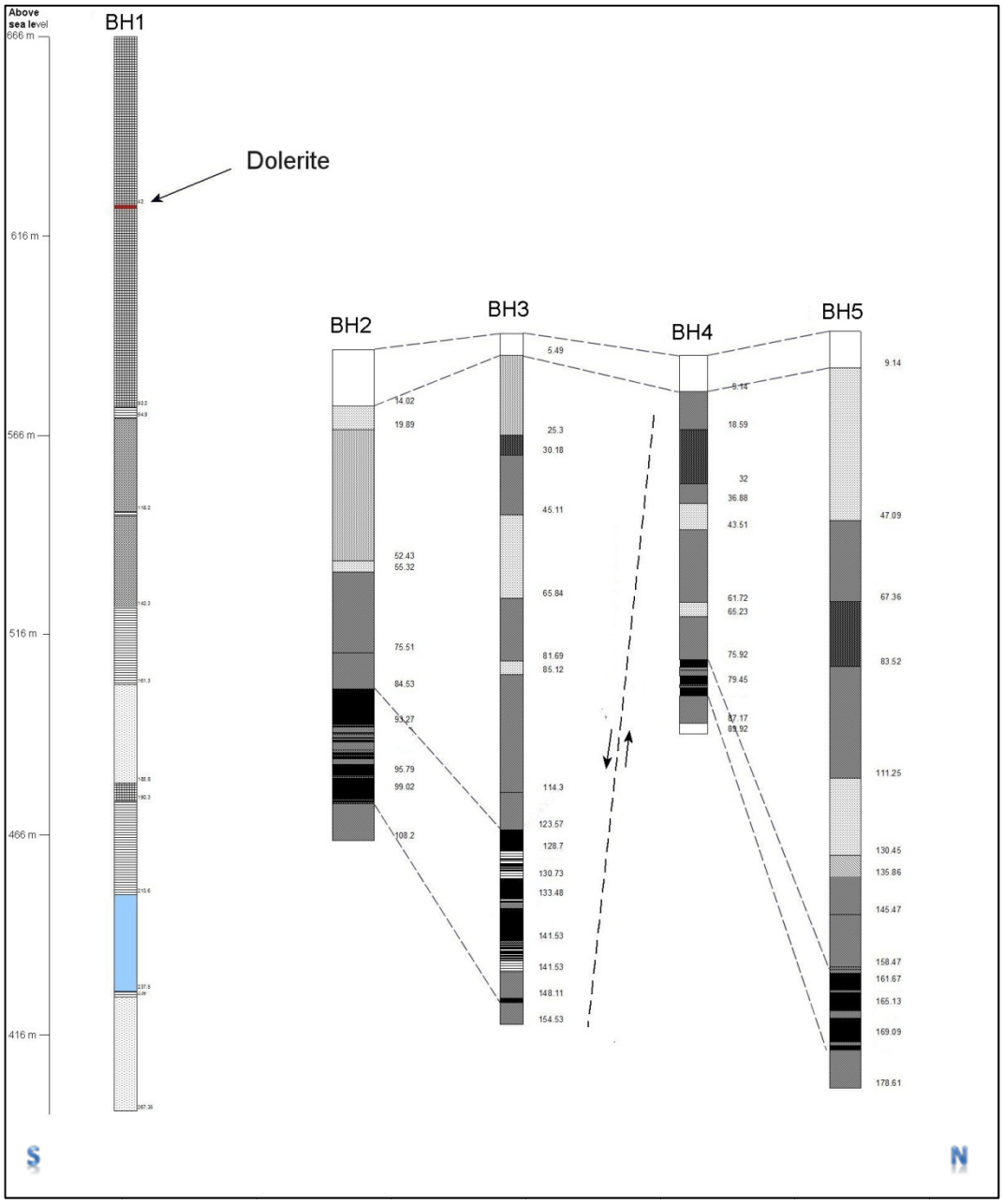


Figure 8.2. Borehole logs of the boreholes adjacent to L155.

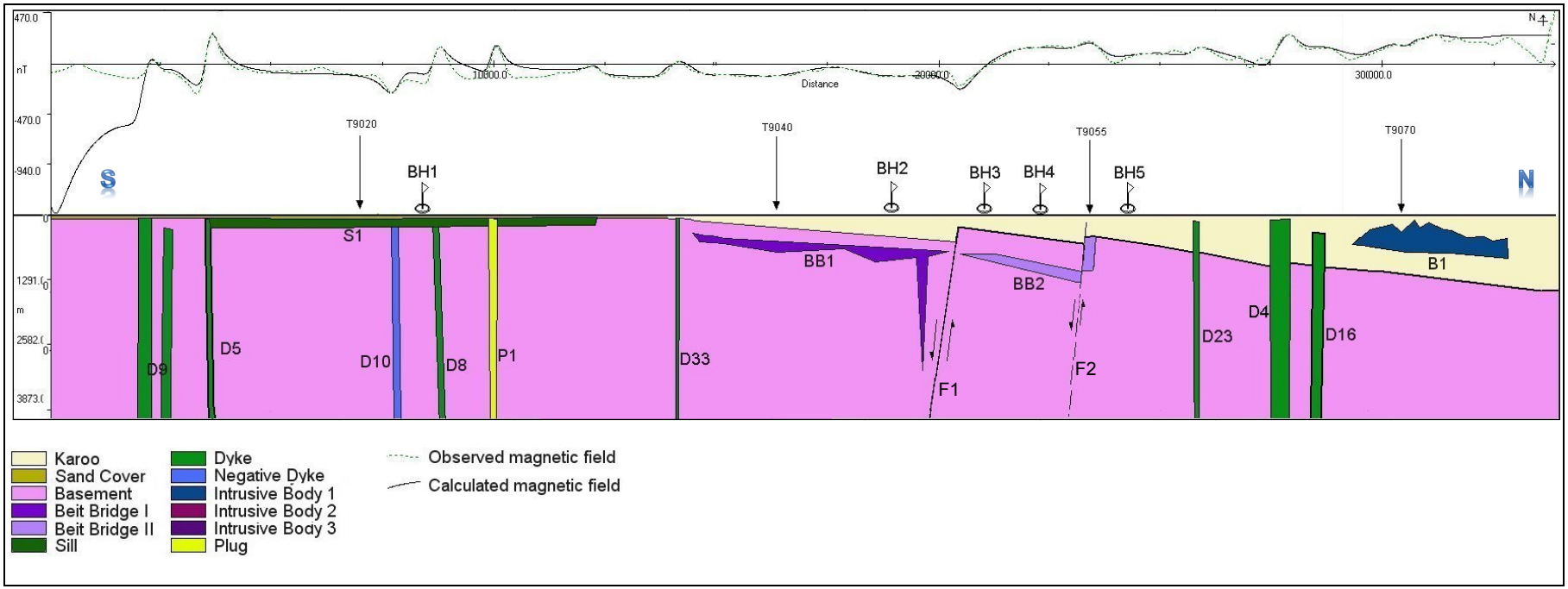


Figure 8.3. L155 modelled in 2.5D using Mag2DC. Depth of profile is 4 km. Not all the geological units in the legend appear in the profile as it is a common key for all models. The mismatch between measured and calculated fields at the ends of the profile is simply due to edge effects of the modelling program.

8.1.2. Flight line L330

Flight line L330 is located roughly in the centre of the study area (Figure 8.1). In the south it covers basement rocks, passes some distance east of the Venetia kimberlite pipes, crosses over various dykes in both basement rocks in the south and Karoo rocks towards the north. Simplified logs of boreholes that are adjacent to L330 are shown in Figure 8.4. With the coal seams used as markers it is clear that the seams dip to the north as far as BH8 (Oriental 1967139). The seams are displaced upward between BH8 and BH9 (Oriental 1967138), interpreted here to be a normal fault. A normal fault also is situated between BH10 (Coila 1967147) and BH11 (Luna 1967140).

The locations of the eight boreholes are indicated on the cross section in Figure 8.5. The same sill or group of sills indicated on cross section L155 appears to extend to the east on the aeromagnetic data and can be modelled in the basement on L330 (S1 on Figure 8.5). The line intersects positive dykes D9, D12, D26, and D3 as well as negatively magnetised dyke D11 (Figure 8.5) south of the Karoo boundary (roughly coinciding with D3 on Figure 8.5). A dyke (D13) and sills (S3) are modelled before the fault with vertical displacement that coincides with D14 is located between BH8 and BH9. A second fault with vertical displacement is modelled between BH10 and BH11. Possible areas of the basement consisting more of Beit Bridge B (BB2) are modelled beneath the Karoo. A portion of what seems to be a graben is mapped beneath BH12. This graben is clearly visible on the magnetic data and tie-line T9055. Quite a large dyke, D4 is modelled south of BH13 towards the northern end of the line. Beit Bridge B (BB2) is modelled beneath S1 in the south of the traverse.

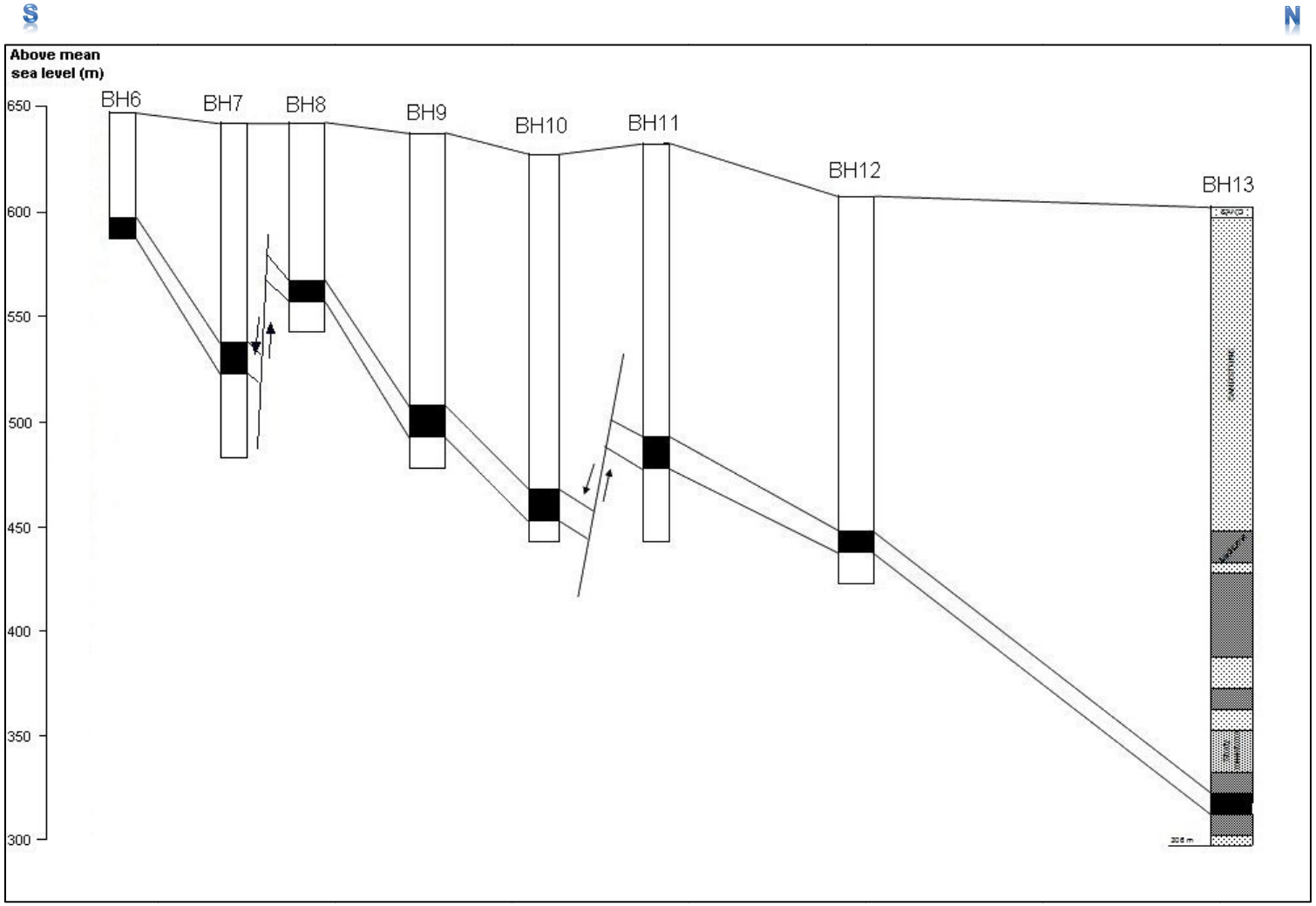


Figure 8.4. Simplified logs of boreholes adjacent to L330. Coal seams are indicated in solid black.

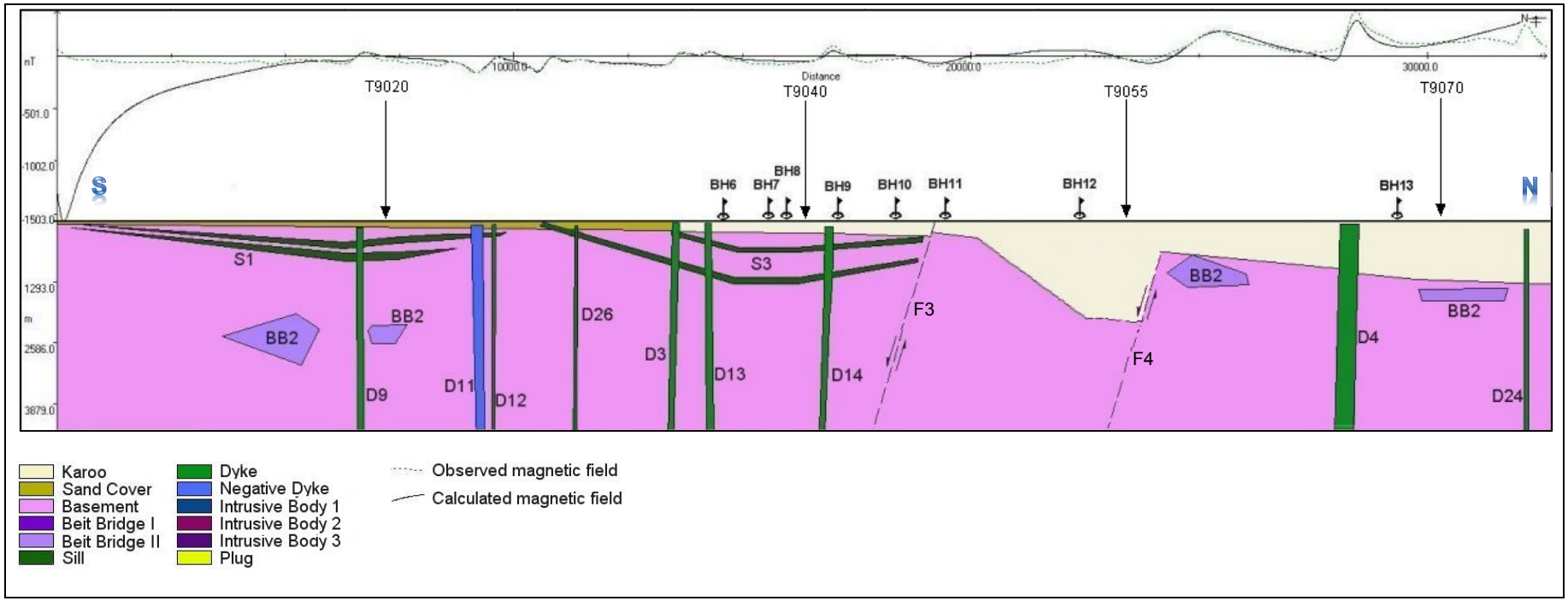


Figure 8.5. Model of L330. South is to the left and north to the right. Depth of profile is 4 km. The mismatch between measured and calculated fields at the ends of the profile is simply due to edge effects of the modelling program.

8.1.3. Flight line L535

The third north-south trending cross section is drawn along flight line L535 near the eastern edge of the study area. In the south it covers basement rocks into which some east-west trending dykes intruded. From there it passes into the Karoo rocks, roughly halfway along the flight line. In the north it crosses some very high amplitude laterally extensive magnetic anomalies. There are numerous boreholes drilled in the Karoo adjacent to L535. Simplified logs of most of them are shown in Figure 8.6. The northward dipping Karoo lithologies are displaced along a normal fault between Lucca 1967210 (BH18) and Lucca 1967117 (BH19). Between BH16 (Schietfontein 1967177) and BH18 (Lucca 1967210) there are seven boreholes ranging between 43.59 m and 163.98 m in depth. BH17 (Schietfontein 1967191) was chosen to represent all these boreholes as it is deep (104.98 m) and very close to L535.

The cross section for this flight line is shown in Figure 8.7. The locations of the seven boreholes are indicated on the image. The basement is intruded by two negative dykes (D7 and D17) and seven positive dykes (D27, D28, D29, D1, D2, D9 and D3). The Karoo boundary is situated between D3 and BH14. The boreholes are clustered in a magnetically quiet area between D3 and D25. The Karoo is quite thin here and the coal seams are close to the surface. The vertical displacement seen in the boreholes coincides with D25. A very magnetic body is modelled in the north (B3). It is not possible to accurately determine from the magnetic data whether the dykes intrude the body or vice-versa. In the image the dyke is modelled to cut B3, but it could be the other way around as well. The source of the anomaly is unknown and the mapped geology of the area does not supply any clues as to what it could be. Drilling will most probably be the only way to determine the source of this anomaly but it could be due to a mafic intrusion. Three positive dykes (D4, D24 and D25) are modelled north of B3. D4 is modelled on L115 and L535.

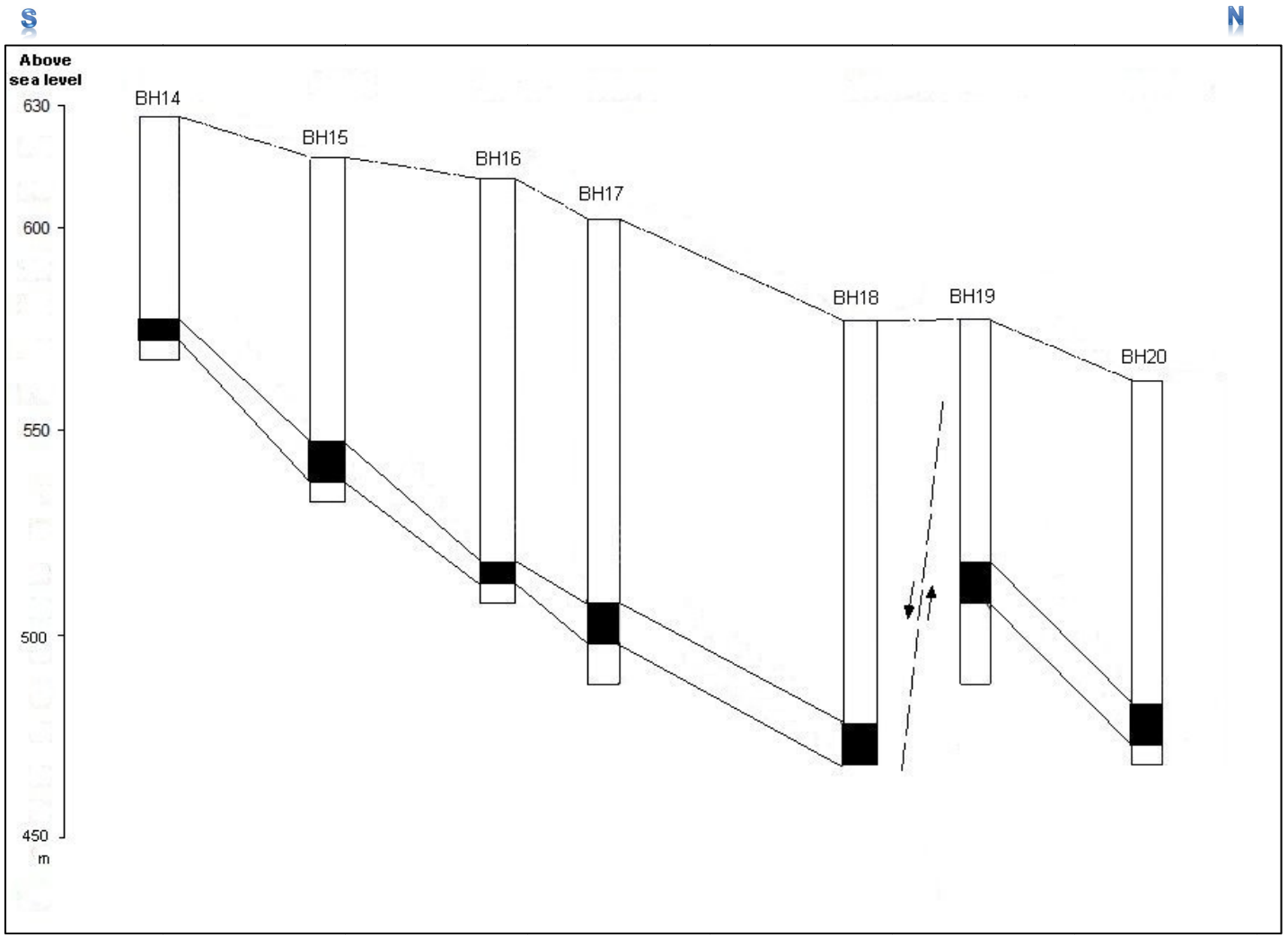


Figure 8.6. Borehole logs of boreholes adjacent to L535. Coal package is indicated in solid black.

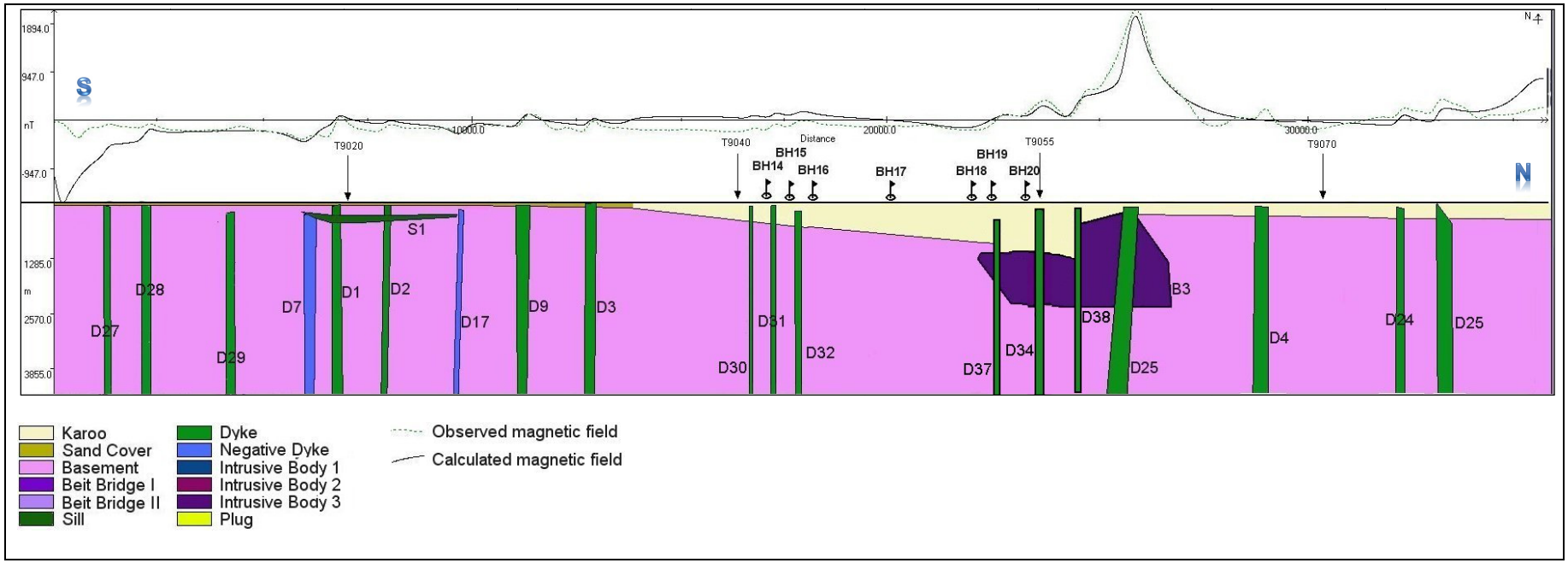


Figure 8.7. Model of flight line L535. Depth of profile is 4 km. The mismatch between measured and calculated fields at the ends of the profile is simply due to effects of the modelling program.

8.2. East-west cross sections

Four east-west trending cross sections were modelled in a similar manner along tie lines.

8.2.1. Tie-line T9020

The cross section (Figure 8.8) along tie line T9020 passes just south of the Venetia Mine and crosses mainly basement rocks. It intersects northeast trending dykes as well as the sill (S1) modelled in cross sections L155 and L330. BH1 is also in the vicinity of the profile.

The model shows three negative dykes in the west (D20 and D10). D10 is displaced and thus is intersected twice along the tie-line. Further east the sill (S1) is encountered followed by a plug (P3). Dyke D9 is also encountered twice due to displacement. Another plug (P2) is traversed further east, followed by two more dykes (D21 and D22) and a negative dyke (D7). The possibility exists that the basement is composed of Beit Bridge B (BB2) is modelled beneath the sills.

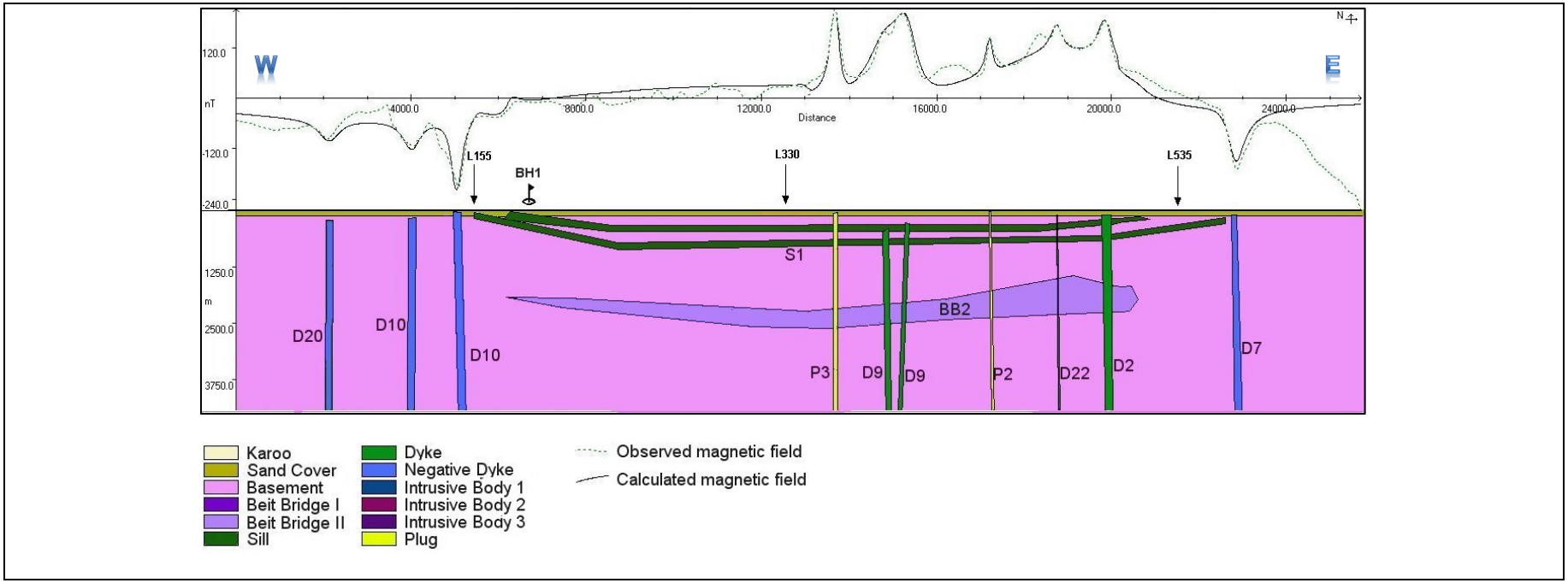


Figure 8.8. Model of Tie-line T9020. West is left and east is right. Depth of profile is 4 km. The mismatch between measured and calculated fields at the ends of the profile is simply due to effects of the modelling program.

8.2.2. Tie-line T9040

The cross section along tie-line T9040 is located at about the centre of the study area. It covers Karoo sediments along its entire length. Between L155 and L535 many northeast trending dykes are intersected. In the far east, it crosses the strongly magnetic body modelled in cross section L535. There are numerous boreholes drilled in the Karoo adjacent to cross section T9040. Simplified logs of most of them are shown in Figure 8.9. The coal seams are dipping towards the west and are displaced along normal faults down thrown to the east.

The locations of the eight boreholes are indicated on cross section T9040 (Figure 8.10). The basement is intruded by three dykes (D8, D17 and D18) and as well as sills (S3), which are also modelled in L330. Beit Bridge B (BB2) is modelled either side of dyke D8. In the east, the same highly magnetic body (B3) as modelled in L535 is indicated. The area is down faulted by three, north to south trending normal faults based on boreholes. The fault between BH21 and BH22 coincides with the topographic ridge that cuts through the area (Figure 5.12). Dyke D18 is modelled to have intruded along the fault between BH5 and BH23.

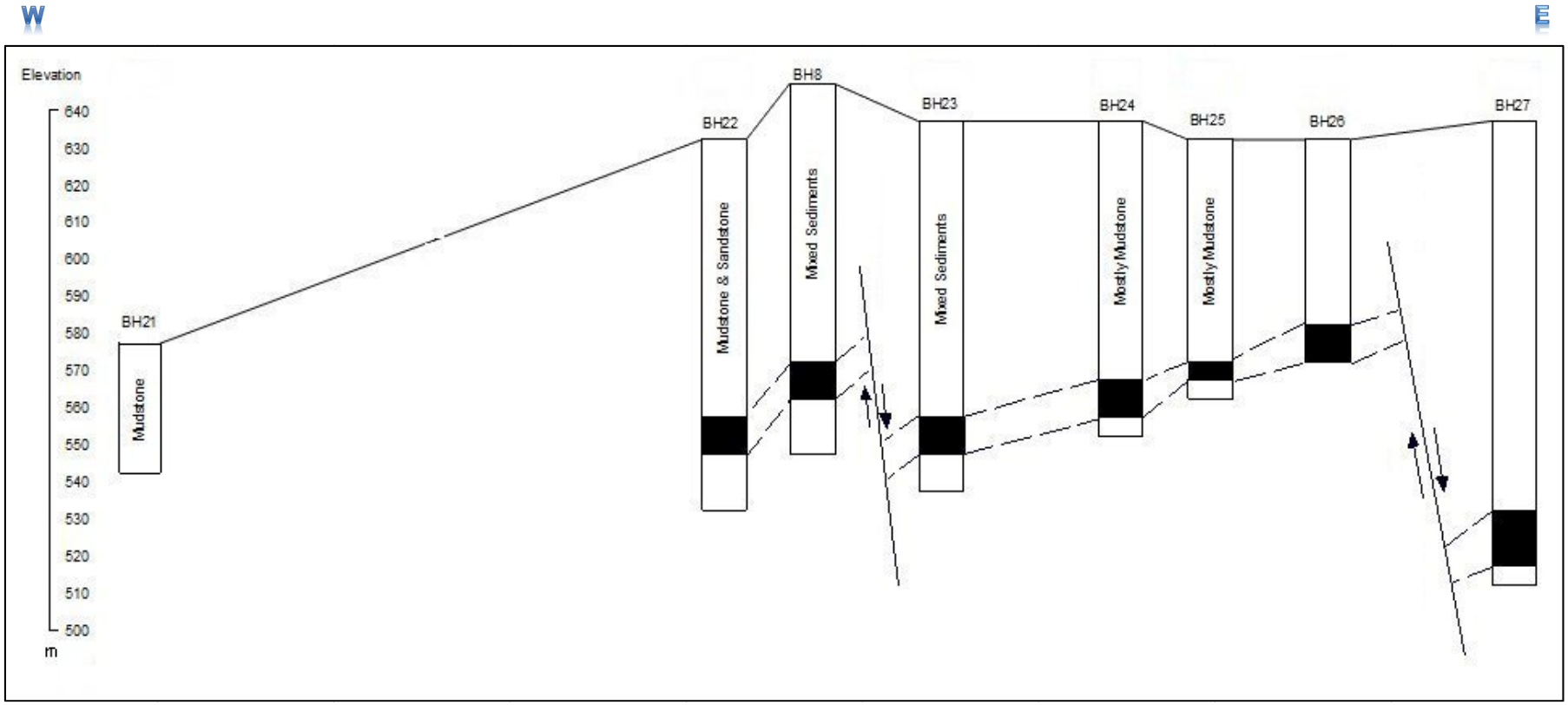


Figure 8.9. Simplified logs of boreholes along T9040. Coal package is indicated in solid black.

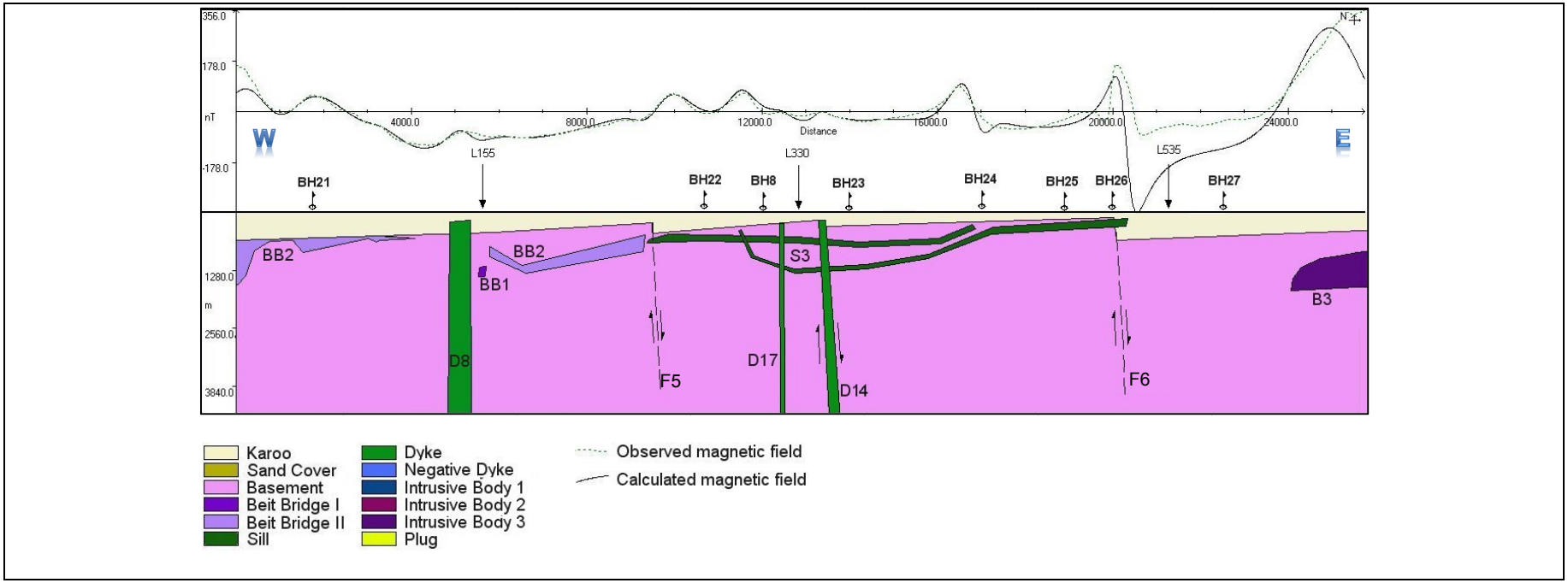


Figure 8.10. Model of tie-line T9040. Depth of profile is 4 km.

8.2.3. Tie-line T9055

The cross section along tie-line T9055 is located in the north of the study area. It covers Karoo sediments along its entire length. Five boreholes were drilled in the Karoo adjacent to cross section T9055 (Figure 8.11). The coal seams suggest a complicated set of faults are present in the area.

The cross section (Figure 8.12) model of the line further shows basement consisting of higher concentration Beit Bridge C rocks (BB2) in the west. The basement is modelled to be down-faulted in the centre of tie-line T9055 to form a graben. BB2 is separated by a normal fault from a body of highly magnetic material (B3). This (B3) magnetic body seems to be displaced by a fault intruded by dyke D24.

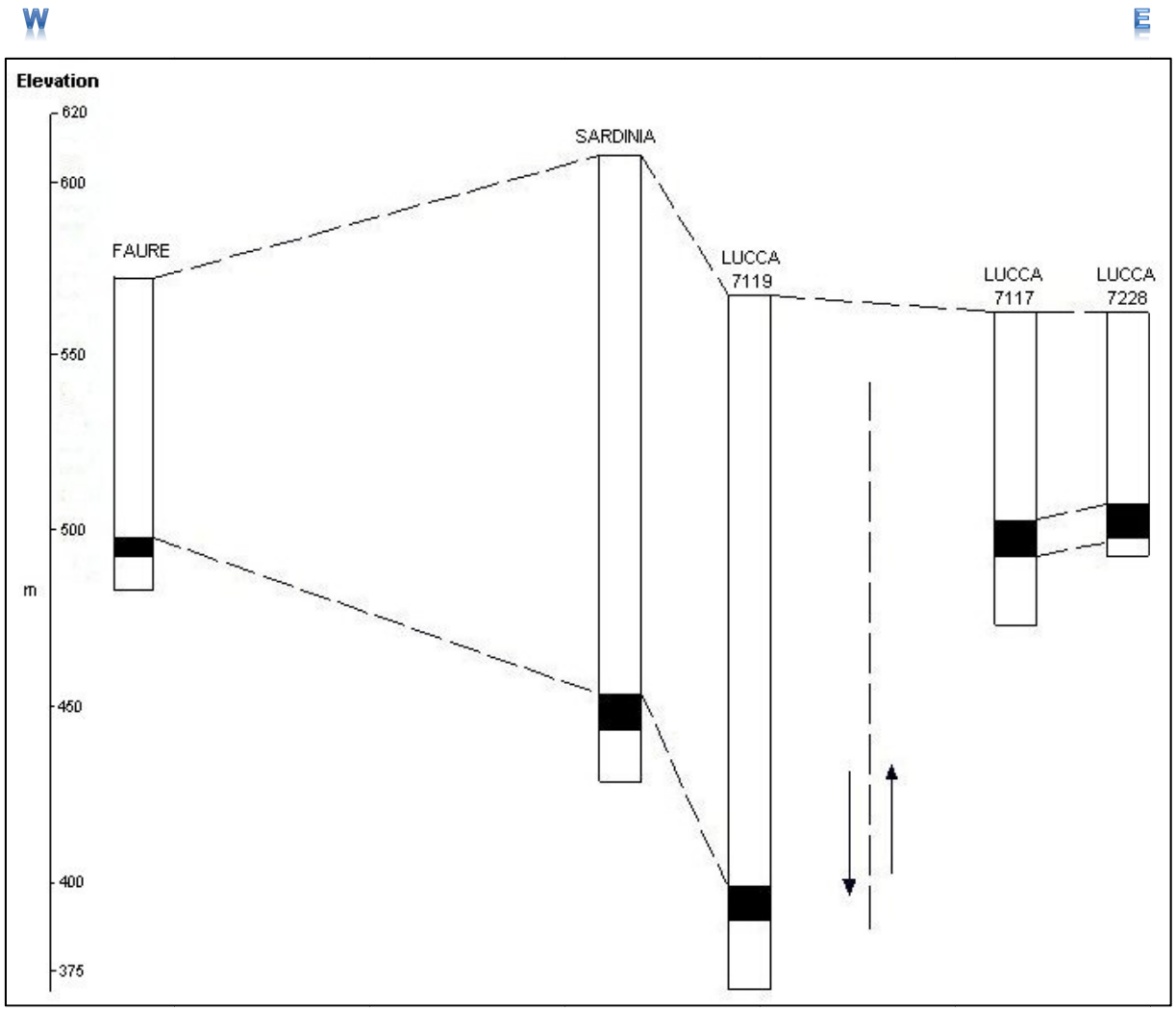


Figure 8.11. Simplified logs of boreholes along T9055. Coal package is indicated in solid black.

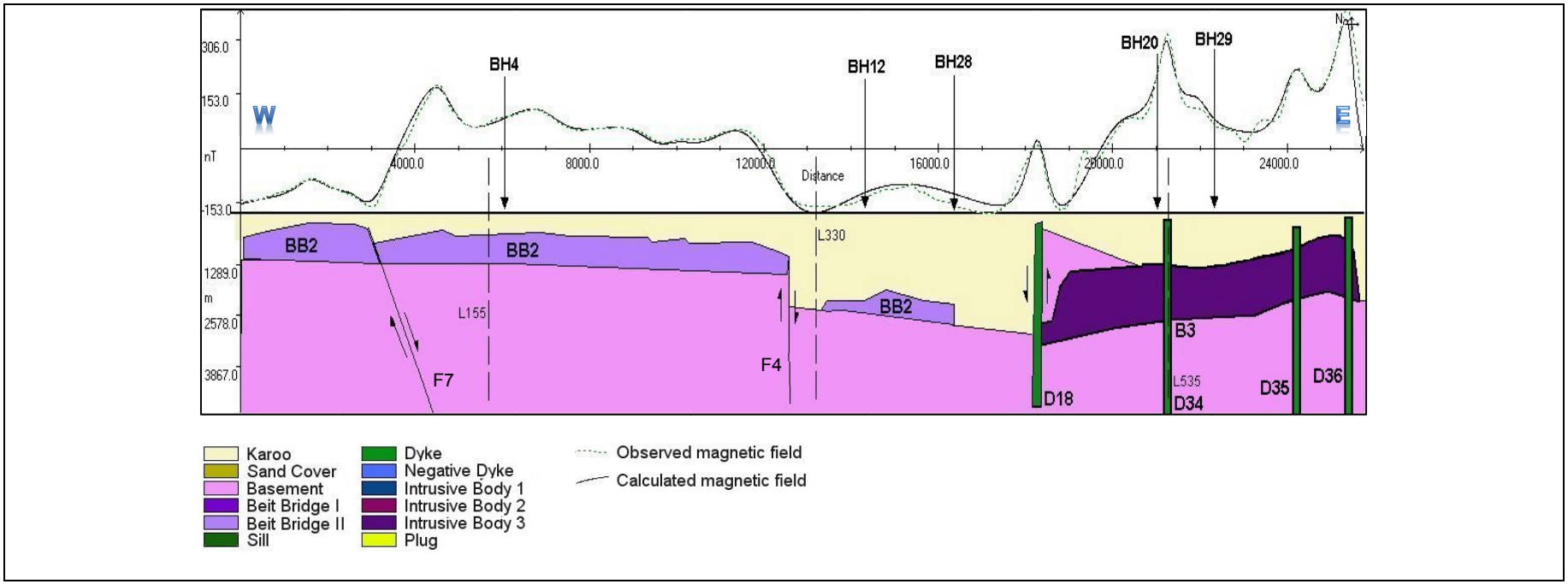


Figure 8.12. Model of tie-line T9055. Depth of profile is 4 km.

8.2.4. Tie-line T9070

The cross section along tie-line T9070 is located in the extreme north of the study area and covers Karoo sediments along its entire length. There are no boreholes which are adjacent to the cross section and hence it is modelled without aid of coal seam markers to indicate dip and possible displacement of layers.

The cross section for this flight line is shown in Figure 8.14. In the west the mottled effect is modelled with a possible basaltic intrusion which may have spatially variable magnetization (B1) in Karoo rocks. It was confirmed using Google Earth that the mottled effect is not due to cultural features (see Figure 8.13).



Figure 8.13. Image from google earth showing the outline of B1 in white.

The elevated magnetic values are modelled to be due to higher concentration of Beit Bridge B (BB2) in the basement. In the east the very high amplitude magnetic anomalies are attributed to a magnetic intrusion (B3). The basement is modelled to be faulted just east of L330, causing the basement in the west to be deeper and thus the Karoo to be thicker.

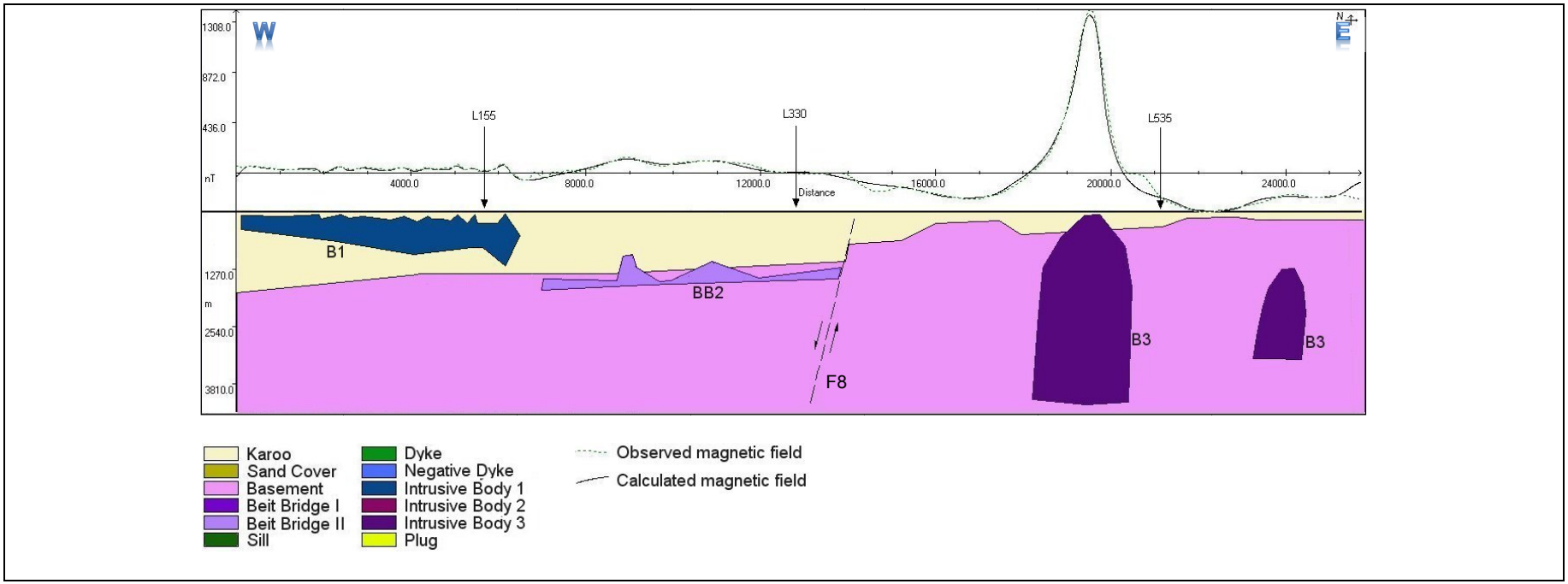


Figure 8.14. Model of tie-line T9070. Depth of profile is 4 km.

8.3. Comparing the geophysical interpretation with mapped geology

When placing the geophysical interpretation and the mapped geology side by side (Figure 8.15) one can compare the interpretation with the geology map. There are similarities between the surface interpretation (Radiometric data) and the geology. The interpreted Karoo sediments in the north fall within the area mapped as Clarens Formation (A on Figure 8.15). The inferred granite and granodiorite in the south of the study area correlate to mapped outcrops of Malala drif gneiss and Alldays gneiss (B on Figure 8.15). The Malala drif gneiss inferred from the radiometric data (C on Figure 8.15) seems to cover the areas where Malala drif gneiss and Mount Dowe outcrops.

The mapped Mount Dowe Metaquartzite corresponds to the locality of the Endora quartzite inferred from radiometric data (D on Figure 8.15). In the southwestern part of the study area mapped outcrops of dolerite, marble or metaquartzite correlate well with interpreted geology.

Similarities between the magnetic interpretation and the mapped geology are less. Mostly the linear features in the northern half of the study area seem to correlate (a, b and c on Figure 8.15 as examples). Furthermore the inferred edge of a magnetic body seems to correlate very well with mapped dolerite outcrop (d on Figure 8.15). The only other correlation between the magnetic data interpretation and the mapped geology is the locality of the inferred sills S1a and S1b and that of numerous dolerite outcrops.

The magnetic interpretation added many features that were not on the mapped geology, such as the dykes in especially the southern part of the area where sand cover obscures them from sight. The magnetic bodies situated at depth in the north as well as the sills delineated in the south are contributions made to the geology from the geophysical interpretation.

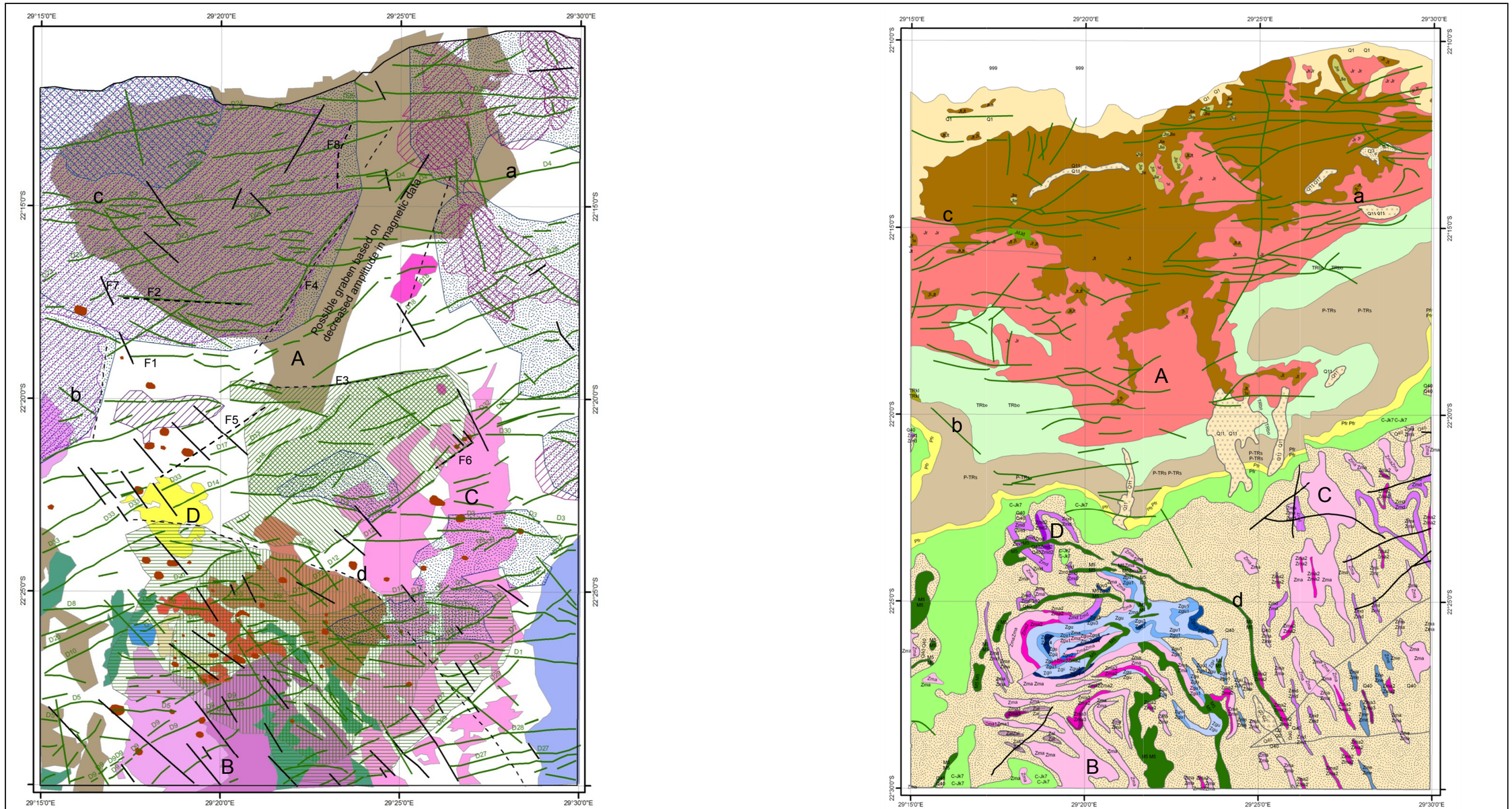


Figure 8.15. The geophysical interpretation map showing the bodies delineated from the magnetic data as hatched areas and the surface interpretation form radiometric data as solid areas. The faults modelled from the flight line and tie-line data are labelled as F1 to F8.

Surface interpretation (Radiometricdata)

- Dolerite
- Karoo Sediments
- Aplite
- Endora Quartzite
- Granite
- Granodiorite
- Malala Drift gneiss
- Transported Malala Drift gneiss
- Marble
- Marble / metaquartzite / dolerite
- Mine dump related
- Slimes Dam

Below surface interpretation Magnetic data)

- Edges of anomalies
- Lineaments
- Faults
- Round anomalies
- Very deep bodies
- B1
- B3 from Analytical Signal
- B3
- BB1
- BB2
- S1a
- S1b
- S3a
- S3b

Legend

- Linear feature
- KAROO DOLERITE
- Diabase (M5)
- Alluvium (Q1)
- Calcrete (Q11)
- Scree (Q2)
- Gravel (Q3)
- Sandy soil (Q40)

KAROO SUPER GROUP:
- KAROO DOLERITE (Jd)
- LETABA FM(Jle)
- CLARENS FORMATION: TSHIPISE MEM (Jt); RED ROCKS MEM (Jr)
- BOSBOKPOORT FM (TRbo)
- KLOPPERFONTEIN FM (TRkl)
- SOLITUDE FM (P-TRs)
- FRIPP FM (Pfr)
- KAROO (C-Jk7)

BEIT BRIDGE COMPLEX:
- ALLDAYS GNEISS (Zal)
- MESSINA (Zme)
- GUMBU (Zgu)
- GUMBU (Zgu1)
- GUMBU (Zgu2)
- GUMBU (Zgu3)
- GUMBU (Zgu4)
- MALALA DRIFT GNEISS (Zma)
- MALALA DRIFT GNEISS (Zma1)
- MALALA DRIFT GNEISS (Zma2)
- MALALA DRIFT GNEISS (Zma3)
- MOUNT DOWE (Zmd)
- MOUNT DOWE (Zmd2)

Description

C-Jk7, Undifferentiated Mikambeni and Madzaringwe
Jd, Network of dolerite sills, sheets and dykes, mainly intrusive into the Karoo Supergroup
Jle, Basic volcanic rocks (tholeiites, picrite basalts and nephelinites)
Jr, Light red, fine-grained, argillaceous sandstone
Jt, Relatively hard, fine-grained, white to cream sandstone
M5, Diabase
P-TRs, Grey, purple (in upper part) and green mudrock, subordinate siltstone and sandstone
Pfr, Coarse-grained felspathic sandstone, thin conglomerate layers
Q1, Alluvium
Q11, Calcrete
Q2, Scree
Q3, Gravel
Q40, Sandy soil
TRbo, Dominantly red mudstone (plus calcareous concretions), siltstone, minor sandstone
TRkl, Fine- to coarse-grained feldspathic sandstone
Zal, Grey, medium-grained, migmatitic, tonalitic-trondhjemitic gneiss
Zgu, Calc-silicate rocks and marble, together with leucogneisses and subordinate pink hornblende granitoid gneiss, metaquartzite and amphibolite
Zgu1, Metaquartzite
Zgu2, Leucocratic quartzo-feldspathic gneiss
Zgu3, Metapelite
Zgu4, Amphibolite, mafic granulite
Zma, Leucogneiss with metaquartzite, hornblende granitoid gneiss, amphibolite, metapelite and calc-silicate rocks
Zma1, Metapelite
Zma2, Amphibolite, mafic granulite
Zma3, Metaquartzite
Zmd, Metaquartzite, leucogneiss, pink biotite-hornblende granitoid gneiss
Zmd2, Metapelite
Zme, Meta-anorthosite, metaleucogabbro, metagrabbo, metapyroxenite

Figure 8.16. Legend of geophysical interpretation and mapped geology maps.

8.4. Combining the profiles to generate a three dimensional picture

The modelled profiles are displayed in three dimensions in Google Earth in Figures Figure 8.18 to Figure 8.21. When combining all the information gathered in the study, an interesting picture begins to take shape. The Karoo in the north-western two thirds of the study area has a north-northwest dip. This became evident from the logs of the boreholes drilled in the area for coal exploration. If it is assumed that the Karoo was deposited in a depositional basin, then it is feasible to accept that the Karoo rocks will follow the dip of the underlying basement it was deposited on. If this is the case then the basement has the same north to north-west dip which must have been acquired after deposition. From the aeromagnetic data, east to north-east trending dykes were delineated. When combining these data with the borehole logs, it became clear that vertical displacement occurred along some (if not all) of these dykes indicating that they intruded along faults.

These faults were modelled to be down-faulting the southern blocks in relation to the northern blocks. This type of faulting indicates extensional stress at a high angle (90°) to the normal faults (i.e. north-northwest). If the maximum extensional stress in the area is directed towards the north-north-west, then normal faults in an east-north easterly direction would be expected, as modelled. Shear zones and strike-slip faults would exist at low angles to the extensional stress direction and is evident as a shear zone mapped on the farm Gotha (Barton, 2011, personal communication) just south ofthe Venetia klippe (Figure 6.1) and a zone of disruption in the structures visible on the magnetic data, trending north-northwest.

These zones of weakness show a spatial correlation with round anomalies that are grouped in two clusters along these directions (east-northeast and north-northwest). The Venetia kimberlite intrusions are situated at the crossing of these two directions. It is conceivable that these existing zones of weakness were controlling the emplacement of the round anomalies, at least in the crust. Silver et al (2004) however showed that the

east-north-east direction also exists in the mantle, thus the weak zones could be due to mantle fabric.

Topographically the southern part of the study area (basement) is higher than the northern part (Karoo). This is probably due to the fact that the basement is more resistant to erosion than the Karoo sediments as well as the fact that the general dip of the basement and Karoo is towards the northwest. There is a topographic high through the centre of the study area, trending north-south. This coincides with a change in magnetic values and is modelled as a fault (Figure 8.10).

The magnetic bodies delineated in Chapter 6 were correlated with the modelled profiles to produce the interpretational map shown in Figure 8.15. The inferred dykes or lineaments are shown in green and those that are referenced in the models are labelled accordingly. The locality of the profiles are shown as stippled maroon lines and they are labelled to ease identification.

In the north west the modelled magnetic body 1 (B1) is shown in blue. The Beit Bridge II (BB2) is shown in lilac with the outline derived from the upward continued data shown as a stippled area covering BB2. In the north east the modelled magnetic body 3 (B3) is shown as dark pink. The outline of B3 from Analytical signal data is shown with a light pink hatching while the outline from the upward continued data is shown as an area with dark stipples covering B3. In the southern part the outlines of the modelled and inferred sills are shown in hatched green. Two deeper bodies delineated from the upward continued data could be more sills at depth.

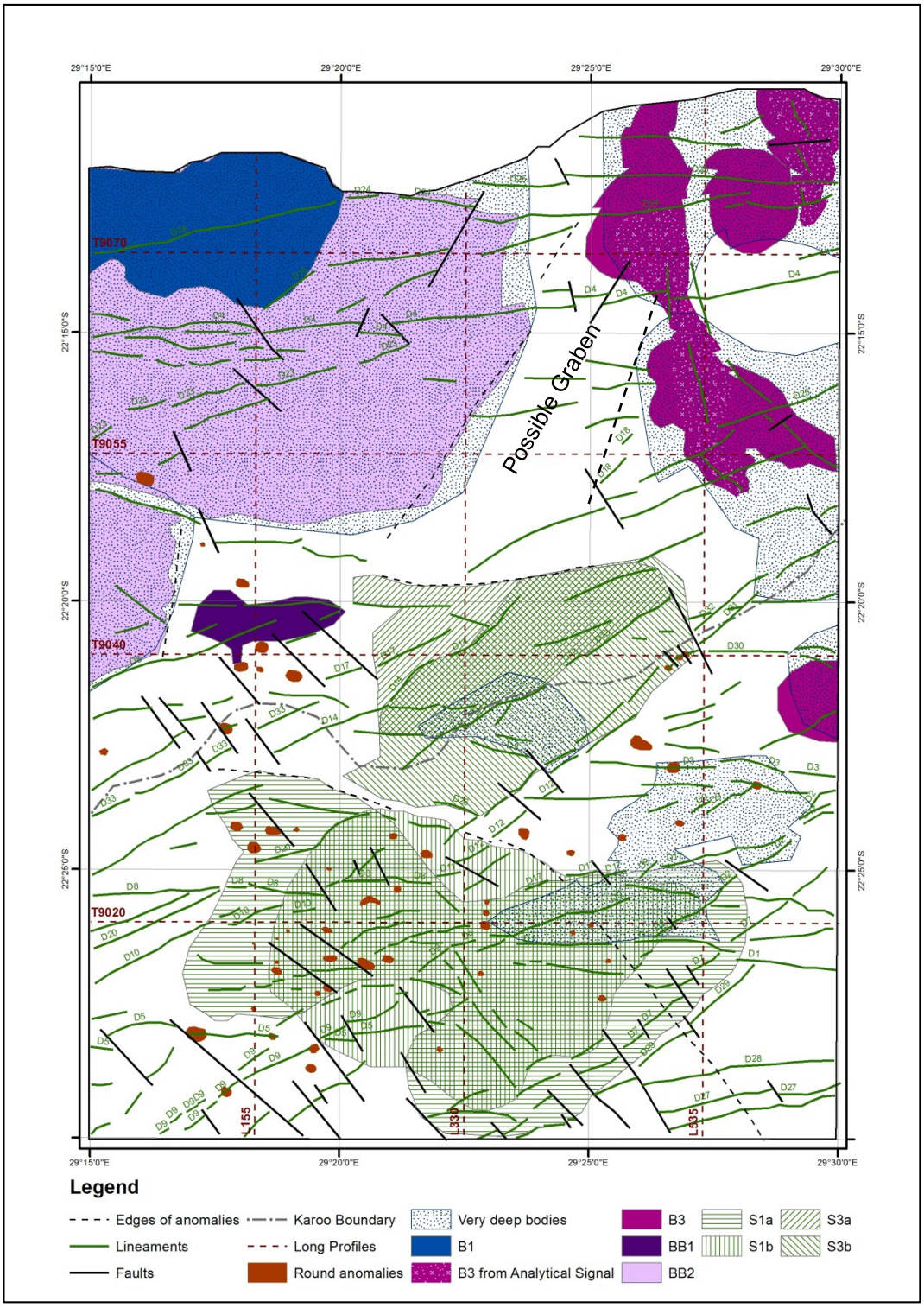


Figure 8.17. The magnetic interpretation map showing the bodies delineated from the magnetic data. The location of the profiles are shown in maroon and the dykes and magnetic bodies are labelled as they are in the profiles.

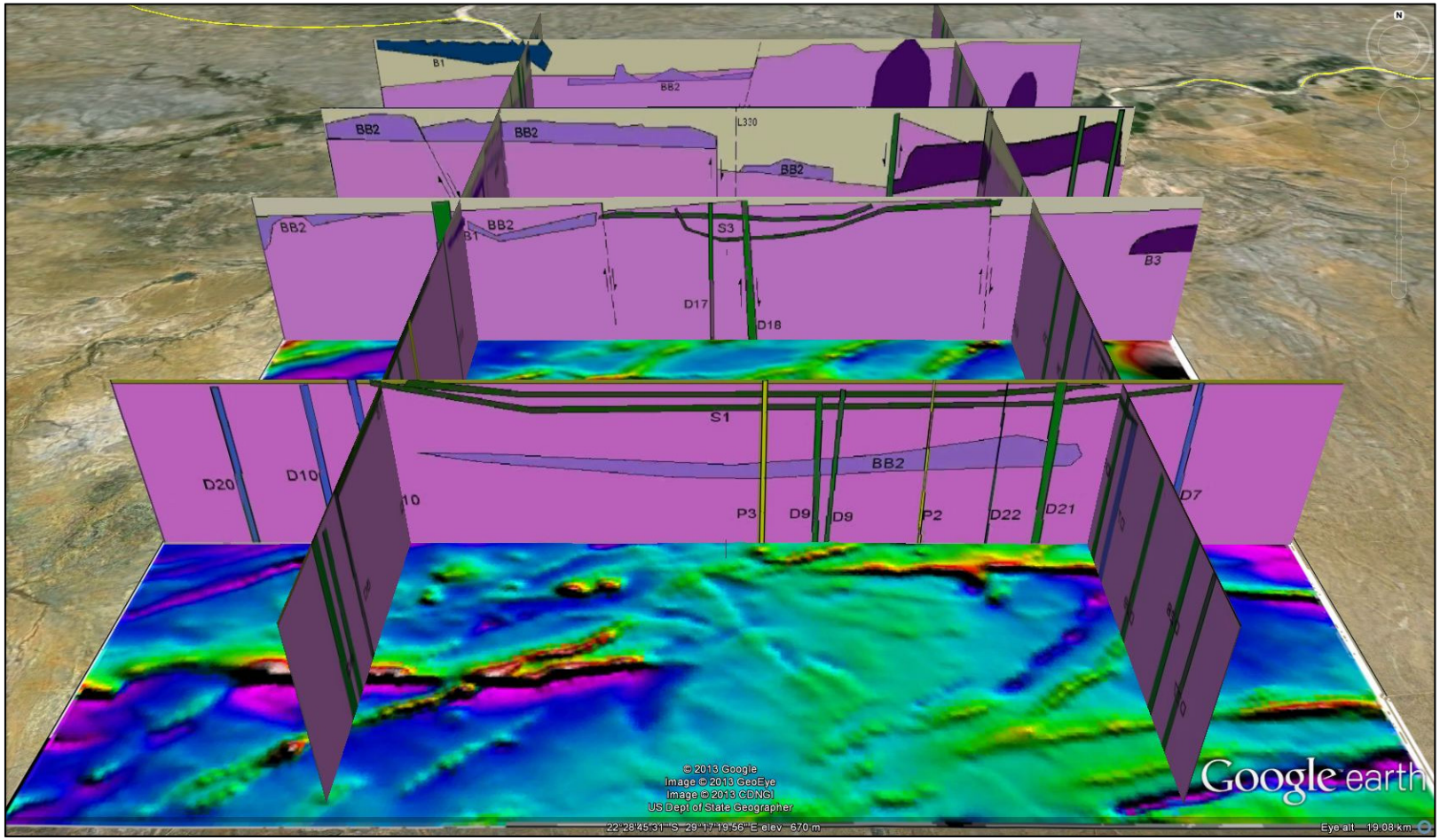


Figure 8.18. Profiles displayed in three dimensions facing due north in Google Earth.

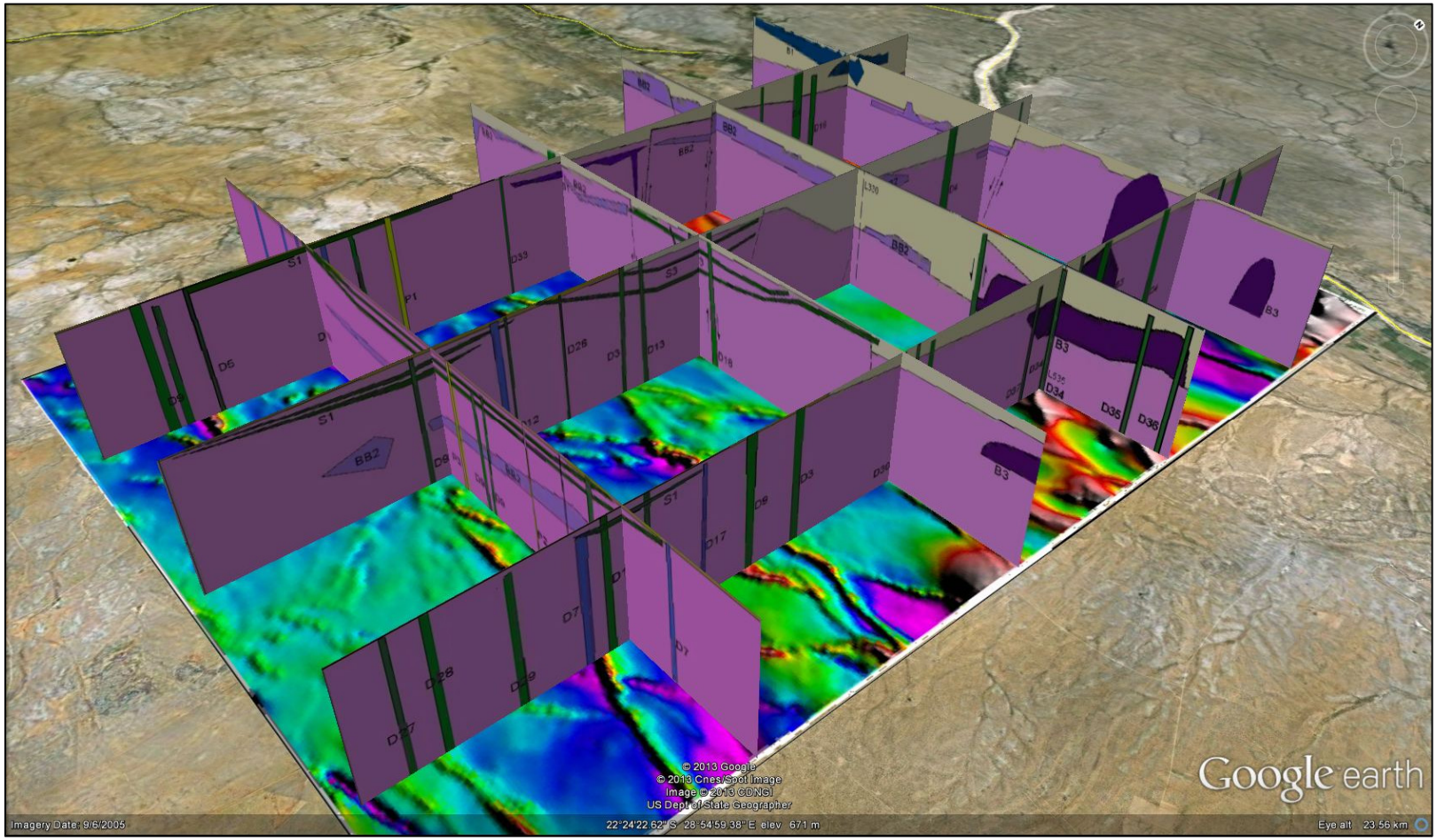


Figure 8.19. Profiles displayed in Google Earth facing northwest overlain on the magnetic data.

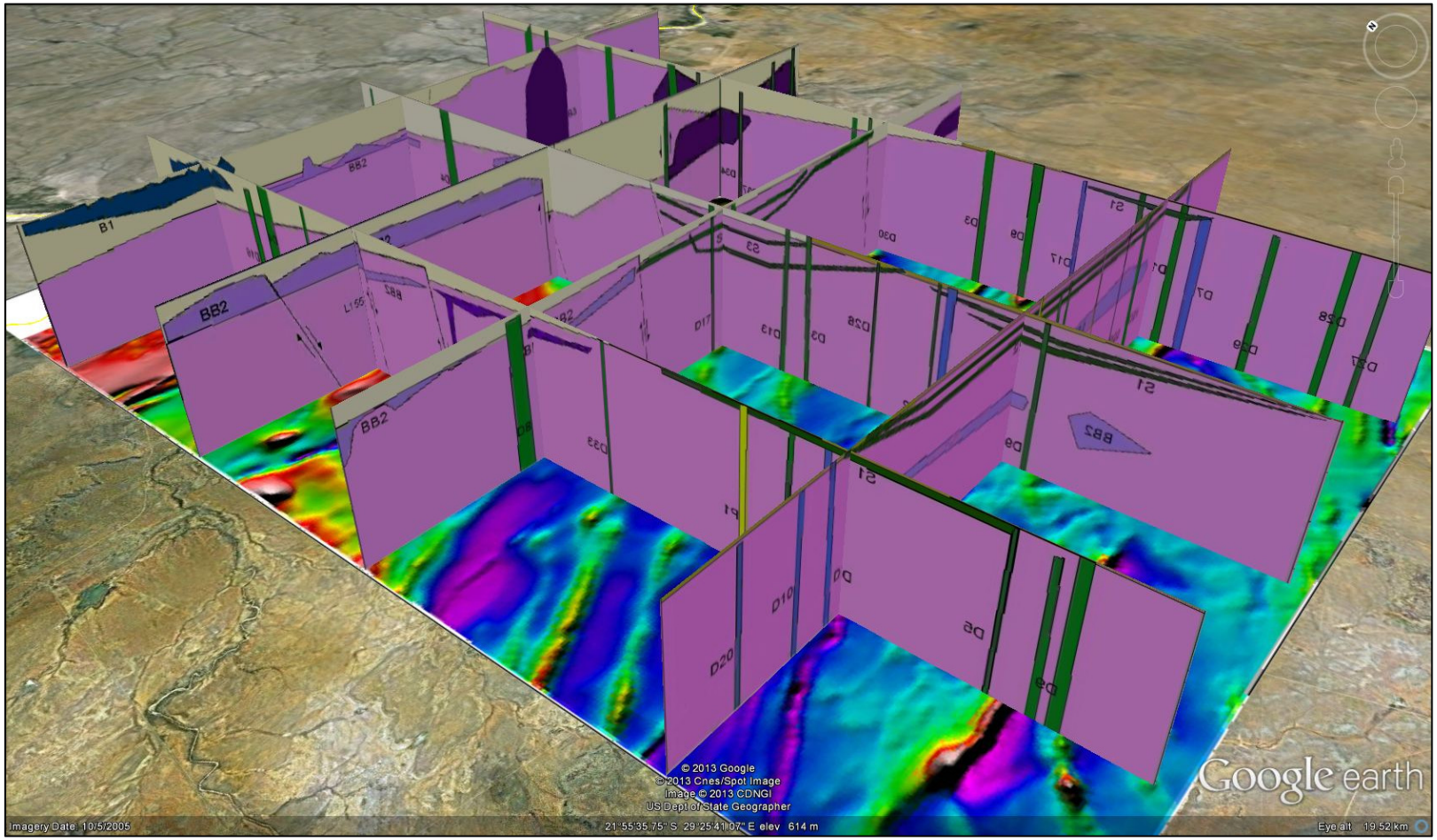


Figure 8.20. Profiles displayed in Google Earth facing northeast overlain on the magnetic data.

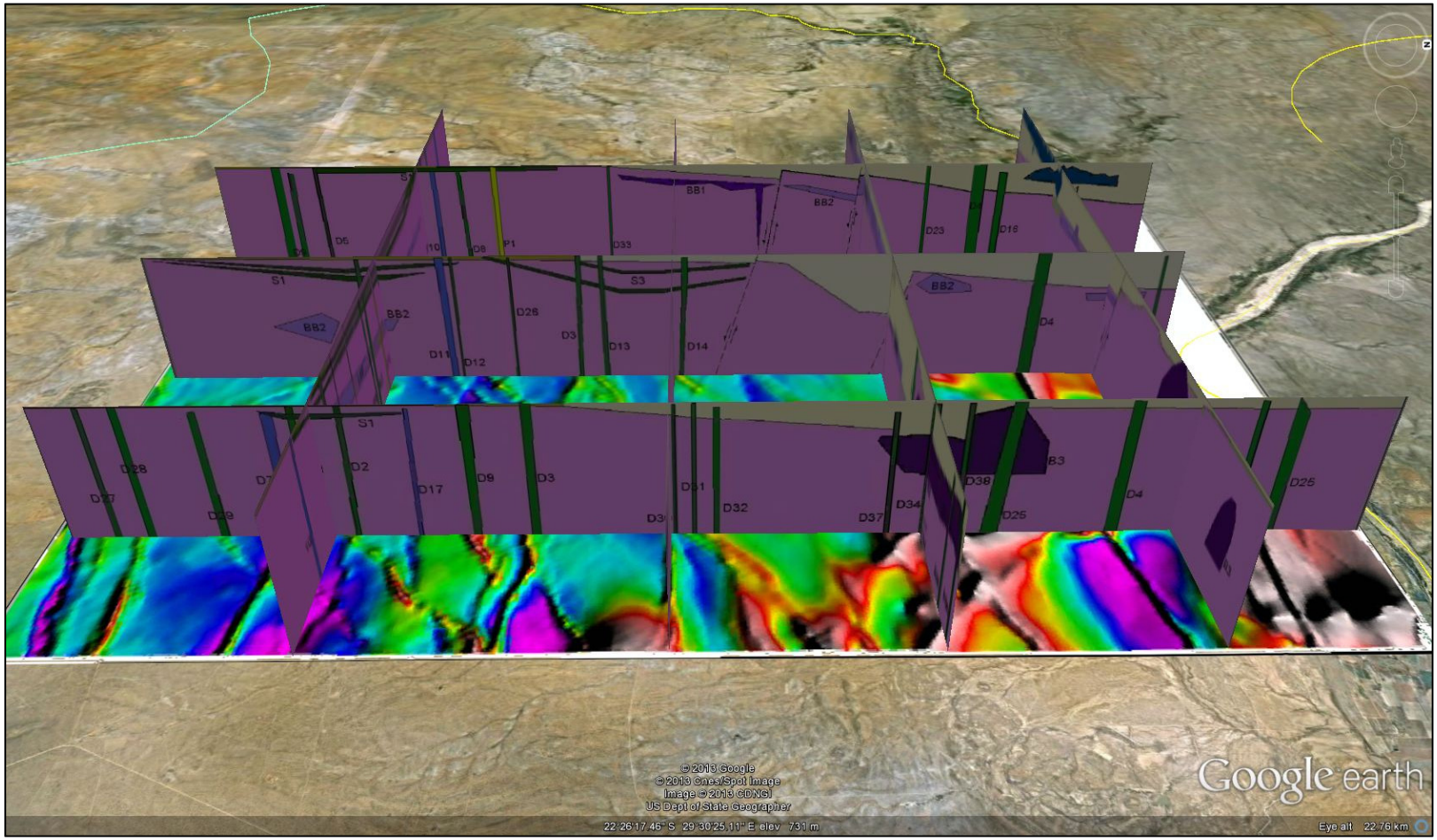


Figure 8.21. Profiles displayed in Google Earth facing west overlain on the magnetic data.

CHAPTER 9. Conclusions

From the new data presented and discussed in the previous chapters, several conclusions may be drawn.

9.1. Magnetic Lineaments

Most of the magnetic lineaments in the study area may be modelled as reflecting mafic dykes even though these may not be exposed at surface. The lineaments seem to be affected by remanent magnetism since there are quite a number of negatively magnetised lineaments. East-west trending lineaments appear to be post Karoo in age i.e. <200 Ma old. However, in the basement underlying the Karoo rocks lineaments with northeast and east-west orientations occur that are not found in the Karoo rocks and hence are pre-Karoo in age and post-Limpopo orogeny at ~2.04 Ga.

9.2. Circular anomalies

A series of north-northwest and east-northeast trending plug shaped magnetic bodies occur primarily in the southern portion of the study area and mostly in the area covered by Karoo sediments. They are confined in two clusters, the east-northeast trending cluster coinciding with the east-northeast trending dykes and the north-northwest trending cluster coincides with a zone of deformation mapped by Kurszlaukis and Barnett (2003) and inferred from the magnetic data as a zone of disruptions in the structures. Some of these bodies may be correlated with doleritic intrusions and others with kimberlite intrusions. Most, however, have no apparent surface expression (see Figure 9.1).

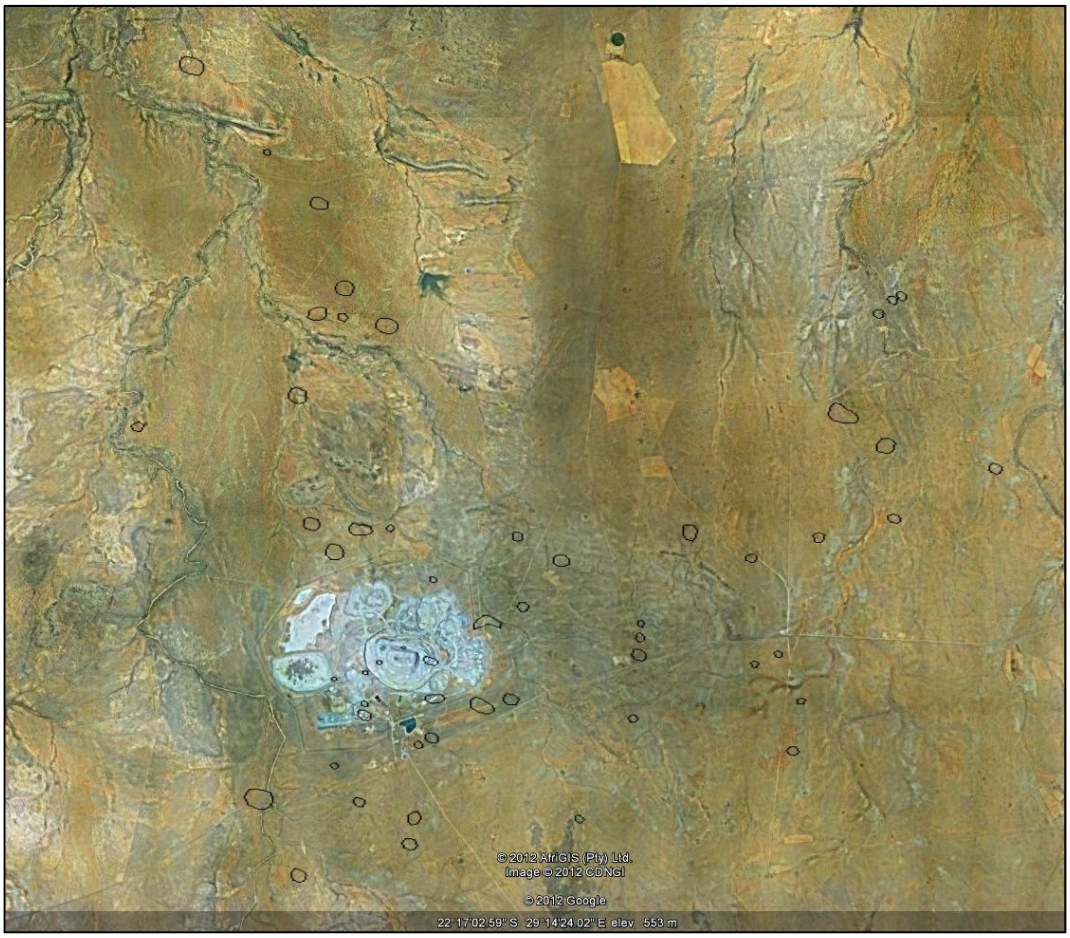


Figure 9.1. Google Earth image with the round anomalies inferred from magnetic data shown as black outlines. Venetia is clearly visible on the crossing of the two clusters and none of the anomalies have surface expression.

9.3. Radiometric data as a mapping aid

Radiometric data for K, Th and U either singly or in combination clearly distinguish distinct geological bodies specifically in the pre-Karoo basement. The shapes of these bodies broadly correlate with the detailed mapping in the southwestern portion of the study area (Barton et al., 2003).

9.4. Cross sections and 3-dimensional modelling

A series of geological cross-sections were modelled for the study area and from these certain three-dimensional bodies were identified. The cross sections constrained by drilling results clearly show that the Karoo strata dip and thicken to the north and that over most of the area they are offset by east-west trending, southerly (based on de Beer and Stettler, 1992) dipping normal faults. In the northeastern portion of the study area, the faulting is more complex.

There are multiple saucer-shaped sills mapped in the area and their edges are visible on the magnetic data. The magnetic data clearly show the extent of the mafic sills at a depth of about 250 m which are intruded by the Venetia kimberlite intrusions. Another sill is modelled at greater depth, but this is only one possible interpretation. It is not possible to determine precisely how many sills there are, their individual thicknesses or precise depths without additional information from drilling and physical property measurements. Magnetic data shows the total effect of all the sills combined.

In the northeastern part of the study area, a magnetic intrusive body was identified that has no surface expression. This could be a mafic intrusive body as modelled or it could be greenstones beneath the Karoo. The only sure way to determine exactly what is causing the anomaly is to drill.

It is recommended that further detailed studies including drilling and ground geophysics are undertaken to determine the source of the magnetic anomalies in the north of the study area.

References

Baranov, V. (1957). A new method for interpretation of aeromagnetic maps: pseudo-gravimetric anomalies. Geophysics, 22 (2), 359-383.

Barnettt, M., (2005). Geological and geochemical study of the quartzofeldspathic rocks from the Farm Gotha, Limpopo Province, South Africa, Unpublished MSc thesis, Rand Afrikaans University, Johannesburg, South Africa, 102 pp. plus appendices and maps.

Barnettt, W.P. (2003). Geological control on slope failure mechanisms in the open pit at the Venetia Mine. South African Journal of Geology, 106, 149-164.

Barnettt, W.P. (2006). The mechanics of kimberlite emplacement. Unpublished Ph.D. thesis, School of Sciences, University of KwaZulu Natal, Durban, South Africa, 277pp. plus appendices.

Barton, J.M., Jr., Doig, R., Smith, C. B., Bohlender, F. and Van Reenen, D.D. (1992). Isotopic and REE characteristics of the intrusive charnoenderbite geographically associated with the Matok Complex. Prec. Res., 55, 451 - 467.

Barton, J.M. Jr.,Holzer, L., Kamber, B., Doig, R., Kramers, J.D. and Nefeler, D.(1994). Discrete metamorphic events in the Limpopo Belt, southern Africa: Implications for the application of P-T paths in complex metamorphic terranes. Geology, 22, 1035-1038.

Barton, J.M. Jr., Barnettt, W.P., Barton, E.S., Barnettt, M., Doorgapershad, A., Twiggs, C., Klemd, R., Martin, J., Mellonig, L. and Zenglein, R. (2003). The geology of the area surrounding the Venetia kimberlite pipes, Limpopo Belt, South Africa: A complex interplay of nappe tectonics and granitoid magmatism. South African Journal of Geology, 106, 109-128.

Barton, J.M. Jr., Klemd, R. and Zeh, A. (2006). The Limpopo Belt: A result of Archaean to Proterozoic, Turkic-type orogenesis? In Reimold W.U. and Gibson. R.L., Processes on the Early Earth: Geological Society of America Special Paper, 405, p. 315 – 332.

Birch, F. (1960). The velocity of compressional waves in rocks to 10 kilobars, Part I, Journal of Geophysical Research, 65, 1083-1102.

Blakely, R. J. (1995). Potential Theory in Gravity and Magnetic Applications. Cambridge University Press, New York. 435 pp.

Brandl, G. (2002). The geology of the Alldays area. Explanation: Sheet 2228, Council for Geoscience, South Africa, 71pp.

Brandl, G., (2007). The geology of the Ga-Mabelebele and Taaiboschgroot areas. Expl. Sheets 2229 CC 2228DD. CGS

Chernicoff, C.J., (1984). A synthesis of the structural geology of the northern Transvaal. Unpublished M.Sc. Thesis, Rand Afrikaans University, South Africa 155pp.

Chudy, T. C., (2007). Geological and petrologican investigation on lithologies from the farm Icon 95 MS in the Central Zone of the Limpopo Beelt, South Africa, Unpublished Diploma Thesis, University of Würzburg, Germany, 157 pp. plus map.

Coetzee, H. (2001). Lecture notes for Gamma-Ray Spectrometry Course, Report, Council for Geoscience, South Africa, 51pp. (Unpublished)

Cole, P., Grace, T., Eberle, D.G., Antoine, L. and Havenga, M. (2009). Airborne magnetic and spectrometric geophysical survey of West-Central Gabon. Council for Geoscience internal report, 2009-0221, 73pp.

Cooper, G.R.J., (2002). An improved algorithm for the Euler deconvolution of potential field data. The Leading Edge 21 (12) p.1197-1198.

Cooper, G.R.J., (2004). The stable downward continuation of potential field data. Exploration Geophysics, 35, 260 - 265.

Cooper, G.R.J., (2004)i. Aeromagnetic Data Precessing Course, Sweden.

Cooper, G.R.J., (2003). Feature detection using sunshading., Computers and Geosciences, 29, 941 – 948.

Cooper, G.R.J. (2009). Balancing images of potential-field data. Geophysics, 74, L17 – L20.

Cooper, G.R.J. and Cowan, D.R. (2005). Differential reduction to the pole. Computers & Geosciences, 31, 989-999.

Cornell, D. H., Thomas, R. J., Moen, H. F. G., Reid, D. L., Moore, J. M. and Gibson, R. L., (2006). The Namaqua-Natal Province. In: M. R. Johnson, C. R. Anhaeusser and R. J. Thomas (Editors). Geology of South Africa, Geological Society of South Africa-Council For Geoscience, South Africa, 325-380.

Council for Geoscience, South Africa. (1997). Magnetic Map of the Republic of South Africa. 1:1 000 000. Regional Aeromagnetic Series.

Council for Geoscience, South Africa. (1997). Total Count Radiometric Map of the Republic of South Africa. 1:1 000 000. Regional Aeroradiometric Series.

Council for Geoscience, South Africa. (2000). 2228 Alldays 1:250,000. Geological Map Series.

Coward, M.P., and Fairhead, J.D. (1980). Gravity and structural evidence for the deep structure of the Limpopo belt, southern Africa. Tectonophysics, 68, 31 - 43.

De Beer, J.H. and Stettler, E.H. (1992). The deep structure of the Limpopo Belt from geophysical studies. Precambrian Research, 55, 173-186.

De Beer, J.H., Stettler, E.H., Duvenhage, A.W.A., Joubert, S.J and Raath, C.J. se W. (1984). Gravity and geoelectrical studies of the Murchison Greenstone belt.

South Africa. Transactions of the Geological Society of South Africa, 84, 347 - 359.

Durrheim, R.J., Barker, W.H. and Green, R.W.E. (1992). Seismic studies in the Limpopo Belt. Precambrian Research, 55, 187-200.

Emiliani, C. (1992). Planet Earth. Cosmology, geology and the evolution of life and environment. Ed. Cambridge University Press, New York, pp 701.

Eriksson, S. C. (1989). Phalaborwa: a saga of magmatism, metasomatism and miscibility. In: K. Bell (Editor). Carbonatites: Genesis and Evolution, Unwin Hyman, London, U.K., 221-254.

Fry, N., (1979). Random point distributions and strain measurement in rocks: *Techtonophysics, 60, 89 - 105*

Gunn, P.J. (1975). Linear transformations of gravity and magnetic fields. Geophys. Prosp., 23, 300 - 312

Gunn, P.J., Maidment, D., Milligan, P.R. (1997). Interpreting aeromagnetic data in areas of limited outcrop. AGSO Journal of Australian Geology and Geophysics, 17, p. 175-185.

Hunt, C.P., Moskowitz, B.M., Banerjee, S.K. (1995). Magnetic properties of rocks and minerals, In: Ahrens, T.J. (Ed.), Rock Physics and Phase Relations: a Handbook of Physical Constants, American Geophysical Union, 236pp

IAEA (1991). Airborne gamma ray spectrometer surveying. International Atomic Energy Agency, Vienna, Tecnical reports series, 323, 56pp.

IAEA (2003). Guidelines for radioelement mapping using gamma ray spectrometry data. International Atomic Energy Agency, Tecdoc 1363, 179pp.

International Association of Geomagnetism and Aeronomy, Working Group V-MOD. Participating members, Finlay, C. C., Maus, S., Beggan, C. D., Bondar, T. N., Chambodut, A., Chernova, T. A., Chulliat, A., Golovkov, V. P., Hamilton, B., Hamoudi, M., Holme, R., Hulot, G., Kuang, W., Langlais, B., Lesur, V., Lowes, F. J., Lühr, H., Macmillan, S., Mandea, M., McLean, S., Manoj, C., Menvielle, M., Michaelis, I., Olsen, N., Rauberg, J., Rother, M.,

Sabaka, T. J., Tangborn, A., Tøffner-Clausen, L., Thébault, E., Thomson, A. W. P., Wardinski, I., Wei, Z. and Zvereva, T. I. (2010), International Geomagnetic Reference Field: the eleventh generation. *Geophysical Journal International*, **183,** 1216–1230.

Ito, H., Tokeida, K., Suwa, K., Kuma, S. (1978). Remanent magnetism of Precambrian and Cretaceous kimberlites in South Africa. Geophys J. Roy. Astron. Soc. (55). 123 - 130.

Jaeckel, P., Kröner, A., Kamo, S.L., Brandl, G. and Wendt, J.I. (1997). Late Archaean to early Proterozoic granitoid magmatism and high-grade metamorphism in the central Limpopo belt, South Africa. Journal of the Geological Society of London, 154, 25 – 44.

Kamber, B.S., Kramers, J.D., Napier, R., Cliff, R.A. and Rollinson, H.R. (1995). The Triangle Shear Zone, Zimbabwe, revisited, new data document an important event at 2.0 Ga in the Limpopo Belt. Precambrian Research, 70, 191 – 213.

Kirchenbaur, M., (2007). Geological and geochemical investigation on granites and gneisses of the Farm Regina 68 MS in the Cental Zone of the Limpopo Bobile Belt, South Africa. Unpublishsed Diploma Thesis, University of Würzburg, Germany, 121 pp plus appedices and map.

Kleywegt, R.J., De Beer, J.H., Stettler, E.H., Brandl, C., Duvenhage, A.W.A. and Day, R.W. (1987). The structure of the Giyani greenstone belt as derived from geophysical studies. South African Journal of geology, 90, 282 - 295.

Kramers, J. D. and Smit, C. B (1983). A feasibility study of U-Pb and Pb-Pb dating of kimberlite using groundmass mineral fractrions and whole-rock samples. Isotope Geoscience, 1, 23-38.

Kröner, A., Jaeckel, P., Brandl, G., Nemchin, A.A. and Pidgeon, R.T. (1999). Single zircon ages for granitoid gneisses in the Central Zone of the Limpopo Belt, Southern Africa and geodynamic significance. Precambrian Research, 93, 299 – 337.

Kurszlaukis, S and Barnettt, W.P. (2003). Volcanological and structural aspects of the Venetia kimberlite cluster - a case study of South African kimberlite maar-diatreme volcanoes. South African Journal of Geology, 106, 165-192.

Ledwaba, L., Dingoko, O., Cole, P. and Havenga, M. (2009). Compilation of Survey specifications for all the old regional airborne geophysical surveys conducted over South Africa. Council for Geoscience internal report, 2009-0130, 45pp.

Letts, S.A. (2007). The palaeomagnetic significance of the Bushveld Complex and related 2 Ga magmatic rocks in ancient continental entities. Unpublished Ph.D thesis, University of the Witwatersrand, 253pp.

Li, X. (2006). Understanding 3D analytic signal amplitude. Geophysics, 71(2), L13-L16.

Luyendyk, A.P.J. (1997). Processing of airborne magnetic data. AGSO Journal of Australian Geology & Geophysics, 17(2), 31-38.

Maré, L.P., Tabane, L.R. (2004). Physical properties of South African rocks, South African Geophysical Atlas, Volume 4, Council for Geoscience, 40 pp.

Martin, J., (2002). Geological and mineralogical investigationon an area adjacent to the Venetia kimberlite pipes (South Africa). Unpublsihed Diploma Thesis, University of Würzburg, Germany, 132 pp plus map.

Mauring, E. and Kihle, O., 2006. Leveling aerogeophysical data using a moving differential median filter. Geophysics, 71(1), L5-L11.

Minty, B.R.S. (1997) Fundamentals of airborne gamma-ray spectrometry. Journal of Australian Geology and Geophysics, 17(2), 39 - 50.

Minty, B.R.S., Luyendyk, A.P.J and Brodie, R.C. (1997). Calibration and data processing for airborne gamma-ray spectrometry. AGSO Journal of Australian Geology & Geophysics, 17(2), 51-62.

Milligan, P.R. and Gunn,P.J. (1997) Enhancement and preserntation of airborne geophysical data. AGSO Journal of Geology and Geophysics, 17, 63 - 75.

Millonig, L., (2004). Geological map of an area adjacent to the Venetia Diamond Mine, Limpopo Province, South Africa. Diploma mapping for the Diploma in

Geology/Palaeontology, Dept. Geology/Palaeontology, Julius-Maximilians-University, Wurzburg.

Parsons, S., Nadeau, L., Keating, P. and Chung, C-J. (2006). Optimising the use of aeromagnetic data for predictive geological interpretation: an example from the Grenville Province, Quebec. Computers & Geosciences, 32, 565 - 576.

Patterson, A. L. (1934). A Fourier series method for the determination of the components of interatomic distances in crystals. Physics Review, 46(5), 372 - 376.

Patterson, A. L. (1935). A direct method for the determination of the components of inter-atomic distances in crystals. *Zeitschrift fuer Krystallographie*, 90, 517 - 554.

Piper, J.D.A. (1975). The palaeomagnetism of Precambrian igneous and sedimentary rocks of the Orange River Belt in South Africa and South West Africa. Geophys J. Roy Astron Soc. (40), 313 - 344.

Perutz, M. F. (1942). X-ray analysis of Haemoglobin. Nature, 149, 491‑494.

Pretorius, S. J. (1986). Die geologie in die omgewing van Swartwater en die westelike deel van die distrik Messina in die sentrale sone van die Limpopo-gordel. M.Sc Thesis, Rand Afrikaans Universiteit, Johannesburg, South Africa.

Pretorius, W. (1996). A geochemical and geophysical investigation of a suite of crustal and upper mantel nodules from Venetia kimberlite pipes, Limpopo Belt, South Africa. Unpublished M.Sc. thesis, RAU, Johannesburg, South Africa, 275pp.

Pretorius, W. and Barton, J.M. (Jr). (2003a). Measured and calculated compressional wave velocities of crustal and upper mantle rocks in the Central Zone of the Limpopo Belt, South Africa - implications for lithospheric structure. South African Journal of Geology, 106, 205-212.

Pretorius, W. and Barton, J.M. (Jr). (2003b). Petrology snd geochemistry of crustal and upper mantle xenoliths from the Venetia Diamond Mine - evidence for Archaean crustal growth and subduction. South African Journal of Geology, 106, 201-230.

Reid, A.B. (1980). Aeromagnetic survey design. Geophysics, 45 (5), 973-976.

Reid, A.B., Allsop, J.M., Granser, H., Millet, A.J., and Somerton, I.W., (1990). Magnetic interpretation in three dimensions using Euler deconvolution. Geophysics 55, 80-91.

Reischmann, T. (1995). Precise U/Pb age determination with baddeleyite (ZrO_2), a study from the Phalaborwa Igneous Complex, South Africa, South African Journal of Geology, 98, 1-4.

Roest, W. R., Verhoef, J. and Pilkington, M. (1992). Magnetic interpretation using the 3-D analytic signal. Geophysics, 57, 116–125.

Schwarz, G.F., Klingele, E.K., Rybach, L. (1992). How to handle rugged topography in airborne gamma-ray spectrometry surveys, First break 10, 11-17.

Silver, P.G., Fouch, M.J., Gao, S.S., Schmitz, M. and Kaapvaal Seismic Group. (2004). Seismic anisotropy, mantle fabric and the magmatic evolution of Precambrian southern Africa. South African Journal of Geology, 2004, 107, 45 – 58.

Southern African Development Community. (1999). Magnetic Map of the SADC countries.

Stettler, E.H., De Beer, J.H., Blom, M.P. (1989). Crustal Domains in the Northern Kaapvaal Craton as Defined by Magnetic Lineaments. *Precambrian Researh,* **45**, 263 – 276.

Stuart, G.W. and Zengeni, T.G. (1987). Seismic crustal structures of the Limpopo mobile belt. Zimbabwe. Tectonophysics, 144, 323 - 335.

Stubley, M. (2004). Spatial distribution of kimberlite in the Slave Craton: A geometrical approach. Long abstract, 8th International Kimberlite Conference, 5pp.

Twiggs, C., (2004). The tectonic evolution of the rocks comprising the Venetia Klippe, Limpopo Belt, South Africa, with emphasis on carbonate and calc-silicate

rocks and pegmatite. Unpublished MSc thesis, Rand Afrikaans University, South Africa, 128 pp.

Van Schmus, W.R., (1995). Natural radioactivity of the Crust and Mantle, in T.J. Ahrens, ed., Global Earth Physics: A Handbook of Physical Constants. American Geophysical Union, AGU Reference Shelf 1, p. 283-291.

Vearncombe, J.R. and Vearncombe, S. (1999) The spatial distribution of mineralization: applications of Fry analysis. Economic Geology, 94, 475 - 486.

Vearncombe, J.R. and Vearncombe, S. (2000) The spatial distribution of grade. In: Fourth International Mining Geology Conference, Mine Geology 2000, Australasian Institute of Mining and Metallurgy, pp. 87‑93.

Wilson, J.F. (1990). A craton and its cracks: some of the behaviour of the Zimbabwe Block from late Archaean to the Mesozoic in response to horizontal movements, and the significance of some of its mafic dyke fracture patterns. Journal of African Earth Sciences, 10, 483–501

Zenglein, R., (2004). Geological and mineralogical investigations on an area north of the Venetia Diamond Mine, South Africa. Diploma mapping and Diploma thesis for the Diploma in Geology / Palaeontology, Dept. Geology/Palaeontology, Julius-Maximilians-University, Wurzburg.